Technische Universität München
Physik-Department
Experimental Physics with Cosmic Particles

High-energy cosmic ray accelerators: searches with IceCube neutrinos

Probing seven years of IceCube muon data for time-integrated emission of point-like neutrino sources.

Stefan Coenders

Vollständiger Abdruck der von der promotionsführenden Einrichtung
Fakultät für Physik
der Technischen Universität München zur Erlangung des akademischen Grades eines

Doktors der Naturwissenschaften (Dr. rer. nat.)

genehmigten Dissertation.

Vorsitzender	Prof. Dr. Björn Garbrecht
Prüfende(r) der Dissertation:	1. Prof. Dr. Elisa Resconi
	2. Priv.-Doz. Dr. Jochen Greiner
	3. Prof. Dr. Miguel Mostafa
	(nur schriftliche Beurteilung)

Die Dissertation wurde am 5.10.2016 bei der Technischen Universität München eingereicht und durch die Fakultät für Physik am 19.10.2016 angenommen.

Abstract

Since the recent detection of an astrophysical flux of high energy neutrinos, the question of its origin has not yet fully been answered. At the same time, connected with cosmic neutrinos, the origin of ultra high-energy cosmic rays is also an open mystery in modern physics. Neutrinos can in principle help solving this puzzle because they trace hadronic interactions.

In this thesis, seven years of data recorded with the IceCube Neutrino Observatory are analyzed with the objective to identify significant clustering of astrophysical neutrinos. The analysis uses the good angular reconstruction[1] and large statistics of muon track events. More than 700 000 events are probed for time-integrated clustering of neutrinos using an unbinned likelihood formalism. In the northern sky, IceCube is now sensitive to fluxes as low as $E^2 \partial\phi/\partial E = 10^{-12}\,\mathrm{TeV\,cm^{-2}\,s^{-1}}$, an improvement of $\sim 40\%$ to the previous published analysis.

No significant clustering of neutrinos was observed either searching in the full sky or in coincidence with high energy gamma ray objects. Upper limits for time-integrated neutrino-emission are calculated, inferring constraints on the nature of the observed astrophysical neutrino signal and the lepto-hadronic composition of the brightest gamma ray objects in the sky.

In a complementary way, a novel study that connects ultra high-energy cosmic rays, neutrinos and gamma rays in a multi-messenger approach has been developed. The goal is to identify gamma ray counterparts of neutrinos and cosmic rays combining the power of the various messengers. Using the most energetic neutrino and cosmic ray events recorded by IceCube, the Pierre Auger Observatory, and the Telescope Array, respectively, an excess of events is found associated to hard Fermi-LAT (2FHL) objects of BL Lac type with high synchroton peak (HBL). The excess is found to be significant at 3.35σ and HBL objects show correlation in other catalogs used as well. Hence, evidence for HBL sources as one source contributing to the cosmic ray and neutrino spectrum is found. This could represent the first step towards the beginning of neutrino astronomy.

[1] The angular resolution of neutrino events is below 1°

Zusammenfassung

Die Frage nach dem Ursprung der höchstenergetischen astrophysikalischen Neutrinos ist nicht zufriedenstellend beantwortet. Darüberhinaus sind, die Quellen der kosmischen Teilchen insbesondere bei den höchsten Energien nicht bekannt. Neutrinos können bei der Identifikation der Quellen von kosmischer Strahlung helfen, weil sie in hadronischen Wechselwirkungen erzeugt werden.
Diese Arbeit beschreibt die Analyse von Daten, die über sieben Jahre mit dem IceCube Neutrino Observatory aufgenommen wurden. Das Ziel der Analyse ist die Identifikation von Quellen der astrophysikalischen Neutrinos durch einen Überschuss an der Position der Quelle. Dazu werden Neutrinos benutzt, die gut rekonstruiert und mit hoher Statistik detektiert werden. Mehr als 700 000 Ereignisse werden auf Zeit-integrierte Emission von Quellen astrophysikalischer Neutrinos mithilfe einer "unbinned likelihood" Analyse untersucht. IceCube erreicht im gesamten Nordhimmel eine Sensitivität, die niedriger ist als ein Fluss von $E^2 \partial\phi/\partial E = 10^{-12}\,\mathrm{TeV\,cm^{-2}\,s^{-1}}$, was einem Gewinn von $\sim$ 40% respektive der vorherigen publizierten Analyse entspricht.
Keine signifikante Quelle von astrophysikalischen Neutrinos wurde in Suchen auf dem gesamten Himmel oder in Koinzidenz mit hochenergetischen Quellen von Gamma-Strahlung gefunden. Limits auf die Zeit-integrierte Emission von Neutrinos für verschiedene Quellen werden aus den Daten abgeleitet. Lepto-hadronische Modelle für spezifische Quellen werden durch die IceCube Daten stark eingeschränkt.
In einem zweiten Test wird eine neue Studie vorgestellt, die kosmische Teilchen mit Neutrinos und astrophysikalischer Gamma-Strahlung kombiniert, um die Quellen der hochenergetischen kosmischen Strahlung zu identifizieren. Die Analyse der höchstenergetischen kosmischen Teilchen, die von dem Pierre Auger Observatorium und dem Telescope Array detektiert wurden, und IceCube's Neutrinos ergab einen Überschuss an kosmischen Teilchen in Koinzidenz mit Fermi-LAT (2FHL) identifizierten Blazaren des Typs BL Lac, deren Synchroton Strahlung bei sehr hohen Frequenzen maximal ist (HBL). Der Exzess hat eine statistische Signifikanz von 3.35σ, und ist auch für HBL Quellen in anderen Katalogen als 2FHL vorhanden. Als Schlussfolgerung daraus bieten sich Blazare (BL Lac vom Typ HBL) als ein möglicher Kandidat als Quelle der kosmischen Strahlung an den höchsten Energien an.

Contents

List of Figures

List of Tables

1 Introduction

The first observation of high-energy neutrinos of extraterrestrial origin obtained by IceCube represents a milestone towards the understanding of the non-thermal universe. The IceCube discovery was awarded the *Physics World Breakthrough of the Year* in 2013.[1] In the acceleration of cosmic rays, neutrinos will be produced in hadronic interactions. Hence, an identification of a source of neutrino emission is a unique *smoking gun* signal for the sources of cosmic rays.

[1] Johnston, *Physics World Breakthrough of the Year*.

The observed signal of astrophysical neutrinos and ultra-high energy cosmic ray (UHECR) events is probed for an identification of their sources throughout this thesis with the title

High-energy cosmic ray accelerators:
searches with IceCube neutrinos

using the most recent multi-messenger data available. The IceCube Neutrino Observatory at the South Pole is currently the largest operational neutrino detector and the only detector to be sensitive enough to detect a diffuse high-energy astrophysical neutrino signal.

Albeit discovering astrophysical neutrinos in multiple, complementary detection channels,[2] no sources of neutrinos are yet identified, nor any connection to other messengers in astroparticle physics, that is, cosmic ray particles and gamma rays.[3] The work realized during this thesis pushes the boundaries of the sensitivity to emission of high-energy neutrinos from cosmic accelerators with improvements in the sophisticated analysis methods, the processing of new years of IceCube data and exploration of new multi-messenger approaches.

[2] Aartsen, "Evidence for High-Energy Extraterrestrial Neutrinos at the IceCube Detector"; Aartsen, "Evidence for Astrophysical Muon Neutrinos from the Northern Sky with IceCube".

[3] Aartsen, "Search for correlations between the arrival directions of IceCube neutrino events and ultrahigh-energy cosmic rays detected by the Pierre Auger Observatory and the Telescope Array"; Glüsenkamp, "Analysis of the cumulative neutrino flux from Fermi-LAT blazar populations using 3 years of IceCube data".

The analyses done in this thesis can be split into two distinct topics. The first one is the search for time-integrated emission of astrophysical neutrinos using seven years of IceCube muon data recorded from June 2008 until June 2015. The existing analysis of four years data[4] is extended using three additional years of IceCube operation. A data sample was developed to give optimal performance for the identification of sources emitting neutrinos at TeV energies and above over the full sky. In total, a vast event sample of more than 700 000 events was tested for the identification of neutrino sources. Multiple hypotheses for the emission were tested and, given the non-detection of a neutrino source, constraints on the nature of neutrino emission are calculated.

[4] Aartsen, "Searches for Extended and Point-like Neutrino Sources with Four Years of IceCube Data".

The second part of a more explorative nature connects IceCube's high-energy neutrinos to UHECR events recorded with the Pierre Auger Observatory and the Telescope Array, using the highest energetic cosmic rays ever observed with energies exceeding 52 EeV. Using a novel approach developed throughout this work, all available messengers, gamma rays, neutrinos, and cosmic rays, are connected for the first time in a quantitative statistical method. The objective of the test is to identify possible counterparts of hadronic emission, that is, gamma ray objects in connection with neutrinos and cosmic rays. In this search, a strong preference for HBL blazars as possible counterparts is found, albeit not explaining the full spectrum of cosmic rays and neutrinos, leaving ample room for other types of sources to the spectrum.

In the following, the structure of the thesis is highlighted briefly, explaining the main topic of each chapter and its connection to the thesis as a whole and other individual chapters.

Chapter 2 – In this part, the signal of astrophysical neutrinos discovered by IceCube is discussed. The current knowledge about the features of the spectrum are highlighted, and the possible connections to other messengers in the acceleration of cosmic rays introduced.

Chapter 3 – This chapter discusses the spectrum of cosmic rays in greater detail. The modeling of the spectrum to account for the features observed are discussed, and the theory of cosmic ray acceleration at shock fronts is introduced. Possible sources of cosmic rays are listed. Finally, the production of secondary particles in cosmic ray induced air showers is taken into account, focusing on the production of muons and neutrinos.

Chapter 4 – The IceCube Neutrino observatory is discussed in this chapter. First, interactions of neutrinos relevant for neutrino telescopes are discussed and the typical event properties as seen in the detector are highlighted. The technical details of IceCube are discussed, and the neutrino reconstruction methods and performance illustrated in greater detail.

Chapter 5 – This chapter is the basis for the statistical method used primarily in this thesis and searches for sources of high-energy particles in the universe in general. The technical implementation is discussed and the additions to the framework useful in searches including neutrinos discussed.

Chapter 6 – As part of this thesis, a data sample optimized for the search of TeV neutrinos sources was developed using the most recent data recorded in IceCube. The development using multivariate selection techniques and validation of the performance of the sample is discussed in this part of the thesis.

Chapter 7 – Results of the statistical analyses described in Chapter 5 using the data samples developed in Chapter 6 and previous analyses are discussed in this chapter.

Chapter 8 – The implications of the results of the clustering analyses listed in Chapter 7 are discussed here. The results are consistent with a background-only hypothesis. Thus, upper limits on time-integrated neutrino emission are calculated. The constraints on current models are highlighted and restrictions of the nature of the observed astrophysical neutrino spectrum are discussed.

Chapter 9 – Given the non-observation of neutrino sources in Chapter 7, this chapter is dedicated to a future outlook on the search for point sources of neutrinos. The prospects for the performance of IceCube in the future and possible improvements with future detectors are discussed.

Chapter 10 – In this part of the thesis, a novel statistical test is introduced that connects UHECRs, neutrinos, and gamma rays to search for counterparts of neutrino and UHECR acceleration to the highest energies. Previous searches are discussed, and the statistical method is described. The implications of the significant excess that was found in this test are discussed at the end of this chapter.

Finally, a summarizing conclusion of the thesis is given in the final Chapter 11. Furthermore, supplementary information is given in the appendices, for example frequently used terms for reference in Section A, or additional Figures that are explanatory to the discussion in the thesis.

2 Multi-messenger astronomy & astrophysical neutrinos

The first measurement of high-energy neutrinos of extraterrestrial origin[1] marks the dawn of a new field of astronomy. Neutrinos as new kind of astrophysical messenger provide complementary information to other messengers. In particular, neutrinos can provide a *smoking gun* signal of hadronic processes occurring in the acceleration of *cosmic rays*. In the following, the most common messengers in astrophysics are discussed and highlighted regarding their unique features. A focus is put on the current knowledge about the signal of astrophysical neutrinos.

[1] Aartsen, "Evidence for High-Energy Extraterrestrial Neutrinos at the IceCube Detector".

2.1 Messengers in astrophysics

When considering messengers in astrophysics, three types are typically taken into account, illustrated in Figure 2.1:

- Cosmic Rays (CR)
- Gamma-rays (γ)
- Neutrinos (ν)

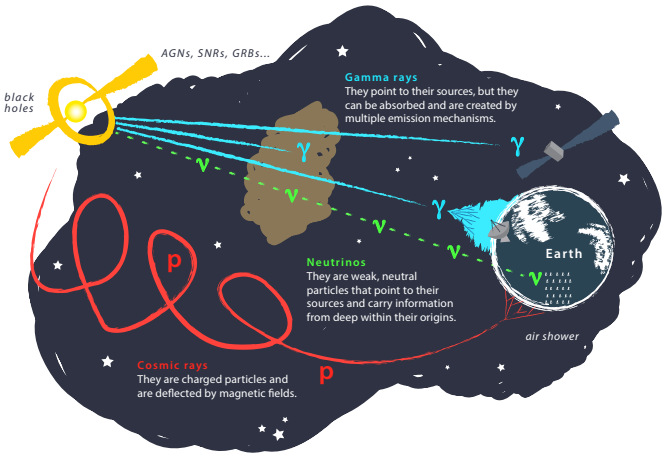

Figure 2.1: Propagation of messengers from their source until detection at Earth with different experimental techniques. Messengers considered here are cosmic rays (mainly protons p, red), photons or gamma rays (γ, cyan), and neutrinos (ν, green). Figure by IceCube Collaboration (May 2016, https://gallery.icecube.wisc.edu/internal/d/318865-1/physicus.pdf).

Cosmic Rays were discovered by Victor F. Hess in 1912 in balloon flights during an eclipse, measuring an increasing amount of radiation at higher altitudes.[2] The origin of CRs — especially at the highest energies[3] — remains a mystery up to now. For more details about physics involving cosmic rays, refer to Section 3. Cosmic rays are charged nuclei and consequently deflected by magnetic fields according to the nuclei's rigidity

$$R = \frac{pc}{Ze} = B \times r_l \tag{2.1}$$

for a charge Ze and momentum p. In a magnetic field of strength B, the rigidity is connected to a deflection in a circle with radius r_l. Hence, directional information for CRs is lost except for the highest energies, when the bending radius $r_l \propto p$ is large against the propagation distance.

Gamma rays, or more generally, photons, are not deflected in magnetic fields. Thus, they point back to their origin. Photons are likely to interact with charged particles, for example via (inverse) Compton scattering or annihilation to electron-positron pairs. As a result, the observable distance in photons is limited. Figure 2.2 shows the attenuation length of photons with respect to their energy. Interactions of photons with the cosmic microwave background (CMB) or extragalactic background light (EBL) limit the distance to the close universe. Above TeV energies, the observable universe is as small as the closest extra-galactic objects and further decreases with energy, increasing the flux suppression at high energies.[4] A large variety of classes emitting high-energy gamma rays is observed, including Galactic and extragalactic objects.[5]

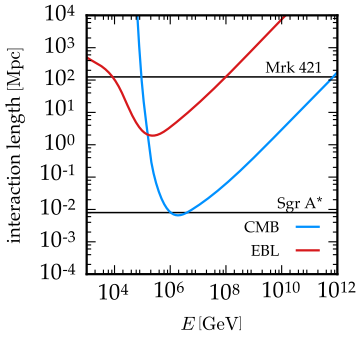

Figure 2.2: Gamma-ray attenuation length versus photon energy for scattering of photons with the cosmic microwave background (CMB, blue) and the extragalactic background light (EBL, red). Data from Ahlers, "Multi-messenger aspects of cosmic neutrinos".

Neutrinos are the third component of messengers in astrophysics and the central topic of this work. Neutrinos come in three flavors linked to the corresponding charged lepton-partner (e, μ, or τ) and they do not carry any electromagnetic charge. In that sense, neutrinos are not deflected by magnetic fields and point back to their origin. In the Standard Model of particle physics, neutrinos are only interacting weakly via the exchange of $W^{\pm}$ or Z^0 bosons. Decays of mesons, mainly charged pions, are the main production process of astrophysical neutrinos that is commonly discussed;[6] therefore, neutrinos trace prior interactions of cosmic rays. Once produced, neutrinos propagate through the universe almost unimpeded due to the low interaction cross section, without suffering from attenuation as photons do. These characteristics make neutrinos a unique and valuable messenger carrying information complementary to photons. On the other hand, the low interaction cross section makes the detection of neutrinos at feasible statistics challenging, and large terrestrial backgrounds are encountered in experiments targeting neutrinos (Section 6.1).

Astrophysical environments are studied in great detail through photons. Including neutrinos will help to distinguish hadronic interactions of cosmic rays from leptonic processes. Furthermore, neutrinos give access to energies above the TeV scale, where photons are

[2] Hess, "Über Beobachtungen der durchdringenden Strahlung bei sieben Freiballonfahrten", awarded with the Nobel prize in Physics (1936).

[3] Ultra-high-energy cosmic rays (UHECRs)

[4] Gilmore et al., "GeV gamma-ray attenuation and the high-redshift UV background".

[5] Hinton and Hofmann, "Teraelectronvolt astronomy".

[6] Anchordoqui, "Cosmic Neutrino Pevatrons: A Brand New Pathway to Astronomy, Astrophysics, and Particle Physics".

mostly absorbed. Large class of sources are potentially hidden in photons, if dense environments do not allow for photons to escape the source. Consequently, with multi-messenger astronomy, a more detailed knowledge of on-going processes at sources can be gained, with the ultimate goal of explaining the origin of UHECRs.

2.2 *Discovery of astrophysical high-energy neutrinos*

The role of the neutrino in multi-messenger physics and the connection to cosmic rays was discussed soon after its discovery in 1956 using reactor neutrinos.[7] The first project targeting astrophysical neutrinos was the DUMAND project,[8] but the first neutrino telescope to detect neutrinos produced in the atmosphere was the Baikal Deep Underwater Neutrino Telescope.[9] Since then, first neutrino telescopes were built in Antarctica and the Mediterranean Sea.[10] IceCube is currently the largest operational neutrino telescope.[11] In this thesis, searches for the origin of astrophysical neutrinos are presented. Hence, in the following, the principles of the discovery of astrophysical neutrinos with IceCube is discussed. For more details about IceCube, refer to Section 4.

In the search discussed here, IceCube, is divided into a *fiducial volume* and a *veto region* (Figure 2.3).[12] When an event is recorded, it is evaluated whether it is starting inside the fiducial volume or entering through the veto region. Only neutrinos can pass the veto without producing light and interact inside of the detector ("starting event"). The main background of atmospheric muons enters the detector from outside and emits light in the veto region. In order to remove the large amount of atmospheric background, a veto efficiency of not more than one false positive in 10^4 events is required. This is achieved only for events with very high energies that deposit at least a charge of $Q_{\text{tot}} = 6000\,\text{pe}$ in the detector (photon equivalent charge). For lower energies, not enough light is emitted in the veto region to be detected by the sparse instrumentation. Improved techniques allow the access to lower energies by using larger veto regions if the charge deposited in the detector is smaller.[13]

With the veto described, not only the background of incident atmospheric muons is removed, but also atmospheric neutrinos produced in the same air showers. If such neutrinos interact inside the fiducial volume of IceCube, there is a chance that muons of the same air shower enter the detector coincident with the neutrino and thus trigger the veto. Due to this *self-veto*,[14] the background of atmospheric neutrinos is partly removed as well in the southern sky where muons of the same air shower can reach IceCube. An additional atmospheric neutrino background originates in *prompt neutrinos* created in decays of charmed mesons in early cosmic ray interactions producing a possible background at higher energies. No component of prompt neutrinos has been observed and upper limits on its flux are given.

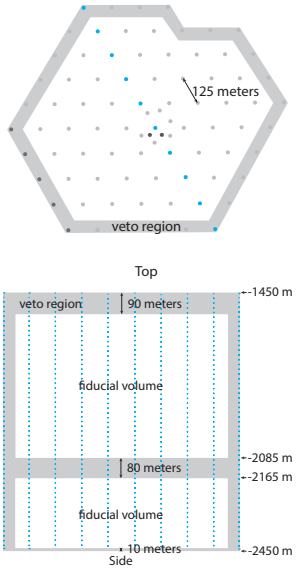

Figure 2.3: Veto region of the IceCube starting event search as seen from top (top figure) and side (bottom). Optical modules in the shaded areas are used as a veto shield against incoming charged particles. Reference to figure in the text.

[7] Greisen, "Cosmic ray showers"; Reines and Cowan, "The neutrino"; Cowan et al., "Detection of the free neutrino: A Confirmation".

[8] Roberts, "The Birth of high-energy neutrino astronomy: A Personal history of the DUMAND project".

[9] Belolaptikov, "The Baikal underwater neutrino telescope: Design, performance and first results".

[10] Andres, "The AMANDA neutrino telescope: Principle of operation and first results"; Ageron et al., "ANTARES: The first undersea neutrino telescope".

[11] Achterberg, "First Year Performance of The IceCube Neutrino Telescope".

[12] Aartsen, "Evidence for High-Energy Extraterrestrial Neutrinos at the IceCube Detector".

[13] Aartsen, "Atmospheric and astrophysical neutrinos above 1 TeV interacting in IceCube".

[14] Schönert et al., "Vetoing atmospheric neutrinos in a high energy neutrino telescope"; T. K. Gaisser, Jero, et al., "Generalized self-veto probability for atmospheric neutrinos".

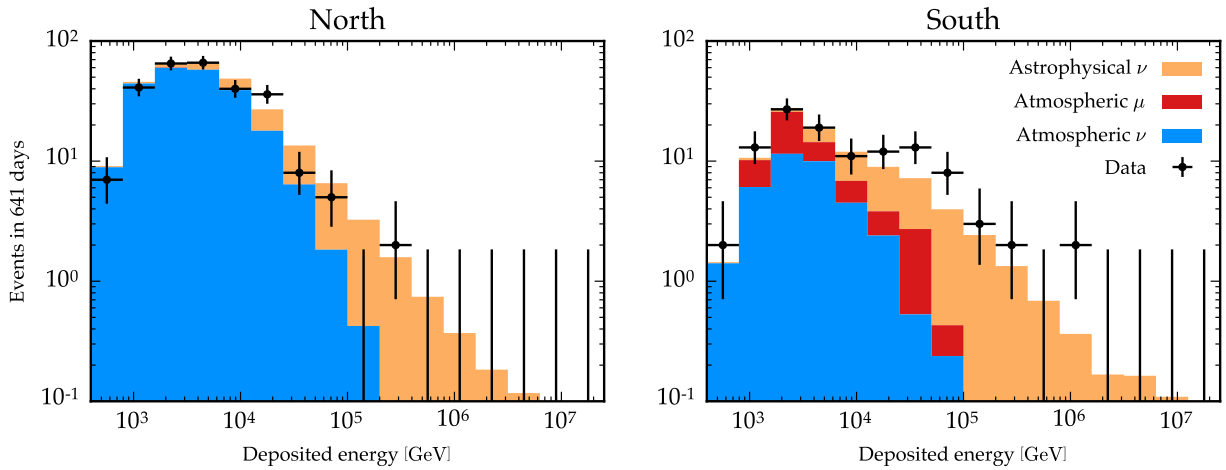

Figure 2.4: Energy distribution of events observed in two years of IceCube operation (2010-2012). The data is compared to different componentes observed with IceCube (Monte Carlo simulation). Reference to data in text.

Four years of detector livetime have been analyzed so far, detecting 54 events in total and observing an additional component of extraterrestrial neutrinos with a significance of more than 5σ.[15] At high energies, the data clearly deviates from the atmospheric expectation, which follows a soft energy distribution of $\partial\phi/\partial E \propto E^{-3.7}$.[16] The energy distribution of events observed for the analysis with lower veto threshold is shown in Figure 2.4 using two years (2010-2012) of exposure. The distribution is shown for the northern and southern sky separately. In the northern sky, no muons are present due to shielding of the Earth, but absorption in the Earth suppresses the neutrino flux at the highest energies. In the southern sky, no absorption is present and atmospheric neutrinos are vetoed due to the self-veto of coincident muons.

The data is well described by an isotropic component of astrophysical neutrinos added to the backgrounds of neutrinos and muons. This component is quantified using an unbroken power-law

$$\partial\phi/\partial E = 2.2 \times 10^{-18}\,\mathrm{GeV}^{-1}\,\mathrm{cm}^{-2}\,\mathrm{s}^{-1}\,\mathrm{sr}^{-1}\,(E/100\,\mathrm{TeV})^{-2.58} \quad (2.2)$$

$$\partial\phi/\partial E = 2.06 \times 10^{-18}\,\mathrm{GeV}^{-1}\,\mathrm{cm}^{-2}\,\mathrm{s}^{-1}\,\mathrm{sr}^{-1}\,(E/100\,\mathrm{TeV})^{-2.46} \quad (2.3)$$

covering energies down from 60 TeV up to 10 PeV[17] and with lower energy threshold using an improved veto in the energy range from 25 TeV to 1.4 PeV,[18] respectively. The result is consistent with a spectral index of E^{-2} that is cut off prior to the Glashow resonance[19] at $\sim$ 6.8 PeV.[20] The samples are dominated by neutrinos of electron and tau flavor since they are well contained in the fiducial volume. Neutrinos of muon flavor are a sub-dominant component, because the muon produced in charge current interactions leaves the detector with significant energy. This results in a lower light yield and thus, the energy threshold for events of muon flavor is increased. Nevertheless, the result is well compatible with a flavor composition of 1 : 1 : 1.[21]

[15] Aartsen, "The IceCube Neutrino Observatory - Contributions to ICRC 2015 Part II: Atmospheric and Astrophysical Diffuse Neutrino Searches of All Flavors".

[16] Honda et al., "Calculation of atmospheric neutrino flux using the interaction model calibrated with atmospheric muon data"; T. K. Gaisser, "Spectrum of cosmic-ray nucleons, kaon production, and the atmospheric muon charge ratio".

[17] Aartsen, "The IceCube Neutrino Observatory - Contributions to ICRC 2015 Part II: Atmospheric and Astrophysical Diffuse Neutrino Searches of All Flavors".

[18] Aartsen, "Atmospheric and astrophysical neutrinos above 1 TeV interacting in IceCube".

[19] Glashow, "Resonant Scattering of Antineutrinos".

[20] Anchordoqui et al., "End of the cosmic neutrino energy spectrum".

[21] Aartsen, "Flavor Ratio of Astrophysical Neutrinos above 35 TeV in IceCube".

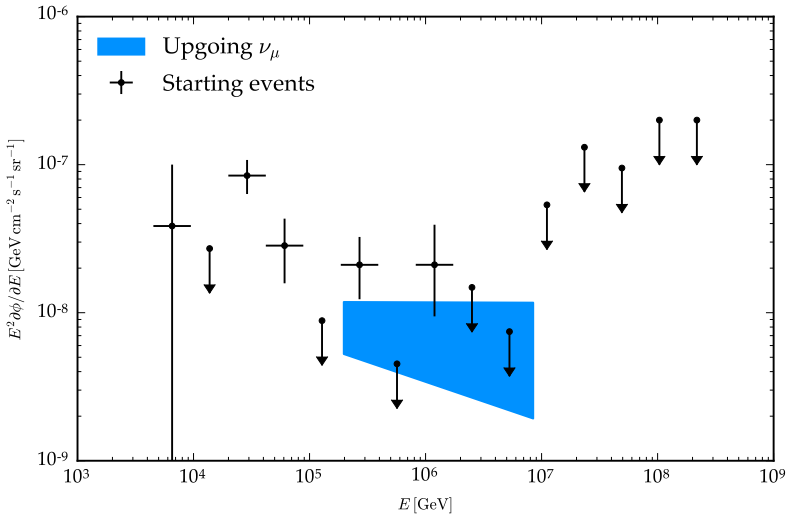

Figure 2.5: Unfolded astrophysical neutrino flux versus energy for starting events and up-going muons. Result from Aartsen, "Atmospheric and astrophysical neutrinos above 1 TeV interacting in IceCube"; Aartsen, "Observation and Characterization of a Cosmic Muon Neutrino Flux from the Northern Hemisphere using six years of IceCube data".

The obtained samples of starting events are very high in neutrino purity, but with an approximate event rate of $10\,\mathrm{year}^{-1}$ and large angular uncertainties for most of the events, a detection of single sources is challenging.[22] No sources have yet been identified in these searches.

[22] Ahlers and Halzen, "Pinpointing Extragalactic Neutrino Sources in Light of Recent IceCube Observations".

2.3 *The signal of astrophysical neutrinos*

Another clear identification of neutrinos apart from starting events is the up-going direction of particles. Neutrinos are the only particles in the Standard Model that are able to travel through the Earth unimpeded, removing all backgrounds of other particles[23]. Muons travel long distances exceeding several kilometers in the Antarctic ice and can be reconstructed well enough to reject all down-going background. Consequently, every up-going muon is a clear identifier of a prior neutrino interaction even if the interaction itself is not observed. In such analyses, a high purity sample ($> 99\%$) of large statistics ($\sim 220\,\mathrm{events\,day}^{-1}$) is obtained.[24] Neutrinos produced in air showers in the northern hemisphere dominate the event rate. At high energies (100 TeV and above), the flux of astrophysical neutrinos starts to dominate over the atmospheric neutrino flux falling steeply with energy. With two years of data, a first evidence for astrophysical muon neutrinos was found in IceCube[25] that by now is refined using six years of detector livetime with more than $5\,\sigma$ significance.[26]

Starting events and up-going muons yield two observations of an astrophysical neutrino flux with two very different methods and statistically independent samples, the measured flux for both analysis is shown in Figure 2.5. Combining both outcomes into a joint analysis of the astrophysical flux gives the current best understanding of the astrophysical neutrino flux.[27] The overall flux is consistent with a

[23] Neutrinos experience Earth absorption above 100 TeV as well for vertically up-going events. Hence, the high-energy flux of neutrinos is only visible for inclined up-going events (see Section 6.1

[24] Aartsen, "Observation and Characterization of a Cosmic Muon Neutrino Flux from the Northern Hemisphere using six years of IceCube data".

[25] Aartsen, "Evidence for Astrophysical Muon Neutrinos from the Northern Sky with IceCube".

[26] Aartsen, "Observation and Characterization of a Cosmic Muon Neutrino Flux from the Northern Hemisphere using six years of IceCube data".

[27] Aartsen, "A combined maximum-likelihood analysis of the high-energy astrophysical neutrino flux measured with IceCube".

diffuse, that is, isotropic, flux of astrophysical neutrinos. The flux expands up to energies above PeV with the observation of three events with 1 PeV to 2 PeV in starting events and one muon event with an energy of 2.5 PeV deposited in the detector.[28]

[28] Schoenen and Rädel, "Detection of a multi-PeV neutrino-induced muon event from the Northern sky with IceCube", this gives a lower limit on the true neutrino interaction because the distance of the neutrino interaction to the first muon detection is unknown.

The flavor ratio of the result is consistent with an equal distribution $1:1:1$ of all flavors, consistent with expectations from neutrino production and incoherent oscillations during propagation (see Section 2.6). However, there is a degeneracy in the amount of electron to tau neutrinos that have a very common event signature. Currently, there is no proof of a detection of astrophysical tau neutrinos, but the sensitivity of such searches is still above the observed flux in Eq. (2.2).[29] With increased statistics, a clear detection of tau neutrinos will give insight into the flavor ratio of the diffuse astrophysical neutrino spectrum.

[29] Aartsen, "Search for Astrophysical Tau Neutrinos in Three Years of IceCube Data".

2.4 Neutrino production in cosmic accelerators

The production of neutrinos in astrophysical environments can be explained using basic interactions of particle physics, and in principle follows the same mechanism of neutrino production by cosmic rays interaction in the Earth's atmosphere that is discussed further in Section 3.6 and reviewed in T. Gaisser, Engel, and Resconi, *Cosmic Rays and Particle Physics*. For astrophysical neutrinos, the connection to gamma rays is of particular interest and can help explaining the processes important for cosmic ray and neutrino production. The remaining section summarizes a review regarding such processes.[30]

[30] Anchordoqui, "Cosmic Neutrino Pevatrons: A Brand New Pathway to Astronomy, Astrophysics, and Particle Physics".

Neutrinos are predominantly produced in decays of charged mesons, mainly charged pions and subsequent decays of secondary particles that decay into muons and neutrinos with $> 99.9\%$ branching ratio:[31]

[31] Olive, "Review of Particle Physics".

$$\begin{aligned} \pi^+ &\to \mu^+ \nu_\mu \to \mathrm{e}^+ \nu_\mu \bar{\nu}_\mu \nu_e \\ \pi^- &\to \mu^- \bar{\nu}_\mu \to \mathrm{e}^- \bar{\nu}_\mu \nu_\mu \bar{\nu}_e \end{aligned} \tag{2.4}$$

The final particles listed in Eq. (2.4) are stable in the Standard Model of particle physics, resulting in a final neutrino ratio of $\nu_\mathrm{e} : \nu_\mu : \nu_\tau = 1:2:0$ at the production site. In decays of neutral pions, two photons are produced,

$$\pi^0 \to \gamma\gamma\,, \tag{2.5}$$

that are related to the neutrinos produced in pion interactions. The reason for that is that both charged and neutral pions are produced in processes of the same particles. For example, in pp interactions, π^+, π^-, and π^0 are produced at approximately equal amount. Using the average values of the decay kinematics of the particles, one arrives at the neutrino to photon relation[32]

[32] Anchordoqui, "Cosmic Neutrino Pevatrons: A Brand New Pathway to Astronomy, Astrophysics, and Particle Physics", p. 25.

$$\left.\frac{\partial \phi_{\nu_X}}{\partial E_\nu}\right|_{E_\nu = E_\gamma/2} = 2 \left.\frac{\partial \phi_\gamma}{\partial E_\gamma}\right|_{E_\gamma}\,. \tag{2.6}$$

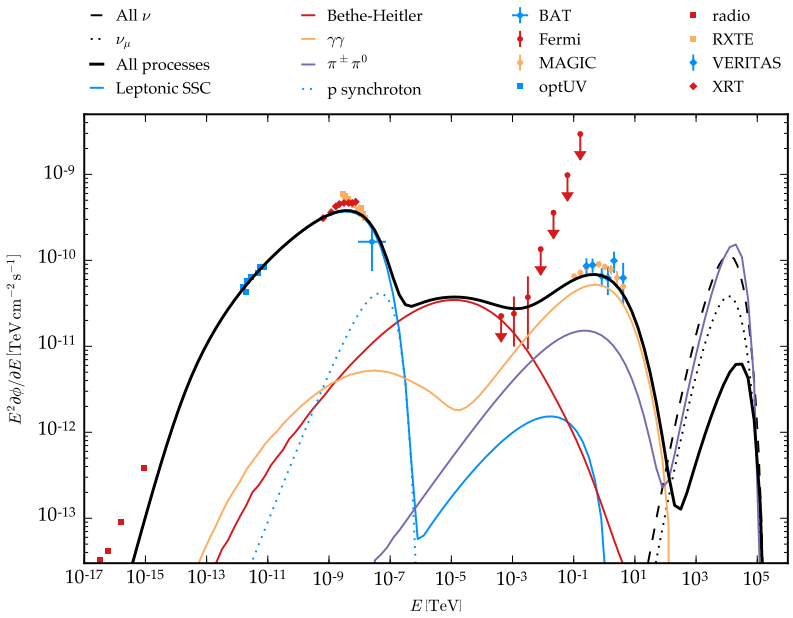

Figure 2.6: Lepto-hadronic modeling of multiwavelength data of Mrk 421. Data from Petropoulou, Coenders, and Dimitrakoudis, "Time-dependent neutrino emission from Mrk 421 during flares and predictions for IceCube" and observation data from experiments referenced in Aleksić, "Unprecedented study of the broadband emission of Mrk 421 during flaring activity in March 2010".

Hence, the flux ϕ_{ν_X} of neutrinos of flavor X is twice as high as the flux ϕ_γ of photons, where the neutrino energy is half of the corresponding gamma ray energy. Note, that in Eq. (2.6), no absorption of gamma rays is taken into account, damping the gamma ray flux that is dependent on the traveling distance, compare Figure 2.2. Moreover, for neutrinos, an equal flavor ratio is assumed that arises in oscillations of neutrino flavors as explained in the Section 2.6.

Using similar approaches, measured gamma ray fluxes can be used to predict astrophysical neutrino fluxes from a source, under the assumption that the gamma rays belong to a π^0 component as in Eq. (2.5).[33] The identification of a neutrino flux could then provide insight into the amount of hadronic interactions within a source.

Besides, one can model the observed multiwavelength data of a source using lepto-hadronic interactions. In such models, all interactions of photons, electrons, and protons, as well as secondary pions are evaluated for their production of gamma rays and interactions among each other. Thus, the ejected cosmic ray, gamma ray, and neutrino spectra are calculated and compared to observations.[34] The multi wavelength and neutrino data of a source gives insight into its properties like the proton luminosity that is then connected to the production of UHECRs.[35]

The decay of pions is not the only mechanism that can produce neutrinos and listed in the following with their flavor ratio ($\nu_e : \nu_\mu : \nu_\tau$) at the source.

Pion decay: In principle the "baseline" model of neutrino production as discussed here. The final neutrino flavor ratio yields 1 : 2 : 0 at the astrophysical source.

[33] Kappes et al., "Potential Neutrino Signals from Galactic Gamma-Ray Sources".

[34] Stecker, "Effect of photomeson production by the universal radiation field on high-energy cosmic rays"; Dimitrakoudis et al., "The time-dependent one-zone hadronic model - First principles"; Petropoulou, Dimitrakoudis, et al., "Photohadronic origin of γ-ray BL Lac emission: implications for IceCube neutrinos".

[35] Petropoulou, Coenders, and Dimitrakoudis, "Time-dependent neutrino emission from Mrk 421 during flares and predictions for IceCube".

Neutron decay: After a lifetime of a few minutes, neutrons decay to protons, electrons and neutrinos ($n \rightarrow p e^- \bar{\nu}_e$), resulting in a flavor composition of $1:0:0$.

Muon damped sources: In processes involving pions, there is a possibility that muons lose a significant amount of energy before decaying according to Eq. (2.4). Thus, high energy neutrinos are only produced in the pion decays, resulting in a flavor ratio of $0:1:0$, that is, pure muon (anti)neutrinos.

Exotic physics like decays of heavy dark matter particles could produce neutrinos as well.[36] Such models are mentioned for completeness but not further considered here. During propagation, neutrinos change their flavor in oscillations as is discussed in Section 2.5 and 2.6.

[36] Dev et al., "Heavy right-handed neutrino dark matter and PeV neutrinos at IceCube".

2.5 Neutrino oscillations

Shortly after the discovery of the neutrino in the 1950's, it was anticipated that flavor oscillations occur during propagation that result in a violation of the lepton number of the individual flavors..[37] First hints on neutrino oscillations where found in the electron antineutrino flux arriving from the Sun,[38] but the first evidence for neutrino oscillation was given by the detection of oscillations of atmospheric neutrinos by Super-Kamiokande[39] and of solar neutrinos with the Sudbury Neutrino Observatory.[40] Both have been recently awarded with the Nobel Prize in Physics (2015).

Oscillations arise when the eigenbasis of the propagation Hamiltonian is rotated with respect to the interaction basis. Neutrinos are identified given their interactions with other particles, whereas the free propagation is described by the *mass basis*. These two states are connected via an unitary transformation

$$\begin{pmatrix} \nu_e \\ \nu_\mu \\ \nu_\tau \end{pmatrix} = U^* \cdot \begin{pmatrix} \nu_1 \\ \nu_2 \\ \nu_3 \end{pmatrix} \qquad \begin{pmatrix} \nu_1 \\ \nu_2 \\ \nu_3 \end{pmatrix} = U \cdot \begin{pmatrix} \nu_e \\ \nu_\mu \\ \nu_\tau \end{pmatrix} \tag{2.7}$$

expressed by the *Pontecorvo-Maki-Nakagawa-Sakata* matrix $\hat{U}$ (PMNS).[41] In the picture of three neutrino flavors, the unitary transformation of the PMNS-matrix is described by three rotation angles θ_{ij} and one complex phase δ. This is commonly done defining the rotations along the three main axes adding the complex phase to the rotation around the intermediate ν_2' axis, resulting in the following parameterization[42] of $\hat{U}$:

[37] Pontecorvo, "Mesonium and antimesonium"; Pontecorvo, "Neutrino Experiments and the Problem of Conservation of Leptonic Charge".

[38] Davis and Harmer, "Solar neutrinos".

[39] Ashie, "Evidence for an oscillatory signature in atmospheric neutrino oscillation".

[40] Ahmad, "Measurement of the rate of $\nu_e + d \rightarrow p + p + e^-$ interactions produced by ^8B solar neutrinos at the Sudbury Neutrino Observatory".

[41] Maki, Nakagawa, and Sakata, "Remarks on the unified model of elementary particles".

[42] Olive, "Review of Particle Physics".

$$
\begin{aligned}
\hat{U} &= U_{23} \cdot I_\delta^* \cdot U_{13} \cdot I_\delta \cdot U_{12} \\
&= \begin{pmatrix} 1 & 0 & 0 \\ 0 & c_{23} & s_{23} \\ 0 & -s_{23} & c_{23} \end{pmatrix} \begin{pmatrix} c_{13} & 0 & s_{13}\,\mathrm{e}^{-i\delta} \\ 0 & 1 & 0 \\ -s_{13}\,\mathrm{e}^{i\delta} & 0 & c_{13} \end{pmatrix} \begin{pmatrix} c_{12} & s_{12} & 0 \\ -s_{12} & c_{12} & 0 \\ 0 & 0 & 1 \end{pmatrix} \\
&\equiv \begin{pmatrix} U_{e1} & U_{e2} & U_{e3} \\ U_{\mu 1} & U_{\mu 2} & U_{\mu 3} \\ U_{\tau 1} & U_{\tau 2} & U_{\tau 3} \end{pmatrix},
\end{aligned}
\tag{2.8}
$$

where s_{ij} and c_{ij} represent the sine and cosine of the mixing angle θ_{ij}, respectively. If neutrinos are Majorana particles, that is, the neutrino is its own antiparticle,[43] two additional complex phases α_1 and α_2 are present. These phases do not affect oscillations of neutrinos.

The free propagation of neutrinos happens in the mass eigenbasis $(\nu_1, \nu_2, \nu_3)^\mathrm{T}$ of the Hamiltonian in vacuum. Neutrinos have very low mass. In fact, only upper limits on the masses are known from tritium decay[44] or cosmology[45] restricting the electron antineutrino mass to $m_\nu < 2\,\mathrm{eV}$ and the sum of all neutrinos $\sum_i m_\nu < 0.2\,\mathrm{eV}$, respectively. Hence, neutrinos can be approximated as highly relativistic particles with energy $E_i = \sqrt{p_i^2 + m_i^2} \approx E + m_i^2/2E$. Consequently, during propagation, neutrinos with different mass m_i propagate differently, resulting in phase differences of the states. This finally leads to coherent oscillations of neutrino flavors and the probability for a neutrino of flavor α to be observed with flavor β is given by[46]

$$
\begin{aligned}
P_{\alpha\to\beta} = \delta_{\alpha\beta} &- 4\sum_{i>j} \Re\left(U_{\alpha i}^* U_{\beta j} U_{\alpha j} U_{\beta j}^*\right) \sin^2 \frac{\Delta m_{ij}^2 L}{4E} \\
&+ 2\sum_{i>j} \Im\left(U_{\alpha i}^* U_{\beta j} U_{\alpha j} U_{\beta j}^*\right) \sin \frac{\Delta m_{ij}^2 L}{2E}
\end{aligned}
\tag{2.9}
$$

for a propagation of length $L = ct$ for neutrinos traveling almost at the speed of light. The argument of the $\sin^2$ uses natural units and is converted to units representing typical experimental or astronomical units

$$
\frac{\Delta m^2 L}{4E} \to 1.27 \times \frac{\Delta m^2}{\mathrm{eV}^2} \frac{L}{\mathrm{km}} \frac{\mathrm{GeV}}{E} \tag{2.10}
$$

$$
\to 3.09 \times 10^7 \frac{\Delta m^2}{\mathrm{eV}^2} \frac{L}{\mathrm{pc}} \frac{\mathrm{PeV}}{E}\,. \tag{2.11}
$$

From Eq. (2.9), it becomes clear that the strength of the oscillations or the amplitude of the conversion depends on the parameters of the PMNS matrix, that is the mixing angles θ_{ij} and the complex phase δ, whereas the oscillation length is determined by the mass-squared difference of the neutrino masses in the mass basis $\Delta m_{ij}^2 \equiv \Delta m_i^2 - \Delta m_j^2$.

The best knowledge about mixing parameters in Eq. (2.8) is given using all available data of solar, atmospheric, reactor, and accelerator neutrino experiments in a global analysis.[47] It turns out that two of the mixing angles are very large (θ_{12} and θ_{23} mixing), corresponding

[43] Majorana, "Theory of the Symmetry of Electrons and Positrons".

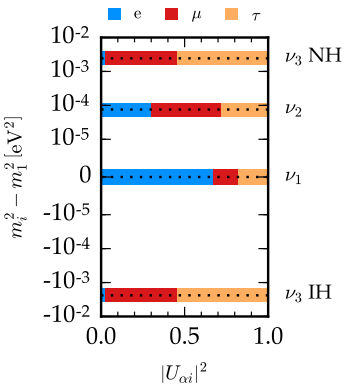

Figure 2.7: Neutrino mass ordering in the normal (NH) and inverted hierarchy (IH) relative to the ν_1 state. For each state, the amount of electron, muon, and tau flavor according to the PMNS matrix (Eq. (2.8)) is indicated on the horizontal axis.

[44] Otten and Weinheimer, "Neutrino mass limit from tritium beta decay".

[45] Lattanzi, "Planck 2015 constraints on neutrino physics".

[46] T. Gaisser, Engel, and Resconi, *Cosmic Rays and Particle Physics*, p. 154.

[47] Capozzi et al., "Status of three-neutrino oscillation parameters, circa 2013".

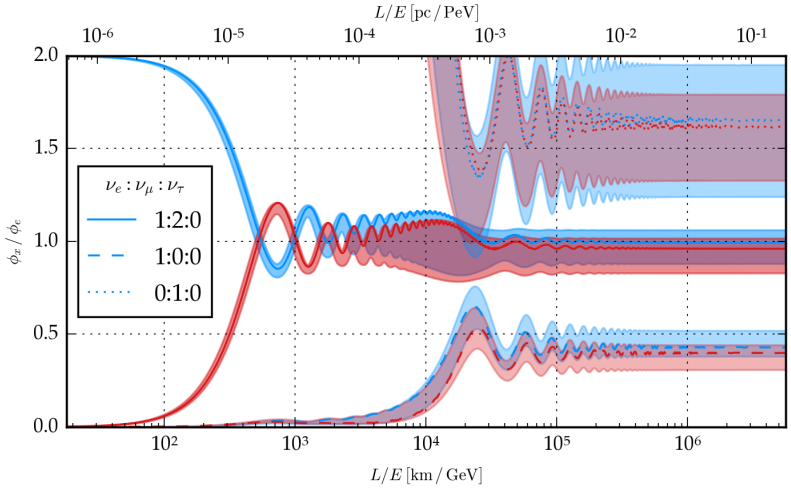

Figure 2.8: Neutrino flux ϕ_X for muon (blue) and tau (red) flavor relative to electron flavor flux ϕ_e with respect to oscillation length L / E. The oscillation length is shown both in SI units (bottom) as well as astronomical units (top). Three scenarios of starting flavor composition are taken into account: Pion decay ($1 : 2 : 0$, solid), neutrino decay ($1 : 0 : 0$, dashed), and muon damped sources ($0 : 1 : 0$, dotted). Shaded areas indicate 90% uncertainties given current oscillation parameter knowledge neglecting correlation between the parameters.

to solar ($\nu_e \leftrightarrow \nu_\mu$ conversion) and atmospheric oscillations ($\nu_\mu \leftrightarrow \nu_\tau$ conversion), respectively. The remaining mixing angle θ_{13} is smaller, but significantly deviates from the non-mixing case ($\theta_{13} > 0°$). The mass differences are at $7.54 \times 10^{-5}\,\mathrm{eV}^2$ and $2.43 \times 10^{-3}\,\mathrm{eV}^2$ scale for the Δm^2_{12}, Δm^2_{23} difference, respectively. Regarding the mixing of the states ν_2 and ν_3, the sign of the mass difference is not known, that is, ν_3 is either the heaviest (normal ordering) or lightest (inverted ordering) of the three neutrinos, as visualized in Figure 2.7. The complex ($\mathcal{CP}$ violating) phase δ is not constrained at significant level at the moment, although the best fitting parameter prefers complex values deviating from $\delta = 0$, $\delta = \pi$ that would conserve $\mathcal{CP}$.[48]

[48] Capozzi et al., "Status of three-neutrino oscillation parameters, circa 2013".

2.6 *Oscillations on astronomical distances*

For astronomical distances, the distance of neutrino propagation usually exceeds the typical oscillation length (see Eq. (2.11)), so called very long baseline neutrino oscillations. Hence, the oscillating terms in the transition probability in Eq. (2.9) reduce to their average value[49] in incoherent neutrino oscillations

$$\langle \sin^2 x \rangle \to \frac{1}{2} \qquad\qquad \langle \sin x \rangle \to 0\,. \tag{2.12}$$

[49] Athar, Kim, and Lee, "The Intrinsic and oscillated astrophysical neutrino flavor ratios".

removing the impact of the complex parts of the PMNS matrix. Figure 2.8 shows the averaging process of the oscillations dependent on the ratio L/E using the ratio of ν_μ and ν_τ flux with respect to the ν_e flux for different scenarios discussed in Section 2.4:[50] the "standard" of $\nu_e : \nu_\mu : \nu_\tau = 1 : 2 : 0$, neutron decay with $1 : 0 : 0$, and muon damped sources with $0 : 1 : 0$. In all three cases, the large mixing angles result in a significant transition from the initial flux to an all-flavor flux. For the benchmark scenario especially, after averaging out the oscillations, almost an equal flavor composition of $1 : 1 : 1$ is obtained at Earth.

[50] Calculated with *nuCraft* (Wallraff and Wiebusch, "Calculation of oscillation probabilities of atmospheric neutrinos using nuCraft")

Using the current uncertainties of the oscillation parameters, conservatively assuming that they are uncorrelated, and that there is no knowledge about the mass ordering of Δm^2_{23} and the $\mathcal{CP}$ violating phase δ whatsoever, the result does not change strongly from the expectations using the best fit values (shaded areas in Figure 2.8 show 90% confidence belts). The uncertainties use the currently best available data in a global fit of three-flavor neutrino oscillation.[51] Due to the large mixing angles for all neutrino flavors, any scenario of initial neutrino flux results in a flux that is close to an equal flavor ratio.

Figure 2.9 shows the resulting neutrino flavor spectrum for any combination of initial flavor ratio. The top figure shows a color coding for any flavor ratio combination at the neutrino source; in the bottom figure, the flavor spectrum after oscillations is shown using the same color coding. Shaded gray points show the widening of the available parameter space accounting for the uncertainties due to uncertainties in the oscillation parameters.

Independent of the staring neutrino spectrum, the resulting spectrum is very evenly divided into all flavors. For searches of astrophysical sources, this is of particular interest since muon neutrinos are detected as *tracks* that can be reconstructed with angular resolution below 1° and are thus well suited for astronomy, as discussed in Section 6. If a deviation from the line in Figure 2.9 (bottom) would be observed in future experiments, this hinted to physics beyond the standard oscillation picture.[52]

[51] Capozzi et al., "Status of three-neutrino oscillation parameters, circa 2013".

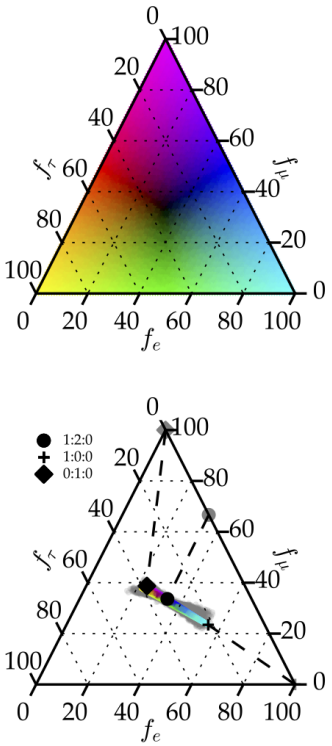

Figure 2.9: Top: Neutrino flavor spectrum at production site. Bottom: Neutrino flavor spectrum after averaged oscillations, color coding as in top figure. Grey markers indicate the allowed region of 10 000 trials within oscillation parameter uncertainties. Oscillation calculations done with *nuCraft*, oscillation parameters neglecting correlations from global fit referenced in text.

[52] Bustamante, Beacom, and Winter, "Theoretically palatable flavor combinations of astrophysical neutrinos"; Argüelles, Katori, and Salvado, "New Physics in Astrophysical Neutrino Flavor".

3 Cosmic rays & astroparticle physics

The highest energetic particles ever observed are ions with a total energy of 100 EeV that arrive at Earth from extraterrestrial origin. These *cosmic rays* and the ones at lower energy are a key ingredient in understanding the most extreme processes happening in the universe, for example in supernovae or active galactic nuclei. Although their origin is not fully understood, they are connected to the production of gamma rays and especially neutrinos. In the following, the details of the spectrum of cosmic rays is discussed and the theory of particle acceleration to such energies is introduced. Lastly, the physics of cosmic ray induced air showers and the production of muons and neutrinos is discussed.

3.1 The high-energy spectrum of cosmic rays

The spectrum of cosmic rays covers a wide range of energies. The lowest energies are at the 1 GeV scale and the spectrum spans up to 100 EeV, more than 11 magnitudes higher in energy. The spectrum over the full energy range is shown in Figure 3.1 and is remarkable in its simplicity at first sight. The flux observed differentially in energy drops with a power law, $\partial\phi/\partial E = E^{-1}\,\partial E/\partial \ln E \propto E^{-\gamma}$. This indicates that non-thermal acceleration processes are responsible for the generation of this spectrum by accelerating particles to such immense energies.[1]

The flux of cosmic rays drops quickly with energy: at energies of 1 GeV, 10^4 particles are observed per square meter and second, while at 10 PeV only a few particles per year remain. At the very high end of the spectrum, this number further decreases to one particle per square meter per century observed above 100 EeV.

Direct detection of cosmic rays using balloon-borne experiments or satellites only detect the lower energies due to their size limitations. This allows a precise determination of the type of particle (electron, positron, proton, Helium, et cetera) and its momentum. Figure 3.1 shows recent results from satellite experiments exploiting similar detection techniques as in particle accelerator detectors.[2] In Figure 3.2, results for helium and carbon for those experiments are shown. At higher energies, the flux is too low to be detected using experiments at altitudes above the Earth atmosphere.

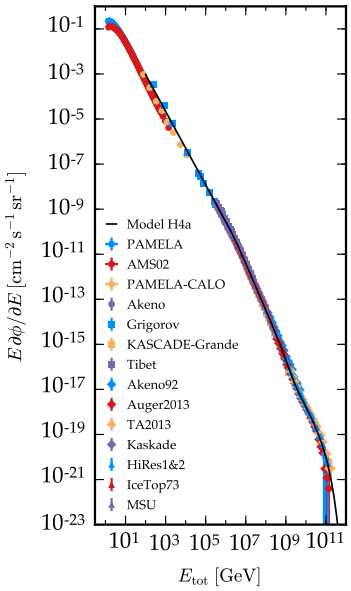

Figure 3.1: Cosmic ray flux incident at Earth shown against the cosmic ray particle's energy. The spectrum is multiplied by the particle's total energy E. For energies below 10 TeV, direct detection experiments show the proton/hydrogen flux, above that energy, ground based experiments measure the total flux. At high energies a model using three accelerating populations with only protons at the highest energies is shown. Data courtesy of T. Gaisser, Engel, and Resconi, *Cosmic Rays and Particle Physics*.

[1] T. Gaisser, Engel, and Resconi, *Cosmic Rays and Particle Physics*.

[2] Aguilar, "Precision Measurement of the Proton Flux in Primary Cosmic Rays from Rigidity 1 GV to 1.8 TV with the Alpha Magnetic Spectrometer on the International Space Station"; Adriani, "PAMELA Measurements of Cosmic-ray Proton and Helium Spectra".

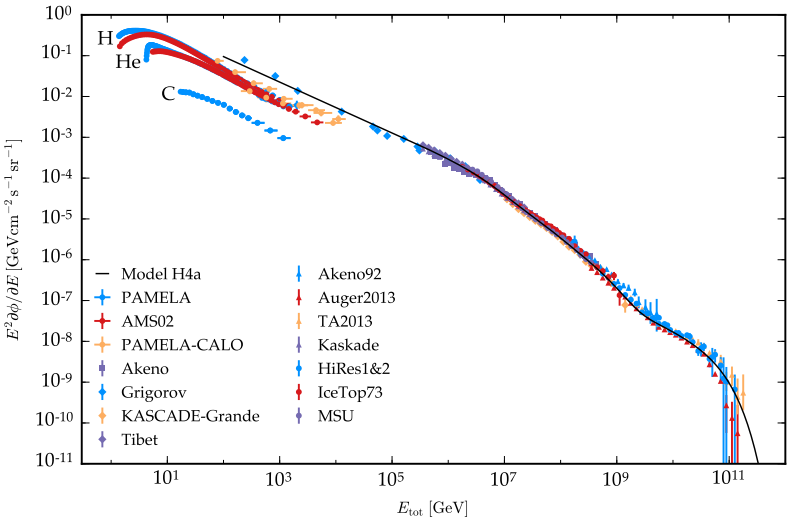

Figure 3.2: Spectral energy density of cosmic rays with respect to particle energy. The flux is multiplied by E^2 to reflect the energy density of cosmic rays. In addition to hydrogen (H), results for helium (He) and carbon (C) are shown for direct detection experiments. The offset in direct detection measurements and ground based measurements is due to direct detection experiments (AMS, PAMELA) identifying the type of cosmic ray, while ground based experiments only measure the total cosmic ray flux (H + He + CNO + ...). Data courtesy of T. Gaisser, Engel, and Resconi, *Cosmic Rays and Particle Physics*.

Large ground-based experiments are needed for measurements at energies above 10 TeV. They detect secondary particles that are produced in air showers induced by cosmic ray interactions in the Earth atmosphere[3] The entire energy range above TeV is covered by ground based experiments, as shown in Figure 3.2 for the spectral energy density. The experiments grow in instrumentation size to observe larger cosmic ray energies with feasible event statistics. The currently largest experiments, the Pierre Auger Observatory[4] and the Telescope Array,[5] probe the highest energy end of the cosmic ray spectrum at 100 EeV and above.

The discussion is focused in this thesis on the high energy part of cosmic rays. Looking at the spectral energy density $E^2\partial\phi/\partial E$ of cosmic rays in Figure 3.2, features in the spectrum become visible. Two main features dominate the spectrum, a softening of the spectrum at the "knee" in the PeV range, and a re-hardening at EeV energies ("ankle").[6] Above 4×10^{10} GeV the flux is suppressed and cuts off above ~ 100 EeV.[7] The features become more visible by multiplying the cosmic ray flux by $E^{2.7}$, as shown in Figure 3.3. At the knee, the spectrum softens to approximately E^{-3} and hardens again to $E^{-2.7}$ before being suppressed at the end of the spectrum. In this visualization a *second* knee is visible above 100 PeV.[8]

3.2 *Modeling of the cosmic ray spectrum*

The characteristics of the CR spectrum can be explained tentatively by a changing composition of the spectrum, first mentioned soon after the discovery of the knee.[9] The incident spectrum of cosmic rays at Earth is affected by the acceleration and propagation mechanisms responsible for cosmic rays. The interactions with magnetic fields depend on the cosmic ray's rigidity $R \approx E/Ze$ for $E/m \gg 1$, Eq. (2.1). Assuming that a spectrum follows a power-law and cuts

[3] The evolution of air showers is discussed in Section 3.6.

[4] Abraham, "Observation of the suppression of the flux of cosmic rays above 4×10^{19}eV".

[5] Abu-Zayyad, "The Cosmic Ray Energy Spectrum Observed with the Surface Detector of the Telescope Array Experiment".

[6] Olive, "Review of Particle Physics".

[7] Abraham, "Observation of the suppression of the flux of cosmic rays above 4×10^{19}eV".

[8] Olive, "Review of Particle Physics".

[9] Peters, "Primary cosmic radiation and extensive air showers".

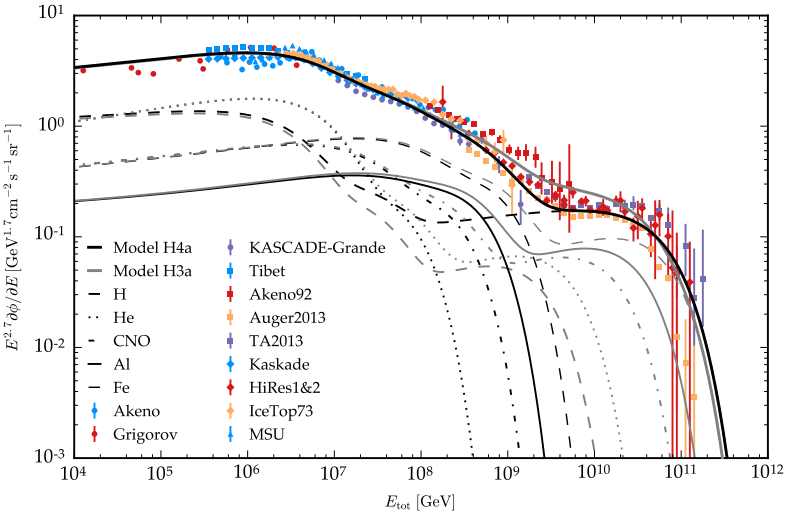

Figure 3.3: Cosmic ray flux at the high energy end multiplied by $E^{2.7}$ in order to enhance the visibility of the features in the spectrum. Same data as in previous figures of the cosmic ray flux is shown. In addition to the data, two models are shown with the total cosmic ray flux (thick solid line), and for each different cosmic ray particle component. The two models are protons only at the highest energies (H4a), or a mixed composition (H3a). Data courtesy of T. Gaisser, Engel, and Resconi, *Cosmic Rays and Particle Physics*.

off at a characteristic rigidity R_c, the flux of a cosmic ray of type i in an accelerating population environment j is given by[10]

$$E\frac{\partial\phi}{\partial E}(E) = a_{ij}E^{\gamma_{ij}} \times \mathrm{e}^{-E/Z_iR_{c,j}} \tag{3.1}$$

for a charge Z_ie at energy E. Thus, cosmic rays with higher charge have a higher cutoff energy, for example, helium at energy $E = 2R_c$, and so on.

The nucleon flux for a particle with A nucleons is connected to the cosmic ray flux by

$$E_N\partial\phi/\partial E_N = A \times E\partial\phi/\partial E \tag{3.2}$$

with the energy per nucleon $E_N = AE$.[11] The type of cosmic ray ions taken into account are the families of hydrogen (H), helium (He), carbon, nitrogen and oxygen (CNO), magnesium, aluminum and silicon (MgAlSi), and iron (Fe). Using such "Peters cycles",[12] three populations are able to describe the observed cosmic ray spectrum at high energies,[13] yielding the total spectrum

$$E\left.\frac{\partial\phi}{\partial E}\right|_i(E) = \sum_{j=1}^{3} E\left.\frac{\partial\phi}{\partial E}\right|_{ij}(E) \tag{3.3}$$

of cosmic rays arriving at Earth. Such a model is shown in Figures 3.1, 3.2, and 3.3, assuming that the third population (highest cutoff rigidity $R_c = 60\,\mathrm{EV}$) consists of protons only (H4a).[14] Figure 3.3 shows the contribution of different types of cosmic rays. Another model (H3a) assumes a mixed composition for the third population with a cutoff rigidity $R_C = 2\,\mathrm{EV}$. Consequently, at the highest energies, the CR spectrum at EeV energies and above is dominated by heavier nuclei ($Z_i > 1$) and no protons are accelerated to such energies. The composition of the spectrum at the highest energies affects

[10] T. K. Gaisser, "Spectrum of cosmic-ray nucleons, kaon production, and the atmospheric muon charge ratio".

[11] T. K. Gaisser, "Spectrum of cosmic-ray nucleons, kaon production, and the atmospheric muon charge ratio".

[12] Peters, "Primary cosmic radiation and extensive air showers".

[13] T. K. Gaisser, Stanev, and Tilav, "Cosmic Ray Energy Spectrum from Measurements of Air Showers".

[14] T. K. Gaisser, "Spectrum of cosmic-ray nucleons, kaon production, and the atmospheric muon charge ratio".

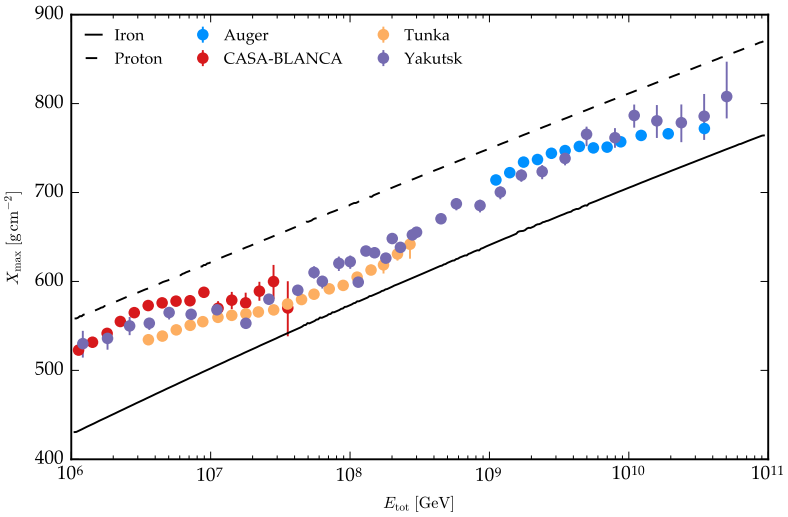

Figure 3.4: Mean interaction height of cosmic rays shown against cosmic ray energy measured in air shower experiments. Expectation from simulation of cosmic rays using a pure proton (iron) is shown as purple (orange) line using the EPOSv1.99 interaction model (Pierog and Werner, "Muon Production in Extended Air Shower Simulations"). Plot reproduced from data shown in Kampert and Unger, "Measurements of the Cosmic Ray Composition with Air Shower Experiments" and references therein.

the production of gamma rays and neutrinos. The interactions involved in the production depend on the energy of the single particle in the nucleus, Eq. (3.2), which is much higher for models assuming only protons at the end of the CR spectrum (model H4a)..[15]

For ground based experiments, the CR detection happens using secondary particles produced in extensive air showers. The mean composition can be measured on a statistical basis, because air showers evolve differently in the Earth's atmosphere depending on the primary cosmic ray type. The interaction cross section of nuclei consisting of A particles grows with $A^{2/3}$. Consequently, the first interaction of a CR nucleus with $A > 1$ is at higher altitude than for protons ($A = 1$) and this results at a lower value of $X_{\max}$.

The mean altitude of the shower evolution of cosmic rays is shown in Figure 3.4. The value is compared to simulation of pure proton or iron showers as extreme scenarios of the possible spectrum of compositions. For the interaction of nuclei, simulation modelling interactions with EPOSv1.99 is used.[16] From the knee (PeV energies) to the second knee, the composition tends to higher masses (iron like). Above the second knee up to the ankle (3 EeV), it turns towards a proton spectrum. Above the ankle up to the cutoff, the spectrum tends to turn again to iron-like compositions.[17]

The trends of the composition together with the features of the cosmic ray energy spectrum could be explained using the three populations of Peters cycles again. From the knee towards the second knee, the first population is suppressed by the rigidity cutoff and the second population becomes dominant. At the second knee, the proton component of the third population starts to be visible, making the composition more "proton-like". Finally, above the ankle, the high-mass component of the population three produces again a composition with high mass. This corresponds to models like H3a (Section 3.2), where the composition at the highest energies is mixed.[18]

[15] Aloisio et al., "Cosmogenic neutrinos and ultra-high energy cosmic ray models".

[16] Pierog and Werner, "Muon Production in Extended Air Shower Simulations".

[17] T. Gaisser, Engel, and Resconi, *Cosmic Rays and Particle Physics*, p. 347f.

[18] Ibid.

3.3 *Acceleration of cosmic rays*

The power-law nature of the cosmic ray spectrum as visible from Figure 3.1 suggests an active process accelerating particles up to high energies rather than interactions of particles at thermal equilibrium or decays of heavier particles. The relevant question is what kind of mechanisms allow for a particle like protons or higher mass ions to be accelerated to energies exceeding 100 EeV.

The energy density of galactic cosmic rays equals $\rho_E \approx 0.5\,\mathrm{eV\,cm^{-3}}$. With cosmic rays escaping the galaxy (volume V_D) at a characteristic time-scale τ_R, a luminosity of

$$L_{\mathrm{CR}} = \frac{V_D \rho_E}{\tau_R} = 7 \times 10^{40}\,\mathrm{erg\,s^{-1}} \tag{3.4}$$

in order to maintain the energy density in equilibrium.[19] Supernova explosions every ~ 30 years could produce an energy outflow of $L_{\mathrm{SN}} \sim 3 \times 10^{42}\,\mathrm{erg\,s^{-1}}$, hence, producing enough energy if only a few percent is converted to cosmic ray acceleration.[20]

The basic formalism relevant for the acceleration is due to deflection in shocks of ionized gas clouds of plasma, commonly known as *Fermi acceleration*.[21] The derivation follows T. Gaisser, Engel, and Resconi, *Cosmic Rays and Particle Physics*. A cosmic ray particle is bound at an astrophysical site and undergoes multiple deflections in magnetic fields. At each deflection, it gains energy at a relative fraction $\Delta E = \xi E$ resulting in a total energy of $E_n = (1+\xi)^n E_0$ after n iterations. In total

$$n(E) = \frac{\ln(E/E_0)}{\ln(1+\xi)} \tag{3.5}$$

iterations are needed to accelerate a particle from E_0 to energy E. Moreover, the cosmic ray particle has the chance to escape the accelerator with probability P_{esc}. The probability to be accelerated n times is hence $(1-P_{\mathrm{esc}})^n$. Consequently, the amount of particles with energy of E or more is

$$N(\geq E) \propto \sum_{m=n(E)}^{\infty} (1-P_{\mathrm{esc}})^m = \frac{1}{P_{\mathrm{esc}}} \left(\frac{E}{E_0}\right)^{-\gamma+1} \tag{3.6}$$

with $\gamma = -(1 + \ln(1-P_{\mathrm{esc}}) / \ln(1+\xi))$. As a consequence, a power-law spectrum is obtained by only assuming that at each acceleration step, the energy is increased fractionally and the particle has a constant chance to escape after each iteration.

The deflection process itself happens due to diffusion of the cosmic ray in magnetic fields of plasma clouds.[22] The cosmic ray particle is considered to be relativistic. Figure 3.5 shows a gas cloud that travels at speed $v = \beta c$ with boost factor Γ. A cosmic ray incident at angle θ_1 is boosted to $E_1' = \Gamma(1 - \beta\cos\theta_1) E_1$ in the rest frame of the cloud. In the cloud, the particle diffuses and leaves the cloud at angle θ_2'. The diffusion is elastic and hence the energy in the cloud's

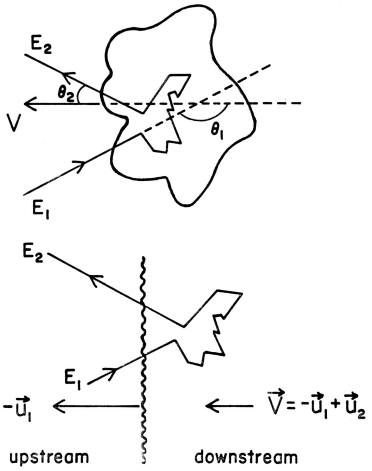

Figure 3.5: Fermi acceleration using diffusion of particles at plasma clouds (top) and planar shock fronts (top). A cosmic ray particle enters the region / shock with an angle θ_1 and leaves it at angle θ_2'. The cloud (shock) moves with speed v (u_1). For the shock, the shocked medium moves with speed u_2 relative to the shock front. Figures from T. Gaisser, Engel, and Resconi, *Cosmic Rays and Particle Physics*.

[19] T. Gaisser, Engel, and Resconi, *Cosmic Rays and Particle Physics*, p. 237.

[20] Ginzburg and Syrovatskii, *The Origin of Cosmic Rays*.

[21] Fermi, "On the Origin of the Cosmic Radiation".

[22] T. Gaisser, Engel, and Resconi, *Cosmic Rays and Particle Physics*, p. 237.

rest frame is unchanged. The relative change in energy yields

$$\xi = \frac{\Delta E}{E_1} = \frac{\beta^2 - \beta\cos\theta_1 + \beta\cos\theta_2' - \beta^2\cos\theta_1\cos\theta_2'}{1-\beta^2} \tag{3.7}$$

for a particular choice of incident and outgoing angle.[23] For a statistical description, the average expectation of the angles has to be taken into account. Naturally, this depends on the scenario considered and its inherent symmetries. Two important scenarios are usually discussed, visualized in Figure 3.5: (1) plasma clouds with isotropic symmetry, and (2) diffusion at a plane with normal vector $\mathbf{n}$, as for example realized at shock fronts.

[23] T. Gaisser, Engel, and Resconi, *Cosmic Rays and Particle Physics*, p. 240.

(1) Plasma cloud: Due to the isotropy in the rest frame of the cloud, the outgoing angle θ_2 is distributed isotropically, $\partial n/\partial\cos\theta_2' = 1/2$ for all possible directions. The expectation is thus $\langle\cos\theta_2'\rangle = 0$ in Eq. (3.7). For the incoming angle, the relative velocity of cosmic ray and cloud has to be taken into account. Due to the assumption before, the cosmic rays are considered relativistic and travel at the speed of light c. The projection of an isotropic incoming distribution onto the traveling direction $\boldsymbol{\beta}$ yields[24]

[24] Ibid., p. 240.

$$\frac{\partial n}{\partial\cos\theta_1} = \frac{1-\beta\cos\theta_1}{2} \tag{3.8}$$

resulting in a mean $\langle\cos\theta_1\rangle = -\beta/3$. Thus, for plasma clouds, the expectation for the relative energy gain of the cosmic particle according to Eq. (3.7) and Eq. (3.8) is

$$\xi = \frac{4\beta^2/3}{1-\beta^2} \to \frac{4}{3}\beta^2 \tag{3.9}$$

and quadratic in β for non-relativistic shock velocities. This is called *second order* Fermi acceleration. Although particles can lose or gain energy dependent on the angles θ_1 and θ_2', a net gain in energy in the laboratory frame is observed because of the boosted rest frame of the cloud in which the acceleration occurs.

(2) Shock front: At a shock front, two regimes exist, the unshocked *upstream* and shocked downstream region. As depicted in Figure 3.5 the shock travels at speed u_1. The shocked medium flows away from the shock with a relative velocity u_2, that is, in the laboratory frame, its velocity is $-u_1 + u_2$ if the shock goes in the negative direction. The velocity of the cloud in Eq. (3.7) corresponds to the downstream region in this case. Moreover, particles leave the shock in the upstream region at angles projected onto the shower plane. Hence the distribution of incident angles yields $\partial n/\partial\cos\theta_2' = 2\cos\theta_2'$ with $0 \leq \cos\theta_2' \leq 1$. In that case, the average value does not vanish, but equals $\langle\cos\theta_2'\rangle = 2/3$. For the incident angle, the same applies with $-1 \leq \cos\theta_1 \leq 0$ with particles passing the shock front into the downstream region, resulting in the negative outcome of $\langle\cos\theta_1\rangle = -2/3$. Hence, the relative energy gain yields[25]

[25] Ibid., p. 241.

$$\xi = \frac{4\beta/3 + 19\beta^2/9}{1-\beta^2} \to \frac{4}{3}\beta = \frac{4}{3}\frac{u_1 - u_2}{c}\,. \tag{3.10}$$

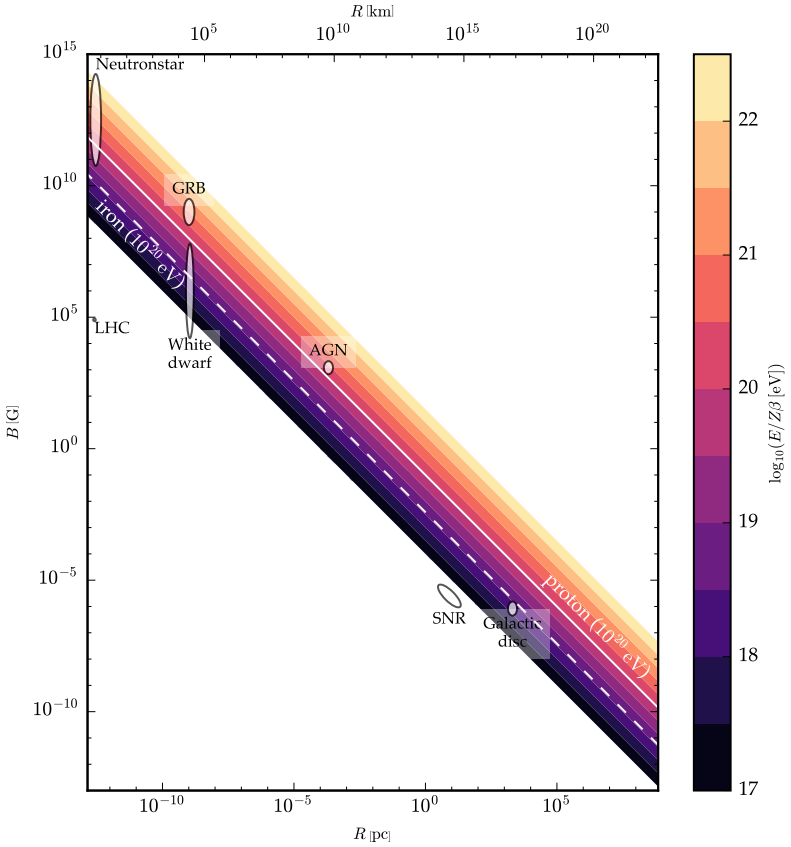

Figure 3.6: *Hillas plot* showing the properties of potential cosmic ray accelerators. The maximum energy an object can accelerate a cosmic ray up to depends on the cosmic ray charge, acceleration region size and magnetic field. Lines indicate the size and magnetic field needed for a source to accelerate protons/iron up to the energies of the very high end of UHECR energies. Data from T. Gaisser, Engel, and Resconi, *Cosmic Rays and Particle Physics*, p. 256.

In contrast to Eq. (3.9), this is linear in β and accordingly known as *first order* Fermi acceleration. The properties of the shock can further be described by the kinetic theory of monoatomic gases, and using the Galactic disk as acceleration region, the spectral index of the acceleration mechanism yields[26]

$$\gamma \approx 2 + \frac{4}{M^2} \to 2 \tag{3.11}$$

for strong shocks with large Mach number M. Hence, the expected intrinsic energy spectrum of cosmic rays in this model is a power law with $\sim E^{-2}$. Due to propagation effects (for example, explained with the "leaky box" model as simple approximation), this softens to the observed $E^{-2.7}$ cosmic ray spectrum.[27]

[26] Ibid., p. 242.

[27] Ibid., p. 193.

Comparing the two scenarios, the acceleration at a shock front is more efficient because a cosmic ray particle is always accelerated while for plasma clouds, deceleration can happen if the diffusion at the cloud is not head on. Hence, for shock fronts, relative energy gain in first order of β is achieved (Eq. (3.10)), while it is a second order effect β^2 for clouds in Eq. (3.9).

The energy a particle can achieve at maximum is given by the movement of the particle within the accelerating environment. At an acceleration site of size R, a cosmic ray particle of charge Ze has a gyroradius r_L as indicated in Eq. (2.1). Acceleration stops once the gyro-radius exceeds the accelerator size, and the cosmic ray escapes

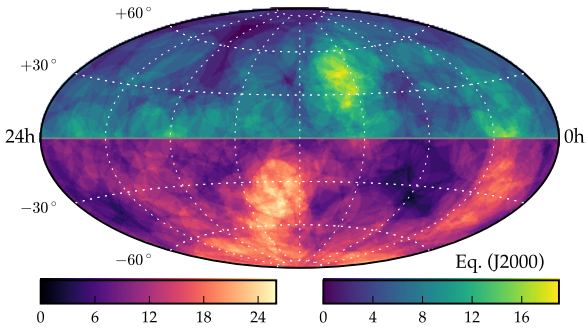

Figure 3.7: Arrival directions of UHECRs using 20° angular uncertainties. The sky is shown in equatorial coordinates (J2000) and separated in northern (green-yellow) and southern (red-yellow) sky. The plot shows public data by the Pierre Auger Observatory and the Telescope Array mentioned in the text.

the local environment. This yields the condition

$$E_{\max} < ZeBR \approx Z\beta \left(\frac{R}{\text{kpc}}\right) \left(\frac{B}{10^{-6}\,\text{G}}\right) \times 10^{18}\text{eV} \tag{3.12}$$

for the maximum energy an accelerator can produce. For a constant energy, $B \propto 1/R$, that is, with larger accelerators, the requirements of the magnetic field get lower. Figure 3.6 shows the landscape of accelerator sizes for typical sources that could be responsible in comparison to the parameters needed to arrive at the highest energies of cosmic rays observed.[28]

[28] Hillas, "The Origin of Ultrahigh-Energy Cosmic Rays".

3.4 *Possible sources of cosmic rays*

The *Hillas* plot shown in Figure 3.6 shows a large variety of classes of objects that could be sources of UHECRs accelerating cosmic rays up to energies of 100 EeV. There is no clear identification of sources of the UHECRs up to now, but numerous efforts are ongoing.[29] At the highest energies of the spectrum, the deflection due to intergalactic magnetic fields mentioned in Section 2.1 becomes small enough so that an angular coincidence of UHECRs and their origin might be possible. Figure 3.7 shows the arrival directions of the UHECRs with highest energies observed by the Pierre Auger Observatory[30] (231 events above $E \geq 52$ EeV mostly in the southern sky), and the Telescope Array[31] (72 events above 57 EeV). In both halves of the sky, two *hot spots* are identified deviating from an isotropic background assumption. The significance is in the region of $2-3\,\sigma$ using an angular deviation of around 20° as shown in Figure 3.7.

In the following, three possibilities for candidate sources are discussed. The physics acceleration of cosmic rays follows the basic principles of Fermi acceleration outlined in Section 3.3. In addition, any interaction of particles during the acceleration process is a possibility of gamma ray and neutrino production as outlined in Section 2.4. The objects considered are Supernova Remnants (SNRs) as Galactic candidate, blazars, a type of active galactic nuclei with its jet pointed towards the Earth and hence extragalactic, and gamma ray bursts (GRBs) as transient extragalactic phenomena.

[29] Aartsen, "Search for correlations between the arrival directions of IceCube neutrino events and ultrahigh-energy cosmic rays detected by the Pierre Auger Observatory and the Telescope Array"; Abbasi, "Indications of Intermediate-Scale Anisotropy of Cosmic Rays with Energy Greater Than 57 EeV in the Northern Sky Measured with the Surface Detector of the Telescope Array Experiment"; Aab, "Searches for Anisotropies in the Arrival Directions of the Highest Energy Cosmic Rays Detected by the Pierre Auger Observatory".

[30] Aab, "Searches for Anisotropies in the Arrival Directions of the Highest Energy Cosmic Rays Detected by the Pierre Auger Observatory".

[31] Abbasi, "Indications of Intermediate-Scale Anisotropy of Cosmic Rays with Energy Greater Than 57 EeV in the Northern Sky Measured with the Surface Detector of the Telescope Array Experiment".

Supernova remnants

At the end of its livetime, massive stars ($> 8M_\odot$) end their stellar evolution with a strong explosion. During that process, large amounts of material are ejected that produce a shell expanding around the center[32] of the explosion for thousands of years.

The evolution of the SNR can be divided into different stages:[33] first, a free expansion of the ejection material (expansion proportional in time) transferring energy to the interstellar medium (ISM). After a few hundred years, a shock in reverse direction is formed due to pressure of the ISM acting on the shock front of the ejected material, defining the *Sedov-Taylor* phase (expansion $\propto t^{2/5}$).[34] The gas temperature downstream of the shock is very high with strong magnetic fields and cannot be efficiently cooled. Hence, the evolution proceeds adiabatically. After $10^3 - 10^4$ years, the amount of relativistic particles is maximal, resulting in the peak luminosity of the SNR.[35]

Moreover, SNRs are prone to occur in *star forming regions* filled with interstellar gas. The shock of the supernova ejected material can interact with the gas of the medium, producing gamma rays and neutrinos.

Supernovae can result in a pulsar as final stage of the progenitor star, a fast rotating neutron star. Supernova remnants of this type are called pulsar wind nebula (PWN). Due to the fast rotation[36] of the neutron star ($f \gg 1\,\mathrm{s}$), strong magnetic fields emerge that can produce relativistic particles. The strongest known steady source of TeV gamma rays, the Crab Nebula as remnant of the SN 1054 at 6500 lyr distance, is a PWN object, shown in Figure 3.8 observed by Hubble.

[32] Black hole or neutron star depending on the mass of the progenitor star.

Figure 3.8: Crab Nebula as seen by Hubble Space Telescope in infrared. Image Credit: NASA/JPL-Caltech, Gerz (July 2016, http://www.nasa.gov/sites/default/files/images/148387main_image_feature_567_ys_full.jpg).

[33] T. Gaisser, Engel, and Resconi, *Cosmic Rays and Particle Physics*, p. 272.

[34] Ibid., p. 273.

[35] Rieger, Ona-Wilhelmi, and Aharonian, "TeV Astronomy".

Active galactic nuclei

The center of galaxies is made up by a supermassive black hole accreting surrounding matter. In this process, large amounts of energy are produced due to the particle releasing its gravitational potential energy. If the accretion rate of mass $\dot{M}$ is very high, the galactic nuclei is considered *active* and outshines the entire galaxy with its luminosity. Thus, AGN are sometimes referred to as quasars, quasi-stellar objects. In a stable accretion rate, a disk of accretion material forms and the energy is released in form of jets parallel to the spin axis. A sketch of an active galactic nuclei is shown in Figure 3.9. The luminosity of such accreting objects is quantified by the *Eddington luminosity* L_{edd}. At this luminosity, the gravitational pull of the nucleus on protons equals the outward pressure due to the radiation in the energy release due to electrons[37] interacting via Thomson scattering. The radial dependence cancels out, leaving the formula

$$L_{\mathrm{edd}} = 1.4 \times 10^{38}\,\mathrm{erg\,s^{-1}} \left(\frac{M}{M_\odot}\right) \tag{3.13}$$

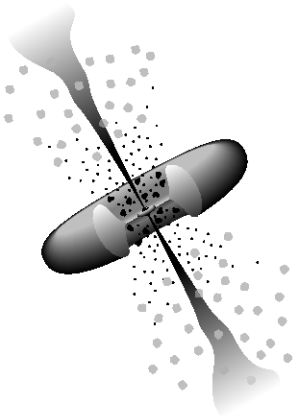

Figure 3.9: Simplified view of AGN in unified scheme. The AGN consists of a supermassive black hole with an accretion disk and a dust torus. Perpendicular to the accretion disk, jets of highly relativistic particle outflow are formed. If the jet points at the observer, the AGN is called a blazar. Figure from Urry and Padovani, "Unified schemes for radio-loud active galactic nuclei".

[36] Becker and Aschenbach, "Rosat HRI observations of the Crab Pulsar: an improved temperature upper limit for PSR 0531+21".

[37] T. Gaisser, Engel, and Resconi, *Cosmic Rays and Particle Physics*, p.270.

for the Eddington luminosity. For a supermassive black hole of $10^8 M_\odot$, the luminosity yields $L_{\text{edd}} \sim 10^{46} \text{erg}\,\text{s}^{-1}$.

The formation of relativistic jets is closely connected to the spin of the black hole and produces a clear symmetry axis. If the jet points towards the Earth, the AGN is called a *blazar*.[38] Blazars belong to the most powerful objects in the universe and are the dominant component of extra-galactic objects observed in high-energy gamma rays. They show strong emission in radio wavelength. Two classes of blazars are known, BL Lacs and Flat-Spectrum Radio Quasars (FSRQs) that are classified due to the lack or presence of broad emission lines, respectively.

[38] Urry and Padovani, "Unified schemes for radio-loud active galactic nuclei".

The jet environment in which the acceleration of cosmic ray particles happens, interactions of the cosmic rays with strong radiation fields and particles can occur, producing large amounts of secondary particles like for example pions, which then produce neutrinos (refer to Section 2.4 for more details). Processes involved in this *astrophysical beam dump* similar to the beam dump in particle accelerators like LHC are synchroton radiation, synchroton self absorption, inverse Compton scattering, pion production, and pair production.[39] In such processes, blazars produce a large spectrum of wavelength visible in photons, dominated by two *humps* due to synchroton and inverse Compton scattering or π^0 decays, Eq. (2.5). Modeling all these processes, blazars are promising candidates for acceleration of cosmic rays and the production of high energy gamma rays and neutrinos.[40]

[39] T. Gaisser, Engel, and Resconi, *Cosmic Rays and Particle Physics*.

[40] Petropoulou, Dimitrakoudis, et al., "Photohadronic origin of γ-ray BL Lac emission: implications for IceCube neutrinos".

Gamma ray bursts

GRBs are the most energetic transient objects with energies of 10^{53} erg and are classified in long ($t > 2\,\text{s}$) and short bursts.[41] The two different scenarios as progenitors of GRBs discussed are core collapse supernovae (CCSN) or a merger of a binary system (neutron star - neutron star or black hole - neutron star) corresponding to long or short bursts, respectively. In the dense medium of a CCSN, cosmic rays can be accelerated, as well as large amounts of gamma rays and neutrinos. Gamma ray bursts are transient phenomena at extremely high energy. No neutrino connection to GRBs has been observed up to now[42] resulting in strong limits on the on-going mechanisms and limiting their contribution to the UHECR flux in the current models.

[41] T. Gaisser, Engel, and Resconi, *Cosmic Rays and Particle Physics*, p. 295.

[42] Aartsen, "An All-Sky Search for Three Flavors of Neutrinos from Gamma-Ray Bursts with the IceCube Neutrino Observatory".

3.5 *GZK-cutoff & cosmogenic neutrinos*

Above energies of 100 EeV, a cutoff of the cosmic ray energy spectrum is observed by the largest detectors.[43] A suppression of the flux of cosmic rays is expected when cosmic ray particles interact with photons composing the cosmic microwave background (CMB) and the diffuse extragalactic background light (EBL).

[43] Abraham, "Observation of the suppression of the flux of cosmic rays above 4×10^{19}eV"; Abu-Zayyad, "The Cosmic Ray Energy Spectrum Observed with the Surface Detector of the Telescope Array Experiment".

The interaction rate is strongest when resonances are formed. The first resonance is due to $p\gamma \to \Delta^+$ with a mass of $m_\Delta = 1.232\,\text{GeV}$. The energy of the proton to interact with photons of the CMB or EBL to produce a Δ resonance is at $\sim 5 \times 10^{19}\,\text{eV}$. This can produce a suppression of the cosmic ray flux named after *Greisen-Zatsepin-Kuzmin*[44] (GZK). A suppression of the flux at this energy scale is observed, but it is not yet clear whether this is due to the GZK cutoff or due to the fact that the strongest extra-galactic accelerators reach their maximum acceleration power.[45]

After an interaction and the formation of a Δ resonance, secondary particles are produced as decay products. This results in a *cosmogenic* neutrino flux at very high energies exceeding the PeV scale reaching up to EeV energies of the neutrino as well as a diffuse gamma ray background. A flux of cosmogenic neutrinos has not been observed so far[46] with no observation of neutrinos beyond a couple of PeV in energy. The flux of cosmogenic neutrinos depends on the composition of the UHECRs at the highest energies. Figure 3.10 shows the prediction of the neutrino flux for a mixed and proton only spectrum of UHECR,[47] compared to the observation of high-energy neutrinos by IceCube.[48]

The UHECR spectrum shown in Figure 3.3 extends beyond the energies relevant for the GZK effect to occur. The fraction of cosmic rays to remain after a certain propagation distance is shown in Figure 3.11 for cosmic rays at 100 EeV. After $\sim 250\,\text{Mpc}$, all types of nuclei are absorbed. Thus, cosmic rays at the highest energies are expected to be produced in the close universe without being deflected completely.

3.6 Atmospheric showers

When a cosmic ray enters the Earth's atmosphere, deep inelastic scattering with the gas molecules occurs. This produces large cascades (or showers) of secondary particles. These cascades are then studied by large ground based experiments to reconstruct the properties of the primary cosmic ray particle. In this section, the properties of the evolution of an air shower will be outlined, and the production of secondary particles in the shower discussed.

Figure 3.12 shows two simulation of a 10 TeV shower of a proton and iron cosmic ray particle entering the atmosphere and interacting at 20 km height.[49] Due to the different properties of the two particles (energy per nucleon), the evolution for both showers shows different characteristics.

For the evolution of a shower, it is important to consider the different processes that are related to the evolution of a particle species as the lifetime τ after which a particle decays. Other particles are then created in such decays. In interactions of particles that occur after traveling a distance d in a medium[50], particles are destroyed and created. This is mathematically described using *cascade equations*

[44] Greisen, "End to the cosmic ray spectrum?"; Zatsepin and Kuzmin, "Upper limit of the spectrum of cosmic rays".

[45] T. Gaisser, Engel, and Resconi, *Cosmic Rays and Particle Physics*.

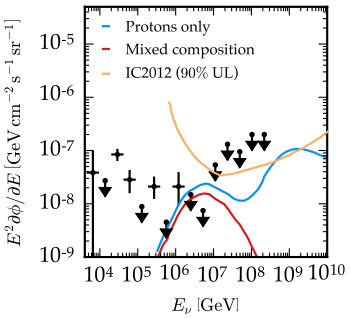

Figure 3.10: Cosmogenic neutrino flux for different compositions of UHECRs. The diffuse astrophysical neutrino observation (black) and limits on EeV neutrino emission (yellow) are shown for comparison.

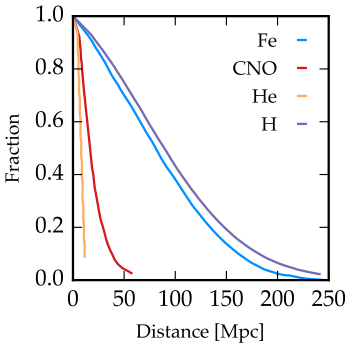

Figure 3.11: Survival fraction of different types of cosmic rays with 100 EeV versus distance. Reference for data in text.

[46] Aartsen, "Constraints on ultra-high-energy cosmic ray sources from a search for neutrinos above 10 PeV with IceCube".

[47] Aloisio et al., "Cosmogenic neutrinos and ultra-high energy cosmic ray models".

[48] Aartsen, "Atmospheric and astrophysical neutrinos above 1 TeV interacting in IceCube".

[49] Heck et al., *CORSIKA: a Monte Carlo code to simulate extensive air showers.*

[50] The distance is usually expressed using the length normalized by the target density of the medium, in units g cm^{-1}.

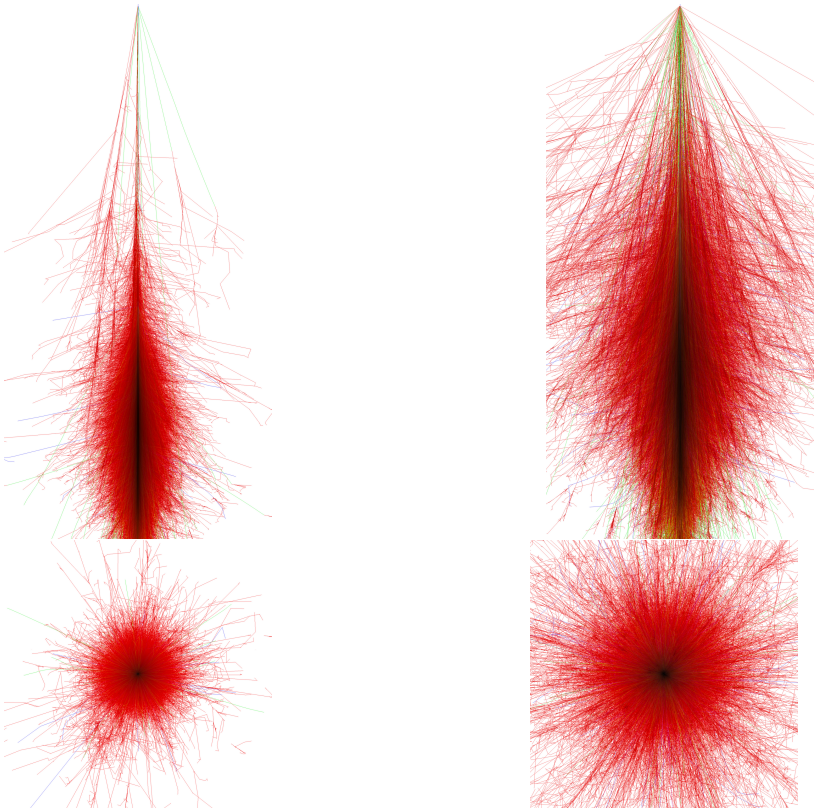

Figure 3.12: Cosmic ray air shower simulation of 10 TeV proton (left) and iron (right) particles. Top panel shows the x-z plane, bottom the x-y plane. Simulation produced with CORSIKA (Heck et al., *CORSIKA: a Monte Carlo code to simulate extensive air showers.*). Red lines show charged particles created in the shower that are above a threshold energy The shower interacts at 20 km altitude.

for each particle of type i

$$\frac{dN_i}{dX}(E_i, X) = -\frac{N_i}{\lambda_i} - \frac{N_i}{d_i} + \sum_{j=i}^{J} \int_{E_i}^{\infty} dE_j \frac{F_{ji}(E_i, E_j)}{E_i} \frac{N_j}{\lambda_j}. \tag{3.14}$$

The number N_i of particles at atmospheric slant depth X with energy E_i decreases due to particles of that type interacting or decaying, both with characteristic length λ_i and d_i, respectively. The particle number increases in the production as secondary particle of other particles of type j at quantity N_j with interaction length λ_j giving a particle yield F_{ij} for a particle i to be produced at energy E_i by particle j at energy E_j, $F_{ij}(E_i, E_j) = E_i dn_i(E_i, E_j)/dE_i$.[51]

Moreover, long-lived particles like electrons or muons lose energy by ionizing the atmosphere or producing radiation of particles (*bremsstrahlung*):

$$dE/dX = -\alpha - E/\xi. \tag{3.15}$$

The critical energy is defined as the energy at which both ionization (α) and radiation ($1/\xi$) are of same strength, $E_C = \alpha\xi$. For electrons, this energy is low ($E_C = 87$ MeV), but due to the higher mass of the muon, the characteristic energy is a factor of $(m_\mu/m_e)^2$ higher ($E_C \sim 500$ GeV).[52] Consequently, electrons quickly lose energy in a shower, whereas muons are *minimum ionizing* and travel long distances before significantly losing energy.

[51] T. Gaisser, Engel, and Resconi, *Cosmic Rays and Particle Physics*, p. 108.

[52] T. Gaisser, Engel, and Resconi, *Cosmic Rays and Particle Physics*, p. 110f.

A detailed review of the ongoing physics is given in T. Gaisser, Engel, and Resconi, *Cosmic Rays and Particle Physics*. The important results for this work will be summarized in the following. Electromagnetic cascades behave in a very simple way that proves very indicative in understanding the basic properties. Only two processes have to be considered, electrons produce a photon via *bremsstrahlung*, and a photon creates two electrons in *pair-production* in vicinity of a nucleus. Hence, at each interaction, the particle number doubles, and the particle number after $n = X/\lambda$ iterations at distance X is $N(X) = 2^{X/\lambda}$, with approximate particle energy $E(X) = E_0/N(X)$. Below the critical energy, processes cannot occur anymore and the cascade evolution stops.[53] Hence, the maximum number of particles created in the shower is $N(X_{\max}) = E_0/E_C$ at an slant depth

[53] Ibid., p. 303.

$$X_{\max} = \lambda \frac{\ln(E_0/E_C)}{\ln 2}. \tag{3.16}$$

The energy of the primary particle is directly related to the number of particles created and the depth of the shower maximum.

For hadronic cascades, the interactions are more complicated and a large variety of particles is created with different propagation properties, but the basic principles are the same. The shower maximum is at

$$X_{\max} \approx \lambda_{\text{int}} + X_0 \ln\left(\frac{E_0}{2 n_{\text{tot}} E_C}\right) \tag{3.17}$$

with interaction length λ_{int}, and electron critical energy E_C. In the *superposition model*, a nucleus with mass number A is approximated as A independent particles with energy E_0/A.[54] This changes the position of the shower maximum in Eq. (3.17).

[54] Ibid., p. 320.

An important quantity for air shower physics is the *shower age*[55]

[55] Hillas, "Angular and energy distributions of charged particles in electron photon cascades in air".

$$s = \frac{3}{1 + 2X_{\max}/X}, \quad s \in (0,3) \tag{3.18}$$

quantifying the shower development empirically in relation to the depth of the shower maximum. With this, the lateral density for shower evolution can be parameterized as

$$\rho_{e^\pm} = C_1(s)\, x^{s-2} (1+x)^{s-4.5} \left(1 + C_2 x^d\right) \tag{3.19}$$

with $x = r/r_1$ ($r_1 \approx 85\,\text{m}$) and shower age dependent parameters $C_{1/2}$ and d.

In modern air shower detectors, two detection techniques are utilized to monitor the shower evolution and reconstruct the shower given the shower evolution functions. The two detection methods are illustrated in Figure 3.13. One component consists of an array of water tanks that detect particles at ground that pass the tank and emit light. The energy of the shower is then related to the number of particles at a certain distance to the shower core, for example electrons and muons.

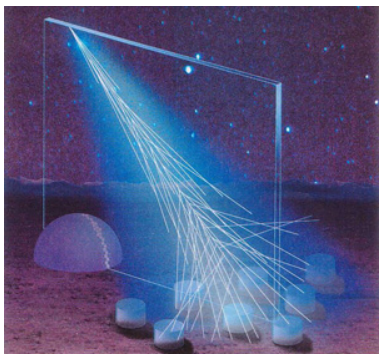

Figure 3.13: Cosmic ray shower detection with Pierre Auger Observatory using water tanks and fluorescence detectors. Figure from Pierre Auger Collaboration (Aug. 2016, https://www.auger.org / images / Cosmic _ Rays / Auger _ cosmic_ray_shower.jpg).

The second technique uses fluorescence detectors to measure the shower evolution in the air. At high energies ($E \geq 10^{17}\,\text{eV}$), nitrogen atoms are excited by the air shower and emit fluorescence light. The

longitudinal profile of the shower can be measured using this light. The amount of light is connected to the ionization energy deposited by the shower.[56] Thus, the atmosphere serves as a calorimeter for the energy reconstruction of the shower. Measuring the fluorescence light only works in dark, moon-less nights, but supplies an independent measurement to the ground stations, hence reducing systematic uncertainties due to one detection technique, if a shower is observed in a *hybrid* mode using both techniques.

[56] T. Gaisser, Engel, and Resconi, *Cosmic Rays and Particle Physics*, p.334.

3.7 Muons and neutrinos in air showers

Cosmic ray induced air showers constitute the largest background for searches of high-energy astrophysical neutrinos. In air showers, both muons and neutrinos are produced in decays of charged kaons and pions. These processes are identical to the neutrino production in the universe as discussed in Section 2.4, especially Eq. (2.4). In the Earth's atmosphere however, the density of the surrounding medium is much higher and distances are shorter. Consequently, muons do not necessarily decay before reaching a detector or significantly losing energy.[57] The energy after traveling a distance X is given by

[57] Ibid., p. 163.

$$\langle E(X) \rangle = (E_0 + E_C)\, \mathrm{e}^{-X/\xi} - E_C \tag{3.20}$$

after solving Eq. (3.15). For a particle at energy E_0, this gives the mean length $X \approx \xi \ln(1 + E_0/E_C)$.[58] The density of material is usually quoted in *meter water equivalent* (m.w.e.). The absorption length for muons is $\xi \approx 3000$ m.w.e.. The depth of the atmosphere is 10 m.w.e and can be neglected for muons. Hence, muons are the principal background in underground detectors.

[58] Ibid., p. 165f.

The production of neutrinos (and muons as well) is described by cascade equations as in Eq. (3.14). The dominant contributors to the atmospheric neutrino flux are decays of kaons and pions. These constitute the *conventional* neutrino flux. An important quantity is the *characteristic energy* ϵ_i of the particle

$$\epsilon_i \equiv \frac{h_0 m_i c}{\tau_i} \tag{3.21}$$

with mass m_i and lifetime τ_i and atmosphere height h_0. For energies far above the characteristic energy, interactions of particles are dominating the cascade evolution, below that energy, decays are more important. In terms of neutrino production, this means that only meson energies below the value of Eq. (3.21) are important for neutrino production. An approximate form for the number of neutrinos is given by[59]

[59] van Santen, "Neutrino Interactions in IceCube above 1 TeV".

$$N_\nu(E_\nu) \approx \frac{N_N(E_\nu)}{1 - Z_{NN}} \sum_i \frac{\mathrm{BR}(i \to \nu)\, A_{i\nu}}{1 + B_{i\nu} \cos\theta E_\nu / \epsilon_i} \tag{3.22}$$

following the primary nucleon flux $N_N(E_\nu)$. The spectrum is modulated by the moments Z_{ij} quantifying the interaction/decay characteristics.[60] The other parameters A_i and B_i are parameterizations

[60] Ibid., p. 11.

of the moment Z_{Ni} and the boost into the laboratory frame. The remaining factor BR is the branching ratio of meson i to decay into particles involving neutrinos.

For energies below the characteristic energy, the neutrino spectrum follows the cosmic ray spectrum N_N, while the spectrum is softer by a power of E for energies much larger than the characteristic energy ϵ_i. For kaons and pions, the characteristic energies are 115 GeV (850 GeV). Consequently, at large energies above TeV energies, the spectrum of conventional neutrinos follows a spectrum $E^{-3.7}$. For muons, a similar equation like Eq. (3.22) exists, with different moments A_μ, Z_μ. In the two body decay of pions ($\pi^\pm \to \mu^\pm \nu_\mu$), the muon is more energetic. As a result, the muon flux is higher than the one for neutrinos, and muons are dominantly produced by pions, while for neutrinos, kaons constitute the majority of the flux above 100 GeV.[61]

Another component of atmospheric neutrinos is given by *prompt* fluxes. Decays of heavy mesons, which have charm quarks, the characteristic energy is much higher $\epsilon \geq 10^7$ GeV. Charmed mesons are produced at very early stages in the shower evolution. At low energies, the prompt flux is much lower than conventional neutrinos produced in decays of pions and kaons. However, due to the higher characteristic energy, the spectrum of prompt neutrinos follows the cosmic ray spectrum and will exceed the conventional fluxes in the 100 TeV to PeV energy regime.[62]

Figure 3.14 shows conventional[63] and prompt[64] neutrino fluxes in comparison to the diffuse astrophysical flux. The difference in the energy spectrum is clearly visible. Astrophysical neutrinos are expected to have an even harder spectrum shown as E^{-2} that is connected to the cosmic ray energy spectrum at the source (as discussed in Section 3.3), while atmospheric fluxes depend on the CR flux at Earth.

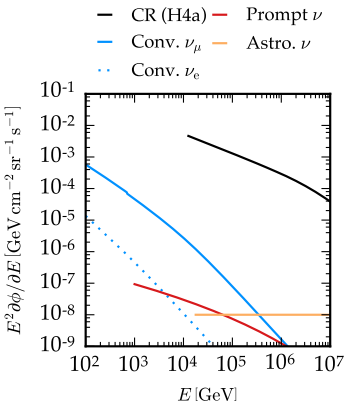

Figure 3.14: Atmospheric neutrinos fluxes with respect to neutrino energies. Conventional neutrino fluxes (by Honda et al.) are shown for electron and neutrino flavor. All-flavor fluxes are shown for prompt neutrinos (by Enberg, Reno, and Sarcevic) and the diffuse astrophysical flux (10^{-8} GeV cm^{-2} s^{-1} sr^{-1}).

[61] van Santen, "Neutrino Interactions in IceCube above 1 TeV", p. 13.

[62] Fedynitch et al., "The contribution of charm to high energy atmospheric neutrinos".

[63] Honda et al., "Calculation of atmospheric neutrino flux using the interaction model calibrated with atmospheric muon data".

[64] Enberg, Reno, and Sarcevic, "Prompt neutrino fluxes from atmospheric charm".

4 The IceCube Neutrino Observatory

The IceCube Neutrino Observatory located at the geographic South Pole is currently the largest neutrino telescope worldwide. IceCube instruments one gigaton of ice at the South Pole. Other neutrino observatories are ANTARES[1] (operational, Mediterranean Sea), KM3NET (under construction, Mediterranean Sea), and Baikal-GVD (under construction, Lake Baikal[2]) that use ocean and lake water as target medium. The detection principle for all these detectors is the same and is introduced in the following discussing IceCube as example.

[1] Adrian-Martinez, "Letter of intent for KM3NeT 2.0".

[2] Avrorin, "Status and perspectives of the BAIKAL-GVD project".

4.1 Neutrino detection

In transparent media like the Antarctic ice, the Cherenkov light that is produced by prior neutrino interactions is collected and used for reconstruction of the neutrino's properties. Neutrinos themselves are not visible because they only interact weakly with their surroundings. Secondary charged particles at relativistic energies emit *Cherenkov radiation*, illustrated in Figure 4.1. The angle (θ_C) under which the radiation is emitted is equal to

$$\cos\theta_C = \frac{1}{n\beta} \tag{4.1}$$

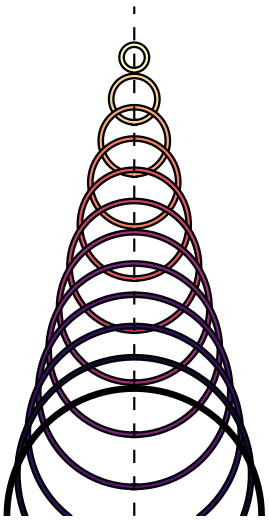

Figure 4.1: Cherenkov effect of a particle traveling in positive y-direction with $\beta = 1$ in a medium with refraction index $n = 4$.

[3] Frank and Tamm, "Coherent visible radiation of fast electrons passing through matter".

for a particle traveling with velocity β in a medium with refractive index n. For ice or water ($n \approx 1.32$), the angle equals $\theta_C \approx 41°$. The number of photons emitted in the wavelength range $d\lambda$ along a path dx is given by the *Franck-Tamm formula*[3]

$$\frac{dN}{dx\,d\lambda} = \frac{2\pi\alpha}{\lambda^2}\sin^2\theta_C\,. \tag{4.2}$$

This assumes a single charged particle; $\alpha = e^2/(4\pi)$ is the fine-structure constant. The radiation is inversely proportional to the square of the wavelength, hence, it appears *blue* in the optical regime.

The energy regime in which IceCube operates are neutrino interactions with neutrino energies above 100 GeV. Deep-inelastic scattering occurs in this regime, when neutrinos interact with the molecules of the ice.[4] Neutrinos only interact via the exchange of weak bosons $W^\pm$, Z^0 in charged or neutral current interactions, respectively. The

[4] Formaggio and Zeller, "From eV to EeV: Neutrino Cross Sections Across Energy Scales".

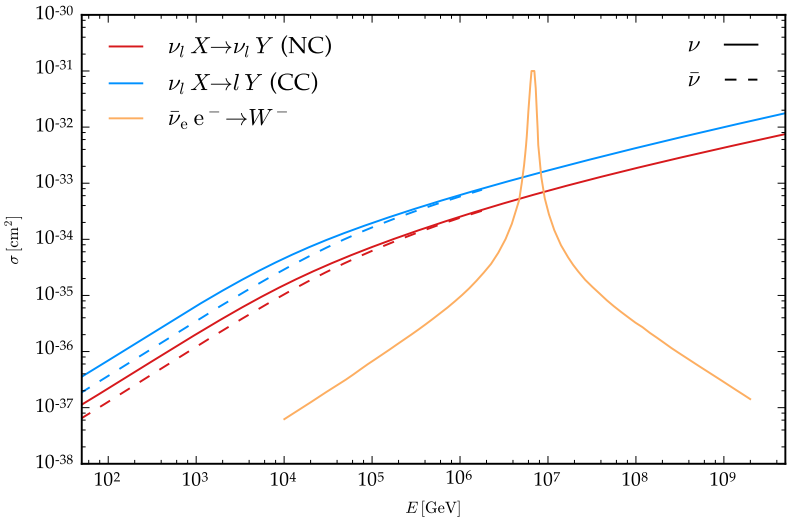

Figure 4.2: Neutrino cross sections at high energies for deep-inelastic scattering with a nucleus. The cross sections σ are shown for neutrinos and antineutrinos separately. Solid lines show charged current interactions, dashed lines neutral current ones. Moreover, the cross section of the Glashow resonance is plotted. Data from Gandhi et al., "Ultrahigh-energy neutrino interactions".

corresponding interactions

$$\nu_l + X \xrightarrow{W^\pm} l^\pm + Y \tag{4.3}$$

$$\nu_l + X \xrightarrow{Z^0} \nu_l + Y \tag{4.4}$$

are the same for all three flavors of neutrinos. For charged current interactions (Eq. (4.3)), the charged lepton $l^\pm$ corresponding to the primary neutrino ν_l is produced, while for neutral current interactions, the outgoing lepton stays a neutrino. At high energies in the deep-inelastic scattering regime, the nucleus X of the interaction fragments into a hadronic cascade denoted by Y in Eq. (4.3) and (4.4).

Neutrinos can scatter with electrons bound in the atoms of the Antarctic ice as well, but the cross section of such an interaction is much smaller than for interactions with the atom's nucleus.[5] For electron antineutrinos however, this scattering becomes resonant when the center of mass energy equals the mass of the $W^\pm$ boson. At this *Glashow* resonance[6]

$$\bar{\nu}_e + e^- \to W^\pm \tag{4.5}$$

the scattering cross section becomes much larger than for the other interactions in Eqs. (4.3), and (4.4). The energy of the resonance is at $m_W^2 / (2m_e) \sim 6.3\,\text{PeV}$. The Glashow resonance is the only interaction that distinguishes particle versus anti-particle because the target material (ice) consists only of electrons. Hence, there is no $\mathcal{CP}$ transformed interaction of Eq. (4.5) for electron neutrinos interacting with positrons due to lack of the target material.

The cross sections for the neutrino interactions mentioned before are shown in Figure 4.2 for deep-inelastic scattering in the energy range interesting in the context of IceCube. Most importantly, one can observe a proportional increase of the cross section with energy, $\sigma \propto E$, up to energies of $\sim 10\,\text{TeV}$. Below this energy, the propagator of the massive bosons is inhibited by their mass. Above that

[5] Formaggio and Zeller, "From eV to EeV: Neutrino Cross Sections Across Energy Scales".

[6] Glashow, "Resonant Scattering of Antineutrinos".

energy, the momentum transfer k^2 becomes important in the boson propagator, changing the cross section

$$\sigma_{\mathrm{CC/NC}} \propto \left(\frac{1}{k^2 + m_{W/Z}^2} \right)^2 E \tag{4.6}$$

resulting effectively in a cross section dependence $\sigma \propto E^{0.36}$.[7] The ratio of charged to neutral current cross section is $\sigma_{\mathrm{CC}}/\sigma_{\mathrm{NC}} \approx 2.4$ throughout the whole energy range. The scattering of neutrinos with bound electrons is a factor more than one hundred below the nucleon scattering cross sections due to the electron's small mass. Only at the Glashow resonance, scattering at electrons becomes important for electron antineutrinos.

[7] Formaggio and Zeller, "From eV to EeV: Neutrino Cross Sections Across Energy Scales".

The cross section of neutrino with respect to antineutrinos is larger by a factor of two[8] below energies of 10 TeV because neutrinos primarily scatter with the three valence quarks (*uud* and *udd* for protons and neutrons, respectively). Thus, the target is $\mathcal{CP}$ asymmetric, resulting in the difference in cross section for neutrinos and their antiparticles. Above 10 TeV, scattering with sea quarks becomes more important, removing the difference of neutrino and antineutrino at higher energies, because the target is visible equally in quarks and antiquarks.

[8] Ibid.

All listed interactions add up to the total cross section for neutrino interactions $\sigma_{\mathrm{tot}} = \sum_i \sigma_i$. The relative energy transferred from the neutrino to the nucleus (inelasticity y) at the highest energies (PeV and above) is about $\sim 20\%$, and larger for lower neutrino energies.[9] The mean free path of the neutrino is calculated as

[9] Gandhi et al., "Ultrahigh-energy neutrino interactions".

$$L_{\mathrm{int}} = \frac{1}{\sigma_{\mathrm{tot}}} \frac{1}{\rho} \tag{4.7}$$

in a medium of density ρ. This is inversely proportional to the cross section and thus the interaction length drops with increasing energy. In fact, above TeV energies, the column density of the Earth gets larger than L_{int}, reducing the probability that a neutrino traverses the Earth unaffected, $P(x) = \mathrm{e}^{-x/L_{\mathrm{int}}}$. If a neutral current interaction occurs (Eq. (4.4)) a secondary neutrino (with energy $(1-y)E$) is produced with lower energy that continues to propagate through the Earth. The same applies for tau neutrino charged current interactions where the τ-lepton decays, producing at least one ν_τ after a short livetime of $\tau_\tau \approx 2.9 \times 10^{-13}$ s.[10] This effect is called *regeneration* and recovers parts of an otherwise absorbed flux visible in neutrino telescopes.[11]

[10] Olive, "Review of Particle Physics".

[11] E. Bugaev et al., "Propagation of tau neutrinos and tau leptons through the earth and their detection in underwater / ice neutrino telescopes".

4.2 *Event topologies*

The detection of neutrino interactions using Cherenkov radiation of secondary charged particles can be classified in three event topologies. The classification is based on the geometry and symmetries of light emission that are typical for these classes, closely connected to the particles involved in the interaction. Figure 4.3 shows the light

emission profile of these three topologies in a 2D random walk simulation of the Cherenkov light produced along the track of charged particles. For the simulation, strong scattering with scattering length of 80 m and low absorption (275 m) was used as typical for the Antarctic ice in IceCube.[12] The topologies are called *cascades* or *showers*, *tracks*, and *double-bangs*.

[12] Aartsen, "Measurement of South Pole ice transparency with the IceCube LED calibration system".

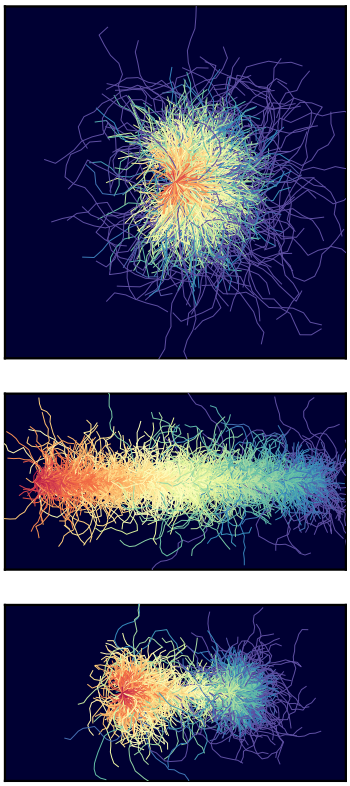

Figure 4.3: Neutrino event signatures. Shown are the three topologies induced by electron (top), muon (middle) and tau (bottom) flavored neutrinos. This toy simulation shows the scattering of Cherenkov light in a random walk assuming 275 m absorption length and 80 m scattering length for 5000 photons from particles traveling in the positive x direction. The scattering angle has a mean of 30° for a *von Mises* distribution modeling Mie scattering in the Antarctic ice. The color coding of the photon path illustrates the passing time from neutrino interaction (red) until photon absorption (blue). The illustrations are *not* to scale with each other.

Cascade/Shower: the spherical symmetry is characteristic for such events. Charged current interaction of electrons or tau neutrinos induce this event topology. In the interaction, hadronic and electric cascades are induced (similar as discussed in Section 3.6 but in a denser medium. The size of the particle shower in the ice is a few meters which is very small compared to the size of the IceCube detector. Due to the scattering of the light, the primary direction of the neutrino is quickly smeared out and the light appears to radiate isotropically from the cascade close to the interaction point. The amount of light produced is connected to the number of particles produced in the cascade and hence connected to the neutrino energy.[13] Because of the spherical symmetry, the angular resolution is only 10° at 50% confidence for energies above 60 TeV.[14] Neutral current interactions produce cascade-like event topologies as well, but part of the energy is not transferred to the particle shower, because the outgoing neutrino escapes the detector unseen. Thus, neutral current interactions look like charged current interactions at approximately 30% of the energy.[15]

Track: whenever a muon traverses the detector, this topology is encountered. Tracks are most commonly connected to charged current interactions of muon neutrinos. Muons are deeply penetrating particles and travel several kilometers at TeV energies (see Section 3.6). The "track" of the muon is observable due to the muons Cherenkov cone and radiation losses along the muon's path that produce Cherenkov light themselves. As illustrated in Figure 4.3 (middle), track events are distinguishable due to the elongated light pattern. This results in a long lever arm for angular reconstruction, resulting in much better angular resolutions than for cascades. The energy resolution is limited to a factor of two because the muon leaves the detector without depositing all the neutrino energy.[16] Hence, the deposited energy in the detector gives only a lower limit on the true muon energy. Moreover, due to the length of the muon track, most muons will enter the detector after a neutrino interacted outside of the detector. Thus, only the muon track traversing the detector is visible as *through-going track*. If a neutrino is interacting inside the detection volume and a muon is produced that leaves the detector, this is called a *starting track*. Tracks are the most abundant topology for neutrino observatories, since not only neutrinos produce such signatures, but muons produced in air showers enter the detector from above, leaving a

[13] Aartsen, "Energy Reconstruction Methods in the IceCube Neutrino Telescope".

[14] Aartsen, "Evidence for High-Energy Extraterrestrial Neutrinos at the IceCube Detector".

[15] Gandhi et al., "Ultrahigh-energy neutrino interactions".

[16] Aartsen, "Energy Reconstruction Methods in the IceCube Neutrino Telescope".

track-like signature in the detector. Tracks can be induced in tau neutrino interactions as well, if the tau lepton decays to muons, or Glashow events where the W^- decays to $\bar{\nu}_\mu \mu^-$.

Double-bang: this topology is connected to the decay pattern of tau leptons produced in prior tau neutrino interactions. Similar to the regeneration process in the Earth discussed above, a τ-lepton produced in a charged current interaction decays after a short livetime. Converting this to a distance traveled, the τ lepton will decay after

$$d \approx 50\,\mathrm{m\,PeV}^{-1} \times E_\tau \tag{4.8}$$

producing a corresponding tau neutrino and hadrons (branching ratio $\sim$ 64.8%), $e\nu_e$ (17.8%), or $\mu\nu_\mu$ (17.4%). For the two first scenarios that happen in $\sim$ 82% of the cases the tau decay will produce a shower. For PeV energies and above, the neutrino interaction point and the position of the tau decay are distant enough that the hadronic shower of the neutrino deep inelastic scattering and the tau decay induced shower are separable[17]. Consequently, two showers are observed that are spatially and timely separated by the speed of light with a dim track in between produced by the tau lepton, as visualized in Figure 4.3 (bottom). Even though such a double bang can be only identified for very high energies, it gives a good angular resolution due to the two separated cascades. Moreover, this signature is a clear identification of astrophysical neutrinos, because there is no atmospheric background of tau neutrinos, compare Sections 2.6, and 3.6. In searches for double bangs, no tau neutrino was identified up to now, but more data is needed to be sensitive to the expected rate of double-bangs given by the astrophysical neutrino flux.[18]

[17] Below this energy, the two cascades are not distinguishable and tau neutrino interactions will produce a *cascade-like* event similar to electron neutrinos.

[18] Aartsen, "Search for Astrophysical Tau Neutrinos in Three Years of IceCube Data".

Glashow events produce a track/double bang if the $W^\pm$ decays to $\mu\nu_\mu/\tau\nu_\tau$ respectively (branching ratio 11% each) or a shower otherwise. In events involving τ-leptons, a muon with comparable low energy can be produced due to the three body decay $\tau \to \mu\nu_\mu\nu_\tau$.

4.3 Neutrino telescope requirements

In the previous section, the interactions of neutrinos were discussed and the details of light emission profiles of secondary particles introduced. In optically transparent media, Cherenkov light produced as a result of the neutrino interaction can be used to detect the neutrino interactions. Such *Water Cherenkov Detectors* are well established experiments. Super-Kamiokande is one notable example[19] that uses a large tank of purified water (50 kt) deep underground to observe neutrinos in the MeV to a few GeV region, and its predecessor was one of the experiments to first observe the neutrino burst connected to supernova (SN1987A).[20]

[19] Fukuda, "The Super-Kamiokande detector".

[20] Hirata, "Observation of a Neutrino Burst from the Supernova SN 1987a".

Despite the same mechanism of neutrino detection, neutrino observatories that target neutrinos at higher energies need to be much larger to detect the faint signal of astrophysical neutrinos. An upper bound on the neutrino flux is given by the *Waxman-Bahcall bound*[21] derived from the energy density of extra-galactic cosmic rays at the highest energies. If neutrinos are produced in photo-meson or p-p interactions, then the upper bound is $2 \times 10^{-8}\,\mathrm{GeV\,cm^{-2}\,s^{-1}\,sr^{-1}}$, very close to the observed diffuse neutrino flux by IceCube.[22] The event count registered in a detector after observation time T is

$$N_{\nu_i} = \int_T dt \int_{\Delta\Omega} d\Omega \int dE\, N_A \rho V_{\mathrm{eff}}(E)\, \sigma_{\nu_i}(E)\, \frac{\partial^3 \hat{\phi}_{\nu_i}}{\partial t \partial\Omega \partial E} \tag{4.9}$$

$$\equiv \int_T dt \int_{\Delta\Omega} d\Omega \int dE A_{\mathrm{eff}}(E, \Omega)\, \frac{\partial^3 \phi_{\nu_i}}{\partial t \partial\Omega \partial E} \tag{4.10}$$

for neutrino of type ν_i in a medium of density ρ and volume V. $N_A \approx 6.023 \times 10^{23}$ is Avogadro's constant and σ_{ν_i} the energy dependent cross section for the neutrino interaction process of interest. The *effective Volume* V_{eff} accounts for detector effects as a selection efficiency, energy threshold, or exposure, as well as muons visible from neutrinos after traveling long distances. The flux in Eq. (4.9) is including opacity effects in the Earth (Eq. (4.7)), that is, it represents the flux at the detector. The effective area (A_{eff}) includes all Earth related effects (detector, Earth absorption, interaction cross section, ...) in one quantity that is related to the incident flux at Earth, Eq. (4.10).

For the flux given by the Waxman-Bahcall bound, about 50 neutrino events are expected per square kilometer per year.[23] Hence, the requirement for a neutrino observatory capable of observing astrophysical neutrinos, a cross sectional area of $1\,\mathrm{km^2}$ is required, or a volume of $1\,\mathrm{km^3}$, much larger than comparable underground facilities like Super-Kamiokande mentioned before.

4.4 The design of IceCube

The IceCube Neutrino Observatory is located at the South Pole close to the Amundsen-Scott-Station.[24] One cubic kilometer of Antarctic ice is instrumented at a depth of 1500 km to 2500 km below the surface. An illustration of the IceCube Neutrino Observatory is shown in Figure 4.4. In total, 5160 digital optical modules (DOMs) are attached to 86 cables ("strings") in a hexagonal shape. A top view of the detector is shown in Figure 2.3 (top). The vertical spacing of the 60 DOMs attached to one string is 17 m; the distance of a string to its neighboring strings is in the range of 125 m with small variations for different strings. The deployment of IceCube started in December 2004 and lasted six years. The strings were deployed by drilling holes into the ice using hot water[25] during the Antarctic summer. During the construction, the detector was operational with already deployed strings, usually abbreviated with *IC*XY with XY representing the number of active strings. Starting with the first data taking season using all 86 strings in June 2011, the naming convention used

[21] Waxman and Bahcall, "High-energy neutrinos from astrophysical sources: An Upper bound".

[22] Aartsen, "A combined maximum-likelihood analysis of the high-energy astrophysical neutrino flux measured with IceCube"; Aartsen, "Observation and Characterization of a Cosmic Muon Neutrino Flux from the Northern Hemisphere using six years of IceCube data".

[23] T. K. Gaisser, "Neutrino astronomy: Physics goals, detector parameters".

[24] Achterberg, "First Year Performance of The IceCube Neutrino Telescope".

[25] Hanson, "Construction status and future of the IceCube neutrino observatory".

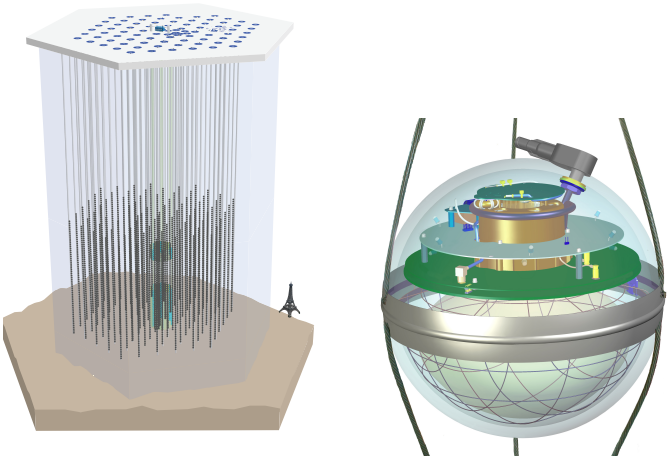

Figure 4.4: Left: IceCube detector at the South Pole deployed in the Antarctic ice. The *Eiffel tower* in Paris is shown for scale. Each dot in the ice represents a digital optical module of IceCube. Figure from IceCube Collaboration (Aug. 2016, https://gallery.icecube.wisc.edu/internal/v/graphics/arraygraphics2011/other/vector/blueTopArray.eps.html). Right: Digital optical module of IceCube. Shown is the interior of the glass pressure sphere with the harness that is attached to IceCube's strings. Figure from IceCube Collaboration (Aug. 2016, https://gallery.icecube.wisc.edu/internal/v/graphics/dom/DOMNoHarnessWhiteback_lg.jpg.html?g2_imageViewsIndex=2).

here switches from *IC86* to *IC-2011* or hybrid versions of those two. The IceCube detector takes data continuously with an detector uptime exceeding 98%[26] and has a field of view of 4π sr, that is, full-sky coverage.

In the center of IceCube, eight strings are instrumented using a denser spacing forming a sub-array called *DeepCore*. With the denser DOM spacing, the energy threshold of the sub-detector reduces to energies as low as 10 GeV,[27] accessing the energy scale of atmospheric neutrino oscillations[28] or neutrinos produced by low mass weakly interacting massive particles (for example, in the Sun[29]). The energy range accessible by DeepCore is lower than the region of interest targeted here. Consequently, DeepCore is not further discussed in this context. On the surface of the South Pole, 82 tanks with 2 DOMs each are located at the entry positions of strings. These tanks form the surface array *IceTop* measuring cosmic ray air showers in the region from the knee to the second knee.[30]

A close-up illustration of a DOM is shown in Figure 4.4. All the electronics is housed inside a glass pressure sphere and connected to the supply of the string with a penetrator.[31] A 25 cm diameter PMT is facing downward in the lower half of the sphere, shielded from magnetic fields with a mu-metal grid. Photons are detected at the PMT by inducing an electric current that is digitized with the on-board electronics of the DOM. This is done using two Analog Transient Waveform Digitizer (ATWD) operating in turns. The ATWDs have three channels with different amplifications ($\times 16$, $\times 2$, and $\times 0.25$).[32] If the channel with largest gain saturates, the second channel is digitized and so on. The memory size of the ATWDs is 128 samples with bin size of 3.3 ns covering a total of $\sim 422ns$. For digitization of longer lasting waveforms, a Fast Analog to Digital Converter (FADC) digitizes the waveform with 256 samples of bin size 25 ns. Thus, 6.4 µs of interval time are covered. The noise rate of IceCube DOMs is very low ($\sim$ 300 Hz) and dominated by radioactive decays in the glass sphere.

[26] DeYoung, "Results from IceCube".

[27] Abbasi, "The Design and Performance of IceCube DeepCore".

[28] Aartsen, "Determining neutrino oscillation parameters from atmospheric muon neutrino disappearance with three years of IceCube DeepCore data".

[29] Aartsen, "The IceCube Neutrino Observatory - Contributions to ICRC 2015 Part IV: Searches for Dark Matter and Exotic Particles".

[30] Abbasi, "IceTop: The surface component of IceCube".

[31] Abbasi, "The IceCube Data Acquisition System: Signal Capture, Digitization, and Timestamping".

[32] Ibid.

The DOM houses also twelve LEDs, six horizontal ones and six facing 30° upwards, evenly spaced in azimuth. The detector is calibrated using the LEDs on the DOMs, and for modeling the optical properties of the Antarctic ice.[33] Furthermore, the DOMs of the detector are calibrated using the light yield of muons stopping in the detector and the light output of a nitrogen laser beam inside the detector.[34]

[33] Aartsen, "Measurement of South Pole ice transparency with the IceCube LED calibration system".

[34] Rongen, "Measuring the optical properties of IceCube drill holes".

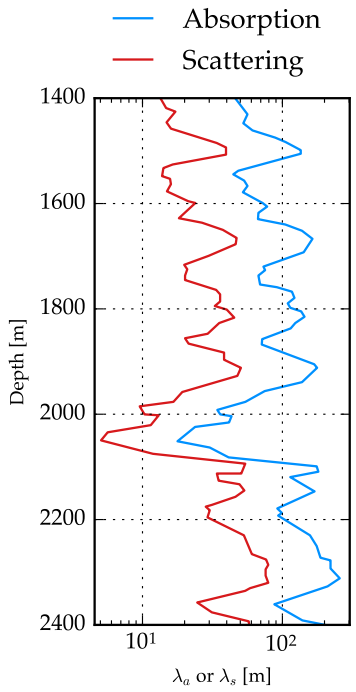

Figure 4.5: Absorption (λ_a) and scattering length (λ_s) in deep Antarctic ice. Data from Aartsen, "Measurement of South Pole ice transparency with the IceCube LED calibration system".

4.5 *Antarctic ice properties*

The light propagation is strongly depending on the properties of the Antarctic ice. Thus, knowledge about the optical properties of the Antarctic ice are of utmost importance for the detection and reconstruction of neutrino events in IceCube. The high pressure at large depth produces ice without air bubbles,[35] resulting in a very clean environment. Consequently, dust trapped in the ice is the most dominant component affecting the scattering of light propagating in the ice. The amount of dust was measured using a *dust logger* during the deployment of strings in IceCube. The ice properties deduced from the dust and LED measurements are shown in Figure 4.5. In general, the absorption length in ice is very large with values of 100 m to 250 m. Due to the dust, scattering is more severe with scattering length that are roughly a factor of 2 to 2.5 lower than for absorption. Hence, photons scatter multiple times before absorption, and with typical string distances of 125 m in IceCube, scattering has to be taken into account, because it reduces the angular information of the photons partially, as illustrated in the neutrino event signatures in Figure 4.3. At a depth of 2000 m a strong layer of dust is observed, largely increasing the scattering and absorption in this region. Below that region, the ice shows the best optical properties. The large scattering of photons due to the dust is unique to ice as a transparent medium. Furthermore, there is an anisotropy observed in the South Pole ice affecting the propagation of light.[36] In water, scattering is much less prominent, but absorption reduces the distance that light travels. Furthermore, the noise rate of modules is much higher due to radioactive potassium decays in the ocean water.[37]

Another important optical property of the ice in IceCube is connected to the drilling of the hole. Once the hole freezes after a string is deployed, air bubbles are trapped inside the ice. Thus, around the strings is a bubble column of *hole ice* that effectively changes the DOMs angular acceptance. Less light is seen from vertically upgoing events, but more light is received from down-going or horizontal light that scatters into the PMT.[38]

[35] Rongen, "Measuring the optical properties of IceCube drill holes".

[36] Chirkin, "Evidence of optical anisotropy of the South Pole ice".

[37] Yepes-Ramirez, "Characterization of optical properties of the site of the ANTARES neutrino telescope".

[38] Rongen, "Measuring the optical properties of IceCube drill holes".

4.6 *IceCube data acquisition*

All 5160 DOMs of IceCube are connected to the *IceCube Lab* at the surface that houses the central computing facilities. If a DOM records a waveform exceeding a charge of 0.25 pe, the individual DOM is

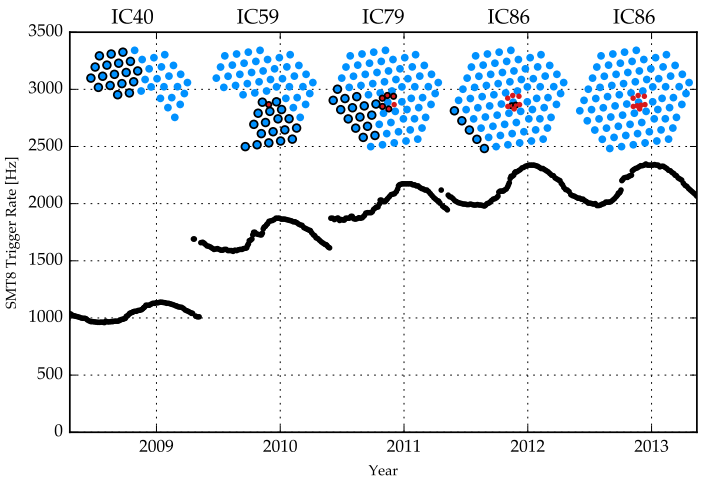

Figure 4.6: IceCube trigger rate for different configurations during and after deployment versus time. Shown is the SMT8 trigger rate as described in the text. For each season, the operational IceCube strings are shown and DeepCore strings highlighted in red. Strings that were newly deployed in this season are circled black.

triggered and considered "hit".[39] This can happen frequently due to dark noise of the PMT. The false trigger rate due to such noise is reduced by imposing *local coincidence* requirements on triggered DOMs. A local coincidence (HLC for *hard local coincidence*) is met when one neighboring or next-to-neighboring DOM triggered as well within a time-window of 1 µs. DOMs with a recorded hit that do not have local coincidences are referred to as *soft local coincidence* (SLC) hits.

In the communication of the IceCube Laboratory with DOMs, trigger conditions are required for the DOM digitized waveforms to be read out. For HLC hits, the full waveform is sent to the surface, while for SLC hits only three samples of the FADC waveform are recorded, enough to register the time of the waveform. Most of the triggers simply count the numbers of HLC hits within a certain time window. The major trigger is a simple multiplicity trigger of eight HLC hits recorded within 5 µs (SMT8). Similar triggers exist for only five HLC hits on one single string within 1.5 µs (*string trigger*) or four within ± 5 DOM layers for a central and its neighboring strings (*volume trigger*). If a trigger condition is met, all hits recorded within a time window of $\Delta t \in [-4\,\mu s, +6\,\mu s]$ are recorded by the detector and form an *event*. If multiple trigger conditions are met, the time window is extended to account for all triggers.

The SMT8 trigger rate of IceCube for different years starting with IC40 is shown in Figure 4.6, together with the detector configuration that was taking data. With bigger instrumented volume or larger cross sectional area, the trigger rate increases. The SMT8 trigger is the dominant trigger in IceCube, ranging from 2 kHz to 2.5 kHz, with approximate total trigger rate of ~ 2.8 kHz. Atmospheric muons produced in air showers at the South Pole represent the largest component of events detected with IceCube at trigger rate. The variations

[39] Abbasi, "The IceCube Data Acquisition System: Signal Capture, Digitization, and Timestamping".

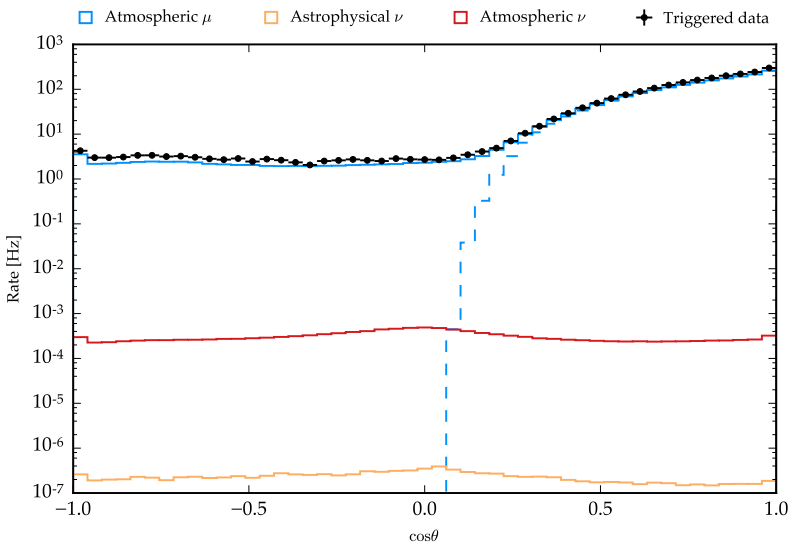

Figure 4.7: Zenith distribution of events at trigger level in IceCube. Values of $\cos\theta = +1$ indicate down-going events (South). Data is compared to simulation of atmospheric muons and neutrinos. The diffuse signal of astrophysical neutrinos is shown as well. Dashed lines show the true arrival direction of atmospheric muons compared to the reconstructed value (solid).

throughout the time correspond to the seasons at South Pole. In summer, the atmosphere is warmer and less dense. Hence, interactions of pions and kaons happen less often and decays producing muons are more frequent.[40]

[40] Tilav et al., "Atmospheric Variations as Observed by IceCube".

Prior to any sophisticated analysis of the detailed physics happening in the entire detector, *features* are extracted from the DOMs' waveforms. The interesting information encoded in the waveform is the photon arriving at the PMT and inducing the waveform. Hence, using a *feature extraction* photon arrival times are extracted from the waveform, resulting in a *pulse* that is characterized by its time, charge, and pulse-width. Strictly speaking, pulses are not directly connected to a photon. Furthermore, *pulse cleaning* removes signatures produced by noise in the PMTs which usually produce SLC hits. Hence, in this pulse cleaning procedure, SLC hits that are isolated in time and space are removed. SLC hits are only considered interesting from a physics point of view if they are causally connected to HLC hits which have a higher probability to be induced by Cherenkov light of a charged particle.

Limited computing resources at the IceCube Laboratory and stringent bandwidth limitations for the data stream to bigger computing infrastructures in the Northern hemisphere require the event stream to be further reduced and optimized before data is transferred. Hence, the trigger data is *filtered* by defining criteria to select the best candidates for the physics that one wants to achieve. The relevant filters in this work are for muons and extremely high energy events (EHE). The latter simply selects events where the total charge by all DOMs exceeds 1000 pe. This reduces the rate to less than 1 Hz because the atmospheric muon spectrum falls steeply in energy. Every high energy event, which is a potential astrophysical neutrino candidate, will be selected through this filter.

The *muon filter* focuses on the selection of track-like events that are induced by muons and connected to interactions of muon neutrinos as discussed in Section 4.1. Muons are the main focus in this work because of the good angular reconstruction and large statistics that can be achieved using muon events[41].

Figure 4.7 shows the reconstructed zenith distribution of IceCube at trigger level. The distribution in azimuth is uniform to first order because of IceCube's unique position at the South Pole that coincides with the Earth's rotation axis[42]. Atmospheric muons produced in air showers of cosmic rays are the dominant component, exceeding atmospheric neutrinos by a factor of more than 10 000 to 1 000 000. Atmospheric muons are so much more abundant than neutrinos that mis-reconstructed atmospheric muons are the dominant component in the up-going region as well[43]. Mis-reconstructions can occur if IceCube detects too few photons for faint events, or muons only pass an edge of the detector without entering. In addition, multiple down-going muons can enter the detector during one detector readout that is then falsely reconstructed as one up-going muon. Coincident events occur for 10% of the IceCube events.

In the muon filter, track-like events of interest are events that are detected with a clear light deposition along the path, as indicated in Figure 4.3 (middle). In the northern sky, the background rate can be effectively removed by requiring that track reconstruction show a good quality fit result. Hence, it is required that there are at least 8 DOMs that recorded hits after cleaning noise hits. Furthermore, the outcome of a likelihood fit[44] has to indicate a good quality of the hypothesis of a track event given the observed data.[45]

In the down-going region, the signal is flooded by the large statistics of truly down-going muons. Thus, selecting well reconstructed events cannot reduce the rate as efficiently as in the northern sky. Thus, a minimum charge requirement is imposed to select only the highest energy events[46]. The charge cut is adjusted to yield a constant rate in zenith, hence, the energy threshold increases for more vertically inclined events where the rate is the largest (Figure 4.7).

With these cuts, the rate is reduced from 2.8 kHz to $\sim$ 34 Hz and the waveform information is transferred North via satellite. Subsequently, using larger computing facilities, the events are reconstructed again using more sophisticated reconstructions that allow for better quality. The rate is further reduced with cuts optimized for the selection of well reconstructed track events,[47] resulting in a final event stream in the range from 2 Hz up to 3 Hz. Using this event stream, the most advanced reconstructions are performed on data to allow best signal-to-background discrimination in the final event selection, which is discussed in Section 6.

[41] For more information about the physics motivation, refer to Section 5.

[42] Small deviations from uniformity in azimuth appear due to the edges of the hexagonal shape of IceCube.

[43] The true arrival direction of atmospheric muons is shown as dashed lines in Figure 4.7.

[44] More about likelihood reconstructions can be found in Section 4.7.

[45] Glüsenkamp, *Muon Filter Proposal IC86-2012*.

[46] The charge is a first guess estimator for an event's energy.

[47] Feintzeig, "Searches for Point-like Sources of Astrophysical Neutrinos with the IceCube Neutrino Observatory".

4.7 Angular reconstruction

Once an event is recorded in IceCube, it is characterized by the number of pulses, each characterized by the detection time t_i, charge q_i and the position $\mathbf{x}_i$ of the DOM that recorded the pulse. The muon track event that was recorded by the detector is characterized by a straight line

$$\begin{pmatrix} x(t) \\ y(t) \\ z(t) \end{pmatrix} = \mathbf{x}_0 + \begin{pmatrix} c_x \\ c_y \\ c_z \end{pmatrix} (t - t_0) \tag{4.11}$$

for a particle traveling with speed $c = \sqrt{\sum_i c_i^2}$ in a specific direction[48]. At reference time t_0, the particle is located at the position $\mathbf{x}_0$ of the support vector. The support vector can be chosen anywhere along the track, for example at the center of the track, but at the first light detection point as well (similar to an event interaction vertex for starting tracks). Furthermore, a track can be characterized by its length l but at the energy range covered here (TeV and above), the length of the muon track exceeds the range of detection by far. Furthermore, most muon tracks enter the detector from outside, hence, track events are usually characterized assuming an infinitely long track.

[48] The speed of a track is usually fixed to the speed of light $c \approx 0.29\,\mathrm{cm\,ns^{-1}}$.

As discussed in Section 4.2 and illustrated in Figure 4.3, a muon track is unique due to the light emission along the path, resulting in a clear directional structure. The Cherenkov cone is opened with a characteristic angle according to Eq. (4.1) into the direction of the particle's movement, The light emission has a cylindrical symmetry around the particle's path. Minimizing the distance of the reconstructed track to all pulses at their respective detection time t_i gives a good estimate of the particle track. Such a fit is called *linefit* and only relies on pure geometrical reasoning and does not account for any physics, as for example the finite traveling time of the light from the particle to the DOM. However, a *linefit* is statistically very robust and can be calculated analytically using χ^2-minimization. Hence, it serves well as a first-guess estimator. To minimize a bias of the result due to obvious noise hits, editions to the standard χ^2 statistics are done improving the overall reconstruction performance.[49]

[49] Aartsen, "Improvement in Fast Particle Track Reconstruction with Robust Statistics".

More sophisticated reconstructions of a muon track take into account the light propagation from the photon production until detection at a DOM. This includes the Cherenkov emission profile as well as the scattering in the ice. The important quantity for the reconstruction is the time residual[50]

[50] Ahrens, "Muon track reconstruction and data selection techniques in AMANDA".

$$t_{\mathrm{res}} = t_i - t_{\mathrm{geo}} \tag{4.12}$$

$$t_{\mathrm{geo}} = t_0 + \begin{pmatrix} c_x \\ c_y \\ c_z \end{pmatrix} \cdot (\mathbf{x}_i - \mathbf{x_0}) / c + \frac{d}{c} \tan\theta_C \tag{4.13}$$

of the detection time t_i at a DOM at distance d_i relative to the expected arrival time t_{geo} of a photon that does not scatter given a track as parameterized in Eq. (4.11). Deviations of the observed detection time from the expectation arise due to different effects. Firstly, a time jitter of the electronics produces a variation that can be explained by a Gaussian uncertainty. Moreover, every recorded hit has the chance to be due to noise. Hence, within the detector readout there is an additional probability that a DOM produces a noise hit. The third effect is due to light emission deviating from Cherenkov light. As discussed in Section 3.6 and Eq. (3.15), muons lose energy stochastically above the critical energy of $\sim 500\,\text{GeV}$. This produces small electromagnetic cascades that produce small shower-like depositions on top of the track signature, compare Figure 4.3. Light that is created in such stochastic losses arrives later than expected for Cherenkov light.[51] Most importantly, the last effect is the light propagation itself. Scattering increases the distance the light travels until detection and thus the detection time. Scattering in the Antarctic ice is a dominant effect. Consequently, the time residual in Eq. (4.12) is expected to grow large as the distance of the DOM to the track increases.

[51] Ibid.

Accounting for the aforementioned effects on the arrival times of photons, from a time residual given by a detection time t_i at a DOM and a parameterized track hypothesis $\xi = (\mathbf{x}_0, t_0, \mathbf{c})$, the probability of observing t_{res} can be calculated. The total likelihood is then given by[52]

[52] Ibid.

$$\mathcal{L}_{\text{SPE}}(\xi) = \prod_{i=1}^{N} p_{\text{SPE}}(t_{\text{res},i}; \xi) \tag{4.14}$$

for N observed pulses and the track parameters ξ. The likelihood in Eq. (4.14) is then maximized to give the best likelihood for the track parameters. In this description of the likelihood, every photon enters the likelihood individually. This is called *single photo electron* (SPE) likelihood and each single photon arriving at a DOM is treated individually.

The calculation of the likelihood can be modified to a *multi photo electron* likelihood (MPE) taking into account all light arriving at a DOM. Due to the scattering of the light, photons are expected to arrive later than one is expecting from Eq. (4.13). Hence, the photon that is detected first at a DOM is the one that scattered least. Such photons are called *direct photons* or *direct hits* at a DOM. For the reconstruction of an event, these photons are most important because they carry more directional information than photons arriving later. Thus, the likelihood is adjusted to only use the timing information of the first hit and using the cumulative distribution of hits for all later hits on the same DOM. This yields the *MPE* likelihood[53]

[53] Ibid.

$$\begin{aligned} p_{\text{MPE}}(t_{\text{res}}) &= N p_{\text{SPE}}(t_{\text{res}}) \left(\int_{t_{\text{res}}}^{\infty} dt\, p_{\text{SPE}}(t_{\text{res}}) \right)^{N-1} \\ \mathcal{L}_{\text{MPE}} &= \prod_{i=1}^{N_{\text{DOM}}} p_{\text{MPE}}(t_{\text{res},i}) \end{aligned} \tag{4.15}$$

for N photons arriving at a DOM with the time residual t_{res} of the first one. An analytical parameterization accounting for the effects of light propagation is given by[54]

$$p\left(t_{\text{res}}\right) \propto \frac{\tau^{-d/\lambda} t_{\text{res}}^{d/\lambda-1}}{\Gamma\left(d/\lambda\right)} \mathrm{e}^{-t_{\text{res}}(1/\tau+\hat{c}/\lambda_a)-d/\lambda_a} \tag{4.16}$$

with $\hat{c} = c/n$, absorption length λ_a and parameters λ, τ estimated from Monte Carlo simulation. Figure 4.8 shows the time residual probability density $p\left(t_{\text{res}}\right)$ for different distances of a DOM to an infinite muon track. With increasing distance, the time residual distribution shifts to later arrival times.

The description of the likelihood in Eq. (4.14) or (4.15) is generic in the evaluation of the probability of t_{res}, for example using analytic approximations like the modified Gamma function in Eq. (4.16). A more detailed description is given by using detailed light propagation simulation where photons are propagated directly until a DOM is hit. Thus, the properties of the ice can be incorporated into the simulation giving a detailed description of the probability for a photon to be observed at an angle θ with arrival time t_{res} at a DOM at distance d. The simulation is interpolated using multidimensional splines[55] that gives a smooth description of the probabilities. These *spline reconstructions* are computationally intensive but give the best angular reconstruction for a wide range of energies. In general, the functions describing the likelihood are convoluted with a Gaussian kernel that accounts for jitter or discrepancies between simulation and observation. Figure 4.10 shows the median angular resolution for the different track reconstructions discussed here. With increasing energy and hence more detected photons per event, the reconstruction quality improves. Over a wide range of energies, the long lever arm of the track results in a good angular resolution of $\Delta\Psi < 1°$. Below 10 TeV an additional smearing due to the kinematic angle in the neutrino interaction limits the reconstruction capabilities because only the secondary muon is observed.

The reconstruction accuracy estimated from Monte Carlo is verified by analyzing the lack of cosmic ray events at the position of the Moon,[56] which shields the cosmic rays from producing muons in an air shower that subsequently are detected in IceCube. The shadow is observed at high significance and with a true size of $\sim 0.3°$ of the Moon in the sky, muons are reconstructed with $\sim 0.5°$ accuracy, improving with muon energy. Similar analyses are done for shadowing of the Sun with the same result.[57]

4.8 Bayesian priors

Another edition to the likelihood formula is the addition of priors to the likelihood in the maximization process. Atmospheric muons that are mis-reconstructed as up-going are the dominant background in the up-going region that should consist of neutrinos only as visible in Figure 4.7. For these truly down-going events it is possible that

[54] Ahrens, "Muon track reconstruction and data selection techniques in AMANDA".

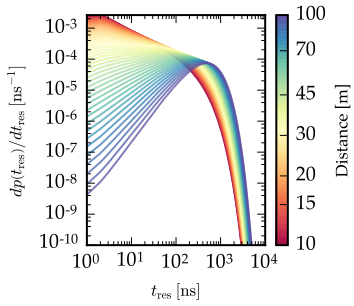

Figure 4.8: Analytic time residual probability for a infinite muon track at different distances to a DOM.

[55] Whitehorn, Santen, and Lafebre, "Penalized Splines for Smooth Representation of High-dimensional Monte Carlo Datasets".

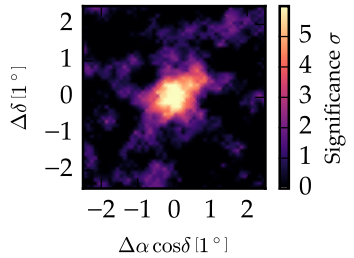

Figure 4.9: Cosmic ray shadow of the moon observed with IceCube.

[56] Aartsen, "Observation of the cosmic-ray shadow of the Moon with IceCube".

[57] Bos et al., "Observation of the Cosmic-Ray Shadow of the Moon and Sun with IceCube".

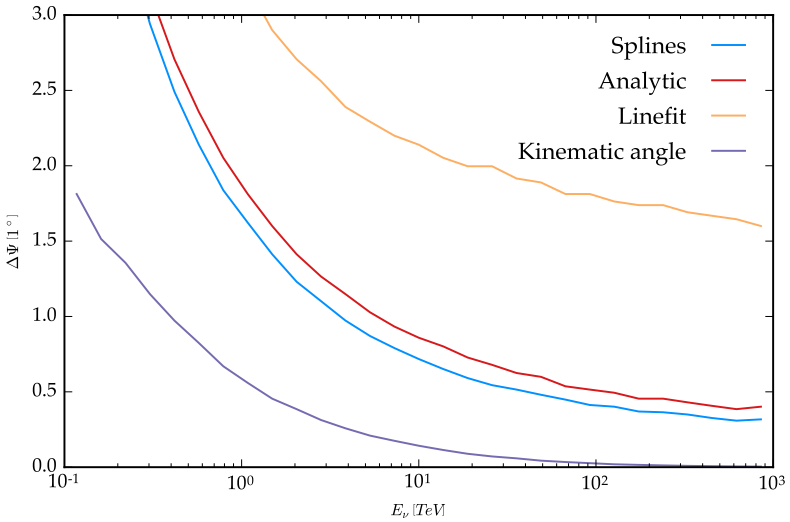

Figure 4.10: Median angular resolution of different track reconstructions discussed in the text. The reconstruction quality improves with neutrino energy. The best results are given by using MPE likelihoods using time residual distributions from simulation spline tables, followed by analytic parameterizations. Linefit performs reasonably well as a first guess algorithm. At low energies, the muon and neutrino are not aligned anymore, weakening the neutrino reconstruction performance.

there is not one sharp likelihood maximum in the parameter-space ξ as for a truly up-going neutrino event, but a second maximum with a down-going fitted direction. In order to search for such second maxima, the likelihood is multiplied with a Bayesian prior probability $\mathcal{P}$

$$\mathcal{L}_{\text{Bayes}}(\xi) \propto \mathcal{L} \times \mathcal{P}(\xi) \tag{4.17}$$

that prohibits the fit to optimize for an up-going direction with $\mathcal{P} \to 0$ if the zenith gets larger than $\sim 80°$.[58] This is particularly interesting when the likelihood value of the two maxima (flat versus Bayesian prior) is compared to each other. If the likelihood difference is small, there is a larger chance of a misreconstructed event. Thus, such a *Bayesian likelihood ratio* is a good discriminator against events falsely reconstructed as up-going.

Analyzing the shape of the likelihood landscape around the maximum that was found minimizing the likelihood description introduced above, uncertainties on the best fitting parameters can be derived. This is especially important for the uncertainties on the direction of the particle that is an important quantity for astronomy. For these two parameters, around the maximum, a contour is given by the values where the difference in likelihood $\Delta \log \mathcal{L}$ with respect to the maximum is $-1/2$. All other parameters, that is, the vertex position and time, are re-maximized. The contour can be approximated to be shaped like an ellipse.[59] The likelihood landscape is sampled at 24 distinct points in three rings around the minimum and a paraboloid[60] is fit to the likelihood values at all these 24 points plus the maximum in the center of the paraboloid. Another method of estimating the uncertainty of a reconstructed track can be statistically given by *bootstrapping* methods. The reconstruction is performed on a set of pulses recorded at the DOMs of the detector. By randomly sampling the pulses from the observed distribution, the track is reconstructed multiple times with different variations of the pulses.

[58] Ahrens, "Muon track reconstruction and data selection techniques in AMANDA".

[59] Neunhöffer, "Estimating the angular resolution of tracks in neutrino telescopes based on a likelihood analysis".

[60] This procedure is thus called *paraboloid fit*.

The variance of the direction of the particle is then an estimate for the uncertainty of the track reconstruction on the observed set of pulses.

4.9 Energy reconstruction

The energy of an event recorded in IceCube is the last quantity not considered so far. The energy of an event is of great interest in order to (1) statistically distinguish low-energy background from high-energy astrophysical neutrinos and (2) measure the energy spectrum of astrophysical neutrinos. It was already mentioned that the amount of light produced is proportional to the energy of the particle above the critical energy of the particle, Eq. (3.15). Thus, the number of hit DOMs and the total charge recorded in the detector already estimate the energy deposited in the detector. Nevertheless, this does not account for the variations in the ice, especially for events close to the dust layer of IceCube, see Figure 4.5, where much less light will be detected. Using Monte Carlo simulation, the expected amount of light measured in a DOM in the ice can be estimated. The likelihood to observe k photons is consequently given by a Poissonian distribution

$$\mathcal{L} = \frac{\lambda^k}{k!} \mathrm{e}^{-\lambda} \tag{4.18}$$

for an expectation of λ photons. For a muon with track-like signature, the light yield can be calculated from the energy depositions along the track.[61] Technically, this is realized by segmenting the track into chunks of small size ($\sim 10\,\mathrm{m}$) and assume one spherical energy deposition E_i at each position. Thus, the whole track is characterized by a vector E of energy depositions. From simulation, the expected DOM response to all of this energy depositions can be calculated by a matrix product $\Lambda \cdot E$. Λ is a matrix quantifying how much light is seen in DOM i given the vector of energy depositions E_j. The total likelihood of Eq. (4.18) is then given by

$$\ln \mathcal{L} = \sum_i \left(k_i \ln \left(\Lambda_i \cdot E + \rho\right) - \left(\Lambda_i \cdot E + \rho\right) - \ln k_i!\right) \tag{4.19}$$

summing over all DOMs and including a noise expectation ρ to produce random hits as well. The likelihood can be maximized for the energy depositions given a track with vertex and direction. However, a complete maximization of energy and direction is possible as well, but at high computation cost. Thus, it is more convenient to use pure angular reconstructions first that give a very good estimate of the angular direction for tracks, and then only use the approach of Eq. (4.19) for the energy estimation. The result of the maximization is then a vector of energy depositions.[62] This can be used to study the detailed propagation of the muon within the detector, for example the identification of a double bang that has two large energy depositions along a line, with faint light in between.[63]

[61] Aartsen, "Energy Reconstruction Methods in the IceCube Neutrino Telescope".

[62] Ibid.

[63] Hallen, "On the Measurement of High-Energy Tau Neutrinos with IceCube".

5 Search methods regarding neutrino point sources

Clustering on small angular scales is a unique signature of a neutrino source, predominantly when point-like sources are considered. Backgrounds consist of large numbers spread out over extended areas. A high density of events is a signature of a point source in this background.

Using a simple "cut-and-count" approach, a point source reveals itself as an excess of events over background expectation. The background is usually well constrained using *off-source* regions of similar exposure to compare the *on-source* region to.[1] The number of background events[2] is dependent on the window size, while the signal is clustered around the source and thus connected to the reconstruction accuracy which defines the window size $\Delta\Omega = 2\pi\,(1 - \cos\Psi)$ for an opening angle Ψ. For very good angular resolution, the background rate is then largely reduced..

Nevertheless, the typical event reconstruction accuracy can vary strongly from event to event and the signal to background discrimination can change as well. In both cases this is encountered when the energy increases: the directional reconstruction of an event improves with energy and the background rate drops steeply with energy. This could be accounted for using multiple observation windows at different energies in the approach mentioned above. A different approach is found in the concept of the unbinned likelihood formalism that is discussed in the following. The unbinned likelihood is used widely in neutrino astronomy[3] and elegantly accounts for any discrimination that can be given for signal and background.

The methods and efforts discussed in this section are realized in a software package called *SkyLab* that is publicly available using the GNU public license.[4]

In the following, details of the technical implementation of the likelihood formalism are discussed. Subsequently, the statistical tests that are performed using the unbinned likelihood formalism are introduced.

[1] Li and Ma, "Analysis methods for results in gamma-ray astronomy".

[2] On small scales this can be assumed to be a homogeneous backgrounds that only slowly varies with position.

[3] Braun, Dumm, et al., "Methods for point source analysis in high energy neutrino telescopes".

[4] Coenders, *Skylab*, a peer-reviewed publication is under consideration.

5.1 Unbinned likelihood formalism

The unbinned likelihood formalism is used here to identify clustering in an event sample over background fluctuations. The unbinned likelihood

$$\mathcal{L} = \prod_i \mathrm{p}\left(x_i\right) \tag{5.1}$$

assigns a probability to each observation, and the total likelihood is given by the product. The product is evaluated for all events i that are observed. The number of events itself is a statistical observable distributed with a Poisson distribution. Thus, the likelihood in Eq. (5.1) accounts for the Poisson probability $\mathrm{e}^{-\lambda}\lambda^N/N!$ to observe N events with expectation λ. This is called an *extended likelihood*.[5] The ordering of the events is not important, eliminating the factor $N!$ of possible permutations. This yields the extended likelihood

[5] Barlow, "Extended maximum likelihood".

$$\mathcal{L} = \mathrm{e}^{-\lambda} \prod_{i=1}^{N} \lambda \times p\left(x_i\right) \equiv \mathrm{e}^{-\lambda} \prod_i P\left(x_i\right) \tag{5.2}$$

for an observation of N events with expectations of λ, and each event observed with a probability of $p\left(x_i\right)$. Compared to Eq. (5.1), the product arguments ($P\left(x_i\right)$) are normalized to λ instead of unity, hence the name extended likelihood.

The total sum of events can be split into different categories, for clustering searches this is the number of clustering or *signal* events n_S and the number of non-clustering background events, $\lambda \to n_S + n_\mathrm{B}$. The probability for each event can be decomposed in a linear combination

$$p = \frac{n_S}{\left(n_S + n_\mathrm{B}\right)^2}\mathcal{S} + \frac{n_\mathrm{B}}{\left(n_S + n_\mathrm{B}\right)^2}\mathcal{B} \tag{5.3}$$

of two terms that are identified as the probability of an event belonging to the signal category $\mathcal{S}$ or background $\mathcal{B}$. In searches for steady emission of neutrino sources as intended here, the event sample is very large in statistics with comparably low statistics of astrophysical neutrinos, for example, $\sim 70\,000$ atmospheric neutrinos per day with less than 100 astrophysical ones in the northern sky.[6] Hence, the expected total number of events is not dominated by the signal that is searched and can be fixed to the total number of events observed and results in the *point source likelihood* used throughout this thesis:

[6] Aartsen, "Observation and Characterization of a Cosmic Muon Neutrino Flux from the Northern Hemisphere using six years of IceCube data".

$$n_S + n_\mathrm{B} \approx N \tag{5.4}$$

$$\mathcal{L}_\mathrm{PS}\left(\mathbf{X}, n_S, \xi\right) = \mathrm{e}^{-N} \prod_{i=1}^{N} \left(\frac{n_S}{N}\mathcal{S}\left(x_i; \mathbf{X}, \xi\right) + \left(1 - \frac{n_S}{N}\right)\mathcal{B}\left(x_i\right)\right) \tag{5.5}$$

The likelihood in Eq. (5.5) is hence evaluated for each event according to its partial probability to belong to signal ($\mathcal{S}$) or background ($\mathcal{B}$), respectively. The likelihood is maximized for the number of signal events n_S in the total observation of N events assuming

a source at position $\mathbf{X}$. In general, negative values of n_S are allowed as long as Eq. (5.4) holds, but under-fluctuations $n_S < 0$ are not a feasible scenario for the identification of neutrino sources and not used here.[7] In searches of cosmic ray shadowing, negative values of n_S are used.[8]

Additionally to the number of signal events n_S, a set of parameters ξ can further discriminate signal from background. As evident from Eq. (5.4), this only affects the evaluation of the signal probability $\mathcal{S}$ but not the background probability $\mathcal{B}$. The reasoning is that additional parameters usually account for properties of a neutrino source, for example time dependencies[9] or extensions of the source.[10] The background on the other hand is commonly constrained using off-source data at large statistics and can be considered fixed.

So far, the only assumptions made regarding the properties of likelihood evaluation are the postulation of two event classes, signal and background, and that the background probability is constant due to estimation from off-source data. Both signal and event probability are evaluated for the same observables (x_i) using the discriminating power of the variables. Differences in the distributions x_i used in the likelihood have to be taken into account; if not, the result of n_S is biased to different values from its original meaning of number of signal events.[11]

In the light of clustering analyses of neutrino telescopes, the most important information is the spatial information of the events. Probing the likelihood for a source at position $\mathbf{X}$, the probability for an event at location $\mathbf{x}_i$ to belong to the source depends on the spatial distance $\Delta\Psi = |\mathbf{X} - \mathbf{x}_i|$ of the two positions, scaled by the angular uncertainty of the event (σ_i). For small angular uncertainties $\sigma < 5^\circ$ as encountered in muon tracks in IceCube, the angular uncertainty can be modeled with a two-dimensional Gaussian distribution of width σ. All other observables only depend on the event's declination, because IceCube's reconstruction and event selection capabilities only depend on declination due to the position at the South Pole. Dependencies on the right ascension are small and are smeared after one day and a full rotation of the Earth. Thus, the probability $\mathcal{S}$ can be split in a spatial part and further probabilities $\mathcal{E}_\mathcal{S}$ evaluated at the event declination:

$$\mathcal{S}\left(x_i; \mathbf{X}, \xi\right) = \frac{1}{2\pi\sigma_i^2} \mathrm{e}^{-\frac{\Delta\Psi^2}{2\sigma_i^2}} \times \mathcal{E}_\mathcal{S}\left(x_i | \sin\delta_i; \xi\right) \tag{5.6}$$

Additional observables that are evaluated in $\mathcal{E}_\mathcal{S}$ in Eq. (5.6) are the event's energy proxy $\log_{10} E_i$ as it is expected to be different for signal (hard spectrum, $\sim E^{-2}$) and background ($\sim E^{-3.7}$ for atmospheric neutrinos). Hence, the likelihood is maximized using the spectral index of the probed source, γ, as additional parameter, evaluating the probability to observe an neutrino event with energy proxy $\log_{10} E_i$ given a source with spectral index $\partial\phi/\partial E \propto E^{-\gamma}$ at the events declination $\sin\delta_i$.

[7] Braun, Dumm, et al., "Methods for point source analysis in high energy neutrino telescopes".

[8] Aartsen, "Observation of the cosmic-ray shadow of the Moon with IceCube".

[9] Braun, Baker, et al., "Time-Dependent Point Source Search Methods in High Energy Neutrino Astronomy".

[10] Aartsen, "Searches for Extended and Point-like Neutrino Sources with Four Years of IceCube Data".

[11] Punzi, "Comments on likelihood fits with variable resolution".

The energy estimation for background $\mathcal{E}_{\mathcal{B}}$ is similar as for signal, but uses the observed data for the estimation of the background distribution, hence, it does not depend on the parameter γ. The spatial part of the background probability only depends on the declination distribution $\mathcal{P}(\sin\delta_i)$ of the observed events. The right ascension distribution is uniform due to the rotation of IceCube around the right ascension axis within one day. Thus, the background probability yields

$$\mathcal{B}(x_i) = \frac{\mathcal{P}(\sin\delta_i)}{2\pi} \times \mathcal{E}_{\mathcal{B}}(x_i) \ . \tag{5.7}$$

The significance of clustering in the unbinned likelihood in Eq. (5.5) is given by a likelihood ratio test of the maximal likelihood ($n_S > 0$) with respect to the null hypothesis of no clustering events ($n_S = 0$). The test statistic of the likelihood ratio test is defined as

$$\begin{aligned}\log\Lambda =& 2\log\frac{\mathcal{L}(n_S,\gamma)}{\mathcal{L}(n_S=0)} \\ =& 2\sum_{i=1}^{N}\log\left(1+\frac{n_S}{N}\left(\frac{\mathcal{S}(\Delta\Psi_i)}{\mathcal{B}(\sin\delta_i)}\mathcal{W}(\log_{10}E_i|\sin\delta_i;\gamma)-1\right)\right) \qquad (5.8)\\ \equiv& 2\sum_{i=1}^{N}\log\left(1+\frac{n_S}{N}\chi\right) \qquad (5.9)\end{aligned}$$

where $\mathcal{S}$ and $\mathcal{B}$ only use the spatial information of Eq. (5.6) and (5.7), and $\mathcal{W}$ implements the ratio of $\mathcal{E}_{\mathcal{S}/\mathcal{B}}$ for the energy dependence of the likelihood. The factor of two is used due to Wilks' theorem. Hence, $\log\Lambda$ should be distributed according to a χ^2 function. The distribution of the test statistic is empirically fitted using background scrambled data sets.

If multiple data sets are used, the likelihood of events of different samples are evaluated separately. This is due to possible differences in event selection, background distribution, and other observables entering the detector. For example, in combinations of IceCube data sets with ANTARES,[12] the two detectors test completely different energy regimes in the southern sky. Thus, a very rare high-energy event in the smaller detector ANTARES would be identified as background in IceCube that has much higher statistics. Hence, such effects have to be accounted for in order to correctly identify clustering.

[12] Adrian-Martinez, "First combined search for neutrino point-sources in the Southern Hemisphere with the ANTARES and IceCube neutrino telescopes".

This is achieved by evaluating the likelihood ratio in Eq. (5.8) individually for data sample j event using different functions $\mathcal{S}_j$, $\mathcal{B}_j$, and $\mathcal{W}_j$. Moreover, testing for steady emission of neutrinos, the number of signal neutrinos is expected to split among the samples given by their individual event rate expectation. Thus, the number of clustering events n_{Sj} in sample j

$$\begin{aligned} n_{Sj}(\mathbf{X},\gamma) =& n_S \times \frac{\int_0^\infty dE\, A_{\text{eff}}^j(\mathbf{X},E)\, E^{-\gamma}}{\sum_{k=1}^{K}\int_0^\infty dE\, A_{\text{eff}}^k(\mathbf{X},E)\, E^{-\gamma}} \qquad (5.10)\\ \equiv& n_S \times f_j(\sin\delta,\gamma) \qquad (5.11)\end{aligned}$$

is a fraction of the total number of n_S events, $\sum_k f_k = 1$. This results in the total likelihood $\log \Lambda (n_S, \gamma) = \sum_k \log \Lambda_k (f_k \times n_S, \gamma)$ only depending on two parameters.

5.2 Unbinned likelihood maximization

The unbinned likelihood allows for a detailed discrimination of signal and background, thus, allowing for a efficient detection of faint clustering. However, the evaluation of the likelihood for every event individually is computationally extensive and benefits largely from optimizations of the algorithm.

The technical implementation of the unbinned likelihood maximization[13] uses the BFGS minimization algorithm implemented in *Python*.[14] The probability distribution $\mathcal{P}$ (see Eq. (5.7) and the ratio $\mathcal{W}$ is implemented using n-dimensional histograms that are evaluated using splines. Most of the computation time is needed in the evaluation of $\mathcal{W}$ for different values of γ which always need re-evaluation at every minimization step. The background probability is only evaluated once and is constant, the spatial signal probability depends only on the position, that is, is constant within one likelihood maximization at fixed $\mathbf{X}$.

[13] Coenders, *Skylab*.

[14] Oliphant, "Python for Scientific Computing", the negative logarithm of the likelihood is minimized instead of maximizing the likelihood.

The calculation is sped up significantly by neglecting the evaluation for clear background events. Muon track events used in the unbinned likelihood formalism have angular accuracies of much less than 5°. Thus, all events outside of a box of 10° spatial distance can be considered pure background, because the spatial part of the Gaussian in Eq. (5.6) will tend to zero making the evaluation of $\mathcal{W}$ irrelevant. Thus, for uniformly spaced points the number of evaluation steps needed reduces by 99% and the likelihood changes to

$$\log \Lambda = \log \Lambda^{N'} + (N - N') \log \left(1 - \frac{n_S}{N}\right) \tag{5.12}$$

with N' out of N events in the selected box and the remaining $N - N'$ being pure background ($\mathcal{S} = 0$). Hence, the likelihood is only evaluated in detail for the N' events ($\log \Lambda^{N'}$).

Furthermore, the BFGS minimization can be done using analytic gradients instead of a "brute-force" estimate of gradients. This saves $2 \times n$ computation steps for n parameters to be minimized and removes the necessity of variable normalization. The gradients of the total likelihood are given by

$$\frac{\partial \log \Lambda}{\partial n_S} = \sum_j f_j \left(\sum_i \frac{\chi_i}{N + n_{Sj} \chi_i} - \frac{N - N'}{N - n_{Sj}} \right) \tag{5.13}$$

$$\frac{\partial \log \Lambda}{\partial \gamma} = \sum_j \left(\sum_i \frac{n_{Sj}}{N + n_{Sj} \chi_i} \left. \frac{\partial \chi}{\partial \gamma} \right|_i + n_S \times \frac{\partial f_j}{\partial \gamma} \left. \frac{\partial \log \Lambda_j}{\partial n_S} \right|_{n_{Sj}} \right) \tag{5.14}$$

and the gradients of χ can be evaluated more quickly using the splines used for the evaluation. The first term in Eq. (5.14) corresponds to the change in the event probabilities (χ) itself, while the second term accounts changes in the expected number of signal events in a sample by Eq. (5.11).

The implementation in *SkyLab* is modular and kept general for the implementation of additional fit parameters of γ. For each sample, the observables are defined that are used for the evaluation. The parameters that are used for the evaluation can be different for different samples, and multi-dimensional. For example an energy cutoff in addition to the spectral index. In the combination of all samples, the likelihood is then optimized using all parameters present. In the realization used here, only the spectral index is used in addition to n_S. With no clear identification of a source so far, only a few neutrinos per source are identified. Thus a cutoff spectra is equally well fit by a soft spectrum without cutoff.

For the estimation of the significance with respect to the null-hypothesis of pure background samples, the analysis is repeated using experimental events scrambled in right ascension. This imitates time scrambling in IceCube due to the constant Earth rotation around the polar axis. The significance estimation is discussed in detail in Section 7.4.

5.3 Full sky searches

The first search done with IceCube is the search for the strongest clustering in the sky. In the likelihood maximization, the source position is always kept fixed at a position $\mathbf{X}$ and optimized for the parameters n_S and γ. The likelihood is maximized on the entire sky using an isotropically spaced grid.[15] The grid is spaced very fine so that it is typically closer than the event reconstruction uncertainty σ. The scan is done in two iterations, the first using 196 584 points at approximately half-degree spacing. After the first scan, the values are interpolated to a grid with more than 3×10^6 pixels at 0.1° spacing. Using this grid, the 6% of the pixels that had the most clustering are maximized again for finer rasterization of the interesting points.

[15] Górski et al., "HEALPix: A Framework for High-Resolution Discretization and Fast Analysis of Data Distributed on the Sphere".

After the grid scan, the global maximum should be identified closely. Two maxima are identified in northern and southern sky, separately. The pixel corresponding to the largest clustering should be close enough to the true maximum. Thus, the likelihood in the vicinity of this region ($\sim 0.2^\circ$) is maximized including the position $\mathbf{X}$ of the neutrino source as one parameter. Hence, the global maximum in each half of the sky is identified.

To calculate the true significance of the largest clustering in the sky, the test statistic has to be corrected for the look elsewhere effect. Because of random fluctuations in the sky, there are always locations of strong clustering expected even for maps of pure background. Given the typical event reconstruction, most of the events

are not causally connected with each other assuming a point-like origin. Hence, the sky can be thought of as N independent observations of the same kind, where N is called the *trial factor*. The most significant spots are quantified by their p-value to belong to background at this position. By definition, the p-value is distributed uniformly for the background hypothesis. Consequently, the probability to observe no p-value lower than $p_{\min} \equiv x$ in N independent observations is given by

$$\mathrm{P}\left(\min_i \{\mathrm{p}_i\} < x\right) = 1 - (1-x)^N \,. \tag{5.15}$$

Thus, the probability density for x for a trial factor of N yields

$$dP = N\,(1-x)^{N-1}\,dx\,. \tag{5.16}$$

The p-value is more commonly given as $y \equiv -\log_{10} \mathrm{p}$ thus changing Eq. (5.16) to

$$dP = \ln 10 \times N\left(1-10^{-y}\right)^{N-1} \times 10^{-y} dy \tag{5.17}$$

$$P\left(-\log_{10} \min_i \{\mathrm{p}_i\} > y\right) = 1 - \left(1-10^{-y}\right)^N \tag{5.18}$$

for the probability density and trial corrected p-value. Using a spacing of 0.3° wide windows, the full sky (4π) can be partitioned into more than 100 000 points, giving a rough estimate of the trial factor N. For this trial factor, a 5σ pre-trial discovery corresponds to only 1.9σ after correction (one-sided convention), as illustrated in Figure 5.1 for different trial factors.

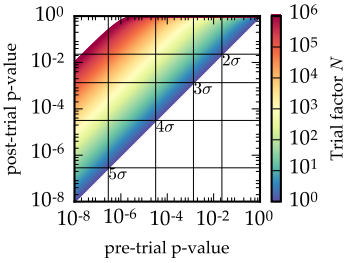

Figure 5.1: P-value correction for different trial factors.

5.4 *Gamma-ray counterparts*

The large trial factor of the full sky scan only allows the identification of very strong sources. The trial factor can be reduced by selecting specific positions *a-priori* of the analysis. Thus, the test statistic and the trial factor are not affected by the *look-elsewhere* effect as in the full sky scan.

Promising positions for neutrino emission are known gamma ray sources, that could emit neutrinos at high energies as well. If neutrinos are observed from such searches, this would possibly explain parts of the observed gamma ray spectrum using a component of pions as discussed in Section 2.4. Thus, promising objects are gathered in lists that are probed in addition to the full sky. Two lists are selected, the separation is mainly due to the evolution of the list, but the lists show clear topological differences.

The first list consists of 44 objects of various types and is shown in Figure 5.2. The focus on the list lies in the northern sky (declination $\delta > -5°$), where IceCube has the highest efficiency for astrophysical muon neutrinos and a low energy threshold of a few TeV in neutrino energy. The northern sky is mostly extra-galactic and thus the

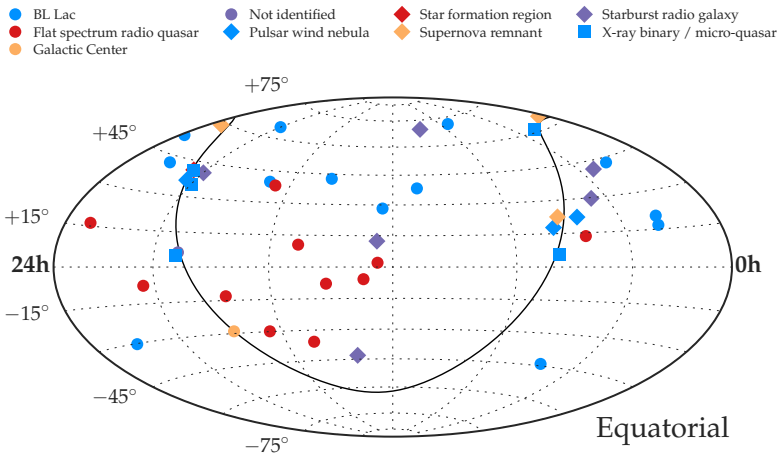

Figure 5.2: Objects collected in first list. The Galactic Plane is indicated as black line.

sample is dominated by active galactic nuclei (AGN), mainly blazars. Blazars are separated in flat spectrum radio quasars and BL Lacs. Refer to Section 3.4 for more information about AGN. Even though, the Galactic Plane is mostly localized in the southern sky, strong objects of Galactic origin are located in the northern sky as well. This includes the Crab Nebula, the strongest steady TeV gamma ray source in the sky and of type pulsar wind nebula, as well as active regions of star formation in the Cygnus region.

In the southern sky, the energy threshold of IceCube is much higher due to large backgrounds, thus, not many Galactic sources are tested, that usually have energy spectra that are cutoff too early for IceCube to be sensitive. The only Galactic source tested in this list is the supermassive black hole in the center of our Galaxy, *Sgr A**. The remaining objects in the southern sky are of extra-galactic origin.

The second source list is added the first time in this analysis. It is originally used by ANTARES and thus located in the northern hemisphere.[16] Hence, low energetic gamma ray sources, primarily Galactic sources are tested more efficiently. In recent efforts,[17] IceCube is able to access lower energies in the southern hemisphere compared to previous analyses[18] by adding starting events to the analysis. Thus, objects shown in Figure 5.3 are probed as well for clustering of neutrinos. The source list consists of mainly Galactic sources, but a few extra-galactic objects as well. The list of 29 objects is located entirely in the southern sky.

In the analysis of the source lists, in total 73 objects are probed. This is affected by a trial factor of that number, but still significantly less than for the full sky. The list with all objects and results are shown in Section 7. The estimation of the significance is done similar to the scan of the full sky by repeating the analysis on pure background maps. The analysis is done separately for northern and southern sky, because the backgrounds in the regions are different, resulting in different event selection techniques and different energy

[16] Adrian-Martinez, "Searches for Point-like and extended neutrino sources close to the Galactic Centre using the ANTARES neutrino Telescope".

[17] Aartsen, "Lowering IceCube's Energy Threshold for Point Source Searches in the Southern Sky".

[18] Aartsen, "Searches for Extended and Point-like Neutrino Sources with Four Years of IceCube Data".

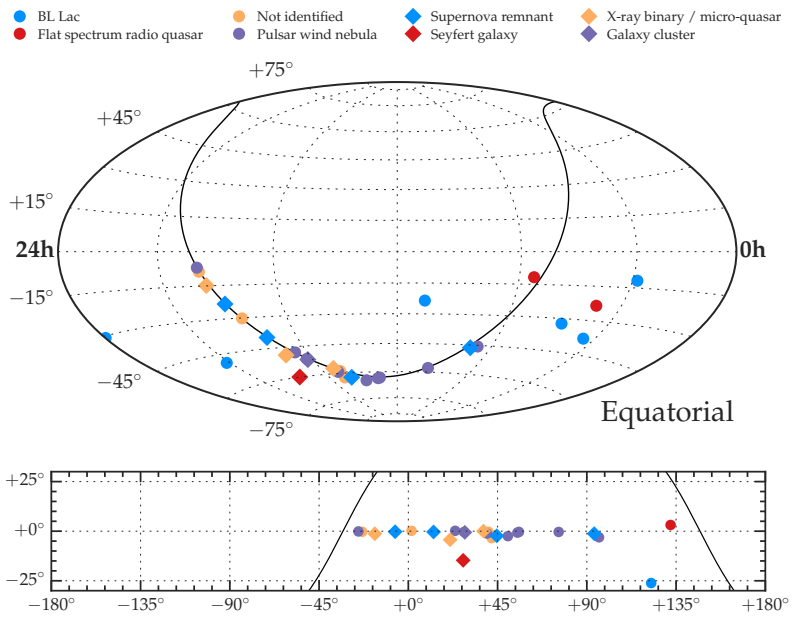

Figure 5.3: Objects collected in second list. Top: Equatorial view of full sky. The Galactic Plane is indicated as black line. Bottom: Zoom into Galactic Plane in Galactic coordinate system. The black line indicates the separation in northern and southern sky. The source list contains only objects in the southern sky.

ranges probed. Thus the first list is split into a northern (34 objects) and southern part (10 objects). Thus, three p-values are reported in total.

5.5 *Searching for populations of sources*

Another scenario of a signal of point sources could be a population of weak sources. The scan of the full sky searches for strong emission of the strongest source in the sky that is within IceCube's energy regime. The scan of known objects tests a connection of neutrinos to known gamma ray emission. If there exists a population of faint sources, their signal in the full sky scan would produce an excess of multiple points that exceed a certain clustering value, while each source does not show very significant clustering itself.

The data recorded with IceCube is probed for such a population by counting the number of spots that exceed a certain threshold $-\log_{10} p_{\text{min}} \geq X$ and compare it to the expectation from pure background. A spot is identified as a local maximum in the grid used for the full sky scan. Iteratively, the most significant pixel in the grid is identified and marks the first spot. Subsequently, a region of 1.5° radius around this position is masked when the next spot is identified. This is done, until the significance $-\log_{10} p_{\text{min}} = 3$ is reached. The selection is done separately for northern and southern sky. As a result of this procedure, for a grid of points in the sky as done in the scan of the full sky, N spots with an individual value $-\log_{10} p_i$ are obtained. The p-value is used as measure of the significance of a spot as it is uniformly distributed[19]. Thus, possible systematic shifts in the test statistic (Eq. (5.8)) are accounted for that could bias the

[19] Or exponentially distributed for $-\log_{10} p$.

distribution to favor specific declination regions over others. In the test, the negative decadic logarithm $-\log_{10} \mathrm{p}$ is used and written as x in the following.

The important metric of the population search is defined as the number of spots that are identified with a test statistic that exceeds the threshold x_{min} out of a total of N selected spots. This can be quantified as

$$n\left(x_{\mathrm{min}}\right) = \sum_{i=1}^{N} \Theta\left(x_i - x_{\mathrm{min}}\right) \tag{5.19}$$

and depends on the threshold x_{min} and the sum is evaluated for every spot i. The metric $n\left(x_{\mathrm{min}}\right)$ is by definition a monotonically falling distribution. To estimate the significance to see n spots above threshold x_{min} is given by Poissonian statistics. Figure 5.4 shows simulated background trials for different thresholds compared overlaid with a Poissonian distribution. The spots were selected using a window of 1.5°, thus, the individual spots are distant enough to be considered statistically independent. Thus, the probability to observe $n\left(x_{\mathrm{min}}\right)$ or more spots given a background expectation of $\lambda\left(x_{\mathrm{min}}\right)$ is

$$\mathcal{P}\left(x_{\mathrm{min}}\right) = \sum_{k=n\left(x_{\mathrm{min}}\right)}^{\infty} \frac{\left(\lambda\left(x_{\mathrm{min}}\right)\right)^k}{k!} \mathrm{e}^{-\lambda\left(x_{\mathrm{min}}\right)} \tag{5.20}$$

and defines the test statistic of the population test. The excess above background expectations is larger for small $\mathcal{P}\left(x_{\mathrm{min}}\right)$. The expectation $\lambda\left(x_{\mathrm{min}}\right)$ is calculated from scrambled background data sets by repeating the identification of local spots and metric as defined in Eq. (5.19) for each trial.

The threshold x_{min} is not fixed, but the threshold is chosen to give the smallest test statistics as defined in Eq. (5.20). The metric $n\left(x_{\mathrm{min}}\right)$ for a given data set is a falling step function, as is the background expectation $\lambda\left(x_{\mathrm{min}}\right)$. Hence, the lowest test statistic will always coincide with the p-value x_i of one of the spots found in the population. The final significance of the result is then repeated using scrambled background data sets that each have a different threshold x_{min} for the lowest test statistic. The significance is then given by the amount of background scrambles with lower test statistic than observed in data.

5.6 Extensions to the formalism

The formalism of the unbinned likelihood maximization can be generically adjusted to account for different physics scenarios. In the scope of this work, steady emission of single point-like sources is tested with the details discussed in Section 5.1. Other additions and extensions of the unbinned likelihood formalism are widely used in multi-messenger astronomy, especially neutrino astronomy and in IceCube, and mentioned for completeness. Moreover, the methods share large amounts in the technical approach, partly realized in *SkyLab* or possible to be implemented in there.

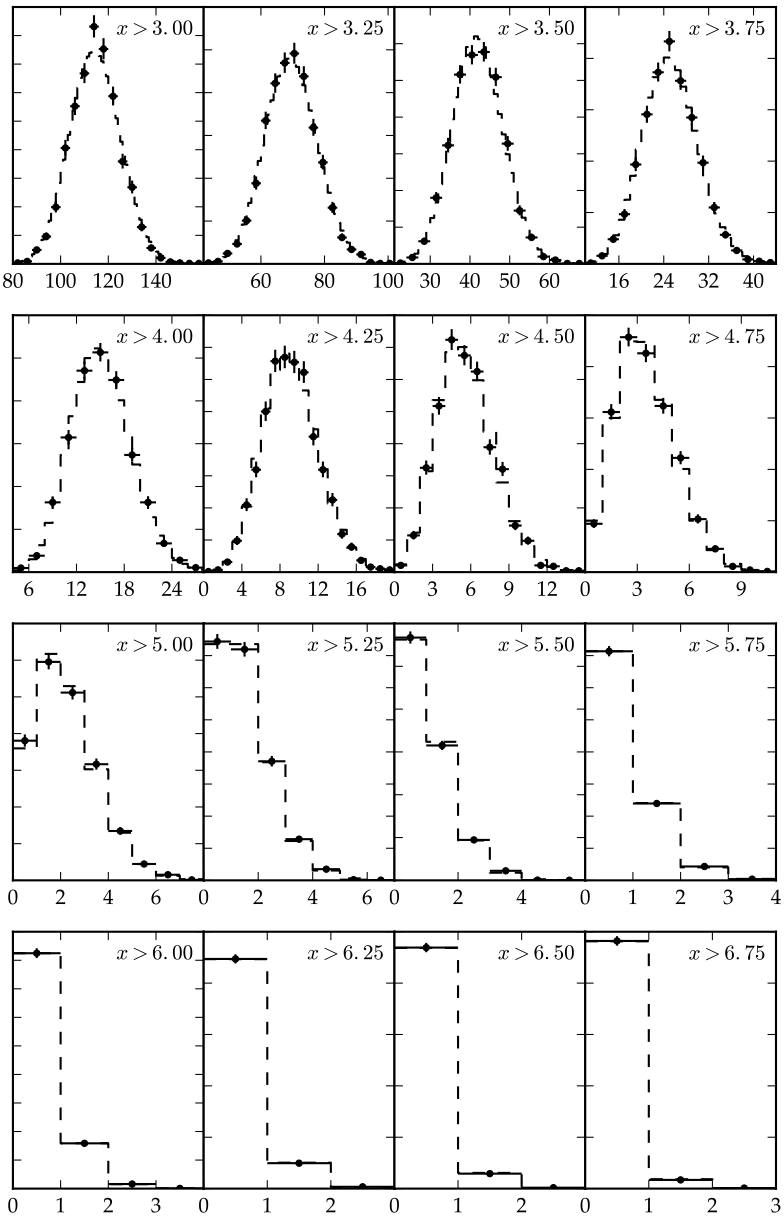

Figure 5.4: Background population distribution for different thresholds x. The trial distributions are compared to a Poissonian distribution.

From gamma ray emission, different classes of high energy sources are known, for example blazars or supernova remnants. In *stacking* analyses, the clustering signal of multiple positions is used together to enhance the signal over background. The signal probability in Eq. (5.6) changes to

$$\mathcal{S} \to \frac{\sum_i \rho_i \omega_i \mathcal{S}_i}{\sum_i \rho_i \omega_i} \tag{5.21}$$

using the weighted mean of the signal probability for all positions considered. The different positions are weighted for a source luminosity ω and the detector response ρ. Thus, entire classes of sources gathered in catalogs are tested for their contribution to the diffuse astrophysical neutrino flux.[20]

[20] Glüsenkamp, "Search for a cumulative neutrino flux from 2LAC-blazar populations using 3 years of IceCube data"; Huber, "Sensitivity Studies for Blazar Stacking Searches with the IceCube Neutrino Observatory".

Another scenario are time-dependent searches[21] that can look for neutrino clustering in space *and* time. For clustering over a short time-scale, the background is greatly reduced. The signal for a flare can be distributed with a Gaussian distribution, whereas the background is flat in time[22]. This adds the additional terms

[21] Aartsen, "Searches for Time Dependent Neutrino Sources with IceCube Data from 2008 to 2012".

[22] Small variations are expected due to seasonal variations of the muon rate.

$$\mathcal{S} \propto \frac{1}{\sqrt{2\pi}\tau} \mathrm{e}^{-\frac{(t-t_0)^2}{2\tau^2}} \tag{5.22}$$

$$\mathcal{B} \propto \frac{1}{T} \tag{5.23}$$

for a flare at t_0 with width τ, whereas the background is uniform for a sample with livetime T. Instead of maximizing the time of the flare t_0, gamma ray observations can be used to trigger the time window used for such analyses.

Such time dependent methods are used in searches for gamma ray bursts (GRB) as well, which are very well constrained in time and only short bursts.[23] Thus, there is a short *on-time* window and the background can be well constrained in *off-time* windows. Thus, the requirement used in Eq. (5.4) can be adjusted to fixing the number of background events $n_\mathrm{B} \approx N_\mathrm{off}$ to the number of events observed in off-time windows. This changes the likelihood formula to

[23] Aartsen, "An All-Sky Search for Three Flavors of Neutrinos from Gamma-Ray Bursts with the IceCube Neutrino Observatory".

$$\log \Lambda = -n_S + \sum_i \log \left(1 + \frac{n_S}{N_\mathrm{off}} \frac{\mathcal{S}}{\mathcal{B}} \mathcal{W}\right) \tag{5.24}$$

used in such searches stacking multiple GRBs and using only events observed in on-time windows.

6 Muon track selection in IceCube

Atmospheric muons are the dominating component of events detected by IceCube. As discussed in Section 4 and shown in Figure 4.7, over all directions, atmospheric muons outnumber all components of neutrinos by a factor from 10^4 up to 10^6. Even in the region with zenith angle larger than 85°, where the Earth matter should shield muons completely, a small fraction of falsely reconstructed muon events is still larger than the rate expected from neutrino interactions.

In this section, the selection of well reconstructed track-like events is discussed that targets an optimal performance for faint signals of steady emission of possible neutrino point sources. The selection uses multivariate selection techniques to reject background over the expected neutrino signal.[1] The selection is done for data that was recorded with IceCube in the seasons from June 2012 until June 2015 and uses the data stream pre-filtered and reconstructed for muon track events[2] (Section 4.6 and 4.7).

The selection is focused on *through-going muons* that enter the detector from outside. This greatly increases the volume accessible for neutrino interaction, resulting in the highest statistics possible, which is necessary for the detection of possible faint signals of neutrino sources. For the development of the selection criteria, 10% of the data was used ("burn sample") and the astrophysical coordinates were not used to ensure a blind analysis procedure.[3] A complementary selection of starting events is discussed in Section 6.4.

[1] Pedregosa et al., "Scikit-learn: Machine Learning in Python".

[2] Feintzeig, "Searches for Point-like Sources of Astrophysical Neutrinos with the IceCube Neutrino Observatory".

[3] Klein and Roodman, "Blind analysis in nuclear and particle physics".

6.1 Signal & background discrimination

In order to remove the copious backgrounds of atmospheric events, the event selection is split into two regions based on the characteristics of the incident background. The regions coincide with the up-going (northern sky, $\theta \geq 85°$) and down-going sector (southern sky, $\theta < 85°$). This separation is due to the Earth shielding atmospheric muons to reach IceCube from the northern sky, resulting in different natures of the background. Figure 6.1 shows the IceCube data rate after pre-processing for the interesting time scale from June 2012 to June 2015 that is used in the selection. In order to be able to identify faint signals of neutrino sources, as much data as possible is used in the analysis. Thus, all data taking runs[4] that have an event rate

[4] The IceCube data stream is split into "runs" that at most consist of 8 hours livetime each.

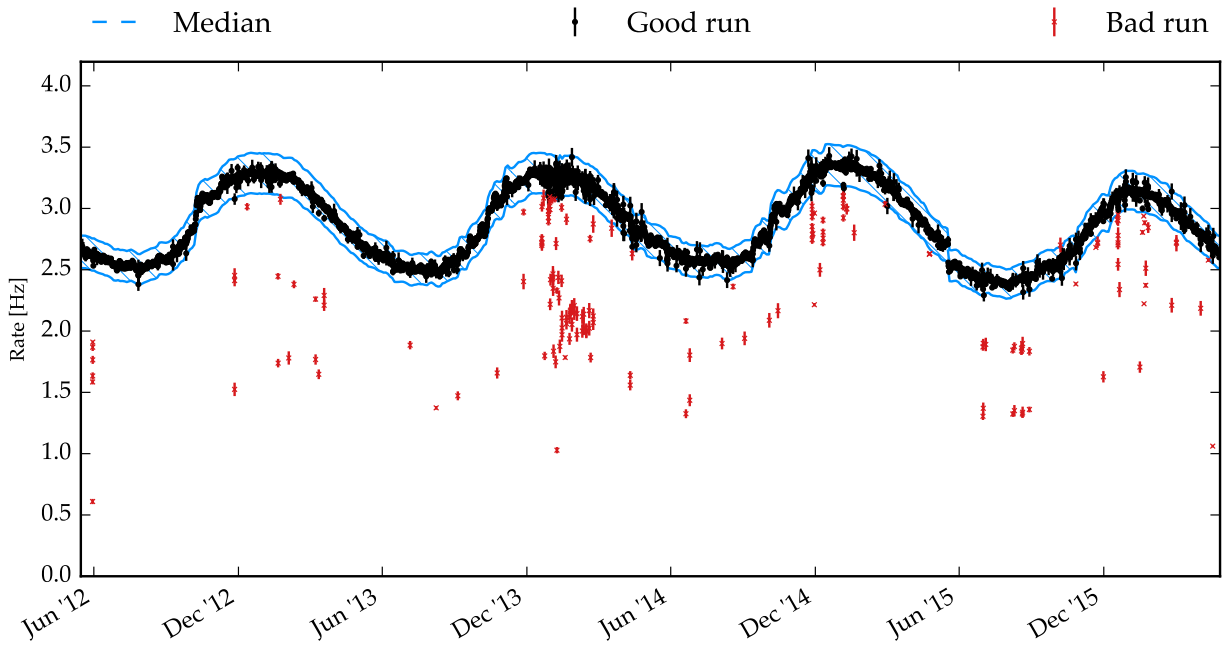

Figure 6.1: IceCube data rate identifying bad runs. Data used in the selection discussed here is from June 2012 until June 2015. Runs that deviate strongly from the median rate (hatched), are identified as "bad".

not differing more than 5% (plus statistical uncertainties) from the local median rate ± 1 week are used in the selection. Hence, data taking periods where parts of the detector were not operational are excluded as this results in a significantly lower rate due to a smaller operational volume.

In the northern sky, most events are due to atmospheric muons that were falsely reconstructed as up-going. One important quantity to identify well reconstructed events are *direct hits*. A pulse observed at a DOM is a direct hit, if the time residual (Eq. (4.12)) is not smaller than 15 ns or larger than a threshold value X. Certain values of X define time windows commonly used in IceCube. In the following, time windows D and E are interesting which correspond to a late arrival time of not more than $X = 125$ ns and 250 ns, respectively.

Direct hits are an important quantity because of their connection to unscattered photons. Such photons carry the most directional information of the track. Thus, a high number of direct photons ($N_{\text{Dir}}^{D/E}$) is connected to a track reconstruction that fits the physics hypothesis well. Moreover, the track is characterized by the constant light emission along the entire path of the muon. Hence, direct hits should be spaced over the entire track length in the detection volume.

A good reconstructed track shows a large distance between the first and last detected direct hit ($L_{\text{Dir}}^{D/E}$), without large distances between subsequent direct hits ($L_{\text{empty}}^{D/E}$). Large *empty lengths* between subsequent direct hits along the reconstructed track can occur for a false reconstruction of coincident events where no light is emitted in the space between the coincident events.

The likelihood value at the reconstructed maximum carries additional information about the event quality. The negative log-likelihood value itself, normalized to the degrees of freedom (*rlogl*, reduced log likelihood) is directly connected to the quality of the event. Moreover, the *paraboloid* fit (σ_{SPE}) of the likelihood landscape around the maximum[5] determines the sharpness of the maximum, and in a likelihood ratio of the up-going reconstruction with respect to a Bayesian fit (Eq. (4.17)), second maxima in the down-going region can be identified.

[5] Neunhöffer, "Estimating the angular resolution of tracks in neutrino telescopes based on a likelihood analysis".

With the observables mentioned before, well reconstructed events can be identified against misreconstructed background, increasing the sensitivity to point-like sources. In the northern sky, a second background of atmospheric neutrinos is encountered (Section 3.6). Astrophysical neutrinos are not separable from the background of atmospheric neutrinos, because their signature is identical. The only discrimination possible is on a statistical basis due to the different spectra of the two components. Atmospheric neutrinos have a softer energy spectrum ($E^{-3.7}$) and zenith angle dependent spectrum, see Figures 3.14 and 4.7, while astrophysical neutrinos are much harder in energy with a spectrum $\sim E^{-2}$ and tentatively arriving from any possible direction.

In the southern sky, the background of atmospheric muons is much more abundant, strongly increasing for events closer to the South Pole, see Figure 4.7. Both the signal of neutrinos as well as the background of atmospheric muons are well reconstructed. Moreover, muons are produced at high multiplicity in the shower. The muons are boosted into the direction of the shower. Consequently, atmospheric muons enter the IceCube detector in bundles imitating the signature of a single track emitting a large amount of Cherenkov light.[6]

[6] Aartsen, "Characterization of the Atmospheric Muon Flux in IceCube".

The details of the light emission of muon bundles differ from the emission of a single muon. A muon bundle consists of a large amount of muons at intermediate energy. Hence, the light emission is a superposition of multiple Cherenkov cones. Thus, compared to a single muon light is expected to arrive at different times than for a single muon.[7] Especially light arriving earlier than expected from a single Cherenkov cone identifies bundles of muons.

[7] Feintzeig, "Searches for Point-like Sources of Astrophysical Neutrinos with the IceCube Neutrino Observatory".

Furthermore, a muon bundle consists of many muons at intermediate energies. Such muons lose energy mainly due to ionization losses and the light-yield for such events is dominated by the muons Cherenkov cone. Above the critical energy of $\sim 500\,\mathrm{GeV}$, energy is lost in stochastic processes. Hence, a single high-energy muon shows large stochastic energy losses with spherical light emission. Hence, a single muon can be identified according to its energy losses reconstructed along the track[8]. A high variability in the energy losses is more probable for a single muon.

[8] Energy deposition reconstruction is discussed in Section 4.7.

In a likelihood ratio test, the preference of a single muon hypothesis ($\mathcal{S}$) can be tested against the hypothesis of a muon bundle ($\mathcal{B}$). Each observable is evaluated using a two dimensional probability

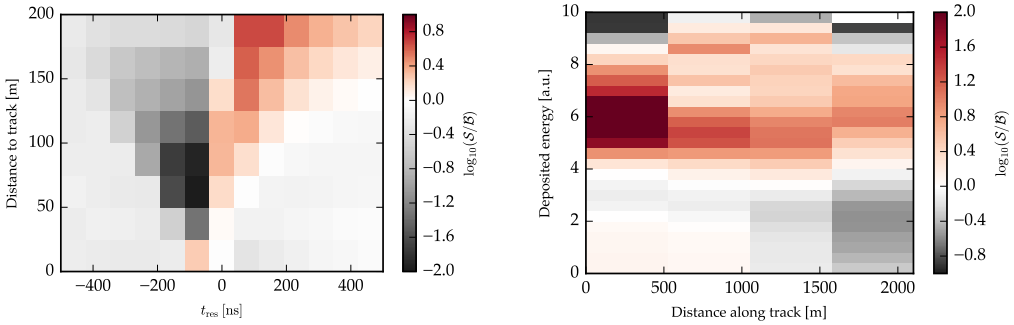

Figure 6.2: Likelihood ratio of single muon versus muon bundles for two parameter spaces. For red colors, the signal hypothesis $\mathcal{S}$ of a single muon is favored over a muon bundle and vice versa for gray-scale values. Left: Time residuals versus distance of DOM to the reconstructed track. Right: Reconstructed differential energy deposition along track versus energy deposition distance along track.

density function that is dependent on the events reconstructed energy. The output of the likelihood ratio test is hence

$$\ln \mathcal{L}(\boldsymbol{\xi}; E) = \sum_i \ln \frac{\mathcal{S}(\xi_i; E)}{\mathcal{B}(\xi_i; E)} \tag{6.1}$$

for one event with reconstructed energy E that has a set of observables $\boldsymbol{\xi}$. This is the description of an unbinned likelihood ratio as in Eq. (5.8) assuming 100% signal ($n_S / N \to 1$).

Figure 6.2 shows the probability density functions using all energies[9] for two realizations of the likelihood ratio Eq. (6.1). The left plot shows the distance of a DOM closer than 200 m to the track against the time residual for individual DOMs with recorded hits. In red, late arrival times for muons from a single track are visible which is favored for single muons, because muon bundles produce a larger amount of light arriving earlier than expected when compared to a single muon traversing the detector.

The second distribution uses the energy depositions that are reconstructed along the track. For single muons, along the track, higher energy depositions are more probable, whereas muon bundles typically show many less energetic depositions. The likelihood is then normalized to the number of photons or number of energy depositions observed, giving a *reduced likelihood*.

Overall, in the down-going region, the large backgrounds of muon bundles that imitate high-energy muons put hard constraints on the capabilities to identify muons as originating from neutrino interactions. Nevertheless, the hard energy spectrum of potential neutrino sources exceeds the energy spectrum of atmospheric muons. Thus, the signal to noise ratio is increased by only selecting the most energetic events observed.

[9] In the realization of this method, this is done binned for different reconstructed event energies accounting for possible variations in energy.

6.2 *Low-level background rejection*

After filtering the IceCube data stream for muons and pre-processing the data with high level reconstructions, as discussed in Section 4.6, the event rate of track candidate events is 2.63 Hz. Figure 6.3 shows the zenith distribution at this stage using the best reconstruction, that is, a MPE likelihood using splines of simulated photon time residual

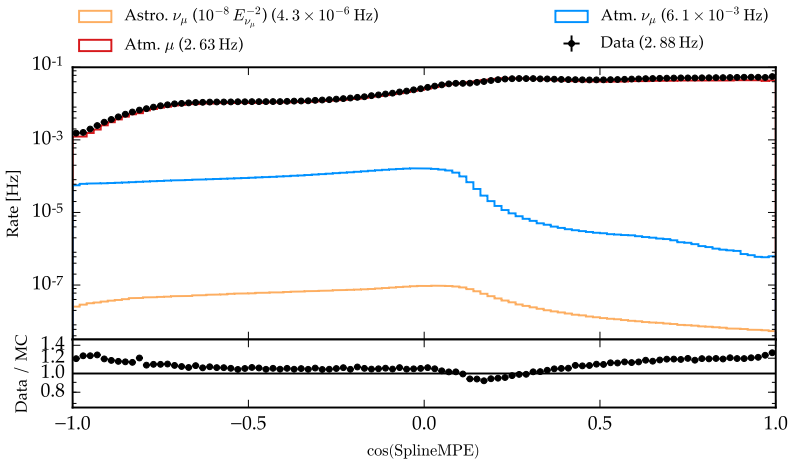

Figure 6.3: Zenith distribution after pre-processing of data. The reconstructed zenith uses a spline table based MPE likelihood reconstruction (*SplineMPE*).

tables (*SplineMPE*). Compared to Figure 4.7, the rate in the down-going region is reduced most significantly due to a charge threshold imposed. Consequently, the expected neutrino rate drops as well due to discarded events at lower energy, and is not symmetric anymore because of less stringent cuts in the northern sky. The backgrounds regarding searches for astrophysical neutrinos are different in the northern and southern sky. Hence, as discussed in Section 6.1, different strategies give the best signal discrimination for both halves of the sky. Prior to the final high-level selection, further cuts are used to remove clear background and regions in the parameter space where simulation and background show trends of disagreement. The rate is further reduced and variables regarding the discrimination of muon bundles in the down-going region are calculated which was introduced in Eq. (6.1).

In the northern sky, which is defined for reconstructed zenith angles of $\theta \geq 85°$, the first rejection of background is done identifying events that show strong disagreement with the expectation of a muon track that is well reconstructed. Thus, an event is required to have recorded hits on *at least* three distinct strings. The hits are "cleaned", that is, noise hits were identified if they are not in spatial or temporal correlation with the majority of hits. Furthermore, very inclined muons from air showers that pass the detector above or below the detector are found ubiquitously as falsely going upwards. Thus, the vertical (z axis) position of the center of gravity is required to be not at the detector boundary $-450\,\mathrm{m} < \mathrm{COG}_z < 450\,\mathrm{m}$. Most importantly, the track reconstruction has to indicate a well fitting direction. Hence, a number of cuts are imposed connected to the quality of the likelihood reconstruction and the recorded hits in IceCube compared to the reconstructed track passing through IceCube. The cuts are listed in Table 6.1 combined using an *and* connection. Hence, all conditions have to be passed. The rate in the northern sky drops

Table 6.1: Low-level cuts applied in the northern sky. For each cut, the lower and/or upper bound of the allowed region is reported.

Variable	"<"	">"
COG_z $[m]$	450	-450
N_{Strings}		2
N^E_{Dir}		5
L^E_{Dir} $[m]$		75
L^E_{empty} $[m]$	400	
rlogl	12	
σ_{SMPE} $[1°]$	15	
$\Delta\Psi$ $[1°]$	60	

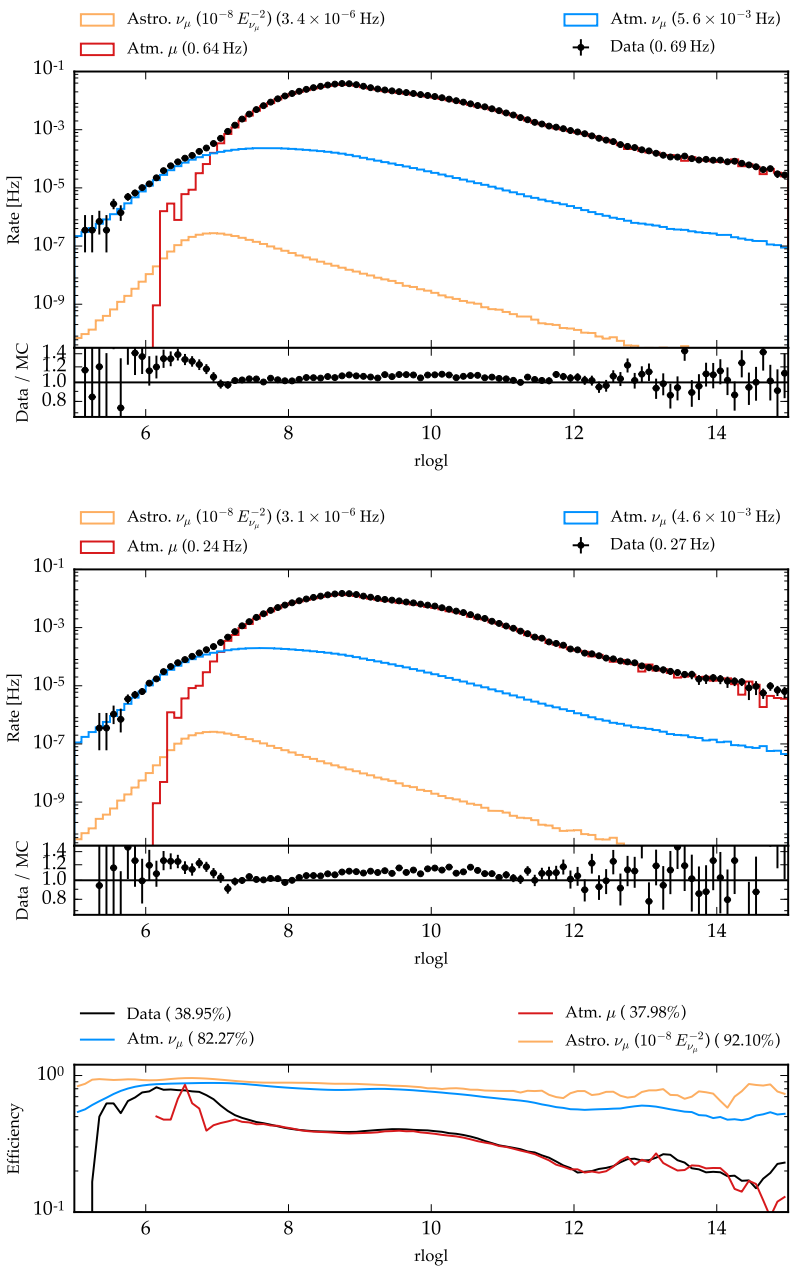

Figure 6.4: Distribution of rlogl before and after low-level cuts. Shown is *burnsample* (Data) and Monte Carlo data for atmospheric muons (H4a model) and neutrinos (Honda 2006), and astrophysical neutrinos (Flux of $10^{-8}\,\mathrm{GeV\,cm^{-2}\,s^{-1}\,sr^{-1}}$). For each component, the rate expectation is given in the legend. The top plot shows the values before the cuts, the middle plot after all cuts except the one on rlogl which is shown. The bottom plot shows the efficiency of all other cuts on rlogl, that is, the ratio of both figures. For both histograms, the data to Monte Carlo comparison is shown at the bottom of each figure.

by 40%. For astrophysical muon neutrinos with spectrum E^{-2}, the efficiency is 90% and improves for the events with better angular reconstruction.

In Figure 6.4, the reduced likelihood (*rlogl*) is shown before (top) and after (middle) applying the cuts listed in Table 6.1. The likelihood value of the reconstruction is directly connected to the quality of the event, hence, for values rlogl < 7, atmospheric muon neutrinos start to dominate over the ubiquitous background of atmospheric muons. The cuts on other variables than rlogl affect the signal in regions, where the background is most dominating. Distributions for the other variables are listed in Figures B.1 to B.8 in Section B.1.

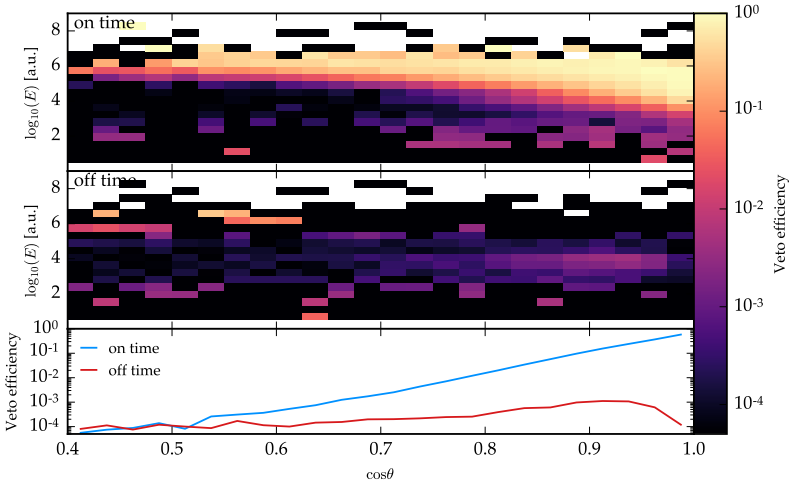

Figure 6.5: IceTop surface veto against coincident air showers. Top: Percentage of events vetoed due to coincident hits in the surface array. The distribution is shown for the reconstructed direction and energy in x, y direction respectively. Middle: Same as top plot but using the data with a off time window, that is, showing random coincidences. Bottom: Efficiency of the veto with respect to reconstructed zenith.

In the down-going regions, the cut variables are very similar. All variables are listed in Table 6.2. Similar to the northern sky, variables are chosen that are connected to the reconstruction performance of the track event candidate, but the large background of atmospheric muons requires harder cuts than for the up-going region. This can be seen in the larger values required for L^E_{Dir} and N^E_{Dir}. Similarly, the reconstruction uncertainty σ_{SMPE} and reduced likelihood are more constrained as before. One additional cut is put on the number of energy depositions reconstructed with at least 1 GeV deposited energy within 15 m segments. Even though this cut is still loose, this requires the track to be reconstructed with enough energy depositions in order to assess the stochasticity of the depositions to evaluate the event as single muon or atmospheric muon bundle, Eq. (6.1) and Figure 6.2. After all cuts listed in Table 6.2, the observed rate in the down-going region drops by 33%, reducing from 2.13 Hz to 1.43 Hz. The rate of astrophysical muon neutrinos is higher at 97.27%, while atmospheric neutrinos at lower energies reduce by a factor of two. Distributions of the variables before and after the selection are listed in Figures B.9 to B.12.

Furthermore, the *IceTop* surface detector is used in the down-going region to veto atmospheric backgrounds.[10] For events that are reconstructed down-going in the underground IceCube detector, IceTop is analyzed for coincident hits. Coincidence is defined that hits are expected when a plane[11] that travels alongside the reconstructed particle passes through a tank of IceTop. If a hit is recorded in a IceTop tank, a time residual is calculated as the time difference of the hit with respect to expected time when the shower plane passes through. If the time residual is within $(-50\,\text{ns}, 500\,\text{ns})$ difference, the hit is considered to be connected to the reconstructed event. An event is vetoed because of a coincident air shower if more than two SLC hits are recorded ($N^{\text{IceTop}}_{\text{SLC}}$) or one or more HLC hits ($N^{\text{IceTop}}_{\text{SLC}}$). The efficiency of this veto can be quantified using experimental data

Table 6.2: Low-level cuts applied in the southern sky. For each cut, the lower and/or upper bound of the allowed region is reported.

Variable	"<"	">"
N_{Strings}		5
N^E_{Dir}		12
$L^E_{\text{Dir}}\,[m]$		250
$L^E_{\text{empty}}\,[m]$	400	
rlogl	9	
$\sigma_{\text{SMPE}}\,[1^\circ]$	5.62	
$N\,(E_i > 1\,\text{GeV})$		4
$N^{\text{IceTop}}_{\text{HLC}}$	1	
$N^{\text{IceTop}}_{\text{SLC}}$	3	

[10] Aartsen, "Search for Time-independent Neutrino Emission from Astrophysical Sources with 3 yr of IceCube Data".

[11] A plane as approximation of a shower front without curvature.

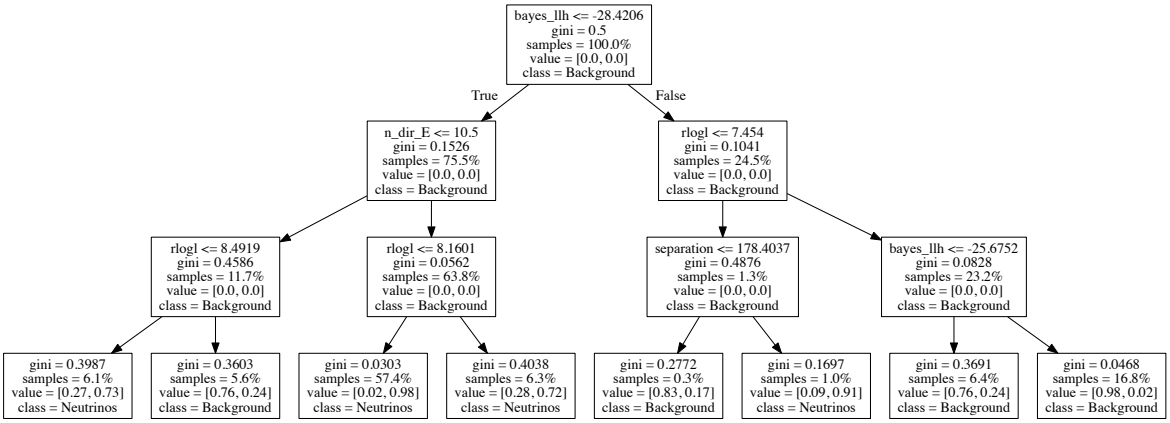

Figure 6.6: Decision tree trained of first iteration of BDT in the up-going region using a hard signal-spectrum. At each node the variable and cut are listed. "Value" lists the fraction of events in class 0 (Background) and 1 (Neutrinos). The decision tree then makes a decision based on the leaf an event ended in. Variables are explained in Narsky and Porter, *Statistical Analysis Techniques in Particle Physics: Fits, Density Estimation and Supervised Learning*.

only. Using a time window shifted by 1 µs to earlier times gives an off-time window that is only affected by random coincidences. Figure 6.5 shows the veto efficiency for the surface veto in the plane of reconstructed event zenith and energy. Random coincidences occur in less than 0.1% of the cases, where the veto is very efficient for high energy events over the whole zenith range larger than 30°. For lower energies, the veto is efficient only above $\cos\theta > 0.9$, vetoing 10% of showers and up to 90% of the showers in the very vertically down-going region.

6.3 *Multivariate selection of through-going muons*

Using the data stream removing obvious background and vetoing air shower events with the surface component of IceCube, the final selection of muon tracks is done using multivariate selection methods[12] in the form of boosted decision trees (BDTs). A decision tree classifies data according to a set of observables. It is characterized by a certain depth and therefore number of decisions before the final node is achieved. A tree is *trained* by analyzing data of which the class is known, in this case if it is signal (1) or background (0). A boosted decision tree uses a large ensemble of decision trees that are each trained with different subsets of data. The subsets are chosen by *boosting* the tree, that is, when more and more trees are trained, trees are focusing on "difficult" cases to discriminate signal from background.[13] After training, a BDT can predict probability of an event to belong to the signal class which is called *(BDT-)score* in the following. Thus, a large set of variables can be transformed into one number conveying information on how likely an event is to belong to the searched category.

When training a BDT, *overtraining* or *overfitting* can occur. Overtraining happens if a (boosted) decision tree has too many degrees of freedom to distinguish the signal from background in the training

[12] Pedregosa et al., "Scikit-learn: Machine Learning in Python".

[13] Narsky and Porter, *Statistical Analysis Techniques in Particle Physics: Fits, Density Estimation and Supervised Learning*, p. 331ff.

phase and thus fine-tunes the selection to work as perfect as possible on the data set used for training. At some point, such a BDT will not work as well using statistically independent data anymore. Hence, overtraining has to be avoided, or data that was used for training cannot be used anymore and is "burned" during the training process. In order to avoid overtraining, the depth of a decision tree (*max depth*) and the number of decision trees used in a BDT can be limited. Moreover, decision trees can be prohibited to further split events at a node, if the statistics are small and statistical artifacts are likely to be present.[14]

[14] Ibid., p. 173.

Here, parts of the burnsample are used as background classified sample, because the background is largely dominated by atmospheric muons even after applying the first cuts, see for example Figure 6.3. For signal, Monte Carlo simulation of muon neutrino charged interactions is used that are well reconstructed ($< 3°$) and do not have coincident events. Because experimental data is used in the training of the BDT, overtraining is not wanted and will be evaluated using *four-fold cross validation* methods.[15] In this method, the sample is split in four parts which all have the same amount of signal and background events. Thus, a BDT is trained four times, each time using three parts for the training and the remaining one for testing the results. Thus, each time the training and testing sample can be verified to give the same outcome each time and if found that they are diverging, overtraining is identified. Moreover, by training four BDTs with varying data, artifacts of the selection are removed, because every event will be used three times for training and once for testing against the trained BDT.

[15] Ibid., p. 181.

The settings used in the BDT training are listed in Table 6.3 and are optimized to give the best power without overtraining issues arising. The optimization for the maximum depth of each decision tree in the ensemble is shown in Figure 6.7 for the sample of up-going events using an E^{-2} spectrum for the signal neutrino spectrum. The performance is estimated using the *AUC* or "area under curve" method as receiver operator characteristic (roc) for BDT performance.[16] For each possible cut on BDT score, the *false positive rate*, that is, background not being rejected, is evaluated against the *true positive rate*, that is the signal efficiency, at the certain cut value. Calculating the area of this curve estimates the performance of the classifier. For values of 100%, the classifier is able to reject all background (no false positives) while retaining all signal (100% signal efficiency).

Table 6.3: Settings used in BDT training

Setting	Value
Number of trees	400
Depth of trees	3
Minimum number of events at leaf	20

[16] Ibid., p. 195.

In Figure 6.7, the performance of the BDT grows with increasing tree depth. At depth larger than three however, the testing sample does not perform as good as the training sample anymore, a clear indication of overtraining of the BDT. Hence, the depth for the decision trees is fixed at three. Thus, here, depth of three are used to avoid overtraining. Note, that even though overtraining is visible for a depth of four or five levels, the BDT is able to perform better than using a depth of three. This can be used in general to have a

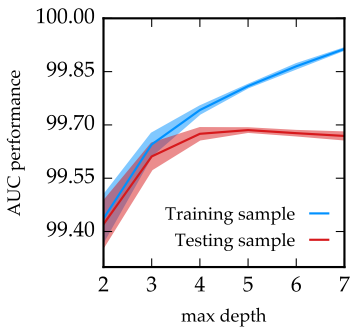

Figure 6.7: BDT performance for variable tree depth. The performance (*AUC* estimator) is shown for the training and statistically independent testing sample. Using four fold cross validation, the performance is averaged using four different combinations of the set, with areas indicating the statistical variation.

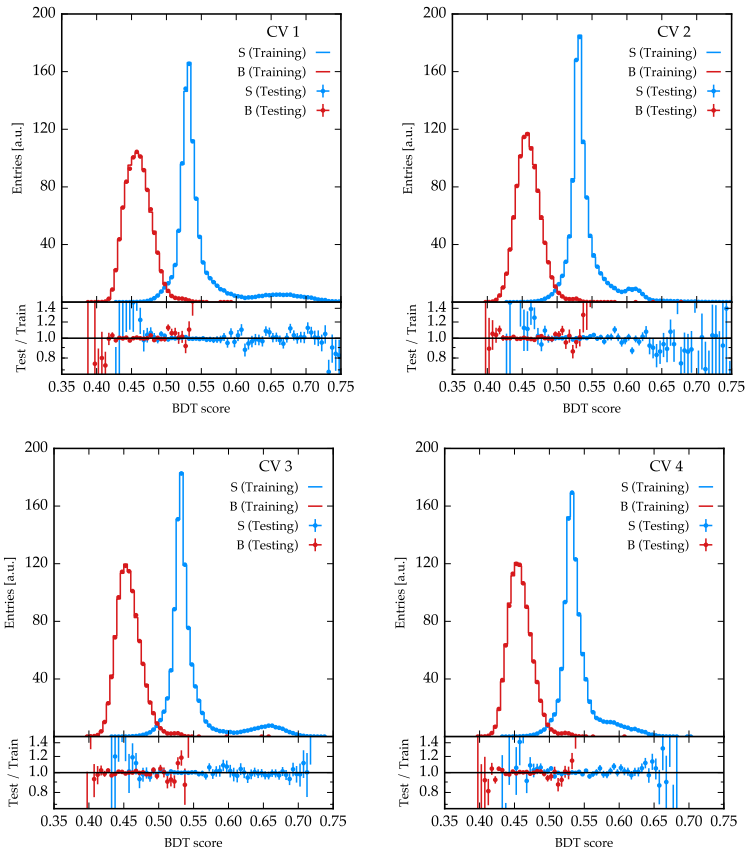

Figure 6.8: Cross validation of BDTs in up-going region with hard spectrum (E^{-2}) used for signal (S) versus experimental data as background (B). The testing and training spectrum show good agreement.

more powerful BDT, but due to the overtraining, data used for training is "burned" and cannot be used anymore in a statistical analysis. Here, experimental data is used as background sample because it is not affected by systematic or physical uncertainties like Monte Carlo simulation, but it is not wanted to disregard 10% of the data used in the training[17] for a slight increase in BDT performance. Hence, here the lower value of a depth of three levels is chosen. The same procedure accounts for the other parameters listed in Table 6.3.

For both halves of the sky, experimental data is used as background sample, as mentioned before. For signal, muon neutrino simulation is used. Only events are used that have charged current interactions with a muon reconstructed to 3° or better and no coincident events in the detector that could bias the reconstruction. The simulation is weighted to a differential energy spectrum of E^{-2}. In the northern sky, another set of BDTs is trained using a spectrum of $E^{-2.7}$ to account for possible signals of soft or cutoff spectra. The results of the cross validation is shown in Figure 6.8 for a BDT in the up-going region using the harder spectrum for signal. Good agreement between the trained sample BDT scores and the testing sample is found for all four iterations of the four fold cross validation. This is true for the other BDTs as well, shown in Figures B.13 and B.14. In general, in the up-going regions, the BDTs can separate the signal and background much better than in the down-going region.

[17] This is equivalent to $\sim$ 1 month of exposure per year

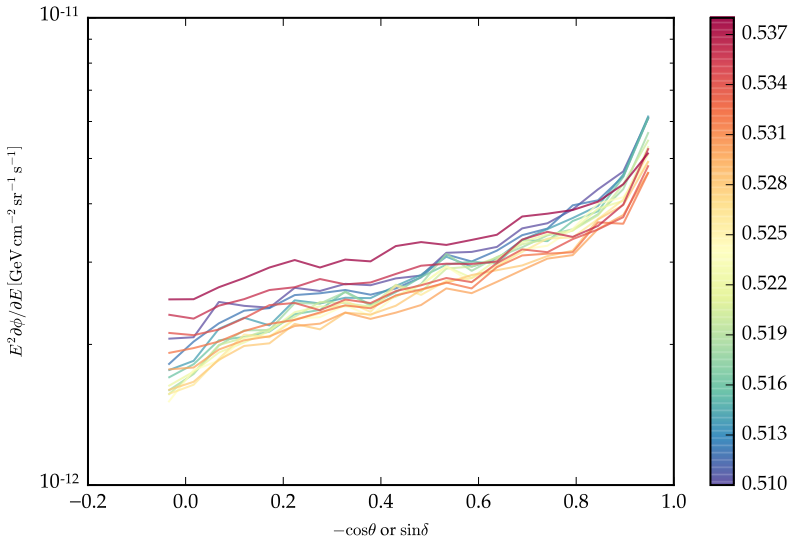

Figure 6.9: Point source sensitivity in up-going region for different cuts on BDT score. The color coding shows the cut value against declination δ or zenith θ.

For both regions, eleven variables are used in the BDT selection. Some variables are used in both regions of the sky. These variables are the radial and vertical position of the center of gravity (COG) using noise-cleaned pulses, the number of direct hits and direct length with time windows E, D, respectively, and the reconstructed event uncertainty σ_{MPE} and reduced likelihood (rlogl) of the spline reconstruction *SplineMPE*. One other variable that was not used before is the distance of the COG of the first and last quartile of hits recorded along the track ("track hit separation"). Variables that are exclusively used in the up-going region target the identification of mis-reconstructed events. This includes the average distance of hits to the reconstructed track and the likelihood difference of an *SPE* track reconstruction compared to one biased with a Bayesian prior. In the down-going region, variables for bundle discrimination are used. This includes the two likelihood ratios shown in Figure 6.2, the amount of hits with early arrival times compared to the total number of hits observed, and the ratio of the maximum charge observed in one DOM compared to the total recorded charge. Lastly, the cosine of the reconstructed zenith is used in the BDT to account for varying variables with zenith direction. This is particularly important for the center of gravity position or variables connected to the track length that depend on how long a particle is visible in the detector. The final cut on the BDT score is done zenith dependent to get the best performance for all directions.

In the up-going region, the BDTs are able to clearly separate the truly up-going muon tracks originating from prior neutrino interactions from the atmospheric neutrino background. The final cut is optimized to give the best sensitivity for a steady neutrino point

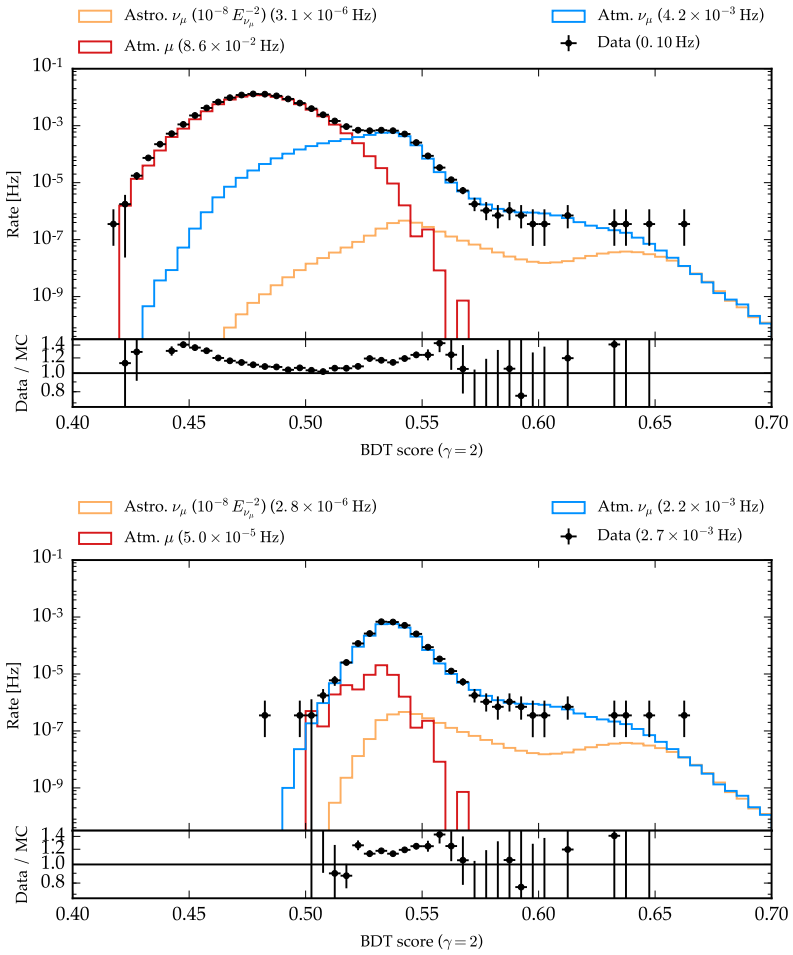

Figure 6.10: BDT score in up-going region before and after cut on the score. Shown is the mean BDT score of all four BDTs trained with a hard signal spectrum (E^{-2}). The top (bottom) figure shows the distribution before (after) the cut, the components shown are the same as in the previous distributions shown.

source flux and results in

$$\mathrm{BDT}\left(\cos\theta\right) > 0.530 + 0.294\left(\cos\theta - 0.07\right) \times \Theta\left(\cos\theta - 0.07\right) \tag{6.2}$$

$$\mathrm{BDT}\left(\cos\theta\right) > 0.527 - 0.02\cos\theta \times \Theta\left(\cos\theta\right) \tag{6.3}$$

for the two BDTs with hard and soft spectra for the signal component, respectively, and the *Heaviside* step-function $\Theta\left(x\right)$. The cut is applied that either Eq. (6.2) or Eq. (6.3) has to be true for an event to pass. The sensitivity to neutrino fluxes ($\partial\phi/\partial E \propto E^{-2}$) for different cuts is shown in Figure 6.9. The BDT score distribution before and after the cuts in Eq. (6.2) and (6.2) is shown in Figure 6.10. The two components of misreconstructed atmospheric muon background and truly up-going neutrino induced track events are clearly separable. The observed data is dominated by neutrinos for high scores.

After the final cut on BDT score, the sample is dominated by neutrinos, and rejecting $\sim$ 99.94% of atmospheric muons, while retaining 90% of the signal. After the cut, systematic shape differences of experimental data and Monte Carlo simulation reduce significantly, apart from a constant rate difference of data and the atmospheric neutrino prediction.[18] This can be matched by re-scaling the total flux of atmospheric neutrinos, as for example done in searches for a

[18] Honda et al., "Calculation of atmospheric neutrino flux using the interaction model calibrated with atmospheric muon data".

diffuse flux of neutrinos.[19] Hence, the data is well described by the prediction of Monte Carlo simulation. Variables that were used in the training of the BDT and other variables used for cross-checking the performance of the BDT output are shown in Figures B.15 to B.26 in Section B.2.

[19] Aartsen, "Observation and Characterization of a Cosmic Muon Neutrino Flux from the Northern Hemisphere using six years of IceCube data".

Investigating the effect on the BDT cut on the distributions of the variables, it can be seen where the best discrimination power for the BDT score is originating. Variables that are connected to the event quality show a clear difference before and after the cut, for example in the reduced likelihood (rlogl) or the Bayesian likelihood difference. Other variables were selected to identify events that are not reconstructed with high enough accuracy to give the pointing necessary for the identification of point-like sources in the analysis. Hence, events with few direct hits and a short distances between first and last hit are discarded for up-going events as well. The BDT selection is not showing preference on the incoming zenith direction, the effect of the cut is shown for the reconstructed distribution in Figure 6.11. For horizontal events, muons start to leak into the sample, reducing the purity. Nevertheless, this component could be reduced by putting stronger requirements on the BDT score in this region. This would diminish the signal efficiency and the cut chosen shows better sensitivity regarding sensitivity to point sources of neutrinos, as evaluated in Figure 6.9. Furthermore, atmospheric backgrounds can be estimated from experimental data in point source analysis, thus, impurities of any kind can be estimated without relying on Monte Carlo predictions.

In the down-going region, a clear separation of the atmospheric muon components from the signal of neutrinos is not possible, because the atmospheric muon component is too large compared to the expected neutrino rate. Furthermore, in the through-going channel, both components leave very similar signatures (tracks of muon bundles versus single high-energy muons). Thus, the final cut is optimized to yield the best sensitivity to point source fluxes at the highest end of the spectrum, that is, above PeV energies, where the contribution of astrophysical neutrinos starts to increase over the ubiquitous background. Nevertheless, the sample is still dominated by atmospheric muon bundles. Lower neutrino energies are accessible using veto techniques, as introduced in Section 2.2 and with focus on searches for point sources in Section 6.4.[20] The zenith distribution after the BDT cut is shown in Figure 6.12 accounting for the IceTop veto for simulation as estimated from Figure 6.5. In the region of the veto, a looser cut on BDT score is chosen resulting in a constant background rate in $\cos\theta$, but with higher rate of neutrinos, especially at lower reconstructed energies.

[20] Aartsen, "Lowering IceCube's Energy Threshold for Point Source Searches in the Southern Sky".

The BDT cuts in both up-going and down-going region are optimized to give matching rates at their boundary $\theta = 85°$, because it is technically difficult to account for steps in the background distribution in the statistical evaluation of clustering at a position of this boundary, using splines in the declination distribution in Eq. (5.7).

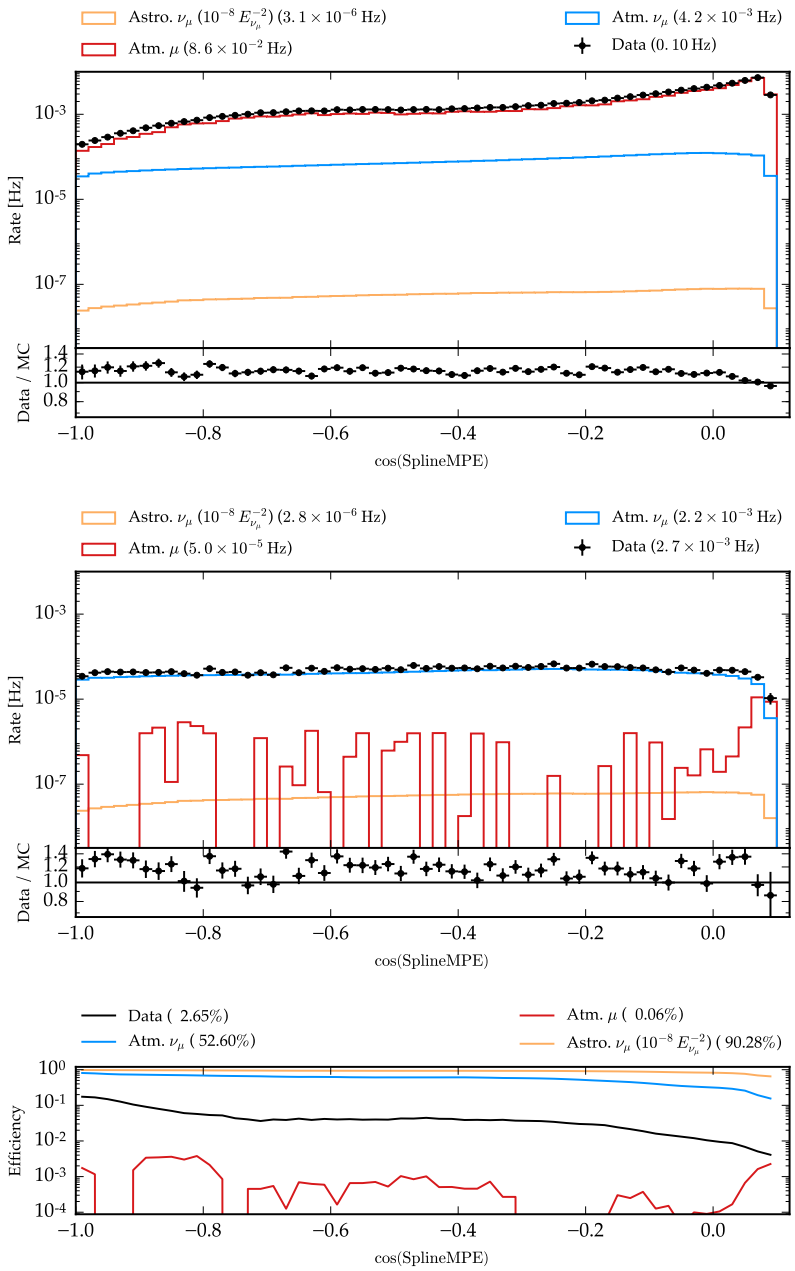

Figure 6.11: Effect of BDT score cut on the reconstructed zenith distribution in the up-going region $\theta > 85°$. The top figure shows the distribution before the cut, and the middle on after the cut. The ratio of both figures is shown in the bottom. Data and components shown are equal to the previous Figures showing data and simulation distributions.

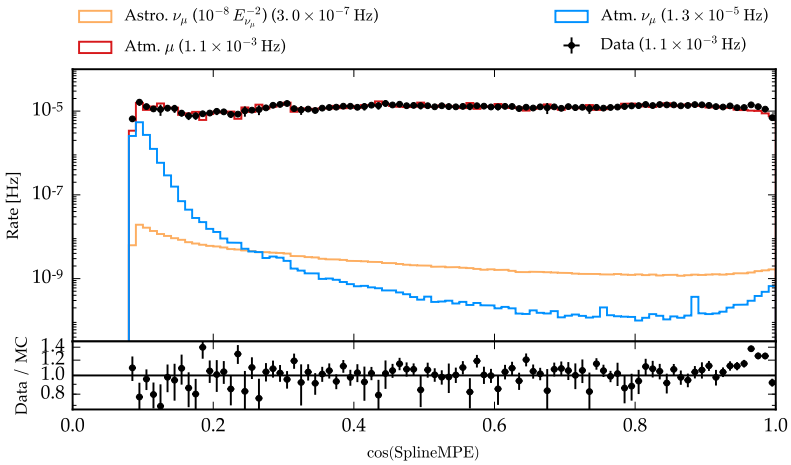

Figure 6.12: Down-going zenith distribution after BDT selection. Same components as in previous figures are shown.

Hence, the cut close to the boundary in the down-going region is adjusted to match the rate in the up-going region, similar to previous searches,[21] this is done using the BDT score in the down-going region.

[21] Aartsen, "Searches for Extended and Point-like Neutrino Sources with Four Years of IceCube Data"; Feintzeig, "Searches for Point-like Sources of Astrophysical Neutrinos with the IceCube Neutrino Observatory".

6.4 *Starting muons*

As visible in Figure 6.12 for the southern sky, the selection of through-going muons induced by neutrino interactions is limited by the large amount of through-going muons created in extended air showers. A large fraction of the background is removed by imposing a charge threshold and only select the best reconstructed and highest energy events where the signal of astrophysical neutrinos ($\partial\phi/\partial E \propto E^{-2}$) has the largest fraction compared to the background ($\partial\phi/\partial E \propto E^{-3.7}$).

With active veto techniques as discussed in Section 2.2, the identification of neutrino events is possible in the down-going region at TeV energies with good background rejection. In searches for point sources, an adjusted veto is used as well to access lower energies.[22] The selection for the observation of the astrophysical diffuse flux requires a high purity with clear identification of neutrinos in the entire southern sky.[23] This is done using a veto with high energy threshold of 6000 pe of deposited charge. In searches for point sources, the purity requirements can be loosened in favor of higher signal efficiency, that is, increased statistics. Consequently, the veto requirement is lowered to 1500 pe resulting in a much higher signal efficiency without increasing the background rate too much for analyses probing local clustering.

With a lower energy threshold using the 1500 pe, the efficiency for muon neutrino events is increased below 100 TeV and approximately 20× larger at energies of 30 TeV than for the veto at 6000 pe.[24] In this energy regime, the expected event rate matches the level of through-going muon selections in the down-going regime that is discussed in Section 6.3, but at higher purity, because a large amount of

[22] Aartsen, "Lowering IceCube's Energy Threshold for Point Source Searches in the Southern Sky".

[23] Aartsen, "Evidence for High-Energy Extraterrestrial Neutrinos at the IceCube Detector".

[24] Feintzeig, "Searches for Point-like Sources of Astrophysical Neutrinos with the IceCube Neutrino Observatory".

background is vetoed as events entering the detector from outside[25]. Above PeV energies, through-going tracks start to dominate because their event rate is much larger, if the volume of neutrino interactions is not restricted to the fiducial volume of the detector. Thus, by using both selections of starting and through-going tracks, a large range of energies from tens of TeV up to EeV is covered.

In addition to the active veto against incoming tracks, three cuts are applied that select well reconstructed events over poorly reconstructed cascades.[26] The first cut compares the angular reconstruction of SplineMPE to the one of linefit. If the angle between those two direction exceeds 41.6°, the event is discarded. Moreover, only events that have a zenith angle $\theta < 85°$ are used. In the other region (northern sky), the through-going track selection does not have the limitations as in the southern sky. Hence, there is no gain in selecting starting tracks separately. The last cut aims for a further discrimination of signal from background. With a lower charge threshold of 1500 pe, more background of atmospheric muons enters IceCube without triggering the veto. Nevertheless, due to the constant emission of light along the track, background events that pass the selection look like a track that starts very close to the boundary of IceCube. Neutrinos on the other hand can interact anywhere in the detector. Hence, if the reconstructed starting point of the muon track is very deep inside of the detector, it becomes more probable to be a neutrino interaction than if the starting point was close to the boundary. Using an energy dependent cut

$$\frac{D}{\mathrm{m}} > -81 \log_{10} \frac{\hat{E}}{\mathrm{GeV}} + 426 \tag{6.4}$$

for an event with reconstructed energy $\hat{E}$ that starts at a distance D away from the detector boundary. The distance is defined as the distance along the track pointing back to the detector boundary. Hence, the higher energetic an event is reconstructed, the closer it can be reconstructed to the boundary,[27] because the veto efficiency improves with higher energy.

6.5 *High-level reconstructions & pull validation*

After the multivariate selection is done, the event rate of the sample reduces to 2.7 mHz in the up-going region and half of that in the down-going region. This rate is low enough to apply high level reconstructions to the data sample that are too exhaustive to be computed at an earlier stage. These reconstructions are uncertainty estimations using the MPE likelihood estimated on splined simulation data. In the multivariate selection, a *paraboloid fit* is used that is calculated with the analytic formulation of time residuals given in Eq. (4.16). The paraboloid fit requires 24 additional minimizations of the vertex at different directions around the best fitting directions, which is too slow at an earlier stage.

[25] The event rate for starting events is $0.09\,\mathrm{d}^{-1}\,\mathrm{sr}^{-1}1$ with respect to $15.5\,\mathrm{d}^{-1}\,\mathrm{sr}^{-1}$ for through-going events.

[26] Aartsen, "Lowering IceCube's Energy Threshold for Point Source Searches in the Southern Sky".

[27] Feintzeig, "Searches for Point-like Sources of Astrophysical Neutrinos with the IceCube Neutrino Observatory".

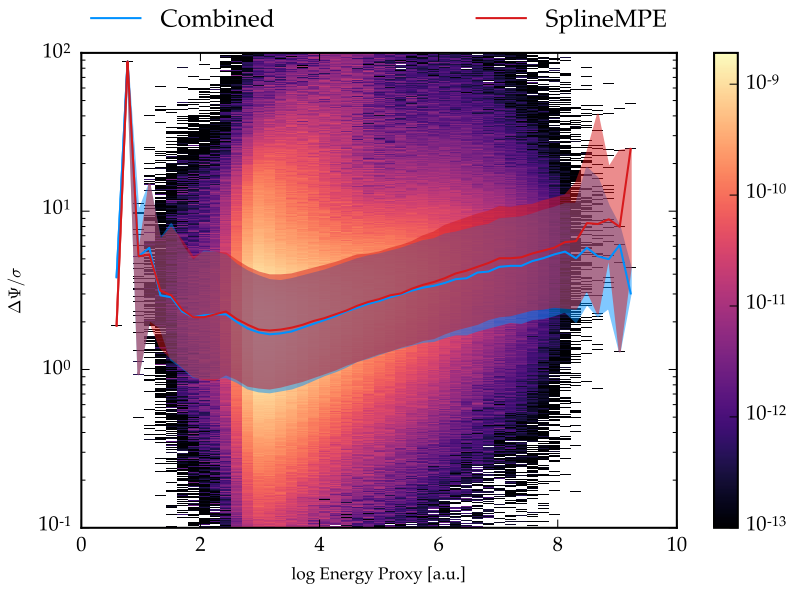

Figure 6.13: Pull correction of uncertainty estimation with respect to true uncertainty from simulation. Two corrections using the combined estimations or paraboloid (SplineMPE) only. The median value and 1σ contours are shown. The estimation is done using simulation of muon tracks induced by neutrinos weighted to an E^{-2} spectrum.

The uncertainty estimate of an event enters the clustering analysis because it carries the information if an event can be associated to a clustering position or not. Hence, calculating the uncertainty estimate for all events that passed the multivariate selection gives additional performance for the statistical analysis.[28]

In addition to the paraboloid reconstruction which gives the most accurate description of the uncertainty of a reconstruction by sampling the likelihood landscape around the maximum, another uncertainty estimation is done by calculating repeating the MPE fit on splined tables using bootstrapped hits eight times. Even though this method performs slightly worse than the paraboloid method, it is more robust. At very high energies, the light yield of the muon is a combination of its Cherenkov cone and spherical emission of stochastic losses along the muon track. The spherical emission is not accounted for in the likelihood calculation and hence, the likelihood landscape can show artifacts that result in a failed paraboloid fit, that is, no maximum was found by the sampling method, but a saddle point. For such events that occur at $\sim 10\%$ at the very highest energies, the bootstrapping result performs better than the saddle point of the paraboloid estimate.[29] Consequently, for the uncertainty estimation, paraboloid is used as baseline, and if a saddle point is found, the bootstrapping method is used as fallback.

Lastly, the uncertainty estimations are calibrated using Monte Carlo simulation. The reason is that the uncertainty reconstruction is not giving the correct estimate, but a systematically *pulled* value. This is on the one hand expected at the low energy end, because not the neutrino but the muon track is reconstructed and for low energies, the kinematic angle becomes a significant effect adding a random smearing on top of the reconstruction uncertainty. Nevertheless, at

[28] Ibid.

[29] Huber, "Sensitivity Studies for Blazar Stacking Searches with the IceCube Neutrino Observatory".

the high energies, the ratio deviates from the expectation as well and the estimated uncertainty is smaller than the true one, as shown in Figure 6.13. This can arise when the assumption of Wilks' theorem does not hold in the analysis of the likelihood landscape, for instance. The discrepancy is corrected for using a pull correction

$$\sigma_i \to \rho\left(\log_{10}\hat{E}\right)\sigma_i = 1.1774 \times \left.\frac{\Delta\Psi}{\sigma}\right|_{50\%}\left(\log_{10}\hat{E}\right)\sigma_i \tag{6.5}$$

for each event i with reconstructed energy $\hat{E}$ by a correction function ρ ("pull correction") calibrated depending on the energy proxy. The factor of 1.1774 arises due to the correction being made on the median of $\Delta\Psi$, but using σ as *standard deviation* of a Gaussian distribution as implemented in Eq. (5.6). In a two dimensional radial Gaussian distribution[30], the median and standard deviation are connected by this factor. From Figure 6.13, it is evident that the *combined* uncertainty estimate of paraboloid with falling back to bootstrapping as mentioned before does not deviate as strongly as only using *SplineMPE* paraboloid at the high energies. Hence, this function is used to correct the final event sample discussed in this section to obtain an estimate closer to the true uncertainty given by the Monte Carlo simulation.

[30] For small standard deviations $\sigma < 5°$, the curvature of the sphere is negligible.

7 IceCube searches for steady neutrino emission

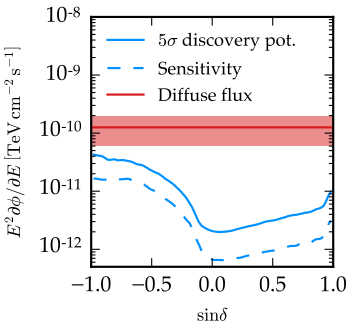

Figure 7.1: Sensitivity and discovery potential (5σ) of previous analysis for an E^{-2} flux (Aartsen, "Lowering IceCube's Energy Threshold for Point Source Searches in the Southern Sky"). The diffuse astrophysical neutrino flux integrated over the full sky is shown as comparison.

THE SENSITIVITY TO NEUTRINO EMISSION by point like objects continues to improve with the addition of new data. In this thesis, more than 300 000 events are added using three additional years of detector livetime (2012-2015). This extends the previous analysis using four years of through-going tracks events[1] that uses the first year of IceCube operation using the completed detector (IC86), and the previous partial detector configurations IC40, IC59, and IC79.[2] In the southern sky, the search was extended using starting tracks selected in three years (2010-2013) that enables the search of neutrino searches below PeV energies in this region.[3] In all previous searches, no significant evidence for sources of astrophysical neutrinos was found by IceCube or other experiments.[4] Figure 7.1 shows IceCube's sensitivity and discovery potential for a time-integrated point-like muon neutrino flux in the previous analysis, compared to the integrated neutrino signal observed in IceCube.[5]

Stacking searches of promising source candidates like blazars,[6] anisotropies of the arrival directions,[7] or time-dependent neutrino emission from point-like objects[8] also did not reveal any hint regarding the sources of neutrinos.

In this section, the results of searches for time-integrated point like emission of neutrinos are discussed.[9] In this thesis, the livetime of the data sample is largely increased[10].

7.1 Performance of IceCube

When estimating the performance of an event sample regarding the sensitivity to a faint point-like neutrino source, three key figures give insight into the capabilities:

The effective area determines the amount of events to expect from a source with a specific neutrino spectral energy density, according to Eq. (4.10).

The background rate adds noise on top of the signal. For large backgrounds, a faint signal can be buried under the random fluctuations, diminishing the sensitivity.

[1] Aartsen, "Searches for Extended and Point-like Neutrino Sources with Four Years of IceCube Data".
[2] Abbasi, "Time-Integrated Searches for Point-like Sources of Neutrinos with the 40-String IceCube Detector"; Aartsen, "Search for Time-independent Neutrino Emission from Astrophysical Sources with 3 yr of IceCube Data".
[3] Aartsen, "Lowering IceCube's Energy Threshold for Point Source Searches in the Southern Sky".
[4] Aartsen, "Lowering IceCube's Energy Threshold for Point Source Searches in the Southern Sky"; Adrian-Martinez, "Searches for Point-like and extended neutrino sources close to the Galactic Centre using the ANTARES neutrino Telescope".
[5] Aartsen, "Observation and Characterization of a Cosmic Muon Neutrino Flux from the Northern Hemisphere using six years of IceCube data".
[6] Glüsenkamp, "Analysis of the cumulative neutrino flux from Fermi-LAT blazar populations using 3 years of IceCube data".
[7] Aartsen, "Searches for small-scale anisotropies from neutrino point sources with three years of IceCube data".
[8] Aartsen, "Searches for Time Dependent Neutrino Sources with IceCube Data from 2008 to 2012".
[9] Aartsen, "All-sky search for time-integrated neutrino emission from astrophysical sources with 7 years of IceCube data".
[10] The event sample of the new data is explained in Section 6.

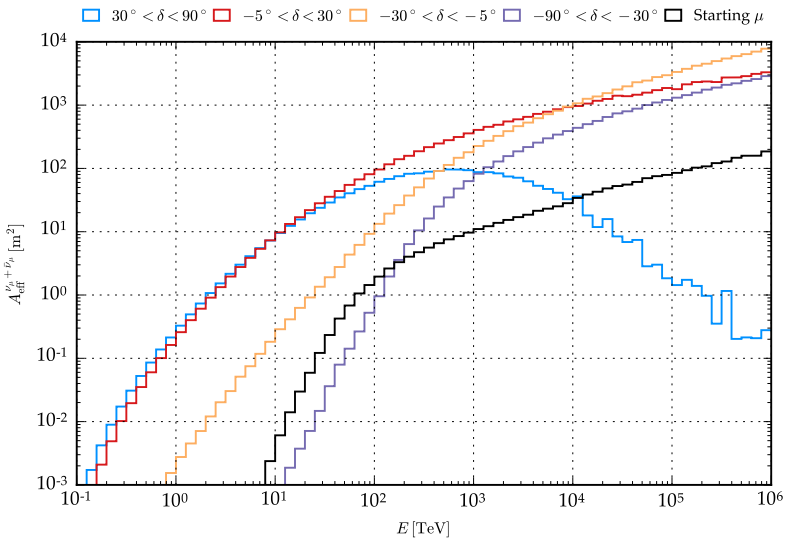

Figure 7.2: Declination dependent effective area of data taken in 2012 and later years.

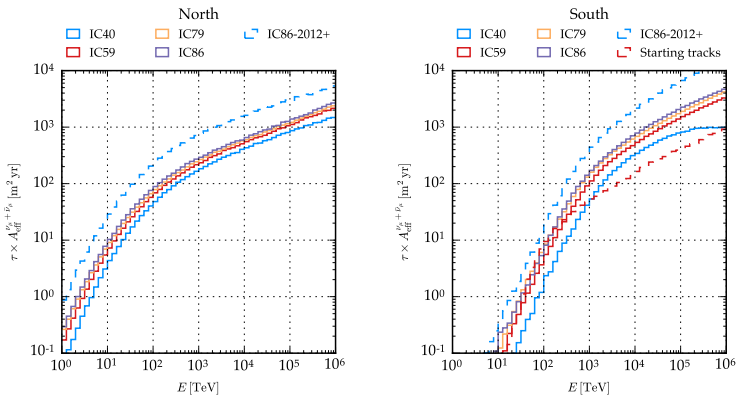

Figure 7.3: Effective area in northern and southern sky for samples used. The effective area is weighted for the total livetime of the sample, that is, the *IC86-2012+* and *Starting tracks* sample are multiplied with a factor of three and five, respectively, to account for the longer exposure. The left plot shows the northern sky, the right one the southern sky.

The reconstruction accuracy reduces the background correlating with the source position. With better reconstruction accuracy, signal neutrinos are clustered more closely, while the background rate reduces in the smaller clustering region.

In general, the *exposure time* of an sample can be considered a key figure as well. Due to the almost continuous operation of IceCube this can be factored out, as for example done in Eq. (4.10), or the exposure time can be included in the effective Area.

Figures 7.2 and 7.3 show the effective area of the added data for different declinations and in both halves of the sky for the different samples used, respectively. The effective area is largest in the northern sky, but absorption in the Earth reduces the incident neutrino flux at the detector significantly for energies above 100 TeV and declinations above 30°. In the southern sky, the effective area is much smaller due to harsh energy cuts needed to remove the atmospheric muon background sufficiently (Section 6.1). At the highest energies, no absorption is present and the effective area grows proportionally to the increase in the neutrino cross section, Eq. (4.6).

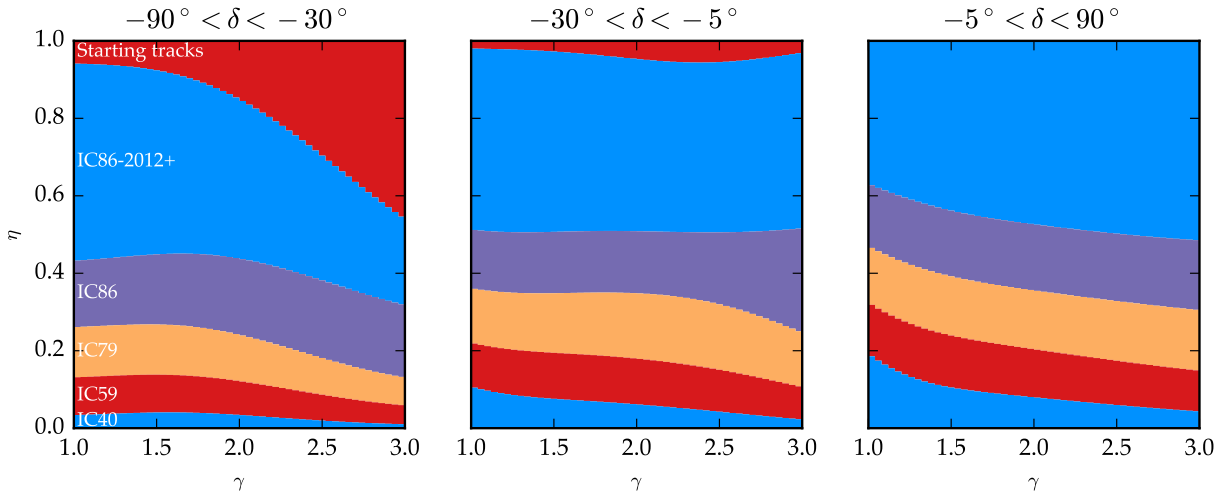

Figure 7.4: Total neutrino fraction split into each sample for different spectral indices assuming a steady emission in time. The fraction is shown for different declination regions shown above each figure.

The starting track sample restricts the detection volume to the fiducial volume of the detector. This reduces the effective area strongly compared to through-going tracks. The background rate of atmospheric muons is on the other hand strongly reduced, resulting in a higher signal-to-noise ratio. Moreover, the energy threshold is lowered and for declinations $\delta < -30°$, the event rate of starting events exceeds the through-going selection.

Figure 7.3 shows the effective area multiplied with the exposure time[11]. With increasing detector size, the effective area continuously grew in size. Thus, much of the expected neutrino signal is shared in the full detector configurations, as shown in Figure 7.4 showing the fraction η of events to appear in which sample for different neutrino energy spectra $E^{-\gamma}$. It is evident that in the down-going region, the starting track sample becomes significant for softer spectral indices, because of the lower energy threshold for starting tracks. For very hard spectra ($\gamma \to 1$) though, the larger collection volume and low backgrounds at high-energies make through-going muon samples more effective. Hence, both selections are completely complementary and give a better performance when combined.

In Table 7.1, the event statistics of all samples are listed, separated in an up-going (northern sky) and down-going (southern sky) region due to different backgrounds present. The samples are dominated by atmospheric background consisting predominantly of neutrinos and muons in the northern and southern sky, respectively. Thus, the numbers quoted in Table 7.1 are good estimates for the background rate. In the southern sky, the starting track sample has a significantly reduced background rate compared to through-going samples ($0.09\,\mathrm{d}^{-1}\,\mathrm{sr}^{-1}$ with respect to $19.8\,\mathrm{d}^{-1}\,\mathrm{sr}^{-1}$, respectively), while the effective area is of similar size in the TeV to PeV region, at the cost of a largely reduced event rate above a couple of PeV with respect to through-going track events.

[11] One year for each sample, but three and five for the new through going data and starting tracks, respectively

Table 7.1: IceCube samples used in this analysis. For each sample, characteristic features are quoted, separated in the two halves of the sky. For up-going regions, the rate of atmospheric neutrinos is quoted. The statistics of all through-going samples are shown as sum as well.

Sample	Livetime (days)	atm. ν (day^{-1})	Up-going events	Down-going events
IC40	376	40	16323	20577
IC59	348	120	48105	58906
IC79	316	180	54823	38310
IC86	333	210	67938	68302
IC86-2012+ (2012-2015)	1058	220	235602	102983
Σ	2431	—	422791	289078
starting tracks	1715	<0.03	0	961

Figure 7.5: Median angular resolution versus neutrino energy for each sample used against the energy of the primary neutrino. The samples of IC79 and later are using SplineMPE reconstructions, for IC40 and IC59, analytic functions are used.

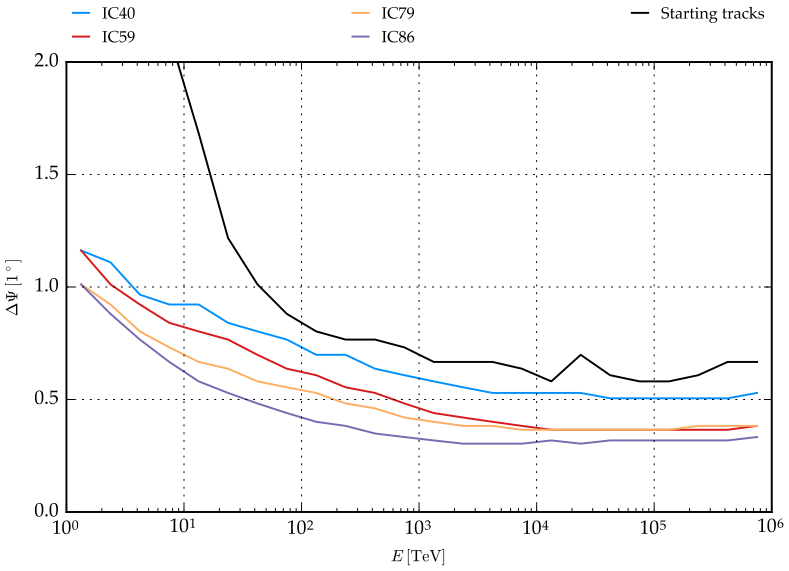

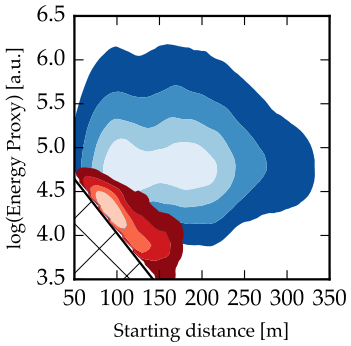

Figure 7.6: Energy and starting distance probability distributions for signal (blue, E^{-2} spectrum) and background (red). The hatched region is excluded due to a hard cut in the event selection.

[12] For through-going tracks, absorption in the Earth and a variable charge cut in the filtering (Section 4.6) affects the energy distribution in the northern and southern sky, respectively.

The median angular resolution for the different event samples is shown in Figure 7.5. With growing detector size and improvements in the reconstruction technique, the angular resolution improves. Starting tracks do not use the full length of the detector. Thus, the lever arm is smaller resulting in a worse angular resolution. The median angular resolution in the targeted energy regime is smaller than 1°, which is very suitable for clustering searches discussed here.

For starting tracks, the evaluation of the likelihood is altered from the one used for trough-going tracks (Eq. (5.6) and (5.7)). Only down-going events are used and a uniform charge cut of 1500 pe is used (Section 6.4). Thus, the distribution of events with energy is not depending on the declination[12] and is not used in the likelihood evaluation. At the same time, the vertex of the starting track gives additional discrimination power of signal and background. Atmospheric muons that passed the veto undetected will be reconstructed as starting track with a vertex close to the detector boundary. The amount of light produced by the track is correlated with the reconstructed energy. Consequently, a clear anti-correlation of energy proxy and

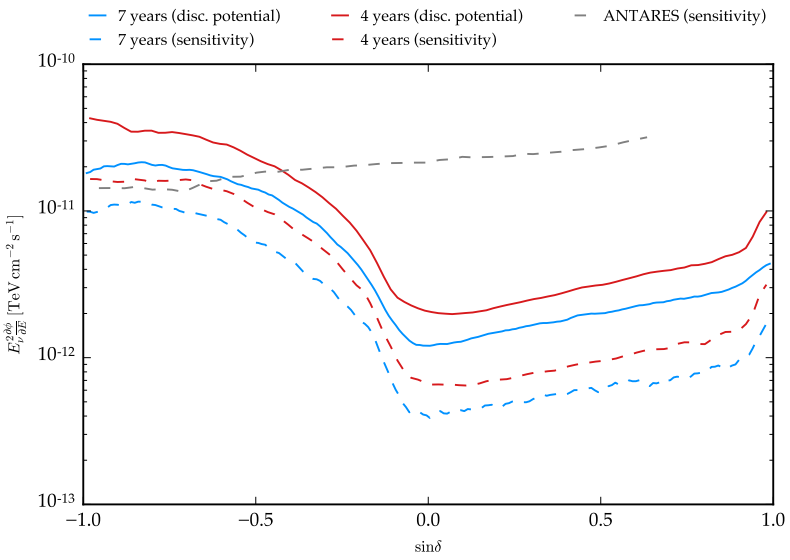

Figure 7.7: Sensitivity and discovery potential (5σ) of full seven year sample for different declinations using an unbroken $\partial\phi/\partial E \propto E^{-2}$ neutrino spectrum. The previous results of four years are shown as comparison. The sensitivity is compared to the sensitivity of Adrian-Martinez, "Searches for Point-like and extended neutrino sources close to the Galactic Centre using the ANTARES neutrino Telescope".

the distance of the point of entry of the track in IceCube to the reconstructed vertex[13] is observed. Neutrinos do not emit light prior to the interaction, hence the two variables are not correlated. Figure 7.6 shows the distributions for signal and background. Hence, using the distance in the likelihood evaluation allows to identify low energy events as signal, if the track starts deeply in the detector. The evaluation of the energy part of the likelihood is hence changed from using energy and declination of the event to energy and the starting distance,

$$\mathcal{E}\left(E_i|\sin\delta_i\right) \rightarrow \mathcal{E}\left(E_i, d_i\right) \tag{7.1}$$

for an event with energy E_i and starting distance d_i.

[13] Feintzeig, "Searches for Point-like Sources of Astrophysical Neutrinos with the IceCube Neutrino Observatory".

7.2 Sensitivity to steady neutrino emission

Using the full seven years of data available with 2431 days of detector livetime and 408 777 selected through-going muon tracks in the northern sky, IceCube is now sensitive to steady neutrino emission of time-independent neutrinos fluxes of less than $E^2\partial\phi/\partial E < 1 \times 10^{-12}\,\mathrm{TeV\,cm^{-2}\,s^{-1}}$ for all the declination ranges. Figure 7.7 shows the sensitivity and 5σ discovery potential. Compared to the results of four years, the flux limits are lowered by 50% due to the increased exposure. In the southern sky, 303 092 muon tracks are selected in the same time scale with an addition of 961 starting tracks in 1715 days. Sensitivities and discovery potential for very high energetic E^{-1} and softer E^{-3} spectra are shown in Figures C.1 and C.2. In the southern sky, the sensitivity for E^{-2} fluxes now surpasses the one of experiments located in the northern hemisphere.[14] These experiments test different energy scales that are in the TeV region compared to the

[14] Adrian-Martinez, "Searches for Point-like and extended neutrino sources close to the Galactic Centre using the ANTARES neutrino Telescope".

PeV region tested with IceCube. The results are thus complementary and were tested for clustering in combined analyses with the first three years of IceCube exposure.[15]

The neutrino energy range that is tested by IceCube can be seen in more detail using 5σ discovery potentials binned differentially in energy. Figure 7.8 shows the discovery potential for three different declinations using energy bins with half-decade width. For each bin, only neutrinos in this energy range are injected as a point source, using an E^{-2} spectrum within the energy range. The best overall performance of IceCube is achieved at the horizon region. There, atmospheric muon background is efficiently removed by the Earth matter and a pure neutrino sample is obtained. Furthermore, no absorption of neutrinos is present at the horizon and the southern sky, allowing IceCube to detect neutrinos in the PeV region and above. Inclined up-going events with declinations $\delta > 30^\circ$ are absorbed, reducing the sensitivity above 100 TeV. In the southern sky, the performance is worse due to large backgrounds, resulting in a much higher energy threshold of 100 TeV and higher flux threshold in general. The addition of starting tracks results in a discovery potential that is improved by a factor of 10 compared to only using starting tracks at 100 TeV, hence significantly reducing the energy threshold from PeV down to energies of 100 TeV.

[15] Adrian-Martinez, "First combined search for neutrino point-sources in the Southern Hemisphere with the ANTARES and IceCube neutrino telescopes".

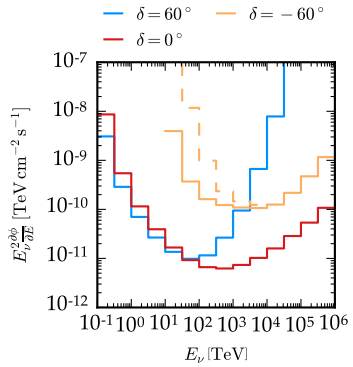

Figure 7.8: Differential discovery potential (5σ) with respect to neutrino energy. The binning uses half-decade binning with $\partial\phi/\partial E \propto E^{-2}$ spectra within the energy range indicated by the bins. For down-going results, the dashed line shows results without using starting track events.

7.3 *Systematic uncertainties and neutrino flavors*

The analysis of clustering for neutrino point sources itself is particularly robust against systematic effects. The significance of the outcome of the statistical tests is evaluated by comparing the test to trials used by scrambling the data in time[16]. Thus, data sets close to the pure background expectation are obtained relying solely on experimental data and the outcome is not affected by detector uncertainties. For the evaluation of neutrino fluxes, signal simulation is injected at the location of the injected source. Consequently, systematic uncertainties in the simulation of the detector response affect the derived fluxes. This accounts in detail to the effective area of the detector, and the energy as well as angular reconstruction. The main systematic uncertainties considered in this work are listed in the following.

[16] Due to the Earth rotation and IceCube's location at the South Pole, time scrambling is equivalent to scrambling in right-ascension.

Light production: Uncertainties in the light yield of Cherenkov radiation produced in the detector and in the detection with the DOMs of IceCube is for example estimated using muons stopping in the detector that have a well known light yield.[17] The light yield is affected by the overall optical transparency of the ice, possible shadowing due to cables and the photon efficiency of DOMs. The uncertainty of the light yield is estimated to $\pm 10\%$.

[17] Feintzeig, "Searches for Point-like Sources of Astrophysical Neutrinos with the IceCube Neutrino Observatory".

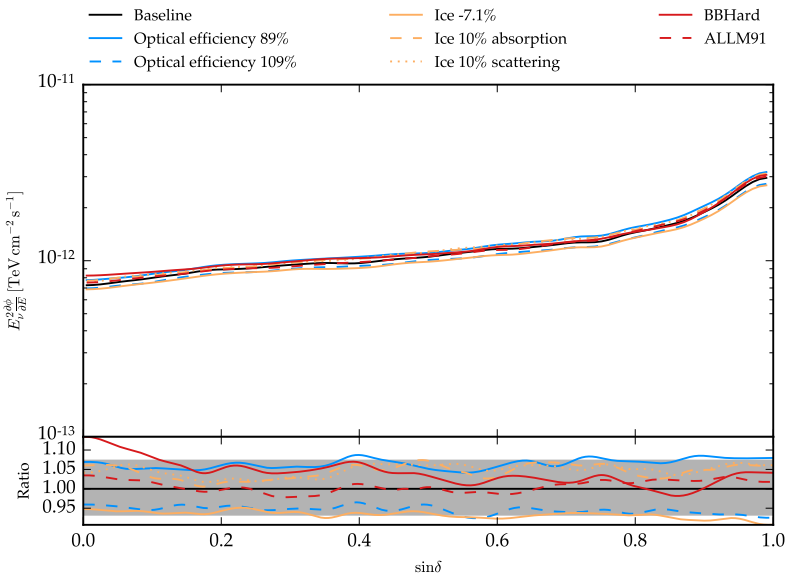

Figure 7.9: Systematic effects on neutrino flux limits. Top: Shown is the sensitivity in the up-going region (E^{-2}) for the baseline and different systematics explained in the text. Bottom: ratio of the different systematics with respect to the baseline. The shaded areas shows the mean value for the minimal and maximal deviation from the baseline. The calculation is done with data from 2012-2015.

Ice uncertainties: The propagation of light is strongly dependent on the optical properties of the ice (see Section 4.5). The model used by the ice is optimized using the LEDs of the DOMs and uncertainties are deduced from these measurements.[18] The systematic uncertainty is estimated using simulation with either the absorption or scattering length changed by $+10\%$. In addition, both quantities are changed simultaneously by -7.1%.

[18] Aartsen, "Measurement of South Pole ice transparency with the IceCube LED calibration system".

Photo-nuclear cross section: Interactions of high-energy muons with the ice is given by photo-nuclear interactions. Variations in the cross section result in different light yields for muon tracks. The uncertainty is estimated using different models for these kind of interactions abbreviated as ALLM91[19] and BBHard.[20]

[19] Abramowicz et al., "A Parametrization of sigma-T (gamma* p) above the resonance region Q**2 >= 0".

[20] E. V. Bugaev and Shlepin, "Photonuclear interaction of high-energy muons and tau leptons"; E. V. Bugaev and Shlepin, "Photonuclear interactions of super-high energy muons and tau-leptons".

Figure 7.9 shows the impact of variations in the systematic uncertainties when propagated through the entire sensitivity calculation. For each systematic, the uncertainty is in the 5% regime, except for the ALLM91 photo-nuclear cross section that shows no strong deviation from the baseline simulation. An increasing absorption, scattering or lower optical efficiency worsens the sensitivity, while improvements in the efficiency or better optical properties of the ice yield lower neutrino fluxes. Adding the uncertainties in quadrature gives a total systematic uncertainty of 11% on the calculated neutrino fluxes.

Another impact on the sensitivity is given by the incident neutrino flux. So far, only pure muon neutrino fluxes were assumed to constitute the flux detected by IceCube. The samples used here select track events which are predominantly connected to muon neutrino charged current interactions, but tracks are produced in other interactions as well. Assuming a mixed flavor ratio of neutrinos due to a

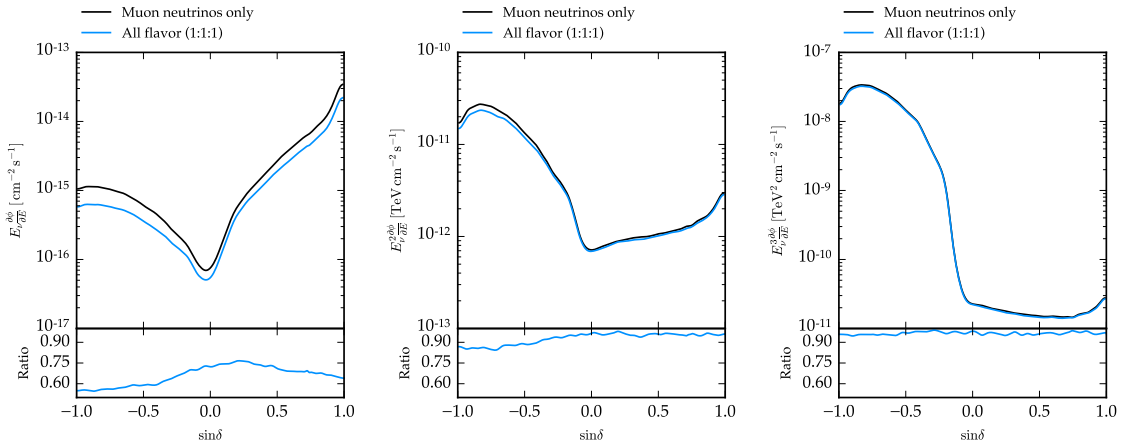

Figure 7.10: Sensitivity to full-flavor neutrino fluxes (1:1:1 flavor ratio) with respect to a muon neutrino only flux (0:1:0). This is shown for spectra of E^{-1}, E^{-2}, and E^{-3} in the left, middle, and right figure, respectively. The calculation is done with data from 2012-2015.

mixed flavor ratio, more track events are expected in IceCube, resulting in an improvement of the sensitivity. In the following, neutrino events that enhance the expected event rate at IceCube are listed.

Tau decay: Tau leptons can decay into muons with 17% branching ratio[21] ($\tau \rightarrow \mu\nu_\tau\nu_\mu$) inducing a track event. The energy of the muon is due to the three-body decay lower than for comparable muon neutrino interactions.

[21] Olive, "Review of Particle Physics".

Glashow events: In the vicinity of the resonance at $\sim 6.3\,\mathrm{PeV}$, the W^- boson produced in the resonant s-channel $\bar{\nu}_e e^-$ interaction decays to $\mu^-\bar{\nu}_e$ with $\sim$ 10.6% branching ratio[22] plus a decay to $\tau^- + \bar{\nu}_\tau$ with subsequent tau decay to tracks ($\sim$ 2%). Albeit this branching ratio being small, the overall event rate expectation is largely enhanced by the resonant cross section (Section 4.2).

[22] Ibid.

Double bangs: At very high energies, tau neutrino interactions produce a double bang structure of two separated cascades, Eq. (4.8) (Section 4.2). If the separation is large enough, such events can be well reconstructed and provide additional neutrino events suited for astronomy.

Neutrino regeneration: At very high energies, neutrinos are absorbed in the Earth (Eq. (4.7)). In tau neutrino interactions as listed above, muon neutrinos are produced in the decay of the tau lepton. Thus, the neutrino flux is regenerated at lower energies and tau neutrinos do not suffer as strongly from absorption as the muon flavor,[23] producing additional neutrinos at low energies.

[23] E. Bugaev et al., "Propagation of tau neutrinos and tau leptons through the earth and their detection in underwater / ice neutrino telescopes".

Figure 7.10 shows the neutrino flux *per neutrino flavor* assuming an incident neutrino spectrum uniform in all flavors. For spectra at medium energies (E^{-2} and E^{-3}), the flux is 5% increased compared to assuming pure muon neutrino fluxes. At PeV energies, for example the down-going region ($\sin\delta < 0$) for E^{-2} spectra), the sensitivity improves due to double-bangs and Glashow events by 10%. For even harder energies significantly producing PeV events and above,

the sensitivity in the southern sky is boosted by more than 40%. In the northern sky, a large increase in sensitivity is observable as well due to *regeneration* effects.

7.4 Significance calculation

For any given result after maximizing for the number of source events n_S and the spectral index γ, the significance of the result is estimated, quantified using the *p-value* of the result to belong to the null hypothesis (no source present). Here, Wilks' theorem of the likelihood ratio (Eq. (5.8)) to be distributed with χ^2 distribution determined by the number of degrees of freedom in between the considered hypotheses does not hold.

- The likelihood is only maximized for $n_S \geq 0$, bounding the parameter-space to over-fluctuations. Hence, any under-fluctuation will be fit to the boundary $n_S = 0$.
- The two fit parameters n_S and γ are partly degenerate. The spectral index is only relevant for signal and hence becomes important for large values of n_S, while it has no impact at all for $n_S = 0$.

Therefore, the background test statistic distribution is fitted to random trials[24] and a *chi*^{2} distribution with variable degrees of freedom is fitted to give the best agreement. This is done for two hundred different positions spaced uniformly in $\sin\delta$. Twenty declinations are shown in Figure 7.11. The test statistic distribution of background changes with declinations due tor the varying composition of the signal in the samples and the reconstructed energy distribution of the background that appears much harder in the southern sky due to muon bundles. This affects the impact of γ in the likelihood maximization procedure and thus the degrees of freedom. The final distribution of the background test statistics is given by

[24] Data sets that are scrambled in right ascension.

$$\begin{aligned}\mathcal{P}\left(\mathcal{TS}; \eta\left(\delta\right), n_{\mathrm{dof}}\left(\delta\right)\right) = &\left(1 - \eta\left(\delta\right)\right) \hat{\delta}\left(\mathcal{TS}\right) \\ &+ \eta\left(\delta\right) \times \chi^2\left(\mathcal{TS}; n_{\mathrm{dof}}\left(\delta\right)\right)\end{aligned} \tag{7.2}$$

for a fraction of η of all trials to be fitted with an over-fluctuation that are then modeled by a χ^2 function with an effective number of degrees of freedom n_{dof}. Both η and n_{dof} depend on the declination that is tested. Underfluctuations are bound to $\mathcal{TS} = 0$ with a Dirac delta-distribution $\hat{\delta}\left(x\right)$. The p-value for an observation of test statistic of α is then given by $\int_\alpha^\infty d\left(\mathcal{TS}\right)\, \mathcal{P}\left(\mathcal{TS}; \eta, n_{\mathrm{dof}}\right)$. Values of $\alpha = 0$ cannot be assigned with a proper p-value due to the step in the function produced by the delta distribution in Eq. (7.2) and assigned to be 100%. The p-value for over-fluctuations is thus given by

$$\mathrm{p}\left(\mathcal{TS}\right) = \eta \int_{\mathcal{TS}}^{\infty} dx\, \chi^2\left(x\right) . \tag{7.3}$$

Figure 7.12 shows the fraction of over-fluctuations and effective number of degrees of freedom for different declinations. The degrees of freedom are varying in between $\sim$ 1.2 to $\sim$ 1.8 with large

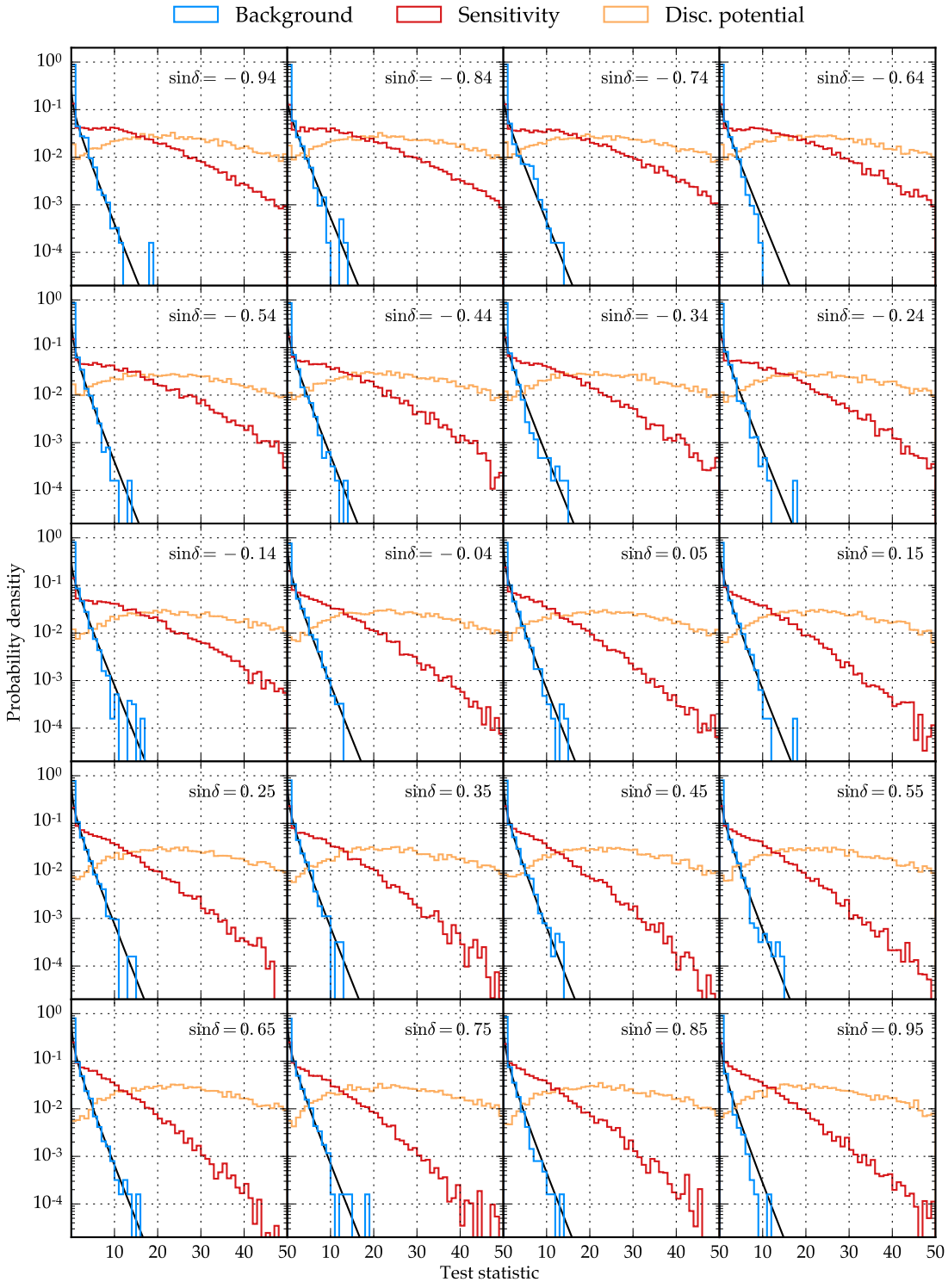

Figure 7.11: Test statistic distributions at different declinations δ shown for background trials and with injected signal. The background is modeled with a χ^2 function. Signal is injected with E^{-2} spectra and corresponds to the sensitivity and discovery potential.

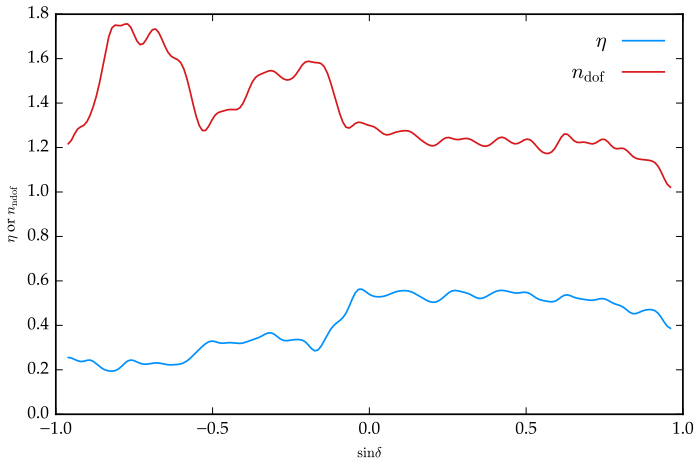

Figure 7.12: Background test statistic parameter distributions against declination.

difference in northern and southern sky, respectively. The number of over-fluctuation is $\sim 50\%$ in the northern, and 20% to 40% in the southern sky, respectively. The model in Eq. (7.3) shows good agreement with the simulated background trials in Figure 7.11. Close to the pole regions, the background distributions shows slight indications of tails that do not fall as steeply as the simulation. The modeling is still in the satisfactory region and the difference to the simulation is conservative, that is, it does not over-estimate the significance of the result. No p-values are calculated for regions less than 5° apart from the poles, that is $|\delta| > 85°$, because the scrambling of events in right ascension does not work there due to a small solid angle.

7.5 *Probing the entire sky for neutrino emission*

As a first test for clustering of neutrinos, the full sky is probed for clustering of neutrinos. This is done using a fine grid spaced isotropically on the sphere[25] and maximizing the likelihood at each point. The grid is spaced finer than the typical event resolution shown in Figure 7.5. The scan of the full sky is shown in Figure 7.13. In the southern sky, large "blobs" with increased significance are observed. These correspond to positions of starting tracks and their angular resolution.[26] Starting tracks have a higher purity and dominate the signal for softer spectra, compare Figure 7.4. Thus, in the vicinity of starting tracks, the likelihood tends to identify clustering at very soft spectra creating this "blob" structure.

For both northern and southern sky, the most significant points are selected given their pre-trial p-values. Information about these two *hot spots* is listed in Table 7.2. The pre trial p-value for both sources is very small with 1.8×10^{-6} and 9.3×10^{-7} for the northern and southern hot spot, respectively. Figure 7.14 shows the pre-trial p-value landscape around the two hot spots, overlaid with the events detected in seven years. The likelihood maxima found are very sharp

Table 7.2: Fit results of most significant spots in full sky scan. In addition to the position and fit-values, the pre-trial p-value and trial corrected p-value are shown. Upper limit fluxes for three power-law spectra $\Phi(\gamma)$ are listed.

Value	North	South
α	32.2°	174.8°
δ	61.9°	−39.3°
n_S	32.6	15.4
γ	2.8	2.9
p-value	1.8×10^{-6}	9.3×10^{-7}
Trials	29.2%	16.6%
$\Phi(1)$	2.6×10^{-14}	1.0×10^{-15}
$\Phi(2)$	4.5×10^{-12}	2.9×10^{-11}
$\Phi(3)$	5.1×10^{-11}	1.3×10^{-8}

— Note: Upper limit fluxes $\Phi(\gamma) = E^{\gamma}\partial\phi/\partial E$ are in units of $\mathrm{TeV}^{\gamma-1}\,\mathrm{cm}^{-2}\,\mathrm{s}^{-1}$.

[25] Gorski et al., "HEALPix - A Framework for high resolution discretization, and fast analysis of data distributed on the sphere".

[26] Aartsen, "Lowering IceCube's Energy Threshold for Point Source Searches in the Southern Sky".

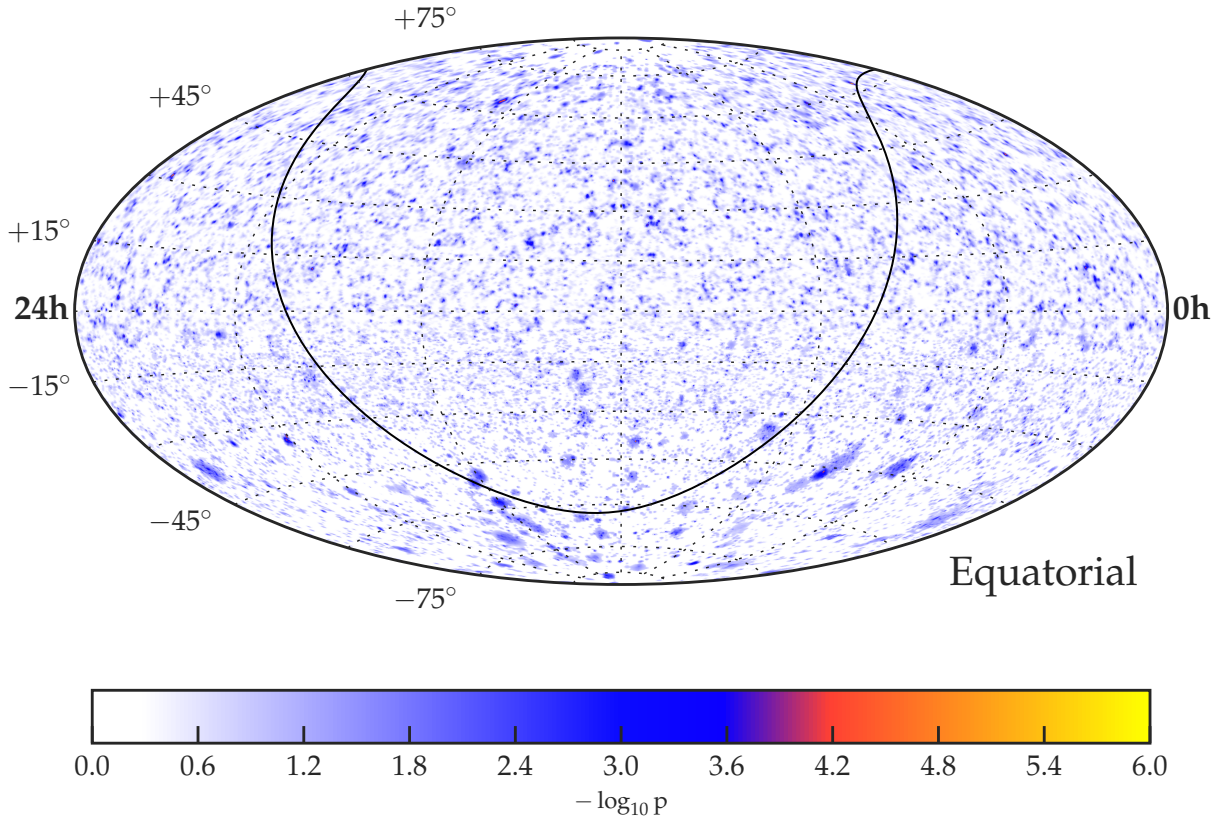

Figure 7.13: Full sky significance map of clustering analysis in equatorial coordinates (J2000). Shown is the negative logarithm of the pre-trial p-value $-\log_{10} p$. The Galactic plane is indicated as black line.

and are significant to sub-degree level using Wilks' theorem for two degrees of freedom in the maximization procedure. In the southern sky, one starting event is found close by the hot spot, increasing the significance in a wide range due to the higher purity of starting tracks with respect to through-going tracks in the down-going region.

To calculate the true significance of this outcome for choosing this position out of the whole full sky shown in Figure 7.13, these values have to be trial corrected for trials which is done by repeating the full sky scan with event samples randomized in event time resulting in purely isotropic background maps generated from experimental data. The pre-trial p-values for these maps is shown in Figure 7.15. The trials are modeled by a trial correction function according to Eq. (5.17). Due to the good angular resolution of muon tracks, each half of the sky can be modeled to be an observation of $N \sim 190\,000$ independent observations. Thus, the most significant spot in a background map has the expectation of a pre-trial significance of $-\log_{10} p = -\log_{10}(N) = 5.27$ resulting from background fluctuations in the sky. Correcting the observed hot spots for this fact yields the final significance for the two hot spots of 29.2% and 16.6%,

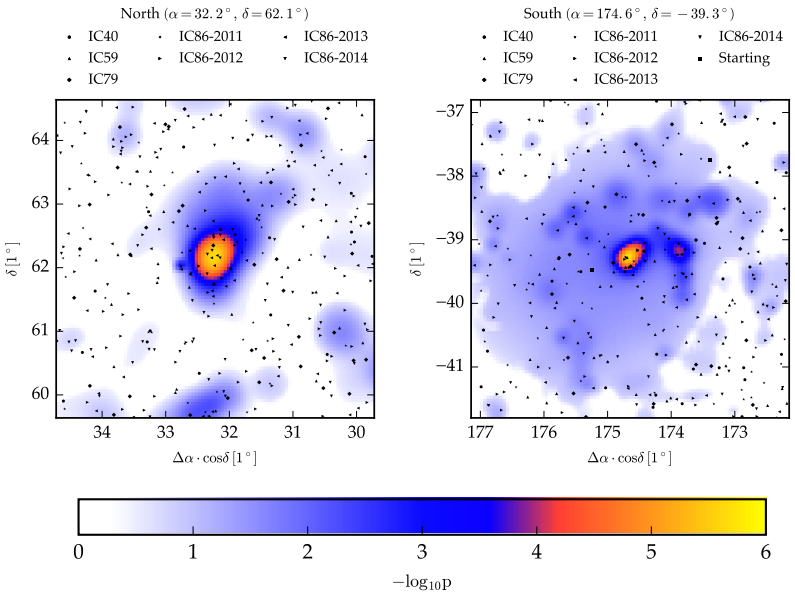

Figure 7.14: Zoom into most significant spots in full sky scan. Left and right figure show the northern and southern sky spots, respectively. The right ascension value is corrected for the curvature that gets stronger in the pole region.

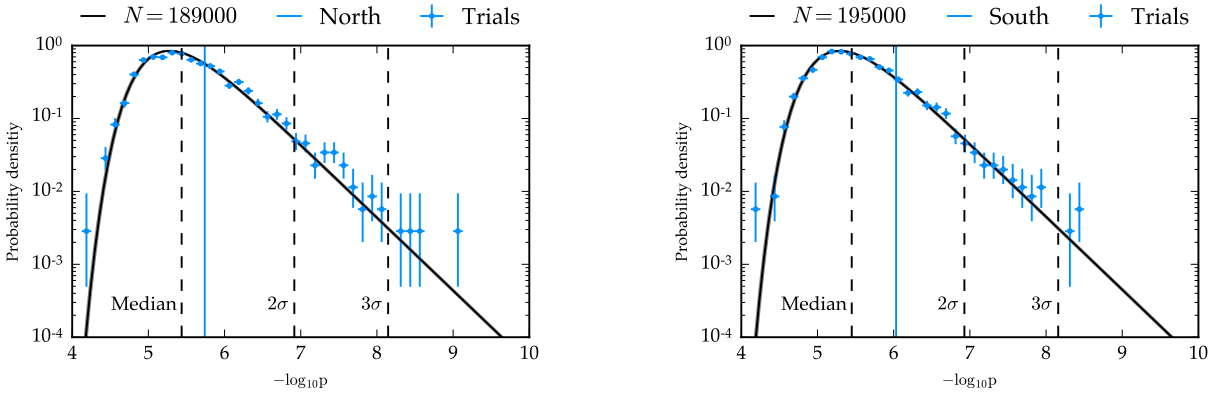

Figure 7.15: Trial correction of most significant spots found. The northern (left) and southern spot (right) are trial corrected with an analytic function that corresponds to $N \approx 1.9 \times 10^5$ independent observations. The thresholds for a detection at 2σ and 3σ are shown.

respectively (Table 7.2). This is in very good agreement with expectations of background fluctuations, hence, no single neutrino source is identified in the scan of the full sky with seven years of IceCube.

7.6 Source candidates

When probing the full sky for emission of neutrinos, large trial factor suppress the potential of the source. Hence, in Section 5.4, lists of gamma ray counterparts were introduced to be probed for neutrino emission in addition to the unbiased scan of the full sky. This way, the trial factor reduces largely.

Table 7.4 and 7.5 show the fit results of all sources in the first source list for extragalactic and Galactic sources, respectively[27]. The most significant sources in northern and southern sky are both blazars, that is, active galactic nuclei with the jet pointing towards the Earth and hence extragalactic objects. The object deviating most from background expectation in the northern sky is 1ES 1959+650, a BL Lac fitted with $n_S = 15.4$ and spectral index $\gamma = 3.1$. The expectation

[27] The tables are listed at the end of this chapter.

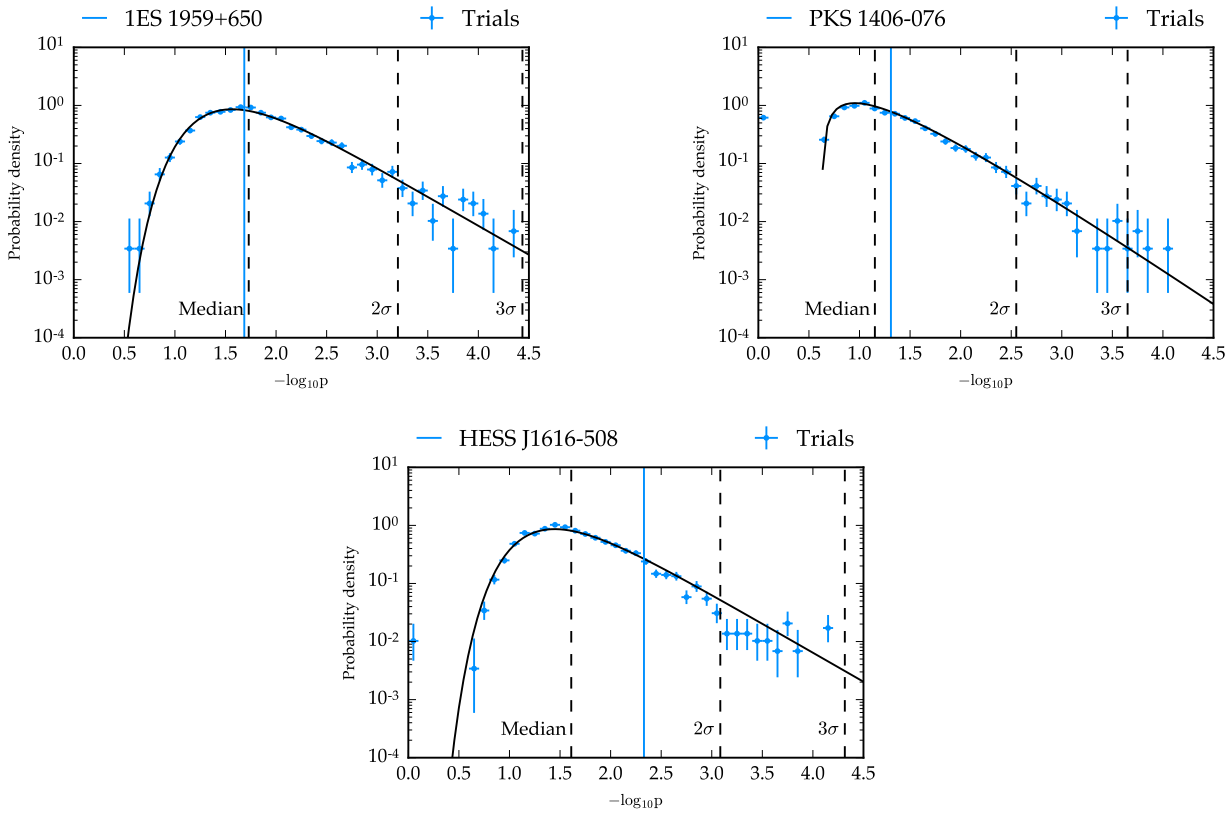

Figure 7.16: Trial correction of most significant objects in the two lists. The correction in the first list is done separately for northern and southern sky (top left and top right, respectively). The second source list is shown in the bottom figure. The trial correction is done using background trials and modeled with an analytic function. Trials with only null-results ($n_S = 0$) for all objects in the southern sky are shown in the far left bin of the histogram.

of background events within 1° around the source location is 42.8 events. The p-value of the observation is 1.8% before correcting for trials given by the number of objects in the list. The flat spectrum radio quasar PKS 1406-076 is the most significant object of the ten sources in the first list that are located in the southern sky. The fit value results in $n_S = 7.3$ at spectral index $\gamma = 2.6$ over an expectation of 50.5 background events, resulting in a pre-trial p-value of 5.3%. The post trial significance for 1ES 1959+650 and PKS 1406-076 are shown in Figure 7.16 and correspond to 54.1% and 37.1%, respectively. This is in agreement with a pure background assumption.

The most significant source in the second source list is HESS J1616-508 at a pre-trial p-value of 0.22%. The post trial significance of the entire list with 29 objects (see Table 7.6 and 7.7 at the end of this chapter for all extragalactic and Galactic objects results, respectively) is 9.3%, hence, no significant excess over background expectation. The object HESS J1616-508 is fitted with a spectral index of $\gamma = 4$ at the boundary of the parameter space, indicating a very soft fit. This is due to the fact that close to this PWN object, a starting track was observed that provides most of the significance to the final result. There is no strong clustering observed in the through-going samples. Such a result can be explained with soft spectral indices, where most of the signal events are expected for starting events for very high inclined objects in the southern sky, compare Figure 7.4. Thus, the fit

prefers soft spectral index where only starting track events are expected. In all source lists, no significant evidence for steady neutrino emission was found and upper limits are calculated for $E^2\partial\phi/\partial E$ spectra, listed in the tables. The p-value landscape around all the objects listed are shown in Figure C.5 to Figure C.17 in Section C.2.

7.7 Populations of sources

The results for searches of weaker populations of sources are listed in Table 7.3. In the northern sky, the number of hot spots above threshold $-\log_{10} p_{min}$ is shown in Figure 7.17. The biggest excess over background expectation is given for a threshold of $-\log_{10} p_{min} \geq 3.35$ with 72 hot spots above an expectation of 56.7 by random fluctuations. The Poissonian p-value of this happening at this threshold is 2.8%, and after accounting for the trial factor due to scanning the threshold above values of $-\log_{10} p > 3$, the final p-value yields 25%.

The results for the southern sky are shown in Figure 7.18. The threshold of $-\log_{10} p_{min} \geq 4.87$ is higher than in the northern sky. Above this threshold, seven hot spots are observed above an expectation of only 2.1, resulting in a Poissonian p-value of $\mathcal{P} = 0.55\%$. After trial correction, this reduces to 8.3%.

Lastly, the region of the sky coinciding with the Galactic plane $\pm 15^\circ$ was tested separately for an excess. The most significant spot in the northern sky is the only spot found above, marking an excess above the background expectation of 0.04 spots. After trial correction, this is compatible with background at 26%. Thus, no population of weak sources was found in the northern or southern sky in the full-sky map of Figure 7.13, nor coinciding with the Galactic Plane.

Table 7.3: Results of population searches

Parameter	North	South
Observation	72	7
Expectation	56.7	2.1
$-\log_{10} p_{min}$	3.35	4.87
$\mathcal{P}$	0.028	0.0055
Significance	0.25	0.083

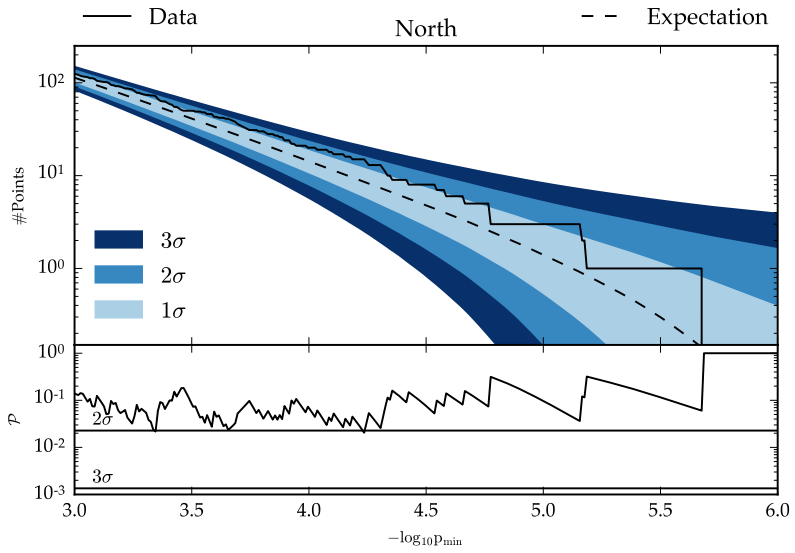

Figure 7.17: Population of hot spots in northern sky for different thresholds in pre-trial clustering significance. The raw number count of spots over background expectation is shown in the top and converted to the corresponding p-value $\mathcal{P}$ the number of spots above the background expectation.

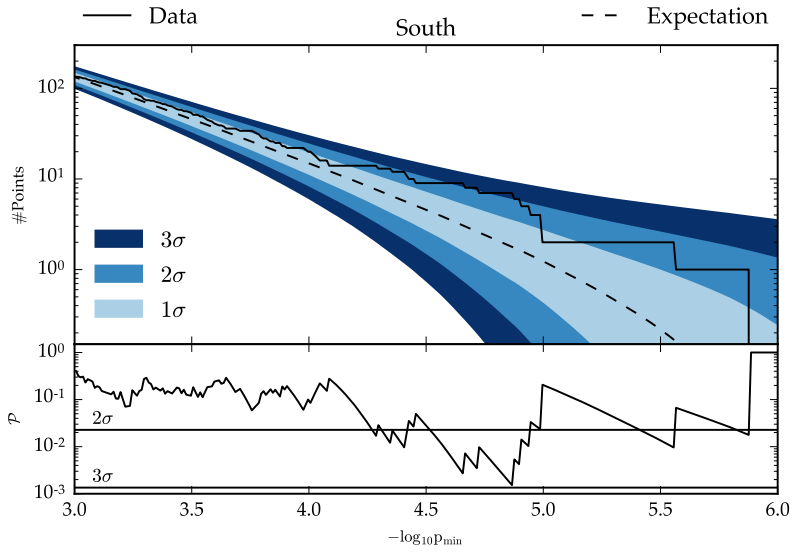

Figure 7.18: Population of hot spots in southern sky for different thresholds in pre-trial clustering significance. Same plot as for northern sky results.

Identifier	α	δ	p	n_S	γ	B_{1°	Φ
	1°	1°					
BL Lac							
PKS 0537-441	84.71	-44.09	—	0.0	—	45.7	9.79
PKS 2155-304	329.72	-30.23	—	0.0	—	52.6	6.07
PKS 0235+164	39.66	16.62	0.12	16.2	3.4	72.0	0.94
1ES 0229+200	38.20	20.29	0.20	9.5	3.5	66.6	0.84
W Comae	185.38	28.23	—	0.0	—	60.8	0.62
Mrk 421	166.11	38.21	0.32	2.7	1.8	53.1	0.94
Mrk 501	253.47	39.76	0.18	10.5	4.0	52.0	1.15
BL Lac	330.68	42.28	—	0.0	—	50.4	0.63
H 1426+428	217.14	42.67	—	0.0	—	50.9	0.70
3C66A	35.67	43.04	—	0.0	—	50.9	0.70
1ES 2344+514	356.77	51.70	—	0.0	—	46.3	0.81
1ES 1959+650	300.00	65.15	0.018	15.4	3.1	42.8	2.36
S5 0716+71	110.47	71.34	—	0.0	—	38.4	1.34
Flat spectrum radio quasar							
PKS 1454-354	224.36	-35.65	—	0.0	—	49.1	7.99
PKS 1622-297	246.53	-29.86	0.11	3.8	2.3	52.7	8.20
QSO 1730-130	263.26	-13.08	—	0.0	—	49.8	2.18
PKS 1406-076	212.24	-7.87	0.053	7.3	2.6	50.5	1.65
QSO 2022-077	306.42	-7.64	—	0.0	—	50.5	0.99
3C279	194.05	-5.79	0.42	0.5	2.0	54.3	0.63
3C 273	187.28	2.05	0.25	7.7	3.2	76.4	0.59
PKS 1502+106	226.10	10.49	0.38	3.1	2.7	73.7	0.59
PKS 0528+134	82.73	13.53	0.44	2.7	4.0	73.0	0.60
3C 454.3	343.49	16.15	0.12	4.1	2.0	72.3	0.93
4C 38.41	248.81	38.13	0.12	6.3	2.4	53.2	1.31
Starburst radio galaxy							
Cen A	201.37	-43.02	0.21	0.5	1.2	46.2	10.41
M87	187.71	12.39	—	0.0	—	73.2	0.48
3C 123.0	69.27	29.67	—	0.0	—	59.5	0.57
Cyg A	299.87	40.73	0.068	2.1	1.4	51.1	1.50
NGC 1275	49.95	41.51	—	0.0	—	50.6	0.71
M82	148.97	69.68	—	0.0	—	39.7	1.09

Table 7.4: Results of the likelihood maximisation for extragalactic objects in the first list. For each source, the equatorial coordinates and the p-value (p) is listed with the number of clustering events n_S and spectral index γ. For events without clustering, no p-value and spectral index is reported. The number of background events B_{1° within a window of 1° is listed as well. For each source, the 90% upper limit for an E^{-2} flux Φ is given in units of $10^{-12}\,\mathrm{TeV\,cm^{-2}\,s^{-1}}$.

Identifier	α 1°	δ 1°	p	n_S	γ	$B_{1°}$	Φ
Galactic center							
Sgr A*	266.42	-29.01	—	0.0	—	52.2	6.08
High mass x-ray binary / microquasar							
SS433	287.96	4.98	0.40	4.1	4.0	75.8	0.47
HESS J0632+057	98.24	5.81	0.10	13.6	3.6	75.4	0.77
Cyg X-1	299.59	35.20	0.31	4.5	4.0	54.4	0.90
Cyg X-3	308.11	40.96	0.077	12.8	4.0	51.3	1.53
LSI 303	40.13	61.23	—	0.0	—	43.8	0.79
Milagro not identified							
MGRO J1908+06	286.98	6.27	0.025	4.5	2.0	74.9	0.99
Pulsar wind nebula							
Geminga	98.48	17.77	—	0.0	—	69.3	0.49
Crab Nebula	83.63	22.01	0.34	6.1	3.8	67.0	0.68
MGRO J2019+37	305.22	36.83	0.23	7.8	4.0	53.2	1.04
Star formation region							
Cyg OB2	308.30	41.32	0.26	5.9	4.0	50.6	0.99
Supernova remnant							
IC443	94.21	22.50	0.22	8.1	4.0	66.0	0.83
Cas A	350.81	58.81	0.14	8.1	4.0	44.5	1.49
TYCHO	6.36	64.18	0.27	4.6	3.4	42.4	1.23

Table 7.5: Galactic object fit results gathered in first list. The information shown is similar to previous tables.

Identifier	α 1°	δ 1°	p	n_S	γ	$B_{1°}$	Φ
BL Lac							
PKS 2005-489	302.37	-48.82	0.071	0.9	1.0	44.7	13.45
PKS 0426-380	67.17	-37.93	—	0.0	—	47.2	8.93
PKS 0548-322	87.67	-32.27	—	0.0	—	51.2	6.79
H 2356-309	359.78	-30.63	—	0.0	—	52.1	6.18
1ES 1101-232	165.91	-23.49	—	0.0	—	52.6	4.64
1ES 0347-121	57.35	-11.99	0.21	1.4	2.4	52.2	2.16
HESS J1632-478	248.04	-47.82	0.16	1.5	2.7	44.7	10.79
Vela X	128.75	-45.60	0.13	2.7	2.4	45.8	10.79
HESS J1837-069	279.41	-6.95	—	0.0	—	48.1	0.89
Flat spectrum radio quasar							
PKS 0454-234	74.27	-23.43	—	0.0	—	52.8	4.58
PKS 0727-11	112.58	-11.70	0.20	2.7	3.7	52.0	2.30
Seyfert galaxy							
ESO 139-G12	264.41	-59.94	—	0.0	—	44.0	11.28

Table 7.6: Extragalactic object fit results gathered in second list. The information shown is similar to previous tables.

Identifier	α 1°	δ 1°	p	n_S	γ	B_{1°	Φ
HESS not identified							
HESS J1507-622	226.72	-62.34	—	0.0	—	43.4	11.02
HESS J1503-582	226.46	-58.74	—	0.0	—	45.5	11.79
HESS J1741-302	265.25	-30.20	0.19	2.1	4.0	52.6	7.33
HESS J1834-087	278.69	-8.76	0.21	1.2	3.7	49.5	1.47
Pulsar wind nebula							
HESS J1356-645	209.00	-64.50	—	0.0	—	42.4	10.90
PSR B1259-63	197.55	-63.52	0.21	1.3	2.0	42.7	11.43
HESS J1303-631	195.74	-63.20	0.076	4.5	2.3	42.3	13.61
MSH 15-52	228.53	-59.16	—	0.0	—	44.9	11.28
HESS J1023-575	155.83	-57.76	—	0.0	—	46.4	11.79
HESS J1616-508	243.78	-51.40	0.0022	2.4	4.0	45.0	19.37
Supernova remnant							
RCW 86	220.68	-62.48	—	0.0	—	43.1	11.02
RX J0852.0-4622	133.00	-46.37	—	0.0	—	45.6	10.40
RX J1713.7-3946	258.25	-39.75	—	0.0	—	45.5	9.22
W28	270.43	-23.34	—	0.0	—	52.9	4.58
High mass x-ray binary / microquasar							
Cir X-1	230.17	-57.17	—	0.0	—	46.3	11.03
GX 339-4	255.70	-48.79	0.15	2.6	2.2	44.8	11.29
LS 5039	276.56	-14.83	0.26	2.1	4.0	52.3	2.72

Table 7.7: Galactic object fit results gathered in second list. The information shown is similar to previous tables.

8 Implications regarding steady emission of neutrinos

With seven years of integrated livetime, no clear evidence in favor of time-independent emission of neutrinos was found in IceCube. Three searches for strong neutrino sources anywhere in the sky, sources in coincidence with known high energy gamma ray sources, and populations of multiple weak sources are in agreement with expectations from pure background. Thus, upper limits (90% confidence level) are calculated for the searches performed and discussed in terms of their implications regarding neutrino and cosmic ray acceleration of potential sources.

8.1 Diffuse neutrino signal

The results of the searches for time-integrated neutrino emission using seven years of IceCube livetime are summarized in Figure 8.1, using an unbroken $\partial\phi/\partial E \propto E^{-2}$ spectrum. Similar plots for E^{-1} and E^{-3} spectra are shown in Figures C.3 and C.4, respectively. In addition to the pre-trial sensitivity and 5σ discovery potential[1], the 90% upper limits of all objects listed in Tables 7.4 and 7.5, as well as Tables 7.6 and 7.7 for the two source lists are shown at their corresponding declination value, respectively. These upper limits are not affected by a trial factor because the upper limit is independent of the p-value of the result. Thus, objects that did not show any clustering match the sensitivity of the analysis of seven years.

[1] Shown in Figure 7.7 as well.

The largest upper limits are given by the two hot spots for both northern and southern sky, respectively, because they are selected from the full sky (Figure 7.13) as largest clustering positions observed in the data. Any possible direction in the sky, which is neither selected as hot spot nor listed in the source catalogs does not have an upper limit calculated. Instead, from the observation of the hot spots, a *post-trial* upper limit of the strongest emission in the sky is calculated for all declinations. This is done using the pre-trial p-values for the two hot spots listed in Table 7.2 and converting this to a declination dependent test statistic $\mathcal{TS}$ using the inverse function of Eq. (7.3). This test statistic is used to calculate an upper limit at the corresponding declination. Thus, an upper limit of the trial

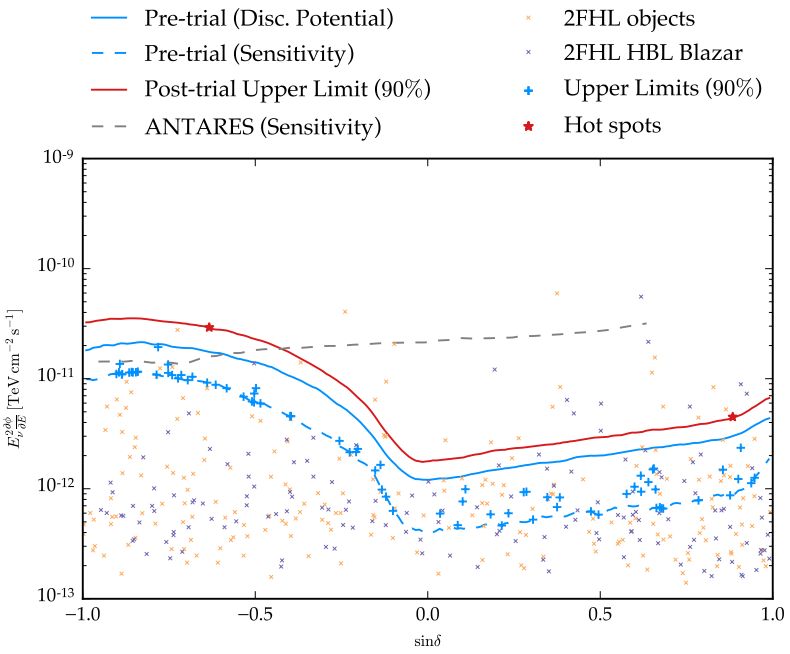

Figure 8.1: Upper limits of seven year search versus declination using an unbroken E^{-2} neutrino spectrum (muon neutrinos only). The upper limits of the two source catalogs are compared to the pre-trial sensitivity and discovery potential. The upper limit of the full-sky scan with the positions of the two hot spots (stars) is shown as post-trial upper limit. Gamma ray fluxes in the energy range from 50 GeV to 2 TeV are shown for objects of the 2FHL catalog, separated in HBL Blazars and the remaining objects. Ackermann, "2FHL: The Second Catalog of Hard Fermi-LAT Sources".

corrected full sky is obtained, as shown in Figure 8.1. Any neutrino point source with a flux that exceeds this limit is dis-favored by IceCube because it would have produced clustering more significant than the two hot spots observed in the data[2].

The post-trial upper limit can be used to test the origin of the diffuse neutrino flux observed in IceCube.[3] The observed diffuse flux is of the order of $\sim 1 \times 10^{-11}\,\mathrm{TeV\,cm^{-2}\,s^{-1}\,sr^{-1}}$ with a spectral index of $\sim E^{-2}$. The flux observed is consistent with an isotropic emission that can be constituted of different components

$$\Phi_\Sigma \times \Delta\Omega = \Phi_\Omega \times \Delta\Omega + \Phi_{\mathrm{PS}}^{\mathrm{resolved}} + \Phi_{\mathrm{PS}}^{\mathrm{unresolved}} \tag{8.1}$$

that consist of truly diffuse or extended fluxes Φ_Ω and the flux of (un)resolvable point-like objects $\Phi_{\mathrm{PS}}^{\mathrm{x}}$. Diffuse emission can be due to the Galactic Plane that produces neutrinos in interactions of incident cosmic rays[4] or connected to the observed diffuse emission of gamma rays.[5] The flux of point sources (PS) can be resolvable as close-by strong sources or unresolvable due to numerous weak sources at large distance. No neutrino sources have been identified, but, the upper limits shown in Figure 8.1 can constrain the amount of point sources to the total observed quasi diffuse flux Φ_Σ in Eq. (8.1).

In the northern sky, where IceCube is most sensitive to emission of neutrinos over a large range of energies, the integrated diffuse flux $\sim 6.3 \times 10^{-11}\,\mathrm{TeV\,cm^{-2}\,s^{-1}\,sr^{-1}}$ is a factor of ~ 20 above the post-trial upper limits. In Figure 8.1, *Fermi*-LAT detected objects with energies above 50 GeV are shown as listed in the *2FHL* catalog[6] with a visible trend in the source count distribution versus luminosity. The flux of neutrinos produced by such objects is expected to follow similar distributions and constitute a part of the diffuse flux.[7] With

[2] This assumes that the flux is either an unbroken power-law from 100 GeV to EeV energies, or at least in the energy range where IceCube is probing the sky, as visualized in Figure 7.8.

[3] Aartsen, "The IceCube Neutrino Observatory - Contributions to ICRC 2015 Part II: Atmospheric and Astrophysical Diffuse Neutrino Searches of All Flavors"; Aartsen, "Observation and Characterization of a Cosmic Muon Neutrino Flux from the Northern Hemisphere using six years of IceCube data".

[4] Joshi, Winter, and Gupta, "How Many of the Observed Neutrino Events Can Be Described by Cosmic Ray Interactions in the Milky Way?"

[5] Murase, Ahlers, and Lacki, "Testing the Hadronuclear Origin of PeV Neutrinos Observed with IceCube".

[6] Ackermann, "2FHL: The Second Catalog of Hard Fermi-LAT Sources".

[7] Padovani, Petropoulou, et al., "A simplified view of blazars: the neutrino background".

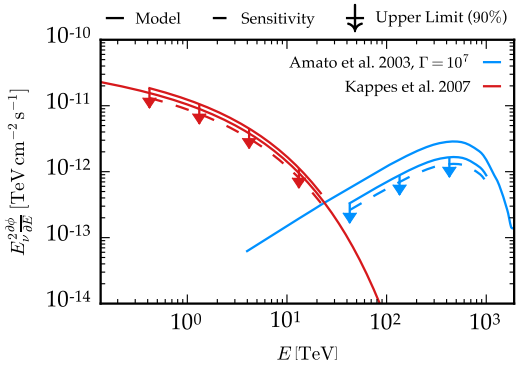

Figure 8.2: Model upper limits for Crab Nebula. Two models are shown with their neutrino SED prediction (thin line) and the corresponding upper limit (thick line). Dashed lines correspond to the sensitivity of IceCube, if no over-fluctuation was seen. The limits are shown in the energy range where most of the constraining power comes from.

the limits given by the observation of the hot-spots, the maximum neutrino flux for the strongest sources is given by IceCube. To test regarding different classes of sources, stacking methods are well suited to access lower fluxes. For example, the contribution of blazars to the astrophysical neutrino flux in the TeV region is sub-dominant.[8]

[8] Glüsenkamp, "Search for a cumulative neutrino flux from 2LAC-blazar populations using 3 years of IceCube data".

8.2 *The Crab Nebula*

The strongest steady TeV gamma ray source in the sky is the Crab Nebula, a pulsar wind nebula, connected to a supernova in 1054 AD. The source is located in the northern sky (declination $\delta = 22.01°$). At its position, an over-fluctuation of clustering is observed with $n_S = 6.1$ and spectral index $\gamma = 3.8$. The pre-trial p-value is 34% with an upper limit of $E^2\partial\phi/\partial E = 6.8 \times 10^{-13}\,\mathrm{TeV\,cm^{-2}\,s^{-1}}$, see Table 7.5.

With the observation of the bright source in gamma rays, predictions about the neutrino spectrum can be done that can be tested directly using the connection of neutrinos and gamma rays in the multi-messenger paradigm as discussed in Section 2.4. The models are tested such that the predicted neutrino spectral energy density (SED) $E^2\partial\phi/\partial E$ is used to inject neutrino events at the position of the object instead of using an unbroken and flat power-law spectrum. The Crab Nebula is tested using two different models shown as thin lines in Figure 8.2. The limits are scaled versions of the predictions and shown for the energy range in which IceCube is most sensitive to the model shown. The energy range is calculated by folding the model SED with the differential discovery potential at the position of the source, which is shown for three declinations in Figure 7.8. Thus, the energy range is obtained where most of the clustering is identified accounting for the reconstruction accuracy and possible background contamination.

The first model considered uses the connection of gamma rays to neutrinos in pion decays (Eq. (2.6)) assuming that the gamma ray spectrum is of hadronic origin.[9] The upper limit regarding this model is 20% above the prediction, hence, not constraining the model. Nevertheless, the sensitivity of IceCube is 15% below the prediction (dashed line in Figure 8.2). Therefore, IceCube is in the regime of

[9] Kappes et al., "Potential Neutrino Signals from Galactic Gamma-Ray Sources".

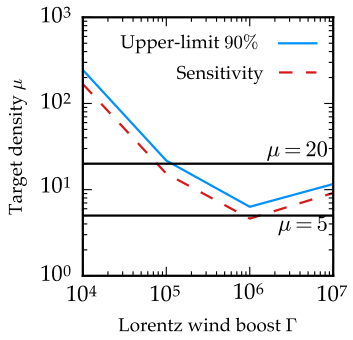

Figure 8.3: Limits on Crab Nebula target density for different Lorentz wind boost factors. The target density is calculated with μ according to Eq. (8.2).

testing fluxes of the level of the Crab Nebula with seven years of livetime and with increasing exposure, more constraining results regarding the hadronic origin of the observed gamma ray spectrum can be deduced.

The second model considered uses Monte Carlo simulation of p-p interaction in the pulsar wind nebula to calculate the produced neutrino spectrum.[10] For different values of the Lorentz boost factor Γ and the target density

$$n_t = 10\mu \frac{M_{N\odot}}{R_{\mathrm{pc}}^3}\ \mathrm{cm}^{-3} \tag{8.2}$$

of the nebula filaments with mass $M_{N\odot}$ and nebula size R_{pc}. The target density is a function of the scaling factor μ, that accounts for unknown quantities like magnetic fields in the filaments. Figure 8.2 shows the expected energy spectrum for $\Gamma = 10^7$ and $\mu = 20$ peaking at ~ 500 TeV. For lower boost factors, the peak of the spectrum moves to lower energies. Uncertainties on the target density are absorbed in the factor μ. The authors mention the allowed values of $1 < \mu < 20$ by upper limits derived.[11] A uniform mass distribution corresponds to $\mu = 5$.[12] The neutrino spectra of p-p interaction with the pulsar wind produce very hard spectra that cut off at some characteristic energy.

As shown in Figure 8.2, models with $\Gamma = 10^7$ and $\mu = 20$ are strongly constrained by IceCube with seven years of exposure. For Lorentz boosts of $\Gamma = 10^7$ down to $\Gamma = 10^5$, the spectrum peaks in the optimal region (TeV energies) regarding detection with IceCube. Hence, the upper limits on the target density are in the physical regime for Lorentz boosts for $\Gamma > 10^5$, as shown in Figure 8.3. For $\Gamma = 10^6$, a uniform mass density ($\mu = 5$) is in the sensitivity regime of IceCube. For values $\Gamma < 10^5$, the neutrino spectrum cuts off too early, suppressing IceCube's capabilities to detect neutrinos. For values below $\Gamma = 10^4$, no neutrino production due to pion decays are possible.[13]

In updated calculations for PWNe including the Crab Nebula, 13.09 neutrinos are predicted to be observed per year in IceCube.[14] The upper limits of an E^{-3} spectrum predict $\sim$ 21 events within seven years using a softer spectrum than expected for the Crab Nebula. This is much lower than the predicted event rate. Hence, the amount of processes producing neutrinos is constrained significantly by IceCube. Other PWNs considered[15] are mostly located in the southern sky and have a much weaker luminosity. Such models are too faint for IceCube and more efficiently tested using experiments in the northern hemisphere.[16]

8.3 *Lepto-hadronic models of BL Lacs*

Active galactic nuclei belong to the strongest objects in the sky[17] and are discussed as possible neutrino sources and accelerators of cosmic rays.[18] Most promising are blazars, AGN with their jets pointing

[10] Amato, Guetta, and Blasi, "Signatures of high energy protons in pulsar winds".

[11] Aharonian, "The Energy spectrum of TeV gamma-rays from the Crab nebula as measured by the HEGRA system of imaging air Cherenkov telescopes".

[12] Fesen, Shull, and Hurford, "An Optical Study of the Circumstellar Environment Around the Crab Nebula".

[13] Amato, Guetta, and Blasi, "Signatures of high energy protons in pulsar winds".

[14] Di Palma, Guetta, and Amato, "Revised predictions of neutrino fluxes from Pulsar Wind Nebulae".

[15] For example in Kappes et al., "Potential Neutrino Signals from Galactic Gamma-Ray Sources"; Di Palma, Guetta, and Amato, "Revised predictions of neutrino fluxes from Pulsar Wind Nebulae"

[16] Adrian-Martinez, "First combined search for neutrino point-sources in the Southern Hemisphere with the ANTARES and IceCube neutrino telescopes".

[17] Urry and Padovani, "Unified schemes for radio-loud active galactic nuclei".

[18] Halzen and Kheirandish, "High Energy Neutrinos from Recent Blazar Flares"; Kadler, "Coincidence of a high-fluence blazar outburst with a PeV-energy neutrino event".

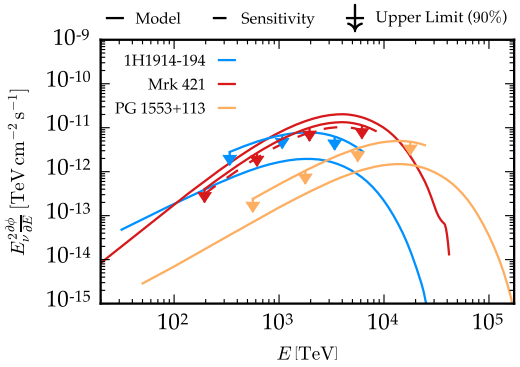

Figure 8.4: Model limits for Mrk 421 and other BL Lacs. Visualization similar to previous figure. Models from Petropoulou, Dimitrakoudis, et al., "Photohadronic origin of γ-ray BL Lac emission: implications for IceCube neutrinos".

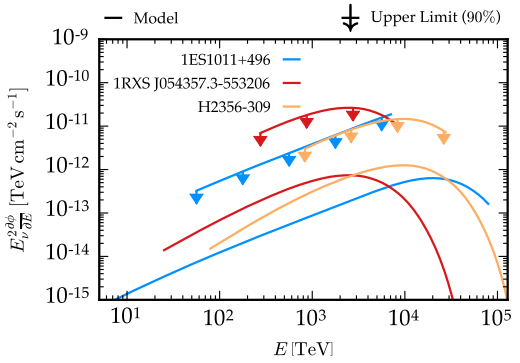

Figure 8.5: Model limits for other lepto-hadronic BL Lacs. Visualization similar to previous figure. Models from Petropoulou, Dimitrakoudis, et al., "Photohadronic origin of γ-ray BL Lac emission: implications for IceCube neutrinos".

towards Earth resulting in an enhancement of visible high-energy emission. The modeling of blazars is compared to multi-wavelength data.[19]

In lepto-hadronic models, a pion component is produced by protons that subsequently create neutrinos detectable at Earth (Figure 2.6). Blazars that were found in spatial and energetic agreement with high energy neutrinos found in IceCube were modeled using lepto-hadronic techniques to calculate the possible neutrino output.[20] An important figure of merit to take into account for such models is the ratio of neutrino luminosity to TeV gamma ray luminosity

$$Y_{\gamma\nu} = \frac{L_\nu}{L_{\gamma,\mathrm{TeV}}} \,. \tag{8.3}$$

The fraction $Y_{\gamma\nu}$ is bound to values ≤ 3, where $Y_{\gamma\nu} = 3$ indicates pure hadronic emission of gamma rays.[21] There is no lower bound, with $Y_{\gamma\nu} \ll 1$ approaching pure leptonic models without neutrino emission. The neutrino flux detectable in tracks in IceCube is reduced to 1/3 due to neutrino oscillations during propagation (Section 2.6). Such models could tentatively explain parts of the high-energy part of the observed astrophysical neutrino flux with a population of such blazars.[22] IceCube neutrino searches above 10 PeV constrain values except $Y_{\gamma\nu} \leq 0.15$ for the population of sources tested,[23] but values for individual blazars can be potentially higher and are tested here.

[19] Boettcher, "Modeling the Emission Processes in Blazars".

[20] Petropoulou, Dimitrakoudis, et al., "Photohadronic origin of γ-ray BL Lac emission: implications for IceCube neutrinos".

[21] Ibid.

[22] Padovani, Petropoulou, et al., "A simplified view of blazars: the neutrino background".

[23] Aartsen, "Constraints on ultra-high-energy cosmic ray sources from a search for neutrinos above 10 PeV with IceCube".

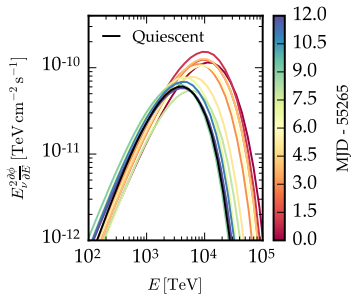

Figure 8.6: Flaring neutrino SED of Mrk 421 modeled from gamma ray flare for each of a 13 day flare. The SED of a quiescent state is shown in black. Published in Petropoulou, Coenders, and Dimitrakoudis, "Time-dependent neutrino emission from Mrk 421 during flares and predictions for IceCube".

[24] Mao, "2MASS observation of BL Lac objects II".

[25] Petropoulou, Dimitrakoudis, et al., "Photohadronic origin of γ-ray BL Lac emission: implications for IceCube neutrinos".

Table 8.1: Correlation of the neutrino flux (ϕ_ν) to gamma rays in different wavebands. For each waveband, the correlation of the fluxes is given. Values exceeding ± 0.55 are statistically significant at 5% level for the data set of $N = 13$ days used. The roman numerals indicate the energy ranges used for neutrinos: (I) 100 TeV to 1 PeV and (II) 1 PeV to 50 PeV.

Waveband	Correlation	
	I	II
> 200 GeV	-0.50	0.97
$0.1 - 300$ GeV	0.00	0.94
$15 - 50$ keV	-0.43	0.89
$2 - 10$ keV	-0.26	0.93

[26] Aleksić, "Unprecedented study of the broadband emission of Mrk 421 during flaring activity in March 2010".

[27] Petropoulou, Coenders, and Dimitrakoudis, "Time-dependent neutrino emission from Mrk 421 during flares and predictions for IceCube".

[28] Petropoulou, Dimitrakoudis, et al., "Photohadronic origin of γ-ray BL Lac emission: implications for IceCube neutrinos".

The models for six BL Lac objects are shown in Figures 8.4 and 8.5. In general, very hard spectra are obtained in the models with cutoff energies above neutrino energies in the high PeV regime. Most of the sources are too distant and in the southern sky, where IceCube's sensitivity is worse. Thus, the limits are multiple factors above the prediction and the amount of hadronic acceleration $Y_{\gamma\nu}$ is not constrained from the prediction.

The closest BL Lac Mrk 421 however shows a much stronger neutrino emission. First of all, the blazar is close enough (redshift $z = 0.031$[24]) to produce a large flux at Earth. Moreover, the lepto-hadronic model is optimized with a high amount of hadronic acceleration, that is $Y_{\gamma\nu} = 0.5$. At the position of Mrk 421, a small over-fluctuation with pre-trial p-value of 32% is observed. The upper limit of the model SED for neutrino emission is constrained by a factor of 0.65, the sensitivity of IceCube is a factor of 2 below the prediction assuming constant emission over seven years. Thus, IceCube is able to test the amount of pion production at Mrk 421, constraining the proton luminosity at the source[25] with $Y_{\gamma\nu} < 0.33$.

8.4 *Time variability of blazars: Mrk 421*

Blazars are highly variable objects and the flux can exceed its nominal value multiple times on short time scales. Hence, the time-integrated flux can be enhanced strongly taking into account flaring periods. In 2010, a thirteen day long flare of Mrk 421 with large coverage in multi-wavelength data[26] was observed. Using lepto-hadronic models, the evolution of neutrino flux during the flare is modeled.[27] In Figure 8.6, the neutrino flux model for each day of the flare is compared to the model of the a long quiescent emission (used in Section 8.3). A strong shift of the peak to higher PeV energies is observed, while the flux in the TeV region does not vary strongly. At later days, the neutrino flux fades back into the quiescent state.[28] Comparing the neutrino flux above and below PeV energies to different wavebands in gamma rays, the model shows strong correlation of the neutrino luminosity above PeV energies with gamma rays (Table 8.1). The correlation is found to be

$$\log_{10} F_\nu = A \log_{10} F_\gamma + B \tag{8.4}$$

with $A = 1.59 \pm 0.17$ and $B = 5.25 \pm 1.64$ for the waveband of $0.1 - 300$ GeV in gamma rays. Figure 8.7 shows the IceCube limit for Mrk 421 in the quiescent state and the first day (MJD55265) of the thirteen day flare. With a large increase at the PeV energy regime and hence a higher cutoff energy, the overall neutrino flux limit is $\sim 22\%$ lower than for the quiescent state in the TeV neutrino energy range.

The gamma ray emission of Mrk 421 on long time scales is monitored by the *Fermi*-LAT satellite. Using the correlation of gamma ray flux and neutrino flux in Eq. (8.4), the neutrino flux can be estimated taking into account flaring periods. Figure 8.8 (top) shows

Figure 8.7: Limits for Mrk 421 using model of quiescent and flaring state. Plot similar to previous limit plots.

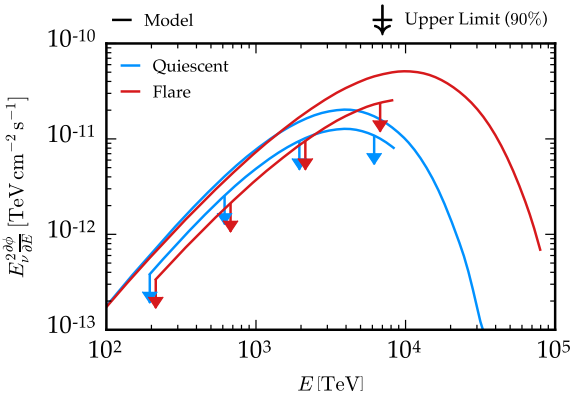

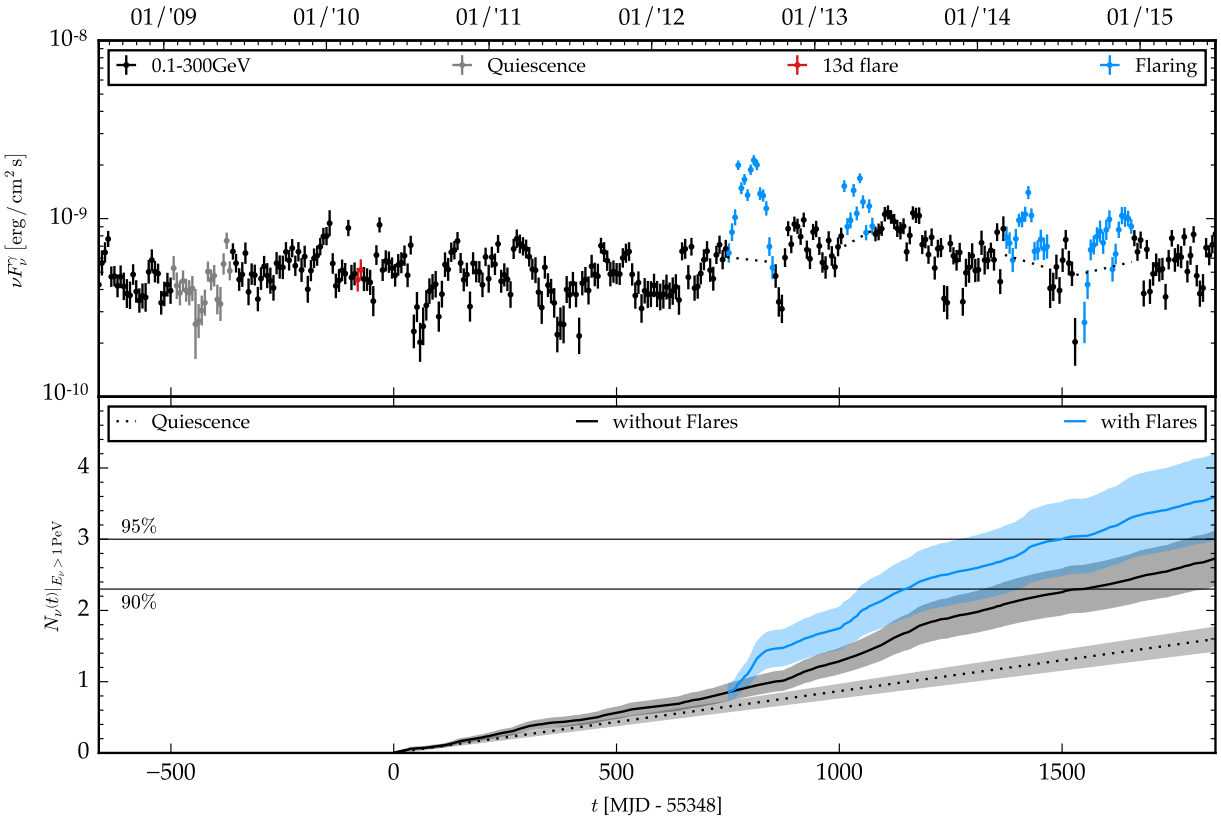

Figure 8.8: Long-term neutrino light curve of Mrk 421 in correlation with Fermi gamma ray observations. Top: Fermi gamma ray monitoring of Mrk 421 in 100 MeV to 300 GeV energies. Bottom: Neutrino event count expected in IceCube with correlation to gamma rays.

the gamma ray flux observed by *Fermi*-LAT. In the years after 2012, three major flares are observed and a generally increased activity of Mrk 421 compared to the quiescent state in 2009, resulting in an expected net increase of neutrino luminosity.

The bottom figure shows the corresponding neutrino flux. Compared to the expected neutrino rate assuming the quiescent state of Mrk 421, the flux in the PeV region is expected to increase significantly after 2012. Using the full light curve predicts a flux $2\times$ higher than for the quiescent state. When major flares are excluded, the correlated neutrino flux is still $\sim$ 70% higher than for the quiescent state[29].

As a result, under the assumption of a correlation of neutrino flux to the observed gamma ray flux of Mrk 421, the time-integrated neutrino flux is expected to be more than 75% (100%) higher accounting for flaring periods when excluding (including) the four most extreme flares.[30] Thus, the expected time-integrated neutrino flux observed by IceCube is increased compared to the quiescent state discussed in Section 8.3, further constraining the amount of possible hadronic acceleration.

[29] By excluding the flares, a constant rate (dotted lines in Figure 8.8 (top)) is assumed. The flares are excluded because at such high intensities, the linear correlation might not hold anymore.

[30] Petropoulou, Coenders, and Dimitrakoudis, "Time-dependent neutrino emission from Mrk 421 during flares and predictions for IceCube".

8.5 Other source candidates

Other lepto-hadronic models of blazars are characteristic for their very high energies, exceeding up to EeV energies.[31] Upper limits for such neutrino SEDs are shown in Figures 8.9 and 8.10. Most of the sources are located in the northern sky and hence, a large fraction of the neutrino flux is absorbed in the Earth, suppressing the sensitivity of IceCube to such high energetic fluxes.

The sources 3C 273 and 3C 279 are at the horizon and no absorption is present. Thus, IceCube is constraining the model due to no observation of clustering. Thus, the amount of hadronic acceleration of such models is constrained.

Other objects tested are supernova remnants with modeled neutrino SEDs.[32] For all these models, IceCube is not sensitive enough to constrain the models. The SNR G40.5-0.5 is close enough with a sensitivity of a factor of two above the prediction, shown in Figure 8.11. Figure 8.12 shows limits for HESS sources that are not yet constrained as well, for the same reasons as mentioned before.

[31] Reimer, "Photon-neutrino flux correlations from hadronic models of AGN?".

[32] Mandelartz and Tjus, "Prediction of the diffuse neutrino flux from cosmic ray interactions near supernova remnants".

Figure 8.9: Model limits for blazars close to the horizon. Visualization similar to previous limit figures. Models from Reimer, "Photon-neutrino flux correlations from hadronic models of AGN?".

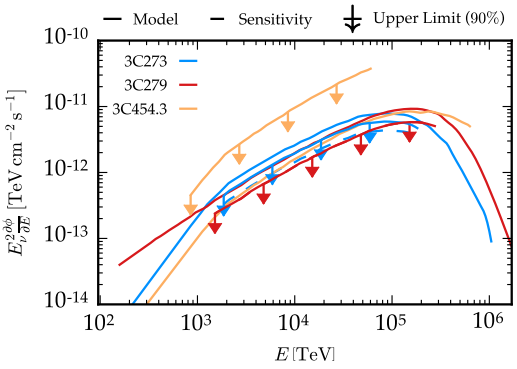

Figure 8.10: Model limits for blazars in northern sky. Visualization similar to previous figure. Models from Reimer, "Photon-neutrino flux correlations from hadronic models of AGN?".

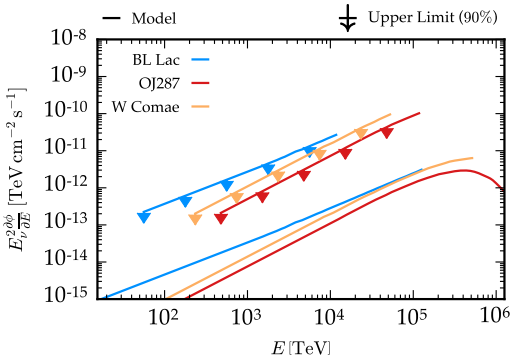

Figure 8.11: Model limits for Galactic supernova remnants. Visualization similar to previous limit figures. Models from Mandelartz and Tjus, "Prediction of the diffuse neutrino flux from cosmic ray interactions near supernova remnants".

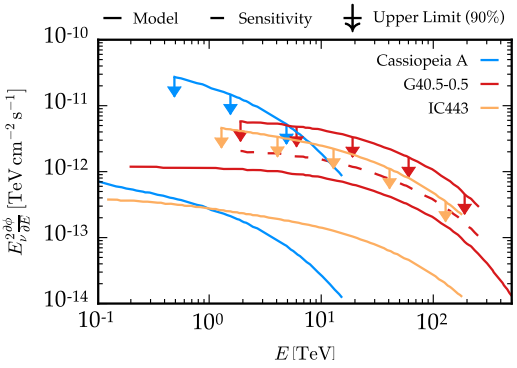

Figure 8.12: Model limits for HESS objects. Visualization similar to previous figure. Models from Mandelartz and Tjus, "Prediction of the diffuse neutrino flux from cosmic ray interactions near supernova remnants".

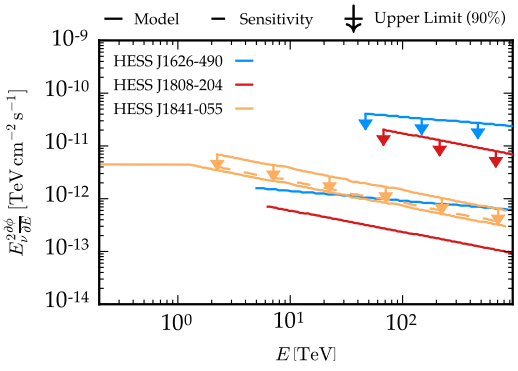

9 Future development & prospects

With continuous operation, IceCube's sensitivity to emission of neutrinos integrated over time increased due to accumulated statistics. The sensitivity with respect to point-like sources is given by the signal event rate, the amount of background present, and the reconstruction quality of track events. In the previous analyses,[1] improvements in the detector size and angular reconstructions[2] boosted IceCube's performance in addition to the increasing exposure. With the first season of data taking in June 2011, IceCube enters a stage of steady operation, realized in this thesis with the addition of joint data taken from June 2012 to June 2015.

[1] Aartsen, "Search for Time-independent Neutrino Emission from Astrophysical Sources with 3 yr of IceCube Data"; Aartsen, "Searches for Extended and Point-like Neutrino Sources with Four Years of IceCube Data".

[2] For example likelihood reconstructions with light arrival tables from simulation.

9.1 Discovery potential improvement with time

The development of the discovery potential is shown in Figure 9.1 for four different declinations for the next ten years of operation. For comparison, two boundary conditions of the possible improvement are shown anchored to the current sensitivity of seven years of livetime. The first one is assuming a development in time (T) proportional to the square root of time:

$$E^2 \frac{\partial \phi}{\partial E}(T) \propto \frac{1}{\sqrt{T}} \tag{9.1}$$

This scenario corresponds to an environment dominated by background statistics. In a small window around a source of size corresponding to the typical event reconstruction accuracy, the number of signal events will grow linear, whereas the statistical fluctuations of background grow with the square root in time. Thus, a peak on top of the background slowly rises from the background.

In a background-free environment, for example in the case of very good angular resolution or at the very high-energy end of the spectrum, the discovery potential simply depends on the amount of signal events accumulated in time. Any event detected is basically a discovery because the expected number due to background is zero. Hence, the growth in time-integrated discovery potential is limited by signal-statistics and grows linearly:

$$E^2 \frac{\partial \phi}{\partial E}(T) \propto \frac{1}{T} \tag{9.2}$$

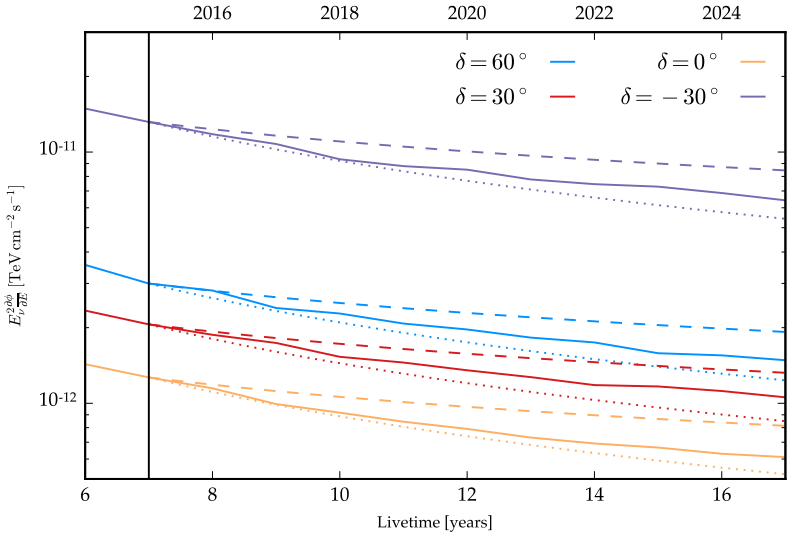

Figure 9.1: Evolution of discovery potential with time for different declinations. The actual evolution (solid) with time T is compared to an increase with $\sqrt{T}$ (dashed) and linear in T (dotted), corresponding to the background and signal statistics limited case, respectively.

The actual evolution in discovery potential for the next ten years assuming an unbroken $E^2 \partial\phi/\partial E$ spectrum lies in between the extreme scenarios of Eq. (9.1) and (9.2). The growth in performance improves with $\sim T^{-0.8}$ over time. Hence, after seven years of accumulated statistics, IceCube is not statistically limited by background. The use of the energy proxy in the likelihood evaluation (Eq. (5.8)) allows for further discrimination of signal at high energies from the background that accumulates predominantly at lower energies. Hence, high energy events have less background than simply accounting for the spatial correlation with a source, boosting the performance with respect to Eq. (9.1).

9.2 *Prospects of source discovery with IceCube*

With seven years of livetime, no evidence of time-integrated neutrino emission by point-like sources was found and upper limits were calculated and discussed in Section 8. In the scan of the full sky, the two most significant spots have pre-trial p-values of 1.8×10^{-6} and 9.3×10^{-7} for northern and southern sky, respectively. Nevertheless, as discussed in Section 7.5, the large trial factor of background fluctuations in the entire sky diminishes the significance to less than 1σ, compare Table 7.2.

The upper limits of the sources are the largest in the respective halves of the sky and thus the most promising candidates to be detected as a source in the scan of the full sky that can overcome the large trial factor of 190 000. In order to simulate the future detection of such sources, additional years of livetime are complementing the existing seven years of data. The existing data remains unchanged, and for the added data, neutrinos are injected at the position of the hot spots according to the expectation given by the upper limits (Table 7.2). The current upper limits correspond to 5.4 (3.6) events

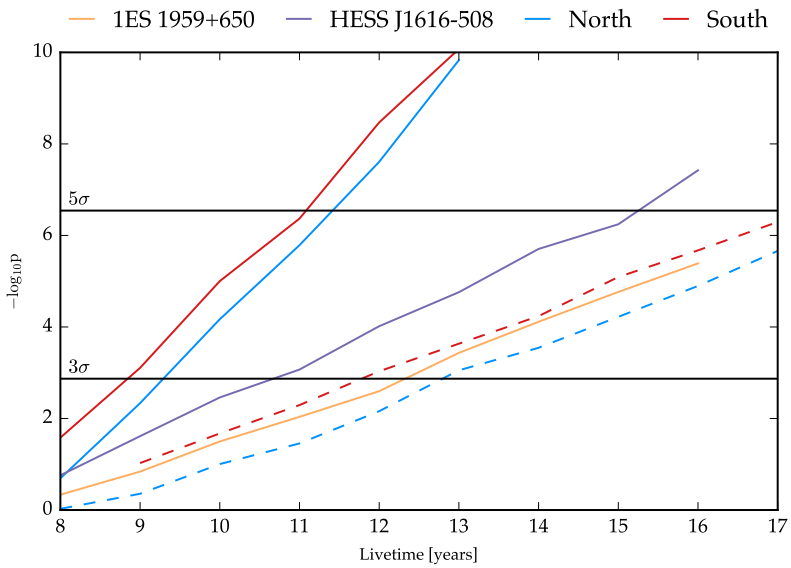

Figure 9.2: Significance evolution of hot spots and sources with increasing time. The current upper limit of the sources is assumed as a true neutrino source injected into data sets of increasing exposure. Dashed lines assume a source strength half of the value of the upper limit.

added per year at the hot spot in northern (southern) sky. This procedure is repeated 10 000 times in order to calculate the median expected significance with added exposure.

Figure 9.2 shows the median expectation using up to ten additional years of livetime. The pre-trial p-value of the additional livetime ($-\log_{10} p$) is corrected for the trial factor $\sim 190\,000$ encountered in the scan of the full sky. According to the median expectation, after approximately four years of additional exposure, that is, with data taken until 2019, the threshold of 5σ would be exceeded in the scan of the full sky.

Under the assumption that the hot spots are due to a weaker neutrino source correlating with upwards fluctuations of background, the procedure is repeated with a source half the strength of the upper limits in Table 7.2. In such cases, the growth in significance is much smaller and the threshold of 5σ is not reached within 10 additional years of livetime in 2025. The threshold of 3σ would be reached within ~ 5 additional years at median expectation.

This test is done as well for the two most significant sources present in the source lists[3]. The upper limits of those sources are shown in Figure 8.1 in comparison to IceCube's sensitivity and the upper limits of the hot spots. The upper limit fluxes are a factor of three to four lower than for the hot spots, but with a significantly lower trial factor as well given by 73 objects gathered in the full sky, 34 and 40 in the northern and southern sky, respectively. In the south, the most promising objects found are 1ES 1959+650, and HESS J1616-508, respectively. For both sources, the threshold of 3σ is reached after 3 or 5 years of additional livetime (median expectation). The growth in significance is lower than for the two hot spots, but with ten years of additional livetime, in the range of a 5σ discovery assuming that the source flux is of the level of its current upper limit.

[3] The objects of the source lists are shown in Tables 7.4 to 7.7.

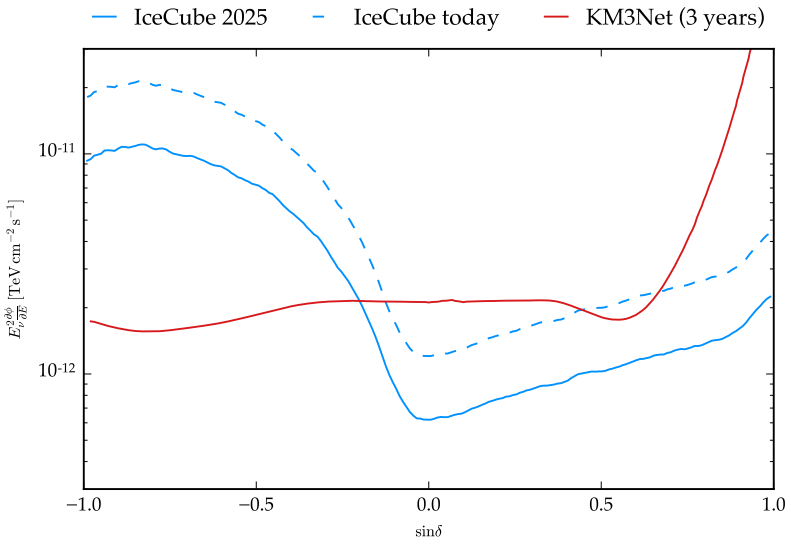

Figure 9.3: Discovery potential as expected in 2025. An improvement in time with $E^2 \partial\phi / \partial E\,(T) \propto T^{-0.75}$ is used to propagate the IceCube discovery potential from today to 2025. Newly constructed experiments in the Mediterranean (KM3NeT) are shown using three years of detector livetime. Data for KM3NeT from Adrian-Martinez, "Letter of intent for KM3NeT 2.0".

9.3 *Future experiments*

The calculations done in the previous sections simply assumed a constant increase of exposure without any changes to the detector, that is, extrapolating the data sample described in Sections 6 and 7.1 to larger livetimes. Improvements in the data selection and reconstruction, as well as detector improvements naturally improve the results discussed before. IceCube is the first detector large enough to successfully detect astrophysical neutrinos and next generation experiments are being constructed and designed to improve the physics reach greatly.

KM3NeT is a water Cherenkov detector that is constructed in the Mediterranean Sea.[4] At a size comparable to IceCube, the optical medium used for neutrino detection is ocean water that shows less scattering of Cherenkov light, at the cost of higher absorption.[5] The discovery potential for an E^{-2} spectrum after three years of operation is shown in Figure 9.3 and compared to IceCube after $\sim$ 15 years of full operation in 2025. Being located in the northern hemisphere, the performance in the southern sky improves by a factor of five within three years, in addition to testing much lower energies than IceCube in the down-going region (Figure 7.8).

Thus, combined searches of IceCube and KM3NeT test a large range of energies, as done previously with IceCube and KM3NeT's predecessor ANTARES.[6] Moreover, the Galactic Plane is predominantly in the southern sky with the Galactic Center and *Sgr A** at right ascension 266.42° and declination −29.01°. Many interesting sources are located in our Galaxy[7] that are currently not constrained by IceCube due to the high-energy threshold given by large atmospheric backgrounds (Section 8.5). Moreover, another gigaton detector is designed and constructed at Lake Baikal in Siberia.[8] The coor-

[4] Adrian-Martinez, "Letter of intent for KM3NeT 2.0".

[5] Yepes-Ramirez, "Characterization of optical properties of the site of the ANTARES neutrino telescope".

[6] Adrian-Martinez, "First combined search for neutrino point-sources in the Southern Hemisphere with the ANTARES and IceCube neutrino telescopes".

[7] Kappes et al., "Potential Neutrino Signals from Galactic Gamma-Ray Sources"; Mandelartz and Tjus, "Prediction of the diffuse neutrino flux from cosmic ray interactions near supernova remnants".

[8] Avrorin, "Status and perspectives of the BAIKAL-GVD project".

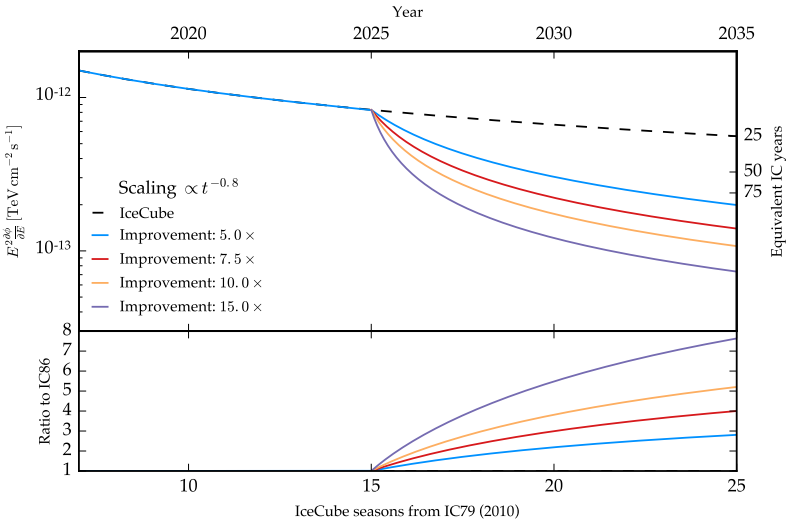

Figure 9.4: Discovery potential improvement with larger detectors starting in 2025. Top: Improvement of a new detector continuing taking data from 2025. The right axis shows the time that the current IceCube detector needs to arrive at this flux level. Bottom: Ratio of improvement of the upgraded detector with respect to current IC86.

dination of all the experiments yields a greatly improved sensitivity compared to today and results in a significant impact of neutrino astronomy connected to other messengers.[9]

There are on-going developments for a successor of the IceCube detector as well, increasing the volume greatly to multiple cubic kilometers using a sparser spacing than now.[10] With an increased instrumented volume, the lever arm for muon tracks increases, resulting in better angular reconstruction, plus larger statistics. Figure 9.4 shows the simulated increase in discovery potential for a *IceCube-Gen2* detector starting in 2025 with different "improvement factors" with respect to the 86-string IceCube detector of one cubic kilometer instrumented volume. The improvement can be due to larger statistics (improves with the square root) and improvements in the reconstruction (linear improvement) due to a larger detector and better reconstruction and analysis techniques. Within ten years of operation, the improvement due to IceCube-Gen2 can exceed the equivalent performance of IceCube by a factor of three to eight. This is a parameter space that IceCube will not be able to establish within 75 years of operation or more.

[9] Smith, "The Astrophysical Multimessenger Observatory Network (AMON)".

[10] Aartsen, "IceCube-Gen2: A Vision for the Future of Neutrino Astronomy in Antarctica".

10 Connecting blazars to cosmic-rays and neutrinos

The origin of ultra high-energy cosmic rays (UHECRs) is not yet known and it is still a big open question in modern physics. Neutrinos can in principle help solving this puzzle because they trace hadronic interactions happening at the acceleration site (Section 2.4). The available neutrino data sets from IceCube might be on one side statistically limited and, on the other side, astrophysical starting events mostly have large angular uncertainties. Thus, the identification of astrophysical counterparts with hadronic interactions using solely neutrinos at the highest energies is challenging.

In this section, a novel study is presented that attempts for the first time to connect all available messengers of high-energy multi-messenger astronomy (Section 2.1), which are ultra-high energy cosmic rays measured by the Pierre Auger Observatory[1] (PAO) and the Telescope Array[2] (TA), high-energy astrophysical neutrinos, and gamma rays. For gamma rays, catalogs of astrophysical objects are used as described in Section 10.2. Neutrinos are considered as "intermediaries" connecting UHECRs to the gamma ray objects. The study presented here is the natural continuation of a previously published study discussed in Section 10.3; the updated results presented here are in review for publication.[3]

[1] Abraham, "Properties and performance of the prototype instrument for the Pierre Auger Observatory".

[2] Abu-Zayyad, "The surface detector array of the Telescope Array experiment".

[3] Resconi et al., "Connecting blazars with ultra high energy cosmic rays and astrophysical neutrinos".

10.1 UHECRs and neutrinos

The UHECRs used in this study are the cosmic ray particles with the highest energies ever observed. In total 303 events are observed, of which 231 were detected by PAO with energies above 52 EeV and mostly in the southern sky.[4] In the northern sky, TA recorded 72 events above 57 EeVi.[5] In both samples, small scale anisotropies ("hot spots") are observed when using $\sim 20^\circ$ of the arrival direction smearing due to cosmic ray deflection. The arrival directions of the 303 UHECRs with this smearing is shown in Figure 3.7. The significance of the hot spots reported in these tests is $2-3\,\sigma$. There is no identification of counterparts yet for the UHECRs, the strongest deviation from isotropy is between PAO UHECRs and Swift AGN closer than 130 Mpc and Cen A.[6]

[4] Aab, "Searches for Anisotropies in the Arrival Directions of the Highest Energy Cosmic Rays Detected by the Pierre Auger Observatory".

[5] Abbasi, "Indications of Intermediate-Scale Anisotropy of Cosmic Rays with Energy Greater Than 57 EeV in the Northern Sky Measured with the Surface Detector of the Telescope Array Experiment".

[6] Aab, "Searches for Anisotropies in the Arrival Directions of the Highest Energy Cosmic Rays Detected by the Pierre Auger Observatory".

[7] Listed in Table 10.1 and 10.2. Only events above 60 TeV and with median angular uncertainty smaller than 20° are used.

Previous correlation tests between neutrinos[7] and UHECRs have been done in Aartsen, "Search for correlations between the arrival directions of IceCube neutrino events and ultrahigh-energy cosmic rays detected by the Pierre Auger Observatory and the Telescope Array". Two results are quoted by the authors with p-values 0.85% and 0.05, corresponding to the background estimation by scrambling neutrinos or UHECRs, respectively. We note that the p-values depends strongly on the scrambling method used, because of the small anisotropies (hot spots) observed in the UHECR arrival directions. The p-value of 0.85% hints to a possible connection of UHECRs and neutrinos, although does not provide information about the sources responsible for such an emission.

Table 10.1: IceCube track events used in correlation analysis. Events from Aartsen, "Evidence for Astrophysical Muon Neutrinos from the Northern Sky with IceCube". One event is excluded because it is already included in the starting event sample (ID 5). For all events, an angular resolution of 0.4° is quoted. Right ascension and declination are in degrees.

α (J2000.0)	δ	MJD	E_ν TeV[a]	ξ^b
254	16.3	55421.5	1693	0.96
88.5	0.2	55497.3	880	0.83
37.1	18.6	55911.3	713	0.88
285.7	3.1	55513.6	709	0.8
331	11	55478.4	466	0.81
346.8	24	55355.5	442	0.86
267.5	13.8	55464.9	400	0.82
238.3	18.9	55987.8	394	0.85
235.2	19.3	55702.8	393	0.77
277.5	52.7	55829.3	198	0.66
323.3	2.8	55405.5	193	0.41
9.4	7.8	55806.1	179	0.5
207.2	6.7	55642.0	185	0.45
152.2	6.8	55768.5	156	0.45
310.5	21.9	55387.5	178	0.55
307.9	1	55589.6	184	0.33
267.6	−4.4	55834.4	191	0.56
221.9	3.2	55896.9	158	0.58
138.9	47.6	55370.7	189	0.37
31.2	11.8	55803.0	190	0.49

[a] The neutrino energy is calculated by unfolding the reconstructed event energy to the observed diffuse astrophysical neutrino flux.
[b] "Signalness" which is defined as the ratio of astrophysical flux over atmospheric flux at the reconstructed energy of the event.

Table 10.2: Selected list of high-energy neutrinos detected by IceCube. List and events from Padovani, Resconi, et al., "Extreme blazars as counterparts of IceCube astrophysical neutrinos", and references therein. The right ascension and declination are in hour angles.

ID	Dep. Energy TeV	$(\nu f_\nu)^a$	α (J2000.0)	δ	σ 1°	b_{II} 1°
3	$78.7^{+10.8}_{-8.7}$	$1.4^{+3.3}_{-1.2}$	08 31 36	−31 12 00	≤1.4	+5
4	165^{+20}_{-15}	$0.8^{+1.9}_{-0.7}$	11 18 00	−51 12 00	7.1	+9
5	71.4 ± 9.0	$1.3^{+3.0}_{-1.1}$	07 22 24	−00 24 00	≤1.2	+7
9	$63.2^{+7.1}_{-8.0}$	$2.1^{+4.7}_{-1.7}$	10 05 12	+33 36 00	16.5	+54
10	$97.2^{+10.4}_{-12.4}$	$1.2^{+2.8}_{-1.0}$	00 20 00	−29 24 00	8.1	−83
11	$88.4^{+12.5}_{-10.7}$	$1.1^{+2.5}_{-0.9}$	10 21 12	−08 54 00	16.7	+39
12	104 ± 13.0	$0.9^{+2.1}_{-0.8}$	19 44 24	−52 48 00	9.8	−29
13	253^{+26}_{-22}	$1.2^{+2.7}_{-1.0}$	04 31 36	+40 18 00	≤1.2	−5
14	1041^{+132}_{-144}	$1.1^{+2.6}_{-0.9}$	17 42 24	−27 54 00	13.2	+1
17	200 ± 27	$1.2^{+2.9}_{-1.0}$	16 29 36	+14 30 00	11.6	+38
19	$71.5^{+7.0}_{-7.2}$	$1.3^{+3.0}_{-1.1}$	05 07 36	−59 42 00	9.7	−36
20	1141^{+143}_{-133}	$1.1^{+2.6}_{-0.9}$	02 33 12	−67 12 00	10.7	−47
22	220^{+21}_{-24}	$0.7^{+1.7}_{-0.6}$	19 34 48	−22 06 00	12.1	−19
23	$82.2^{+8.6}_{-8.4}$	$1.5^{+3.5}_{-1.3}$	13 54 48	−13 12 00	≤1.9	+47
26	210^{+29}_{-26}	$1.1^{+2.6}_{-0.9}$	09 33 36	+22 42 00	11.8	+45
27	60.2 ± 5.6	$1.8^{+4.0}_{-1.5}$	08 06 48	−12 36 00	6.6	+10
30	129^{+14}_{-12}	$0.8^{+1.9}_{-0.7}$	06 52 48	−82 42 00	8.0	−27
33	385^{+46}_{-49}	$1.4^{+3.2}_{-1.2}$	19 30 00	+07 48 00	13.5	−5
35	2004^{+236}_{-262}	$1.4^{+3.3}_{-1.2}$	13 53 36	−55 48 00	15.9	+6
38	201 ± 16	$1.2^{+2.9}_{-1.0}$	06 13 12	+14 00 00	≤1.2	−2
39	101^{+13}_{-12}	$0.9^{+2.0}_{-0.7}$	07 04 48	−17 54 00	14.2	−5
40	157^{+16}_{-17}	$0.8^{+1.8}_{-0.6}$	09 35 36	−48 30 00	11.7	+3
41	$87.6^{+8.4}_{-10.0}$	$1.4^{+3.2}_{-1.2}$	04 24 24	+03 18 00	11.1	−30
44	$84.6^{+7.4}_{-7.9}$	$1.4^{+3.1}_{-1.1}$	22 26 48	+00 00 00	≤1.2	−46
45	430^{+57}_{-49}	$0.9^{+2.0}_{-0.7}$	14 36 00	−86 18 00	≤1.2	−24
46	158^{+15}_{-17}	$0.8^{+1.8}_{-0.7}$	10 02 00	−22 24 00	7.6	+26
47	$74.3^{+8.3}_{-7.2}$	$1.6^{+3.8}_{-1.4}$	13 57 36	+67 24 00	≤1.2	+48
48	105^{+14}_{-10}	$0.9^{+2.1}_{-0.8}$	14 12 24	−33 12 00	8.1	+27
51	$66.2^{+6.7}_{-6.1}$	$2.2^{+5.0}_{-1.8}$	05 54 24	+54 00 00	6.5	+14
52	158^{+16}_{-18}	$0.8^{+1.8}_{-0.7}$	16 51 12	−54 00 00	7.8	−6
[b]	2600 ± 300	—	07 21 22	+11 28 48	0.27	+12

[a] Fluxes in units of $10^{-11}\,\mathrm{erg\,cm^{-2}\,s^{-1}}$. This is converted to $\mathrm{TeV\,cm^{-2}\,s^{-1}}$ units by multiplying the numbers in this column by ~ 0.614.

[b] Reported in Schoenen and Rädel, "Detection of a multi-PeV neutrino-induced muon event from the Northern sky with IceCube".

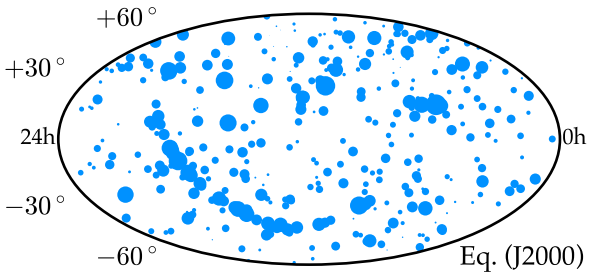

Figure 10.1: Second FHL catalog in equatorial coordinates. The size of the dots indicates the photon flux of the objects relative to each other. Catalog published in Ackermann, "2FHL: The Second Catalog of Hard Fermi-LAT Sources".

10.2 *High-energy gamma ray catalogs*

In the correlation study of the three messengers, gamma rays are the only one that have clearly associated astrophysical objects as counterparts. Three catalogs are used in the correlation study and listed in the following.

2FHL: The "second catalog of hard Fermi-LAT sources"[8] is the higher energetic complete (flux limited) catalog. It is the catalog closes in energy to the neutrino and UHECRs events observed. The catalog consists of 360 objects. Active galactic nuclei constitute the majority of events (75%, extra-galactic) and 11% are Galactic objects. Most of the objects (86%) are known objects. The catalog is based on the 50 GeV to 2 TeV waveband. Most of the sources (193) are blazars of BL Lac type. Figure 10.1 shows the map of all objects in equatorial coordinates. The size of the dot indicates the observed flux above 50 GeV, in the following written as $F_\gamma\,(>50\,\mathrm{GeV})$. The high-energy gamma ray flux is tentatively a good indicator for the neutrino and UHECR luminosity.[9] The 2FHL catalog is the smallest one used, but collects the strongest high-energy objects known and it realizes a complete set because it is limited by the flux of the sources.

2WHSP: The "second WISE high synchroton peaked" catalog is a large collection of BL Lacs classified as *HBL*[10], that is, the synchroton frequency ν_s exceeds 10^{15} Hz,. A sample of 1681 objects is obtained using the ALLWISE survey.[11] The catalog is shown in Figure 10.2. For each source, a "figure of merit" (FoM) is calculated that quantifies the chance to detect the object in the TeV band. The FoM is defined as the flux at the synchroton peak frequency divided by the flux of the faintest source detected in the TeV band. A FoM>1 thus describes a source potentially detectable by current gamma ray detectors. In the first version of the catalog, 112 objects that are potentially detectable by current detectors were found, but only $\sim 1/3$ have by now an identified counterpart.

[8] Ackermann, "2FHL: The Second Catalog of Hard Fermi-LAT Sources".

[9] Petropoulou, Coenders, and Dimitrakoudis, "Time-dependent neutrino emission from Mrk 421 during flares and predictions for IceCube", discussed in Section 8.4.

[10] High-energy cutoff BL Lac

[11] Arsioli et al., "1WHSP: An IR-based sample of ∼1000 VHE γ-ray blazar candidates"; Chang et al., "2WHSP: A catalog of HE and VHE gamma-ray blazars and blazar candidates".

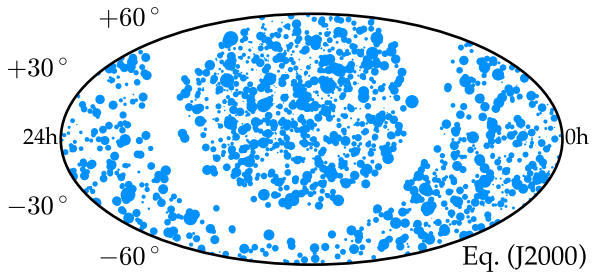

Figure 10.2: Second WHSP catalog in equatorial coordinates. The size of the dots indicates the "figure of merit" as described in the text relative to the other objects. Catalog published in Chang et al., "2WHSP: A catalog of HE and VHE gamma-ray blazars and blazar candidates".

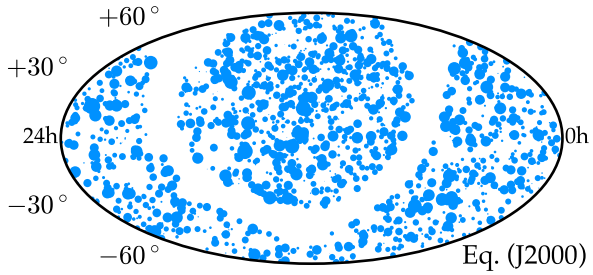

Figure 10.3: Third LAC catalog in equatorial coordinates. The size of the dots indicates the photon flux with respect to the other objects. Catalog published in Ackermann, "The Third Catalog of Active Galactic Nuclei Detected by the Fermi Large Area Telescope".

3LAC: The third catalog is the third Fermi-LAT catalog of active galactic nuclei (AGN).[12] It consists of AGN well identified above 100 MeV ($F_\gamma\,(>100\,\mathrm{MeV})$). Figure 10.3 shows the catalog, all sources are at least 10° off the Galactic Plane. In total, this amounts to 1444 objects and in contrast to the other two catalogs this is evenly shared between BL Lacs (mostly HBL type, 386) and flat spectrum radio quasars (FSRQ, 415). For all sources, the observed flux above 100 MeV is given to identify the most luminous sources in the catalog.

[12] Ackermann, "The Third Catalog of Active Galactic Nuclei Detected by the Fermi Large Area Telescope".

10.3 Neutrino correlation with gamma ray catalogs

In a previous study,[13] neutrino events were correlated with the three catalogs that are discussed in Section 10.2. The correlation of neutrinos to a catalog is tested by counting the number of neutrinos that have at least one gamma ray counterpart

[13] Padovani, Resconi, et al., "Extreme blazars as counterparts of IceCube astrophysical neutrinos".

$$n\,(x) = \sum_{\nu} \Theta\left(\sum_{\gamma \in x} \Theta\,(\sigma_\nu - \sphericalangle\,(\nu,\gamma))\right) \tag{10.1}$$

with the Heaviside step-function $\Theta\,(x)$ using the convention that $\Theta\,(0) = 0$. A neutrino (ν) has a counterpart if the object (γ) of the catalog lies within the median angular uncertainty σ_ν of the neutrino,

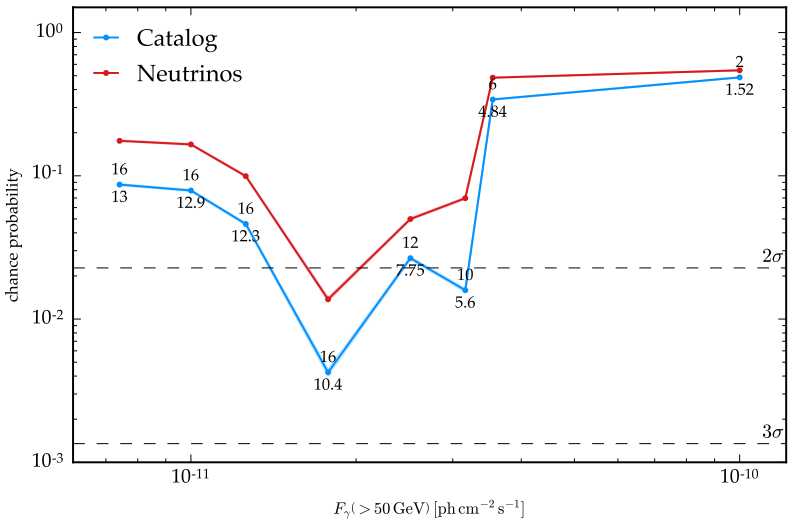

Figure 10.4: HESE correlation to 2FHL HBL blazars for different thresholds in the observed flux above 50 GeV in Fermi-LAT. The results are shown for scrambling the neutrinos and the objects of the catalog. For the scrambling in the catalog, the number of observed neutrinos with counterparts are shown (top number) with respect to the expectation from background (bottom number). Result published in Padovani, Resconi, et al., "Extreme blazars as counterparts of IceCube astrophysical neutrinos".

that is, the angular separation $\sphericalangle(\nu, \gamma)$. This procedure is done for different partitions of the catalog ($\gamma \in x$) using only objects that have luminosities exceeding the threshold x.[14]

The significance of an outcome of Eq. (10.1) giving the number of neutrinos with a gamma ray counterpart is calculated by comparing the result to background scrambled data sets. This is done for all thresholds x used and the largest excess is used as the final result. The result is then trial corrected due to scanning in the threshold x.

The result of the test is shown in Figure 10.4 for either scrambling the gamma ray objects or the neutrinos. When scrambling the positions of the neutrinos, the results are less significant. This is due to an anisotropy in the catalogs which only use objects 10° off the Galactic Plane. By scrambling the neutrinos, the number of events coinciding with this cutoff region is altered and thus changing the results. In the procedure of scrambling the catalog, the cut-out region of the Galactic Plane is accounted for. Thus, it is a more precise description of the procedure and used for the calculation of the significance.[15]

At a flux of $F_\gamma\,(>50\,\mathrm{GeV}) = 1.8 \times 10^{-11}\,\mathrm{ph\,cm^{-2}\,s^{-1}}$, the strongest excess is observed with 16 events over an expectation of 10.4. By comparing this to background trials, this corresponds to a local p-value of $\sim$ 0.4%, and 1.5% after trial correction (2.17σ). Similar results were obtained using the 2WHSP and 3LAC catalog, indicating a possible correlation with HBL blazars over other types.

[14] The measured luminosity or "figure of merit" used as discriminator for the threshold is explained in Section 10.2 for the different catalogs used.

[15] Padovani, Resconi, et al., "Extreme blazars as counterparts of IceCube astrophysical neutrinos".

10.4 Multi-messenger correlation test

If the excess observed in $n\,(x)$ described in Section 10.3 is interpreted as a connection between high-energy neutrinos and HBL blazars, primary cosmic rays have to be accelerated in the same objects. This has then motivated a further test dedicated to include UHECRs in the test.

Similar to the test using only neutrinos in Eq. (10.1), the number of cosmic rays with *at least* one gamma ray object at angular distance smaller than θ is counted. In this test, θ is not fixed but scanned at different angles due to the unknown deflection of cosmic rays during propagation[16]. Neutrinos are used as "intermediaries" in the counting process, that is, the correlation is only done using gamma ray objects that have a neutrino counterpart ($\nu_\oplus$ scenario) as defined in Eq. (10.1). The same procedure is done also for gamma ray objects *without* associated neutrinos ($\nu_\ominus$). The counting is thus given by

[16] For neutrinos, this is not necessary because they are not deflected, but the angular uncertainty is dominated by the reconstruction accuracy.

$$n_\oplus(x,\theta) = \sum_{\mathrm{CR}} \Theta\left(\sum_{\gamma\in x}\sum_{\nu} \Theta\left(\sigma_\nu - \sphericalangle(\nu,\gamma)\right)\Theta\left(\theta - \sphericalangle(\mathrm{CR},\gamma)\right)\right) \tag{10.2}$$

$$n_\ominus(x,\theta) = \sum_{\mathrm{CR}} \Theta\left(\sum_{\gamma\in x}\sum_{\nu} \Theta\left(\sphericalangle(\nu,\gamma) - \sigma_\nu\right)\Theta\left(\theta - \sphericalangle(\mathrm{CR},\gamma)\right)\right) \tag{10.3}$$

and is depending on the partitioning x of the gamma ray catalog, and the angular deflection θ of the UHECRs. For the partitioning, the same binning as in the neutrino correlation analysis is used. For the angular binning, one degree step size up to 30° is used.

The 2FHL catalog is extended to the full sky with respect to the test using only neutrinos.[17] Thus, the loss in significance due to the cutoff region coinciding with the Galactic Plane is resolved and the significance estimation is done using background maps created by scrambling neutrinos in right ascension. Furthermore, the median angular uncertainty values for cascade neutrino events are swapped randomly among each other. By relying on the scrambling on the neutrinos, the anisotropies in the sky maps of UHECRs remain untouched and do not bias the significance of the correlation test as was noted in the autocorrelation analysis of UHECRs and neutrinos.[18]

[17] Padovani, Resconi, et al., "Extreme blazars as counterparts of IceCube astrophysical neutrinos".

[18] Aartsen, "Search for correlations between the arrival directions of IceCube neutrino events and ultrahigh-energy cosmic rays detected by the Pierre Auger Observatory and the Telescope Array".

In the correlation test, we take all the sources in spatial coincidence with neutrinos. Sub-sets of the catalogs are considered to allow the identification of some type of objects. For 2FHL, this includes HBL blazars, non-HBL blazars, and the entire catalog. Additionally, the partition of HBL blazars is tested also including the with Galactic latitude $2^\circ < |b_{\mathrm{II}}| < 10^\circ$. Unclassified sources have a high chance of being blazars if they are not on the Galactic Plane, hence, this addition gives an upper limit on the number of HBLs in the 2FHL catalog. The 2WHSP consists only of HBL type objects, the 3LAC catalog is tested for HBL objects, FSRQs, and other types, in addition to using the complete catalog.

As a last test, the preference of a neutrino connection to gamma rays and UHECRs is tested in a likelihood ratio test of the two scenarios in Eq. (10.2) and (10.3). The likelihood ratio is defined as the ratio of the p-values of both hypotheses

$$\Lambda = \frac{\mathcal{P}\left(n_\oplus\left(x_\oplus,\theta_\oplus\right)\right)}{\mathcal{P}\left(n_\ominus\left(x_\ominus,\theta_\ominus\right)\right)} \tag{10.4}$$

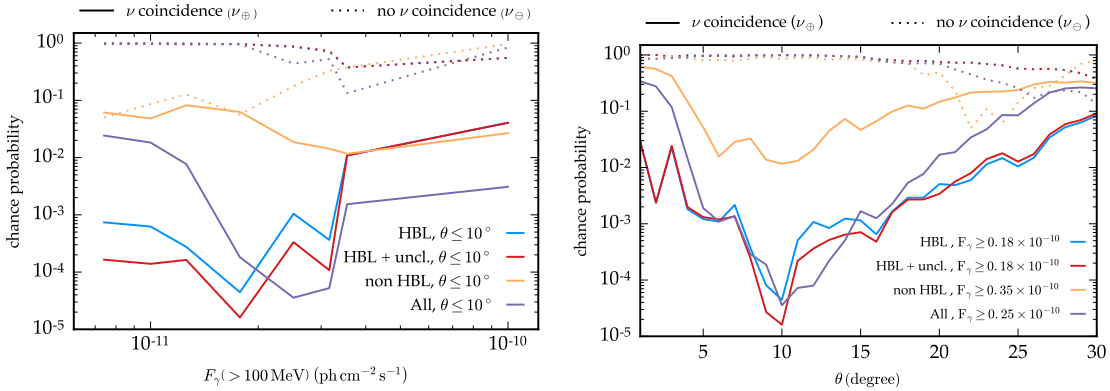

Figure 10.5: Correlation p-value of different partitions of the 2FHL catalog when scanning in flux (left) and angular distance (right). In the figure where flux/angular distance are scanned for, the other variable is fixed to the point marking the overall lowest p-value, as indicated in the legend. Dotted lines show the same result for the non-correlating result ($n_{\ominus}$).

where both p-values are minimized separately to give the best significance for the considered hypothesis. The results of the correlation and likelihood ratio test are trial corrected by repeating the analysis with data sets of scrambled neutrinos.

10.5 Results

The full result of the correlation of cosmic rays with the partitions of the catalogs using neutrinos as intermediaries is listed in Table 10.3. The biggest excess is given for the 2FHL catalog for the sample of HBL blazars with unclassified sources. In total, 80 UHECRs are observed in connection to gamma ray objects with flux and angular separation

$$F_{\gamma}\,(>50\,\mathrm{GeV}) \geq 1.8\times10^{-11}\,\mathrm{ph\,cm^{-2}\,s^{-1}} \tag{10.5}$$

$$\theta \leq 10^{\circ}\,. \tag{10.6}$$

The expected number of counterparts is 41.9, the distribution of identified number of counterparts is shown in Figure D.1. This marks an excess with a p-value of 1.6×10^{-5} at this choice of flux and angular distance. The results for the other partitions of the catalog are similar, but slightly less significant.

The trial correction due to scanning in eight bins for the flux $F_{\gamma}\,(>50\,\mathrm{GeV})$ and thirty bins in angular separation θ ranging from 1° to 30° is shown in Figure 10.6. The trial correction is very similar for all the catalogs and corresponds to a trial factor in the range of 30 to 40. Hence, the final significance of the HBL blazars and unclassified sources of the 2FHL in the correlation test is 5.5×10^{-4} or 3.32σ in terms of standard deviations (one-sided convention). The results of the other catalogs are slightly less significant, but for the HBL-only part of the catalog with 2.98σ close to the 3σ threshold. The non-HBL fraction of the 2FHL shows no significant correlation with a p-value of 15%.

The test of UHECR correlation with gamma ray objects that are *not* in correlation with neutrinos ($n_{\ominus}$ hypothesis) shows no significant correlation (Figure 10.5). For none of the catalogs, the local

γ-ray catalog	#	flux (x) or FoM	θ (deg)	#γ-ray above flux (FoM)	$n_\oplus(x,\theta)$ obs.	exp.	p-value local	global
2FHL	360	0.25	10	146	83	45.8	3.6×10^{-5}	1.5×10^{-3}
HBL	173	0.18	10	110	75	40.0	4.5×10^{-5}	1.4×10^{-3}
+ uncl.	186	0.18	10	114	80	41.9	1.6×10^{-5}	5.5×10^{-4}
non-HBL	174	0.35	10	56	37	19.8	1.2×10^{-2}	1.5×10^{-1}
2WHSP	1681	2.51	17	38	75	30.6	2.7×10^{-4}	1.1×10^{-2}
3LAC	1444	0.56	18	1000	231	200	1.9×10^{-2}	2.4×10^{-1}
FSRQ	415	1.00	18	438	174	165	3.1×10^{-1}	8.9×10^{-1}
HBL	386	0.71	16	115	131	92.4	4.7×10^{-3}	9.3×10^{-2}
other	645	1.00	3	285	19	11.8	3.3×10^{-2}	3.2×10^{-1}

Note – For 2FHL (3LAC), the flux $F_\gamma\,(>50\,\mathrm{GeV})$ ($F_\gamma\,(>100\,\mathrm{MeV})$) is in units of $10^{-10}\,\mathrm{ph\,cm^{-2}\,s^{-1}}$ ($10^{-8}\,\mathrm{ph\,cm^{-2}\,s^{-1}}$). The 2WHSP catalog is scanned in the dimensionless quantity "figure of merit" (FoM) as introduced in the text and Chang et al., "2WHSP: A catalog of HE and VHE gamma-ray blazars and blazar candidates".

Table 10.3: Correlation test results: local and global p-values obtained with respect to the gamma ray catalogs tested. The local p-value is the minimum p-value observed partitioning the catalogs in F_γ (or FoM) and scanning in angular distance θ between neutrino spatially selected sources and CRs. The global p-value is the corresponding one penalized for the relative trials applied through the two dimensional scan. The p-value calculation is done using $10^6 - 10^7$ trials depending on the significance of the result. The results of the likelihood ratio test and the p-value of the outcome are listed in the last two columns.

γ-ray catalog	$\log_{10}\Lambda$	Λ p-value	Significance (std. deviations)
2FHL	3.57	2.0×10^{-3}	2.88
HBL	3.93	1.0×10^{-3}	3.09
+ uncl.	4.37	4.1×10^{-4}	3.35
non-HBL	0.63	2.4×10^{-1}	0.71
2WHSP	2.68	9.8×10^{-3}	2.33
3LAC	0.40	3.1×10^{-1}	0.50
FSRQ	-0.99	8.3×10^{-1}	-0.95
HBL	1.61	7.2×10^{-2}	1.46
other	0.19	4.0×10^{-1}	0.25

Table 10.4: Results of the likelihood ratio test. For each partition of the catalogs used, the likelihood ratio and the significance of the result is quoted. The significance is given as p-value and converted to standard deviations in the one-sided convention.

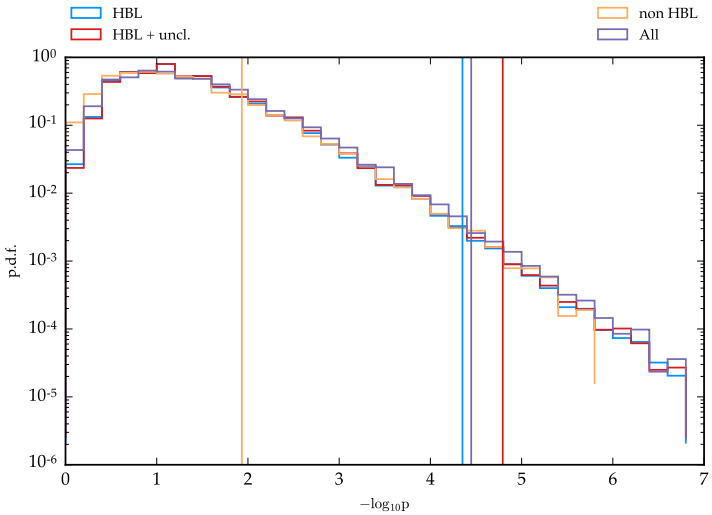

Figure 10.6: Trial correction of 2FHL correlation test. Shown is the negative decadic logarithm of the local p-value that is compared to results of background scrambles.

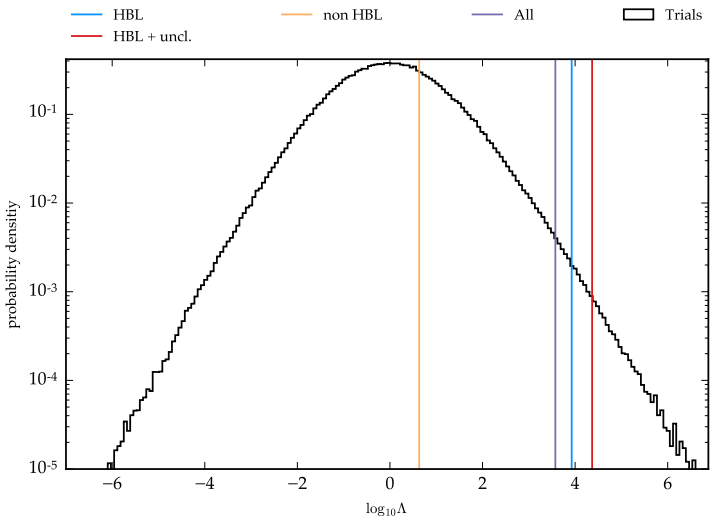

Figure 10.7: Likelihood ratio test for the 2FHL catalog. The outcome for the different subsets of the catalog are depicted as vertical lines and compared to the background expectation.

p-value exceeds the level of 1%. The connection of the two hypotheses of correlation with(out) neutrinos is quantified in the likelihood ratio in Eq. (10.4). The outcome of the likelihood ratio and the significance of the result are listed in Table 10.4, and shown in Figure 10.7 for the 2FHL catalog. The significance for both HBL blazars and HBL blazars with added unclassified sources exceeds the 3σ level in the likelihood ratio test. In the data, the HBL part of the 2FHL catalog shows clear preference of the scenario involving neutrinos in the correlation process, whereas the non HBL scenario shows no preference for either scenario.

The results of the 2WHSP and 3LAC catalog are shown in Figures D.4 to D.9 in Section D. The 2WHSP catalog accumulates only HBL blazars at longitude $|b_{\mathrm{II}}| > 10^{\circ}$ as can be seen in Figure 10.2. The scan is done in the "figure of merit" (FoM) quantifying that a blazar is detectable as a TeV gamma ray emitter.[19] The result of the likelihood ratio test is significant at 2.33σ. Due to the missing object coverage in the region close to the Galactic Plane, the significance is

[19] Chang et al., "2WHSP: A catalog of HE and VHE gamma-ray blazars and blazar candidates".

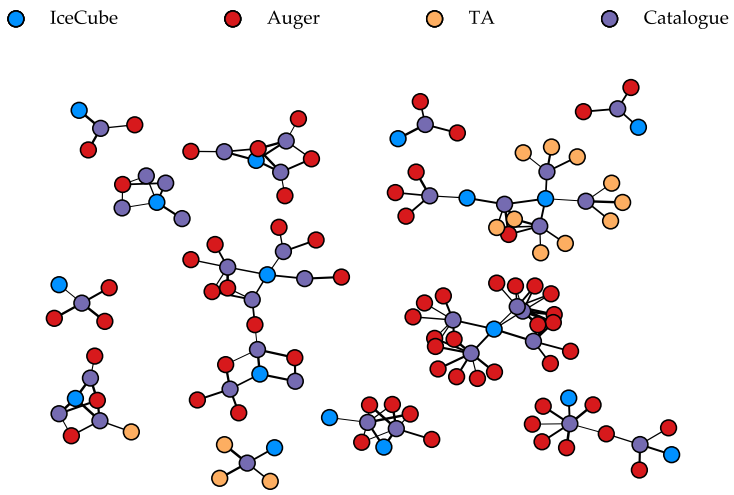

Figure 10.8: Graph representation of the correlating messengers for the 2FHL catalog. Neutrinos are correlated to HBL blazars. Subsequently, these are connected to cosmic ray events. The width of the lines indicate the angular separation of the clusters

smaller than for the 2FHL, as discussed in Section 10.3. The same applies to the 3LAC catalog, showing most significance using the HBL part of the catalog, resulting in a significance of 1.46σ. There is a trend observable that the most significant result is again in the HBL part of the catalog, while the remaining parts show less correlation, or a strong underfluctuations for the FSRQ part. Nevertheless, the overall correlation of HBL blazars of the 3LAC is still compatible with background expectation.

10.6 Discussion

For the 2FHL catalog using HBL blazars, one additional neutrino is found in spatial agreement with a gamma ray object above the threshold flux of $F_\gamma\,(50\,\mathrm{GeV}) > 1.8 \times 10^{-11}\,\mathrm{ph\,cm^{-2}\,s^{-1}}$ due to the addition of objects closer to the Galactic Plane. In total 17 out of 22 neutrino cascades are associated to a astrophysical object, the expectation given by pure background is 13.13 random associations. The excess is approximately $\sim 17.5\%$ of all events[20]. The cosmic ray sample shows correlation of 80 events with 41.9 random associations by background estimation. Compared to the total sample of 303 cosmic rays, this is 12.5% of the total flux. These two numbers are both of the same magnitude and do not saturate the total sample size, pointing towards possible additional populations constituting the flux.

The frequency of the synchroton peak of all the sources is shown in Figure 10.9, but no trend is observed for correlating sources. No correlation was found for non HBL objects, which are defined as $\nu_S < 10^{15}$ Hz.

Figure 10.8 shows a graph representation of the messengers with a positive correlation. In total, thirteen independent clusters are identified for the 17 neutrinos found in the test for the 2FHL catalog using HBL and unclassified sources. The complete list of all the sources is

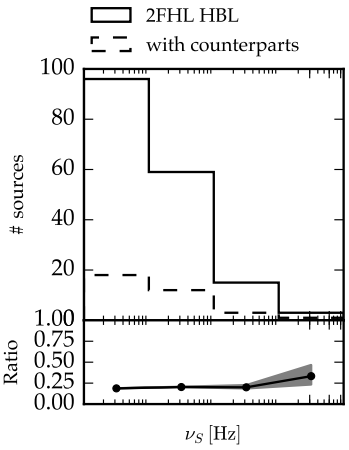

Figure 10.9: Synchroton peak distribution of 2FHL HBL objects. Sources found in correlation test are shown as dashed line.

[20] Regarding the astrophysical neutrino component, the fraction is $\sim 19.6\%$ assuming 90% of the events are of astrophysical origin.

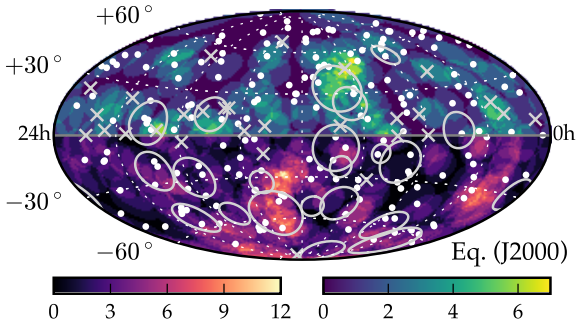

Figure 10.10: Sky map of neutrino and cosmic ray arrival directions. Cosmic rays are shown in colors with different colors for northern and southern sky, respectively. Neutrinos are crosses (tracks) and circles (cascades). All objects of the 2FHL catalog (HBL + unclassified) are shown as white dots.

shown in Table 10.5, prominent sources like Mkn 421, PKS 2005-489, and 1ES 1011+496 are part of the clusters. Those sources are well-known TeV emitters and discussed as candidates for neutrino and cosmic ray acceleration in the literature.[21]

A determination of the redshift is challenging for BL Lac objects due to the lack of broad emission lines in their spectrum. Thus, only a small set of the objects in the catalogs has a redshift measurement. The sources in correlation could be in conflict with a suppression of UHECRs due to the GZK cutoff, as discussed in Section 3.5. The mean energy loss distance in terms of redshift is $z \approx 0.2$ for energies of $\sim 55\,\mathrm{EeV}$.[22] Nevertheless, the correlating cosmic rays are only a small fraction of all cosmic rays (one quarter of 303 cosmic rays in total), and half of those are random background connections as listed in Table 10.3. Moreover, the intrinsic power spectrum of cosmic rays is unknown. Hence, it is at the moment not clear if the scenario proposed is in tension with the GZK cutoff.

Ultra-high energy cosmic rays associated to HBL blazars will constitute neutrinos and gamma rays to the extra-galactic diffuse background during propagation, for the HBL blazar population that does not show evolution with redshift.[23] The fraction of HBL blazars to the total population of blazars is very small and HBL blazars do not evolve cosmologically. Consequently, the contribution to the extra-galactic diffuse gamma ray and neutrino background is small.[24] The diffuse background is then dominated by HBL blazars itself.[25]

Figure 10.10 shows the cosmic ray arrival map with neutrinos overlaid for the result of this test, that is, using 10° angular circle for cosmic rays. Of the correlating neutrinos, only cascades with large angular uncertainties were found with counterparts.

No neutrino-induced muon tracks were identified to be associated to HBL sources. Most of the tracks used in the analysis come from the up-going muon track search,[26] whereas 17 out of 22 cascades of the starting event sample have at least one counterpart. Because of the good pointing of track events, the background of random associations is very small.

In order to evaluate a possible tension between the null result in tracks and the excess observed in cascades, a Feldman-Cousins construction[27] is used to estimate the signal strength in both channels,

[21] Petropoulou, Dimitrakoudis, et al., "Photohadronic origin of γ-ray BL Lac emission: implications for IceCube neutrinos"; Fang et al., "Is the Ultra-High Energy Cosmic-Ray Excess Observed by the Telescope Array Correlated with IceCube Neutrinos?"

[22] Ruffini, Vereshchagin, and Xue, "Cosmic absorption of ultra high energy particles".

[23] Gavish and Eichler, "On ultra high energy cosmic rays and their resultant gamma rays".

[24] Taylor, Ahlers, and Hooper, "Indications of Negative Evolution for the Sources of the Highest Energy Cosmic Rays".

[25] Giommi and Padovani, "A simplified view of blazars: contribution to the X-ray and γ-ray cosmic backgrounds"; Ajello, "The Origin of the Extragalactic Gamma-Ray Background and Implications for Dark-Matter Annihilation".

[26] Aartsen, "Evidence for Astrophysical Muon Neutrinos from the Northern Sky with IceCube".

[27] Feldman and Cousins, "A Unified approach to the classical statistical analysis of small signals".

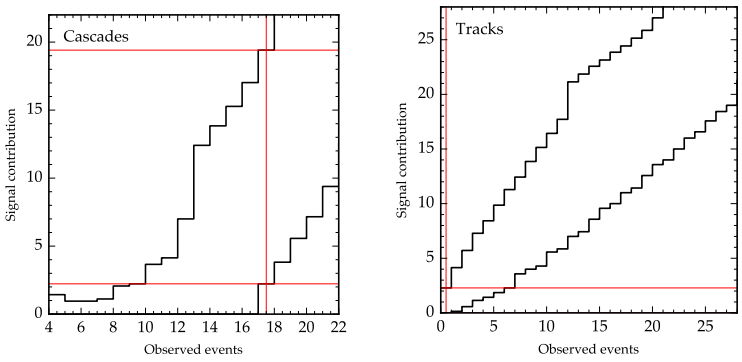

Figure 10.11: Feldman-Cousins limits for neutrino cascades and track events shown in the left and right figure, respectively. For both samples, seventeen and zero events were observed , respectively (red line). From that, the signal strength can be deduced given by the 90% bands by Feldman-Cousins construction.

with the counting method Eq. (10.1) used in the test. The calculation is done in the following steps:

1. The distribution of random associations is evaluated by repeating the analysis 500 000 times with neutrino events scrambled in right ascension. Each background simulation is characterized by N randomly assigned counterparts.

2. Signal at different strengths is added to the random sample. The number of signal events follows a Poisson distribution with mean K events.

3. The probability to have k signal events (out of K in total) without a random association is a binomial distribution

$$P\left(k|K\right) = \binom{K}{k} \left(\frac{N}{M}\right)^{K-k} \left(1 - \frac{N}{M}\right)^{k} \tag{10.7}$$

   if N random associations are seen in a sample of total M events ($M = 22$ or 28 for cascades or tracks, respectively).

4. The number of observed events increases by k signal events that have a newly identified astrophysical counterpart compared to the background only case. The sum of added signal and random counterparts cannot exceed the total number M of the sample size.

Figure 10.11 shows the 90% Feldman-Cousins limits for cascades (left) and tracks (right). The number of observed events in data is seventeen and zero for the two event classes, respectively, and marked in the figures. The resulting confidence regions are then converted to a fraction ρ of the astrophysical flux. This is given by

$$\rho = \frac{N_{\mathrm{X,FC}}}{\eta_X \times M_X} \tag{10.8}$$

for a signal count $N_{\mathrm{X,FC}}$ given by the Feldman-Cousins construction and normalized to the expected total number of astrophysical events in the sample, that is, the sample size M_X times the astrophysical neutrino purity η_X of the sample X. For cascades, the sample consists of 22 events and the purity of the selection is assumed to be 90% given by the background expectation of IceCube.[28] The result-

[28] Aartsen, "Evidence for High-Energy Extraterrestrial Neutrinos at the IceCube Detector".

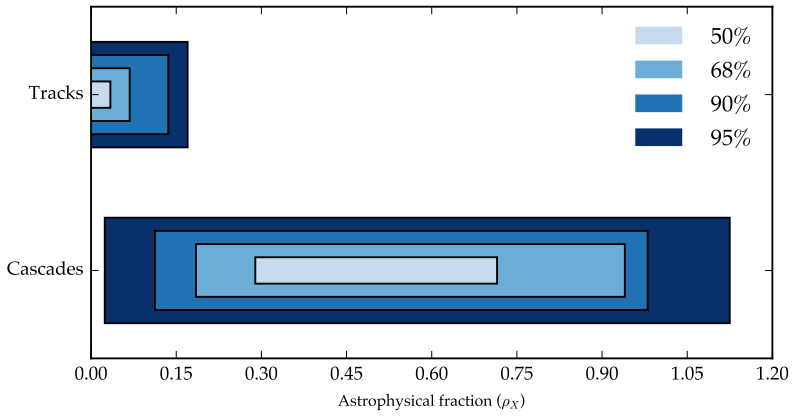

Figure 10.12: Feldman-Cousins bands at different confidence levels for the for the contribution of events correlating with blazars of type HBL to the total astrophysical neutrino flux.

ing confidence region is shown in Figure 10.12 for different coverage. Due to the large angular uncertainties of cascades, the number of random associations is large, resulting in large range of possible signal strengths, but the null-result is excluded above 95% confidence.

Regarding tracks, 28 tracks are used in the test, and eight originate in the starting event sample (90% purity) and the remaining twenty in the up-going muon analyses ($\sim$ 50% purity, see Table 10.1). The resulting Feldman-Cousins confidence bands for the contribution of the events to the astrophysical flux is shown in Figure 10.12. No events were seen for tracks, hence, only upper-limits are given.

Both channels are in agreement within 90% confidence and a fraction of $\sim$ 15% contribution of HBL blazars to the diffuse astrophysical signal. With additional data for both tracks and cascades, the refined confidence bands of the signal in both channels is an important test to validate the results obtained here.

Table 10.5: IceCube neutrinos, 2FHL objects (type HBL and unclassified) and Auger/TA UHECRs selected in correspondence with the minimum p-value obtained ($F_\gamma \geq 1.8 \times 10^{-11}$ ph cm^{-2} s^{-1} and $\theta \leq 10°$). We report for each neutrino the ID number, the energy and the median angular uncertainty (median$(\theta)_{\rm IC}$) as quoted by IceCube; for the γ-ray objects the *Fermi* source name and common name, and if known, the redshift; for the UHECRs the year of detection, the coordinates, the dataset, the energy and angular distance from the 2FHL object.

Neutrino			γ-ray object			UHECR					
ID	Energy TeV	σ 1°	2FHL name	Common name	z	Year	α	δ	Dataset	Energy EeV	θ 1°
9	63.2	16.5	J0915.9+2931	B2 0912+29	0.19	2013	138.6	26.1	Auger	62.1	3.4
						2008	140.0	28.7	TA	59.2	1.0
						2010	129.0	29.1	TA	60.5	8.5
			J0910.4+3327	Ton 1015	0.35	2013	138.6	26.1	Auger	62.1	7.4
						2008	140.0	28.7	TA	59.2	5.1
						2010	145.0	40.7	TA	92.2	9.1
						2010	137.0	41.5	TA	68.9	8.1
						2010	129.0	29.1	TA	60.5	8.3
			J1104.4+3812	MKN 421	0.03	2011	163.7	28.9	TA	62.3	9.5
						2011	157.0	38.8	TA	72.9	7.3
						2012	160.0	35.6	TA	57.4	5.7
			J1015.0+4926	1ES 1011+496	0.20	2008	152.4	45.8	TA	79.3	3.7
						2010	139.0	49.6	TA	63.7	9.5
						2013	165.0	52.4	TA	62.5	7.8
11	88.4	16.7	J1027.0–1749	1RXS J102658.5–174905	0.65	2009	147.2	-18.3	Auger	64.1	9.1
						2011	150.0	-10.3	Auger	100.0	9.9
						2011	149.0	-13.0	Auger	57.2	9.0
						2013	154.0	-15.8	Auger	53.9	3.1
			J0952.9–0841	1RXS J095303.4–084003	–	2006	142.3	-13.1	Auger	54.0	7.3
						2009	147.0	-18.3	Auger	64.1	9.6
						2011	150.0	-10.3	Auger	100.0	2.4
						2011	149.0	-13.0	Auger	57.2	4.3
						2013	154.0	-15.8	Auger	53.9	9.3
12	104	9.8	J2009.4–4849	PKS 2005–489	0.07	2006	305.6	-46.3	Auger	60.0	3.3
						2007	315.0	-53.8	Auger	72.7	9.4
						2008	306.0	-55.1	Auger	55.1	6.8
			J1959.6–4725	SUMSS J195945–472519	–	2006	305.6	-46.3	Auger	60.1	4.0
						2008	306.0	-55.1	Auger	55.1	8.7
						2013	308.0	-39.5	Auger	67.3	9.9
			J1936.9–4721	PMN J1936–4719	0.26	2006	305.6	-46.3	Auger	60.1	7.8
						2013	287.0	-55.0	Auger	52.9	9.0
14	1041	13.2	J1713.9–2027	1RXS J171405.2–202747	–	2008	252.7	-22.7	Auger	64.2	5.9
			J1823.6-3454	NVSS J182338–345412	–	2013	284.5	-37.6	Auger	54.4	7.4
						2009	286.0	-37.8	Auger	61.0	8.8
						2009	276.0	-33.4	Auger	65.8	1.5
						2011	284.0	-28.6	Auger	80.9	9.2
			J1829.0–2417	1RXS J182853.8–241746	–	2010	284.7	-28.2	Auger	65.2	7.6
						2009	276.0	-33.4	Auger	65.8	9.1
						2011	284.0	-28.6	Auger	80.9	7.1
			J1741.2–4021		–	2010	258.1	-44.9	Auger	72.9	7.0
						2012	260.0	-32.7	Auger	61.8	8.9
17	200	11.6	J1555.7+1111	PG 1553+113	0.44	2007	245.8	8.5	Auger	54.9	7.3
						2011	239.0	3.9	Auger	60.3	7.3

Continued on next page

Table 10.5: continued

Neutrino			γ-ray object			UHECR					
ID	Energy TeV	σ 1°	2FHL name	Common name	z	Year	α (1°)	δ (1°)	Dataset	Energy EeV	θ 1°
19	71.5	9.7	J0543.9–5533	1RXS J054357.3–553206	0.27	2010	80.2	-64.1	Auger	54.3	9.0
						2013	92.1	-64.1	Auger	65.4	9.1
						2013	91.4	-60.6	Auger	72.5	5.8
20	1141	10.7	J0352.7–6831	PKS 0352–686	0.08	2012	37.0	-75.8	Auger	58.7	9.6
						2014	45.2	-65.8	Auger	63.6	5.7
						2010	80.2	-64.1	Auger	54.3	9.8
						2013	56.6	-67.8	Auger	70.7	0.9
						2013	64.7	-70.1	Auger	68.8	2.8
						2014	72.8	-73.5	Auger	60.0	6.8
22	220	12.1	J1958.3–3011	1RXS J195815.6–30111	0.12	2011	295.1	-27.6	Auger	54.8	4.7
						2008	304.0	-26.2	Auger	52.6	5.8
						2011	305.0	-34.5	Auger	67.4	6.6
			J1917.7–1921	1H1914–194	0.14	2010	284.7	-28.2	Auger	65.2	9.8
						2011	295.0	-27.6	Auger	54.8	9.8
						2009	294.0	-20.5	Auger	59.5	4.9
			J1921.9–1607	PMNJ1921–1607	–	2009	294.5	-20.5	Auger	59.5	5.8
26	210	11.8	J0905.7+1359	MG1 J090534+1358	1.07	2011	132.8	12.9	Auger	55.9	3.7
						2007	137.0	6.2	Auger	53.6	7.9
						2009	129.0	15.2	Auger	52.2	6.9
			J0915.9+2931	B2 0912+29	0.19	2013	138.6	26.1	Auger	62.1	3.4
						2008	140.0	28.7	TA	59.2	1.0
						2010	129.0	29.1	TA	60.5	8.5
27	60.2	6.6	J0816.3–1311	PMN J0816–1311	–	2010	131.9	-15.5	Auger	76.1	7.9
						2013	123.0	-6.2	Auger	85.3	7.0
33	385	13.5	J1933.3+0725	1RXS J193320.3+072616	–	2008	287.7	1.5	Auger	118.0	8.2
						2013	299.0	8.7	Auger	54.6	5.4
						2011	288.0	0.3	TA	136.0	8.8
			J1931.1+0937	RX J1931.1+0937	–	2008	287.7	1.5	Auger	118.3	9.6
						2013	299.0	8.7	Auger	54.6	5.9
			J1942.8+1033	1RXS J194246.3+103339	–	2006	299.0	19.4	Auger	82.0	9.4
						2013	299.0	8.7	Auger	54.6	3.5
35	2004	15.9	J1328.6–4728	1WGA J1328.6–4727	–	2005	199.1	-48.5	Auger	52.1	2.3
						2006	201.0	-55.3	Auger	69.5	7.8
						2006	201.0	-45.3	Auger	59.5	2.4
						2007	200.0	-43.4	Auger	60.0	4.3
						2008	202.0	-54.9	Auger	53.4	7.4
			J1304.5–4353	1RXS 130421.2–435308	–	2004	199.7	-34.8	Auger	84.7	9.4
						2005	199.0	-48.5	Auger	52.1	5.1
						2006	201.0	-45.3	Auger	59.5	3.7
						2007	200.0	-43.4	Auger	60.0	3.0
						2007	193.0	-35.3	Auger	60.7	9.0
						2009	194.0	-36.4	Auger	72.5	7.7
			J1307.6–4259	1RXS 130737.8–425940	–	2004	199.7	-34.8	Auger	84.7	8.4
						2005	199.0	-48.5	Auger	52.1	5.8
						2006	201.0	-45.3	Auger	59.5	3.7
						2007	200.0	-43.4	Auger	60.0	2.4
						2007	193.0	-35.3	Auger	60.7	8.4
						2009	194.0	-36.4	Auger	72.5	7.0
						2013	201.0	-34.6	Auger	62.7	9.0

Continued on next page

Table 10.5: continued

Neutrino			γ-ray object			UHECR					
ID	Energy TeV	σ 1°	2FHL name	Common name	z	Year	α (1°)	δ (1°)	Dataset	Energy EeV	θ 1°
			J1353.5–6640	1RXS J135341.1–664002	–	2007	195.5	-63.4	Auger	61.9	6.3
						2008	196.0	-69.7	Auger	71.1	5.5
						2013	199.0	-63.9	Auger	53.2	4.9
						2004	208.0	-60.1	Auger	58.6	6.6
						2008	187.0	-63.5	Auger	65.3	9.3
						2010	216.0	-66.5	Auger	60.3	3.1
						2010	219.0	-70.8	Auger	89.1	5.6
			J1507.4–6213		–	2013	240.3	-68.9	Auger	61.5	8.7
						2004	208.0	-60.1	Auger	58.6	9.3
						2007	220.0	-53.9	Auger	61.5	9.2
						2010	216.0	-66.5	Auger	60.3	6.3
						2010	219.0	-70.8	Auger	89.1	9.2
						2010	232.0	-56.6	Auger	54.9	6.2
39	101.3	14.2	J0649.6–3139	1RXSJ064933.8–31391	–	2007	105.9	-22.8	Auger	60.8	9.3
			J0622.4–2604	PMNJ0622–2605	–	2007	105.9	-22.8	Auger	60.8	9.9
			J0631.0–2406	1RXSJ063059.7–240636	–	2007	105.9	-22.8	Auger	60.8	7.6
			J0639.9–1252		–	–	–	–	–	–	–
41	87.6	11.1	J0416.9+0105	1ES 0414+009	0.29	2008	67.7	4.0	Auger	52.0	4.5
						2012	56.4	-3.2	Auger	53.3	9.0
46	158	7.6	J1027.0–1749	1RXS J102658.5–174905	0.65	2009	147.2	-18.2	Auger	64.1	9.1
						2011	150.0	-10.3	Auger	100.0	9.9
						2011	149.0	-13.0	Auger	57.2	9.0
						2013	154.0	-15.8	Auger	53.9	3.1
48	104.7	8.1	J1440.7–3847	1RXS J144037.4–38465	–	2004	224.7	-44.0	Auger	58.2	6.2
						2008	221.0	-42.8	Auger	73.1	4.0
						2011	219.0	-41.9	Auger	58.8	3.2
51	66.2	6.5	J0540.5+5822	GB6 J0540+5823	–	2009	99.2	62.7	TA	80.7	8.1
						2010	78.8	61.4	TA	61.2	4.4
						2011	82.5	57.7	TA	74.7	1.6

11 Conclusion

Even after more than a hundred years after the first discovery of cosmic rays,[1] their origin is not yet fully understood. Astroparticle and cosmic ray physics is an active branch of modern physics and the ongoing efforts are bigger than ever.

In the recent years, larger detectors probed the highest energy end of the cosmic ray spectrum, high-energy astrophysical neutrinos were observed for the first time and big advancements in gamma ray astronomy were made. Using the entire information that is given by the three messengers, detailed knowledge about the ongoing processes in the universe can be gained.

This thesis presented most recent searches for time-integrated emission of high-energy neutrinos with the IceCube Neutrino Observatory. Seven years of recorded data were analyzed and no evidence for the origin of the observed diffuse neutrino spectrum has been found. In this work, previous analyses are extended by three years of data obtained over the full sky. Hence, an overall improvement of $\sim 40\%$ with respect to the sensitivity towards a faint neutrino signal of astrophysical sources is realized by a largely increased exposure.

In the northern sky, IceCube's sensitivity exceeds the integrated isotropic neutrino flux by more than a factor of ten. Thus, a larger population of faint point-like sources has to be responsible for the integrated flux, or other scenarios like large scale structures. For the closest blazars observed at Earth, IceCube is now able to constrain the amount of hadronic acceleration strongly in the energy range from TeV to multiple PeV energies, constraining the proton component in lepto-hadronic models. Thus, the cosmic ray output of such sources can be constrained using the (non-)observation of neutrinos coinciding with the sources.

With increased exposure, IceCube continues to push the boundaries to even fainter signals of neutrino emission. The growth is faster than would be expected by background limitations. New detectors are under construction and in consideration. Especially the realization of KM3NeT in the northern hemisphere will allow to observe large fractions of the Galactic Plane at much better sensitivity with lower energy threshold than currently possible with IceCube.[2] Moreover, the data sample developed in this thesis provides three years of muon data that can be tested using other hypotheses than the scenarios tested here. This involves stacking analyses of large populations of gamma ray objects like HBL blazars[3] or Galactic supernova

[1] Hess, "Über Beobachtungen der durchdringenden Strahlung bei sieben Freiballonfahrten".

[2] Adrian-Martinez, "Letter of intent for KM3NeT 2.0".

[3] Huber, "Sensitivity Studies for Blazar Stacking Searches with the IceCube Neutrino Observatory".

remnants, time-dependent analyses,[4] spatially extended sources[5] or autocorrelation studies.[6]

In a novel study as part of this thesis, high-energy blazars of BL Lac type with high-frequency peak are identified as possible counterparts of neutrinos and ultra-high energy cosmic rays at high significance, deviating more than 3σ from the background hypothesis. In this study, only the highest energetic particles available were used, and the correlation of the messengers with the counterparts is only found for one class of sources. The overall strength found however cannot describe the entire flux of neutrinos and cosmic rays observed at Earth. The results have to be further tested against the redshift distribution of the astrophysical counterparts found, and additional data is available at lower energies, which will provide additional insight into the results when used in the test.

Therefore, even though the sources of neutrinos and cosmic rays still defy clear identification, recent improvements presented in this thesis continue to give insight into the possible mechanisms producing such particles. The knowledge about cosmic rays grew considerably in the last years, continuing to confine the possibilities of cosmic ray acceleration in the universe further and at a faster pace. Thus, with the increasing insight into cosmic rays nature, the field of astroparticle physics continues to grow and the mystery of the origin of astrophysical neutrinos and ultra-high energy cosmic rays is possibly deciphered in the not too distant future.

[4] Aartsen, "Searches for Time Dependent Neutrino Sources with IceCube Data from 2008 to 2012".
[5] Aartsen, "Searches for Extended and Point-like Neutrino Sources with Four Years of IceCube Data".
[6] Aartsen, "Searches for small-scale anisotropies from neutrino point sources with three years of IceCube data".

Acknowledgments / Danksagung

The work presented here and the realization of this thesis would not be possible without the support of many people that I want to thank at this point.
First, I want to thank my supervisor, Elisa Resconi, for her guidance in the last three years. It is a pleasure working with you and thank you for showing me the exciting field of (high-energy) astroparticle physics within the IceCube experiment.
I want to thank Jochen Greiner for agreeing to be the second reviewer of this thesis, and Björn Garbrecht for being the chair of the review commission.
The research stay at UW Madison in Summer 2014 would not have been possible with the financial support of the DAAD. Here, I want to thank my colleagues from UW that welcomed me to work with them and learn many new things.
I am grateful for the financial support by the TUM Graduate School and the Dr.-ing. Leonhard Lorenz Stiftung that allowed me to show my results at various international conferences.
To my colleagues in Munich I cannot be grateful enough. It is a great pleasure working with you, as well as discussing whatever topics in the "Coffice" or at the *Kicker*. This goes especially to my office mates Kai, Matthias, and Andrea, who as well were kind enough to give feedback while writing this thesis. To my former colleagues Andreas, Anna, Joost, and Martin I want to say thank you as well for the time we have worked together in my first years.
Being part of the IceCube collaboration is a great experience where I met many kind and interesting people. Here, I especially want to thank the muon and point source working group.
Additional thanks go to Paolo Padovani and Maria Petropoulou for their discussion and the work we accomplished together. Moreover, I want to thank Paolo for being the contact person for my work in the TUM Graduate School.
Last but not least I want to thank my family that supported me all this way, and for their interest in the work I am doing.

A Abbreviations and definitions

Throughout this thesis, many variables or abbreviations are occurring multiple times and are commonly written with the same character or abbreviated for convenience. In the following, the most common are listed for reference.

Acronym	Meaning
AGN	Active galactic nucleus
DOM	Digital optical module in IceCube
FoM	Figure of merit, quantity used in the 2WHSP to describe the possibility to identify an event with current gamma ray detectors.
FSRQ	Flat spectrum radio quasar
IC*XX*	IceCube detector operation with *XX* strings. The full operational detector uses 86 strings.
HBL	"High-energy cutoff BL Lacs": Blazar of type BL Lac with high synchroton peak frequency (here: $\nu_S > 10^{15}$ Hz.
hot spot	Most significant location found in the clustering analyses, that is, the location with smallest p-value for the background only hypothesis.
MPE	Multi photo electron – description used in likelihood reconstructions in IceCube.
pe	Photo-equivalent charge detected by DOMs in IceCube
PWN	Pulsar wind nebula
Pulse	Photon-induced waveform recorded in IceCube DOMs.
SNR	Supernova remnant
Starting event	Events that are detected in IceCube and start within the detector. Only neutrinos events can produce such a signature.
String	IceCube consists of 86 deployed strings that each host 60 DOM along cables.
SPE	Single photo electron – description used in likelihood reconstructions in IceCube.
SplineMPE	MPE reconstruction using simulation tables that are evaluated using B-splines.
Through-going track	Muons that traverse the IceCube detector.
UHECR	Ultra-high energy cosmic ray

Variable	Description	Reference
α	Right ascension in equatorial coordinates (J2000.0 epoch). In IceCube this is simply connected to the azimuth with one rotation per day: $\alpha = \varphi_0 \pm 2\pi \times t$ / d.	–
δ	Declination in equatorial coordinates (J2000.0 epoch). This is directly related to the zenith angle in IceCube with $\sin\delta = -\cos\theta$.	–
φ	Azimuth observed in IceCube.	–
θ	Zenith angle observed in IceCube. In Section 10, this is used for the deflection angle of cosmic rays.	Section 6, Section 10
$\partial\phi/\partial E$	Differential (neutrino) flux in energy. The units are usually in $\mathrm{TeV}^{-1}\,\mathrm{cm}^{-2}\,\mathrm{s}^{-1}$.	–
σ	In the discussion of interactions, σ is the cross section of an interaction. Otherwise, it is the angular uncertainty of the reconstructed arrival direction of an event.	Section 4, Section 5
n_S	Number of signal events used in the likelihood maximization of clustering analyses.	Section 5
γ	Spectral index of a neutrino source with power law $\partial\phi/\partial E \propto E^{-\gamma}$. Used in the physics descriptions of a source and in the likelihood maximization as a fitting parameter.	Section 2, Section 5
$\mathcal{L}$	The likelihood function of a statistical test.	–
$\mathcal{TS}$	The test statistic defined in an analysis.	–

In the description of the event sample and the selection for the best neutrino candidates regarding searches for neutrino point sources, typical event variables are used. These variables are briefly explained here and appear throughout the thesis (Section 6 and figures of variable distributions).

Number of direct hit DOMs– A direct hit is defined as a pulse recorded by a DOM that has a time residual (Eq. (4.12)) smaller than a certain time window. Small time residuals identify unscattered light that carries the most information about the muon direction. The time windows used here are $(-15\,\mathrm{ns}, 125\,\mathrm{ns})$ and $(-15\,\mathrm{ns}, 250\,\mathrm{ns})$ called time window *D*, *E*, respectively.

Length between direct hit DOMs– A muon emits light constantly along its track. The length along the reconstructed track from the first to last observed direct hit[1] quantifies the length of the lever arm. Long lengths indicate large lever arms that guarantee good reconstructions.

[1] Same time window definitions as before

Empty track length– Similar to the direct length of first to last direct hit, the *empty length* is the distance of two subsequent direct hits. A muon track constantly emits light along the path, hence, the empty length is expected to be small. Coincident events that are falsely reconstructed as one up-going event can have large empty length values because there is no light emitted between the tracks.

Charge center of gravity– The center of gravity using the DOM charge q_i (Q_{tot} charge of total detector) is defined as $\mathbf{x}_{\text{cog}} = \sum_i q_i \mathbf{x}_i / Q_{\text{tot}}$. Values close to the edges of the detector identify events not entering the detector.

Hit separation along track– The constant emission of light along the track should be visible as a "cloud of light" that travels alongside the track. Hence, the hits are separated into the first and last quartile of hits recorded in time. For both, the *center of gravity* is calculated. A large distance between those positions indicates a long track with long lever arm. Corner-clipping events or cascades have small distances between the two positions.

Angular difference of two reconstructions– By comparing the direction of different reconstructions, insight about the stability of the reconstruction is gained. If two hypotheses for the reconstruction yield vastly different minima, this can be due to a mis-reconstructed event.

Reduced log-likelihood– The reduced logarithm of the likelihood *rlogl*, that is the logarithm normalized by the degrees of freedom for the event[2]. Usually, the negative likelihood is used. Smaller values indicate a better reconstruction.

[2] The degrees of freedom for an event reconstruction are the number of observed hits minus the number of parameters used for observation.

Bayesian likelihood ratio– As discussed in Section 4.7 and Eq. (4.17), the reconstructed fit (up-going) can be compared to another *Bayesian fit* that was forced to be reconstructed down-going. The comparison is done by calculating the likelihood ratio of the two reconstructions, $\log(\mathcal{L}/\mathcal{L})_{\text{Bayes}}$. Small values of the ratio indicate a second likelihood maximum in the down-going region which is probable to appear for mis-reconstructed atmospheric muons.

Reconstruction uncertainty– As discussed in Section 4.7, the likelihood landscape around the reconstruction direction can be used to estimate the uncertainty of the maximum found by fitting a parabola around that direction.[3] If the parabola is very narrow, the maximum is very sharp, indicating a well reconstructed event.

[3] Neunhöffer, "Estimating the angular resolution of tracks in neutrino telescopes based on a likelihood analysis".

B Data distributions

B.1 Low-level filtering

The low-level filtering described in Section 6.2 uses cuts on multiple variables to remove clear background. The cuts are listed in Table 6.1 and 6.2. Distributions of multiple variables are shown from Figures B.1 to B.8 for the northern sky and from Figures B.9 and B.12 for the southern sky, respectively.

For all variables, 10% of the recorded data is shown and compared to atmospheric muons (model H4a, see Section 3.2), conventional atmospheric muon neutrinos,[1] and the observed diffuse astrophysical neutrino signal in IceCube (E^{-2}, Section 2.3). The distributions are shown before applying the first cuts, and after the low-level filtering. The ratio before and after the cuts are shown as a ratio plot at the bottom.

[1] Honda et al., "Calculation of atmospheric neutrino flux using the interaction model calibrated with atmospheric muon data".

B.2 Boosted decision tree training and variables

Figures B.13 and B.14 show the cross validation for overtraining using the BDTs trained with soft spectra in the up-going region and the single spectrum trained in the down-going region, respectively.

Figures B.15 to B.26 show the distributions of different variables when applying the final cut on BDT score in the multivariate event selection (Section 6.3). The visualization of the plot is similar to the low-level figures shown in this appendix as well. For all distributions, the Monte Carlo is not accounting for any systematic effects. Especially for variables related to the light yield (number of hit modules or total charge in detector), the rate of data events seems to be larger than prediction from MonteCarlo. With larger light yields or a slightly harder spectral index than the model predicts,[2] this difference can be effecitively absorbed, as realized in fits of the astrophysical spectrum.[3]

[2] Ibid.

[3] Aartsen, "Observation and Characterization of a Cosmic Muon Neutrino Flux from the Northern Hemisphere using six years of IceCube data".

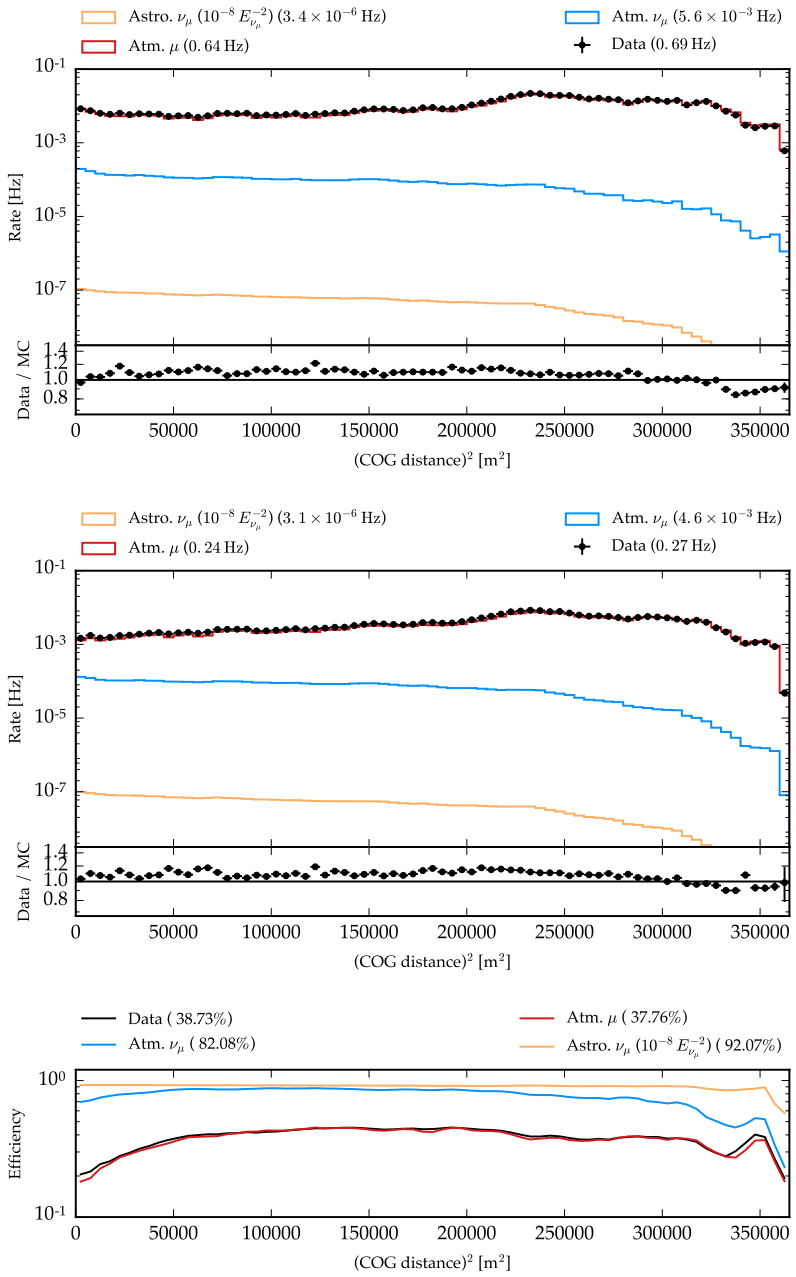

Figure B.1: Distribution of COG radial distance at low-level cuts. Shown is *burnsample* (Data) and Monte Carlo data for atmospheric muons (H4a) and neutrinos (Honda 2006), and astrophysical neutrinos (10^{-8} GeV cm^{-2} s^{-1} sr^{-1}). For each component, the rate expectation is given in the legend. The top plot shows the values before the cuts, the middle plot after all cuts except the one on rlogl which is shown. The bottom plot shows the efficiency of all other cuts on rlogl, that is, the ratio of both figures. For both variable distributions, the data to Monte Carlo comparison is shown at the bottom.

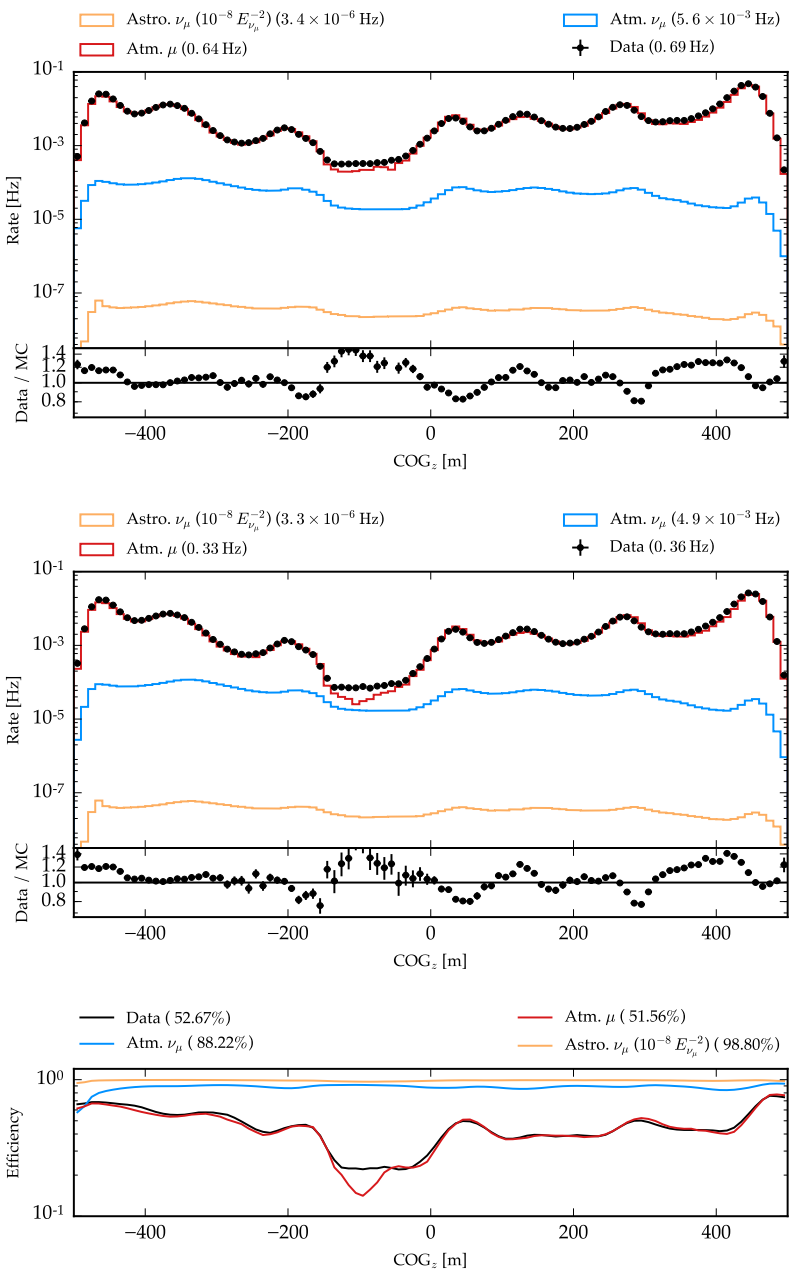

Figure B.2: Cosine of angle between MPE with spline likelihood and linefit. Shown in same way as for previous Figure.

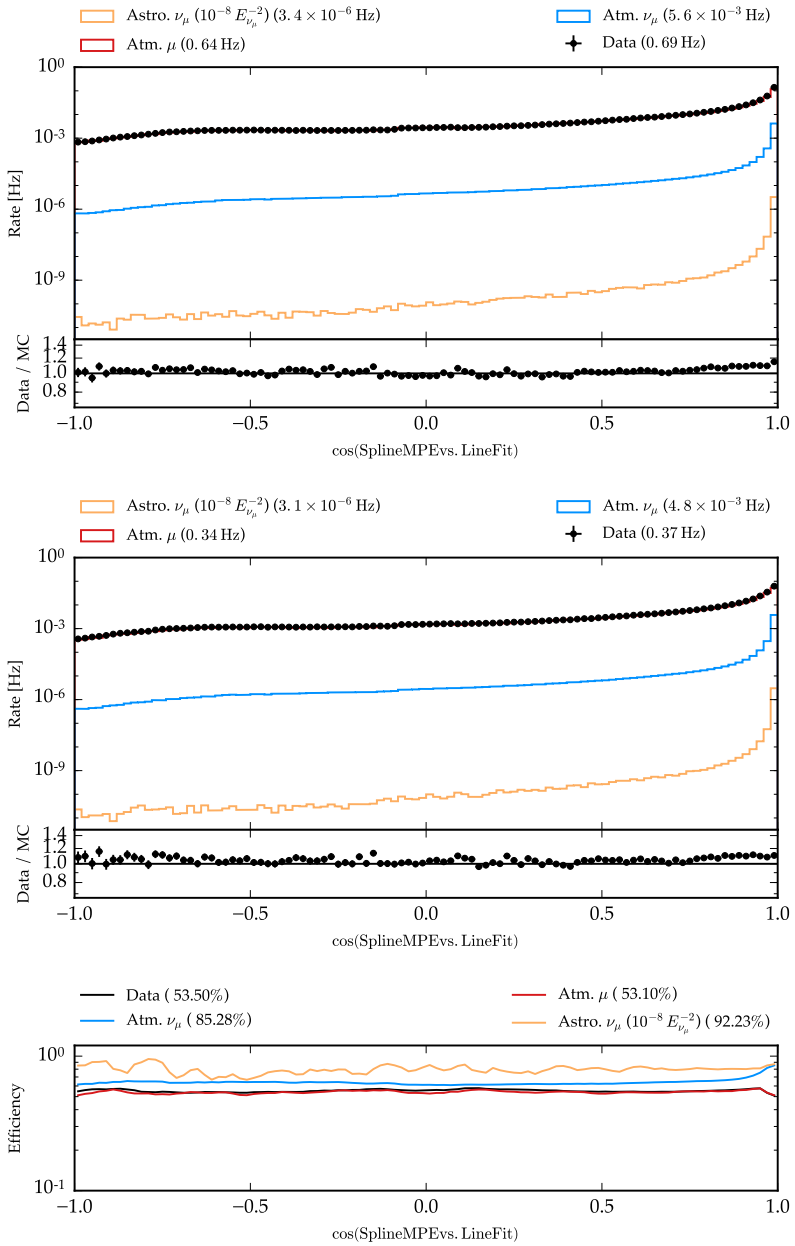

Figure B.3: Cosine of angle between MPE with spline likelihood and linefit. Shown in same way as for previous Figure.

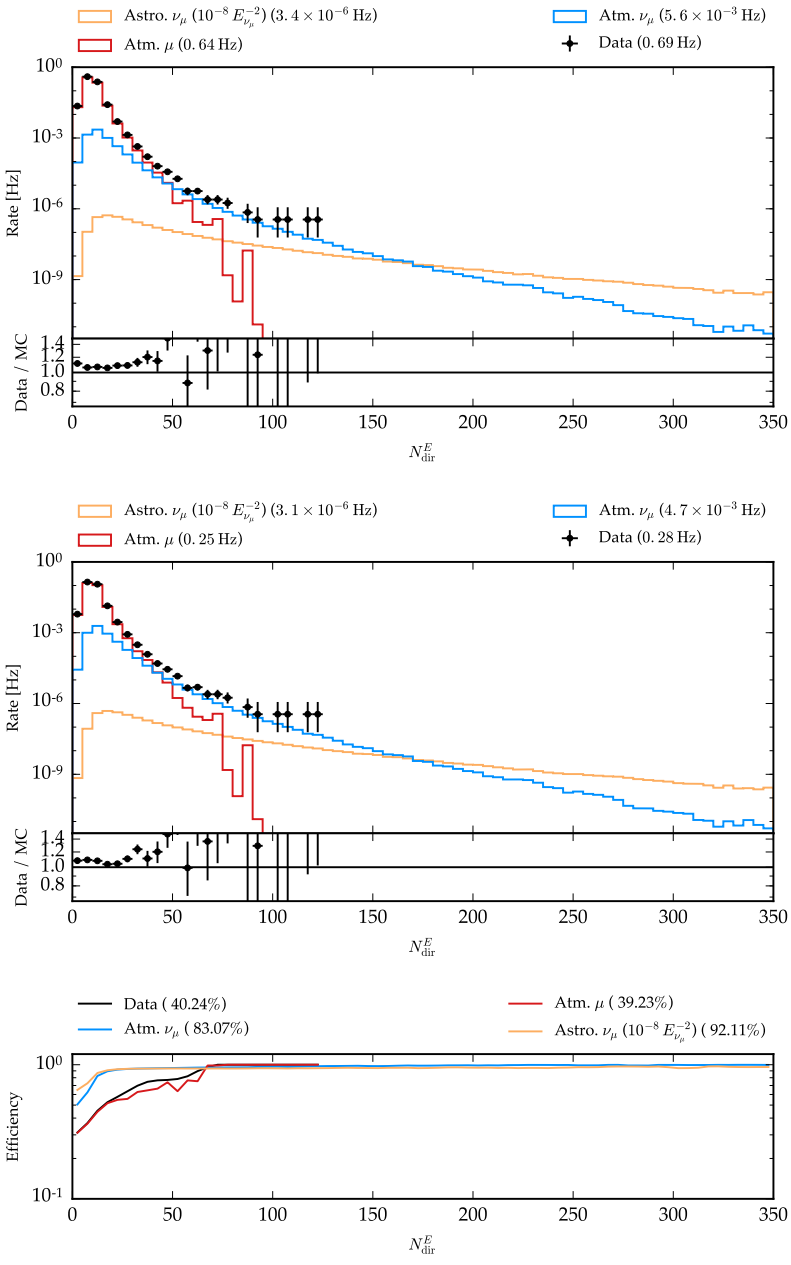

Figure B.4: Direct hit DOMs using time window E. Shown in same way as for previous Figure.

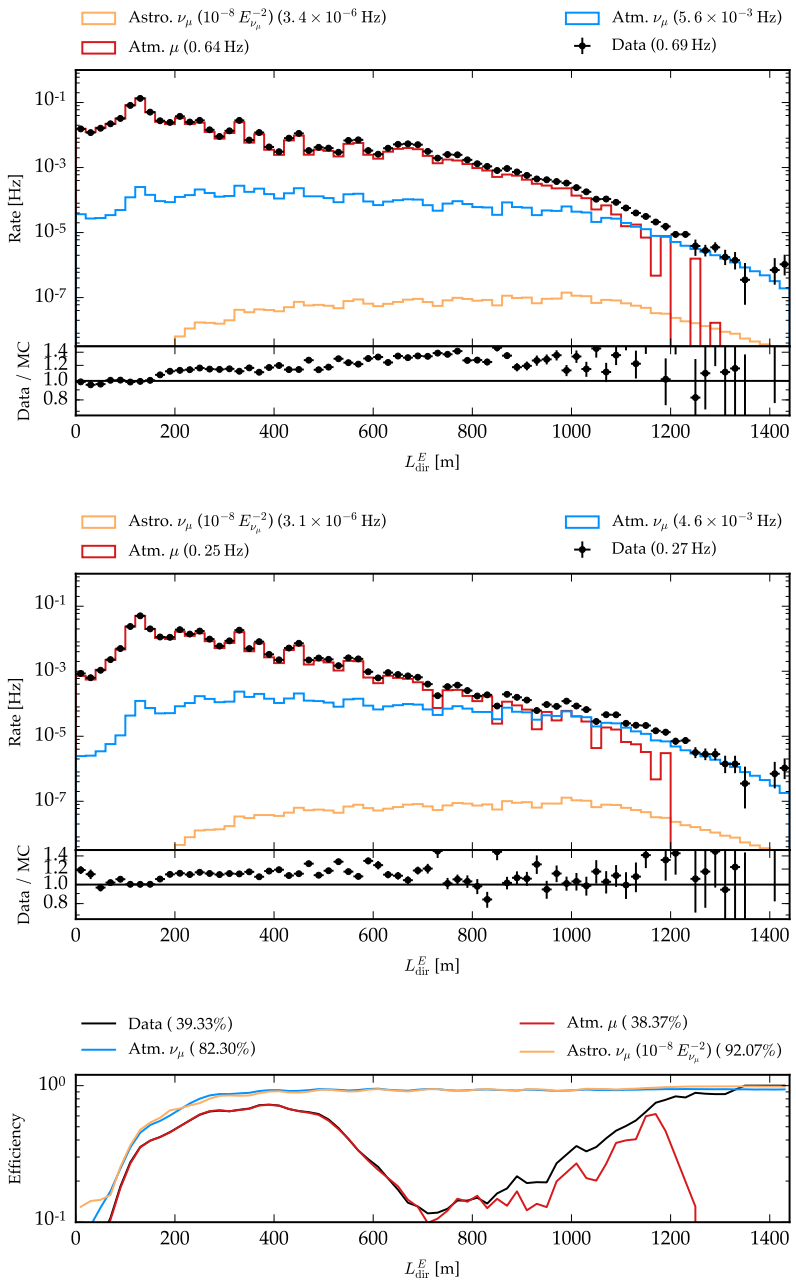

Figure B.5: Direct length with time window E. Shown in same way as for previous Figure.

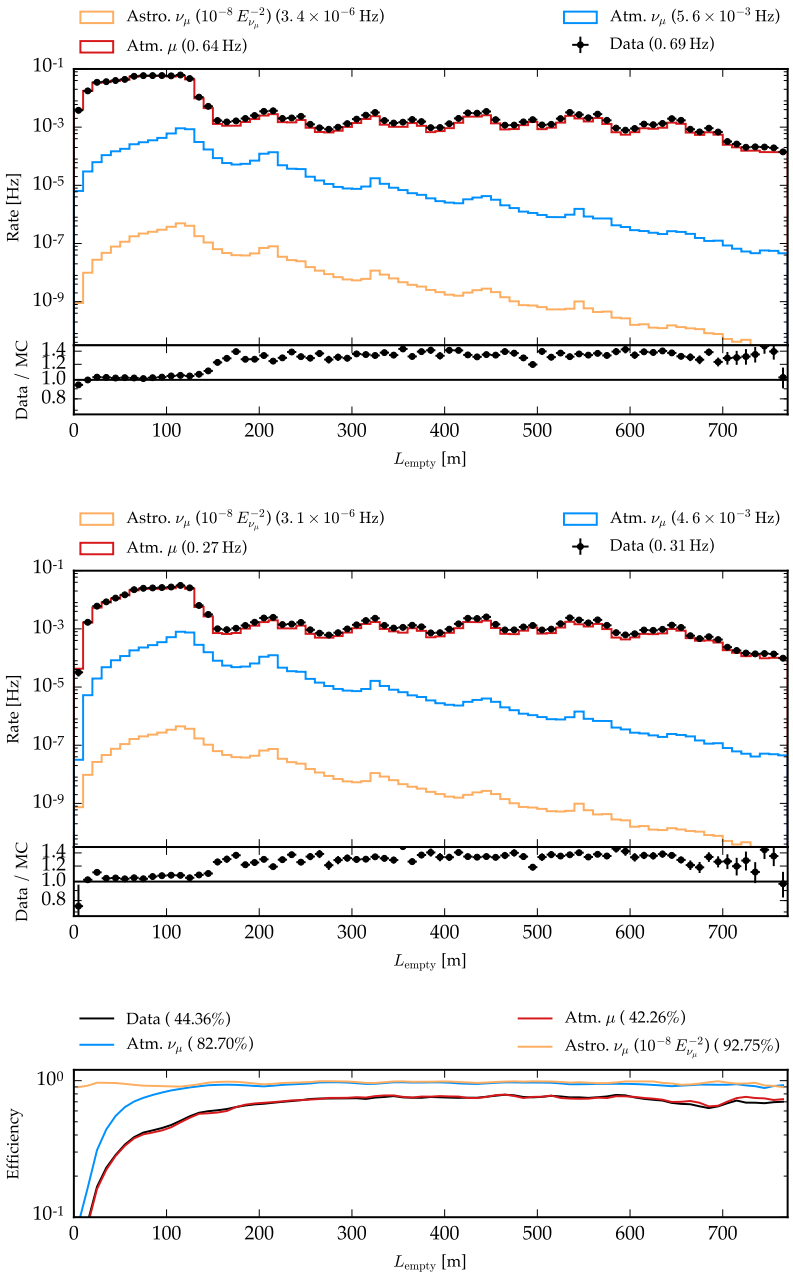

Figure B.6: Empty track length using direct hits with time window E. Shown in same way as for previous Figure.

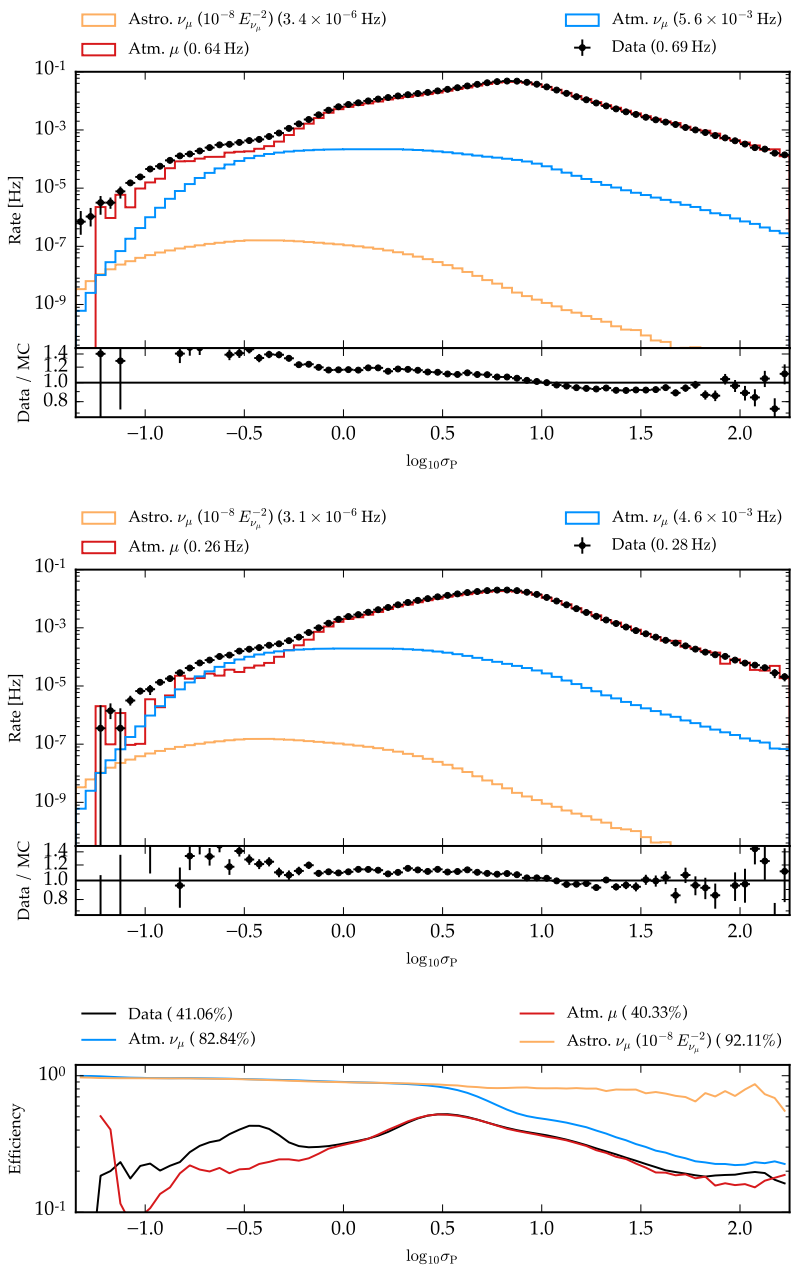

Figure B.7: Logarithm of paraboloid uncertainty reconstruction. Shown in same way as for previous Figure.

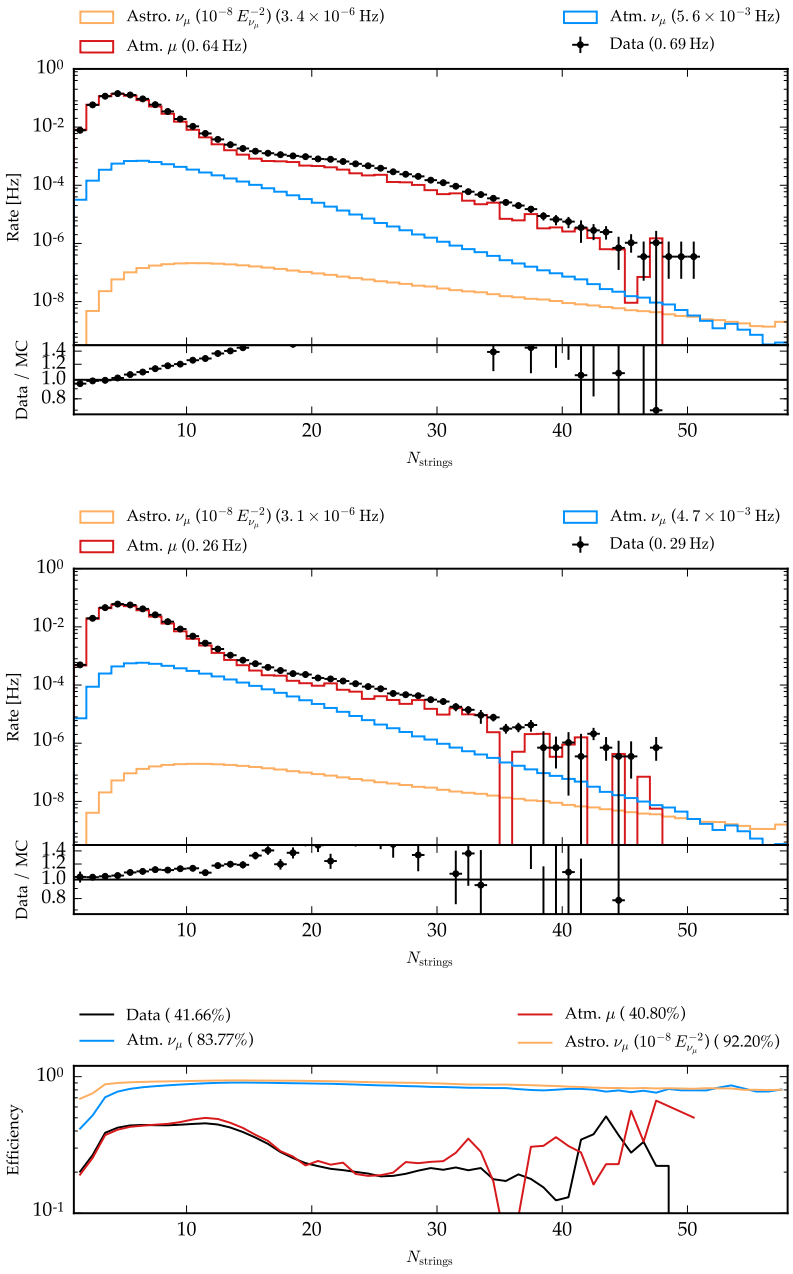

Figure B.8: Number of strings with recorded hits after cleaning probable noise hits. Shown in same way as for previous Figure.

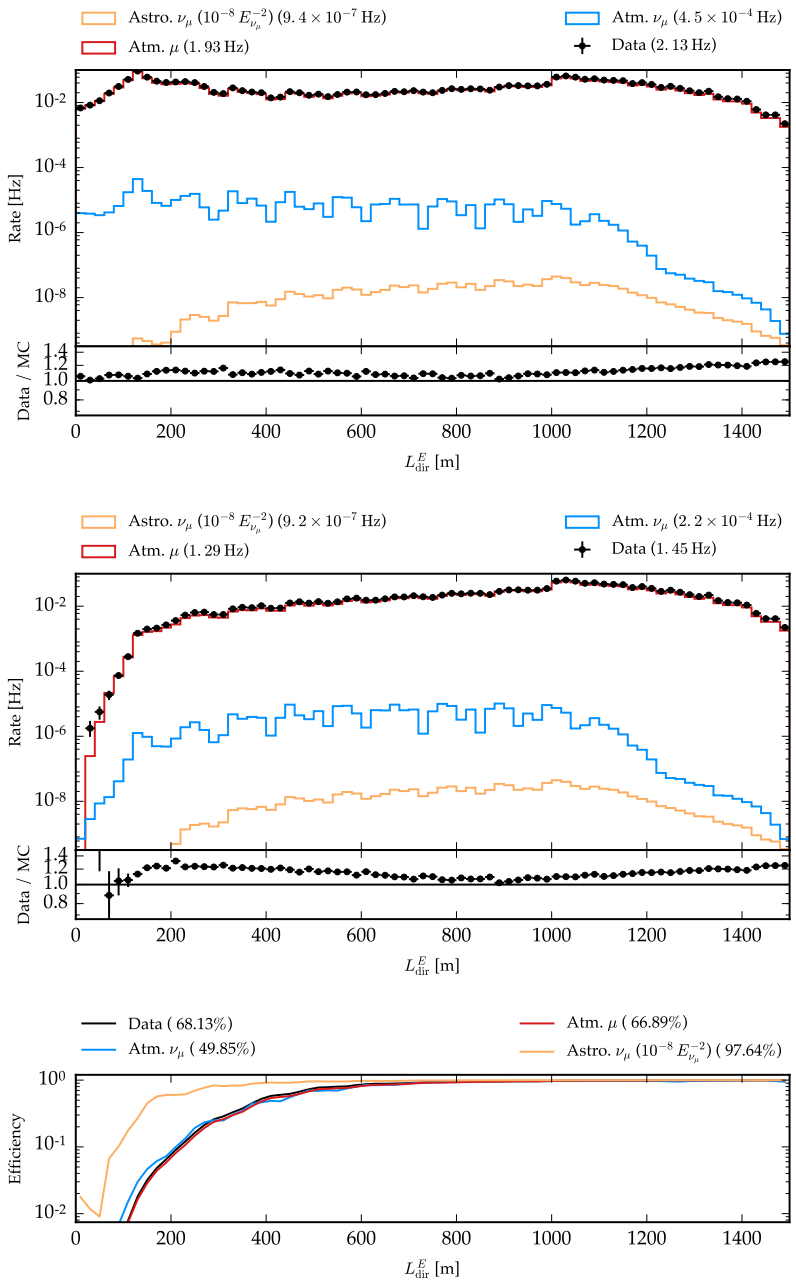

Figure B.9: Direct length with time window E. Shown in same way as for previous Figure.

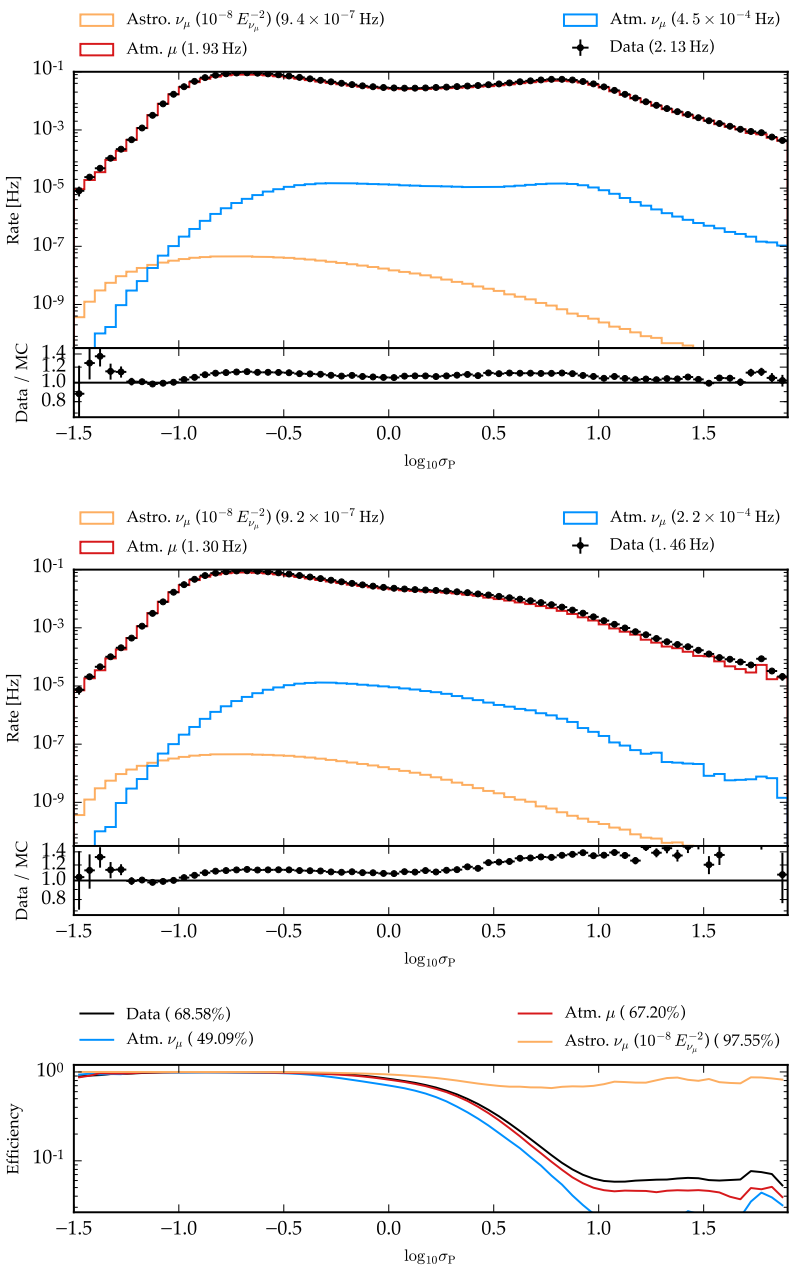

Figure B.10: Paraboloid uncertainty reconstruction. Shown in same way as for previous Figure.

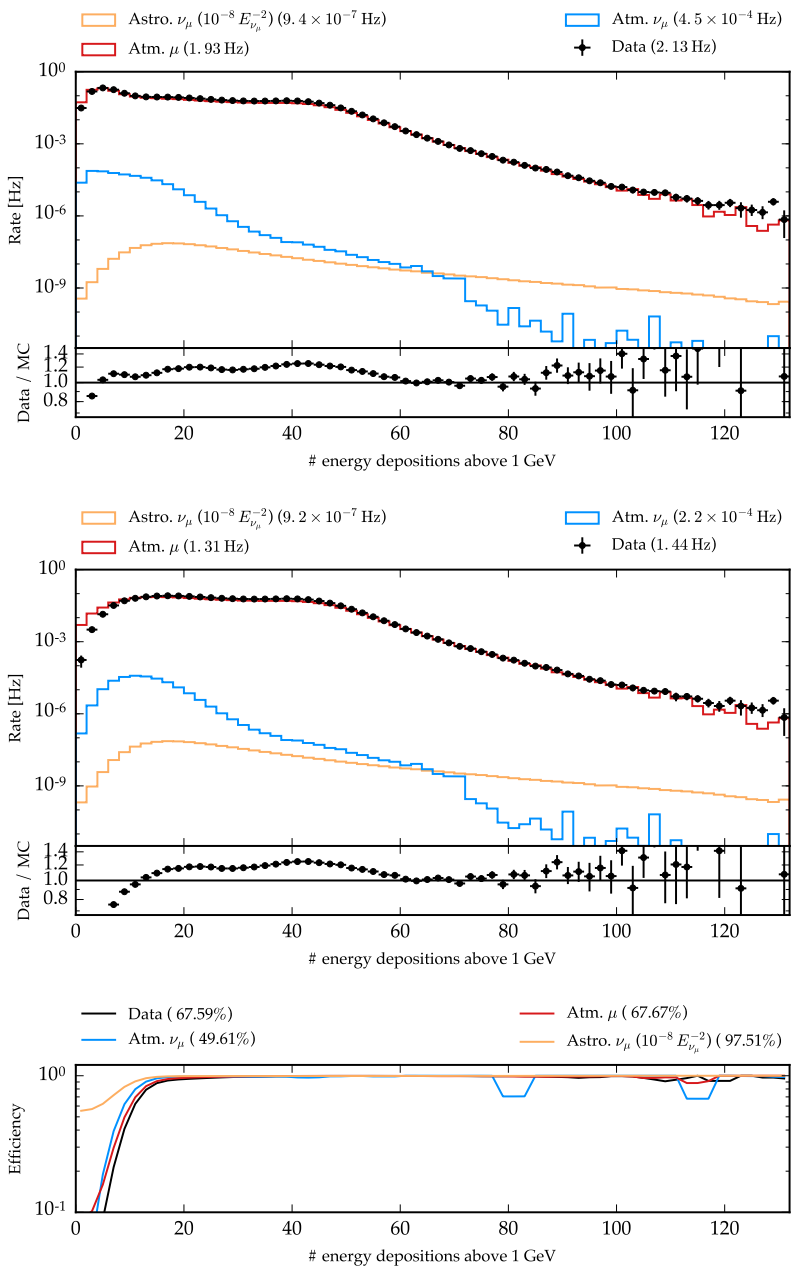

Figure B.11: Number of energy depositions above 1 GeV along track. Shown in same way as for previous Figure.

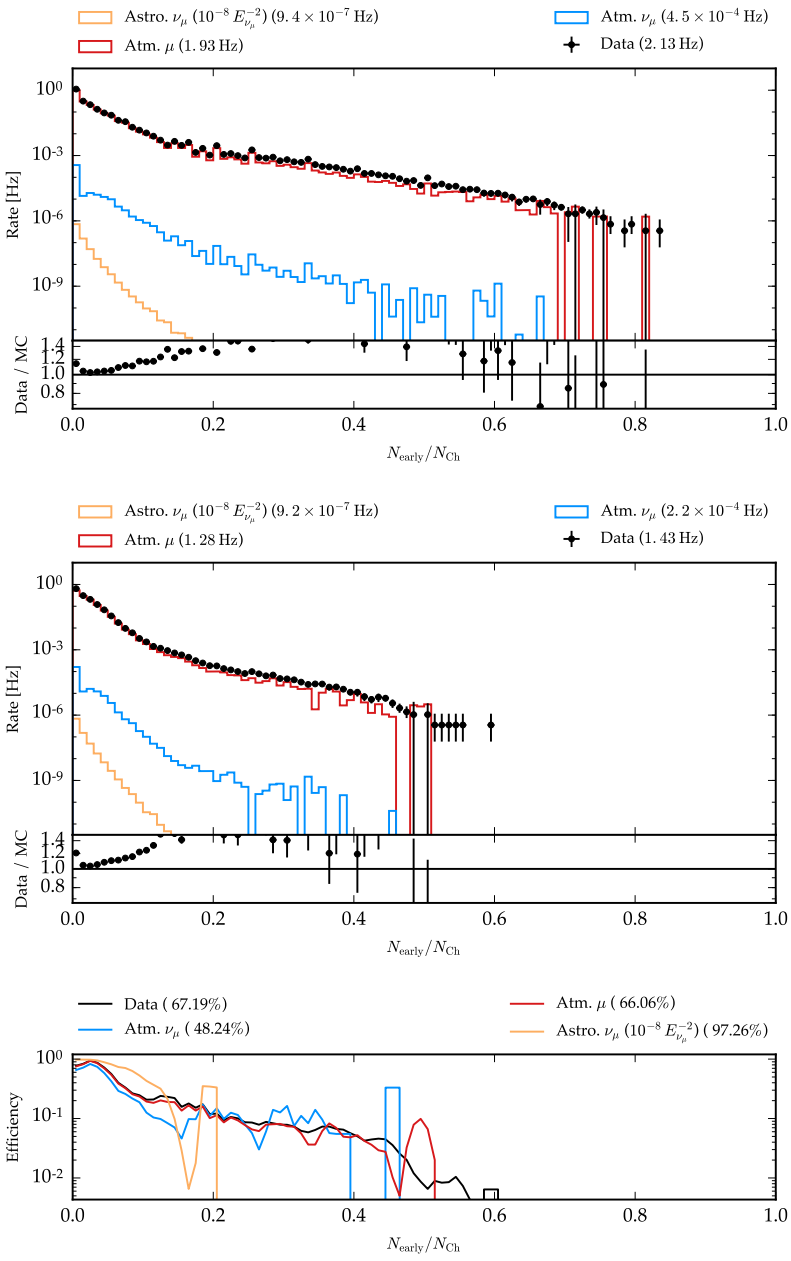

Figure B.12: Ratio of hits with early arrival times and total number of hits. Shown in same way as for previous Figure.

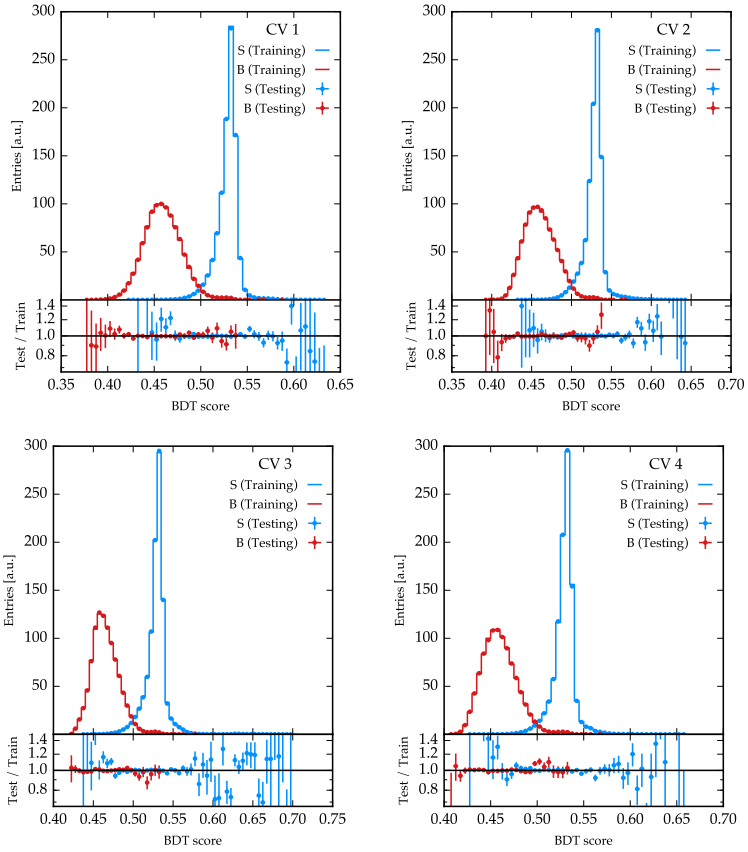

Figure B.13: Cross validation of BDTs in up-going region with soft spectrum ($E^{-2.7}$) used for signal (blue). The testing and training spectrum show good agreement.

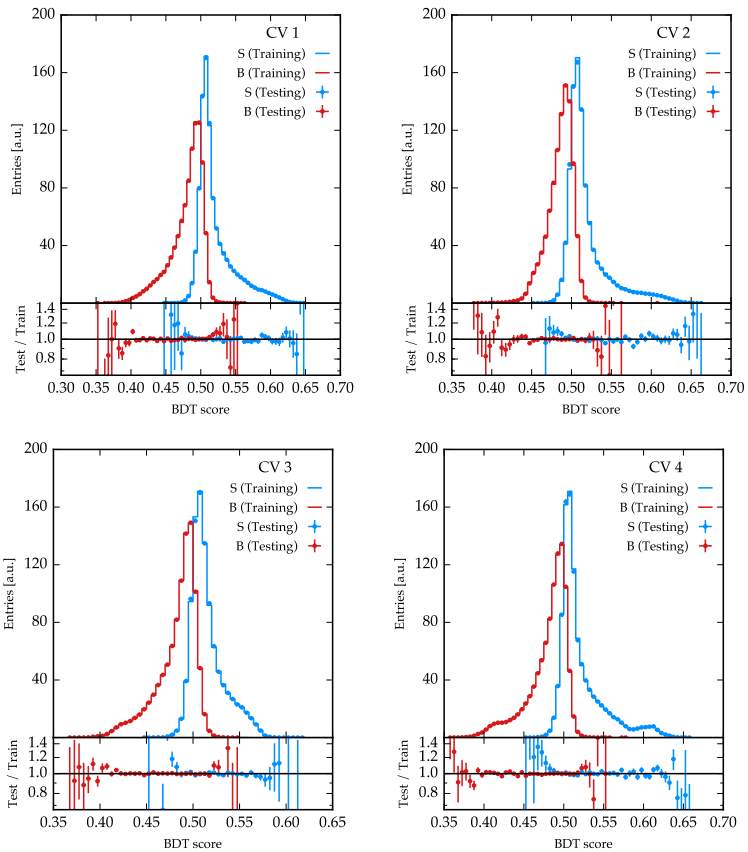

Figure B.14: Cross validation of BDTs in down-going region used for signal (blue). The testing and training spectrum show good agreement.

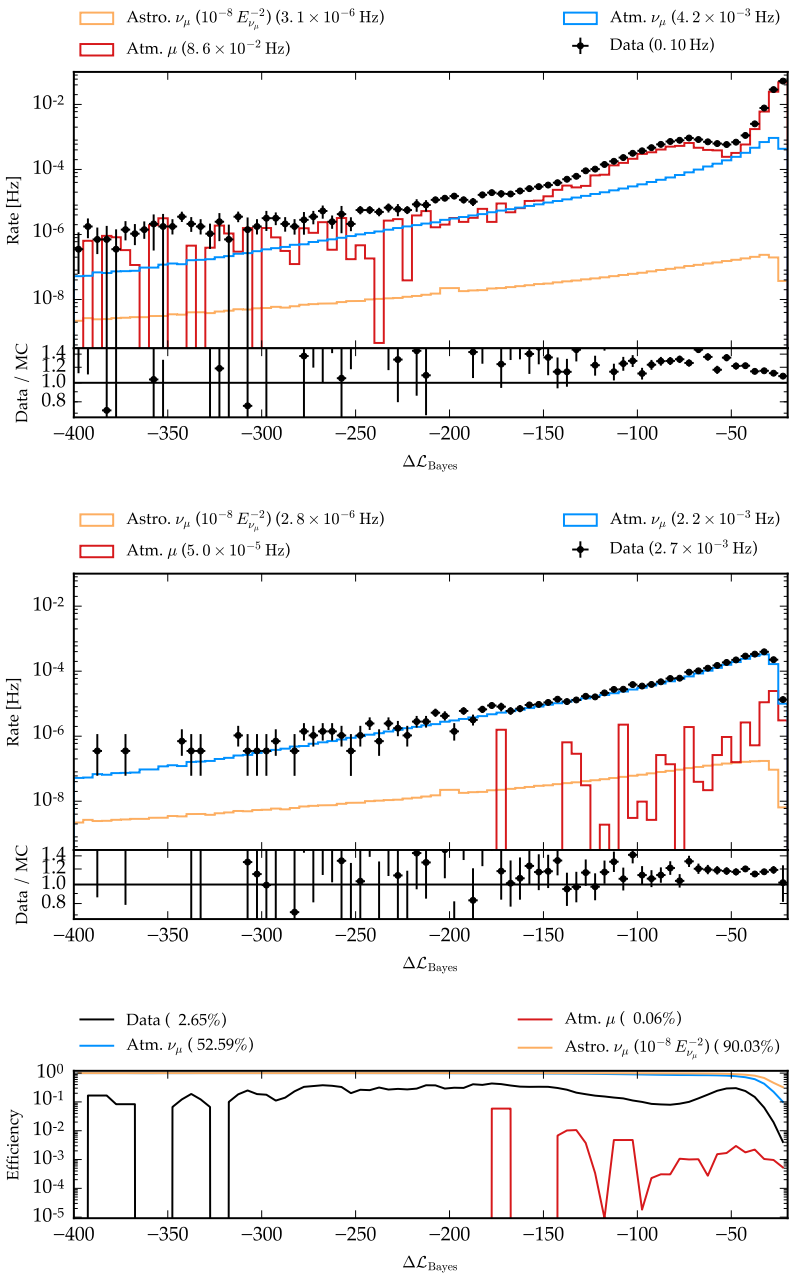

Figure B.15: Bayesian likelihood difference at BDT score cut in up-going region. Components shown are the same as for low-level cut.

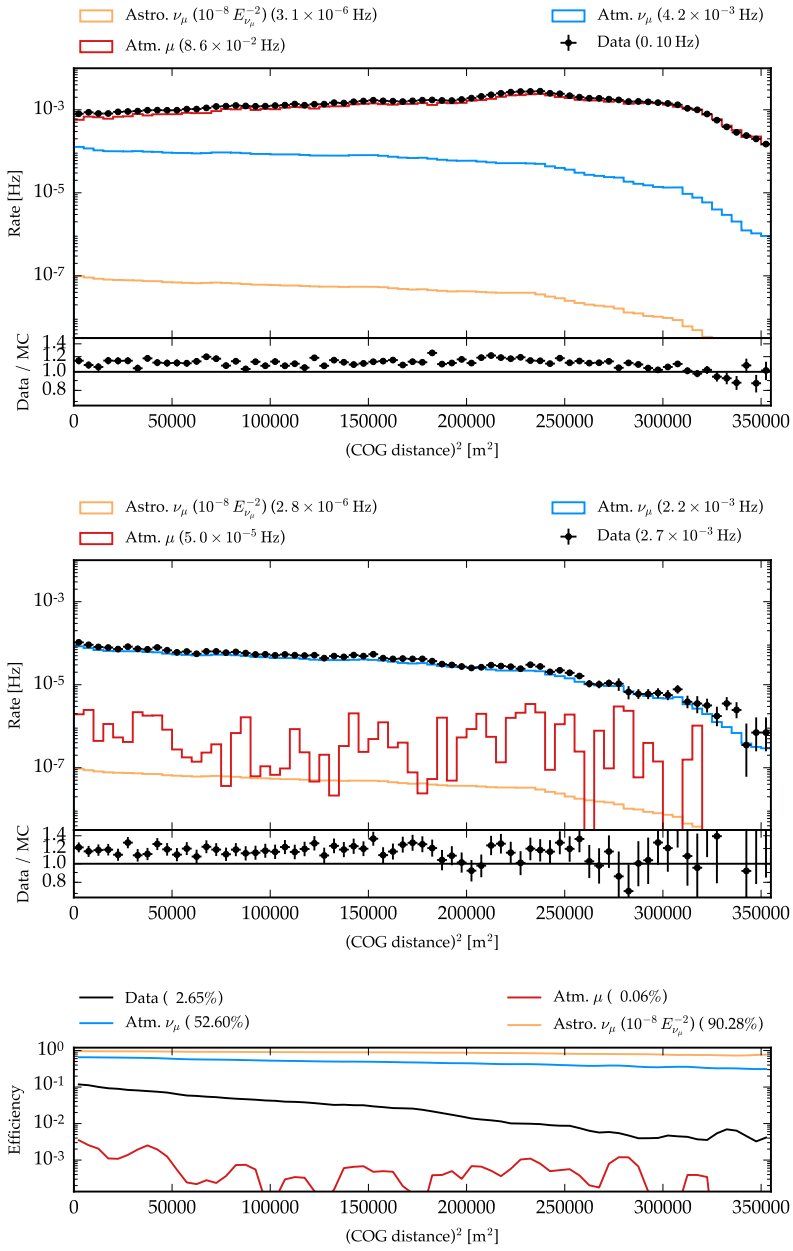

Figure B.16: COG radial distance at BDT score cut in up-going region. Components show are the same as for low-level cut.

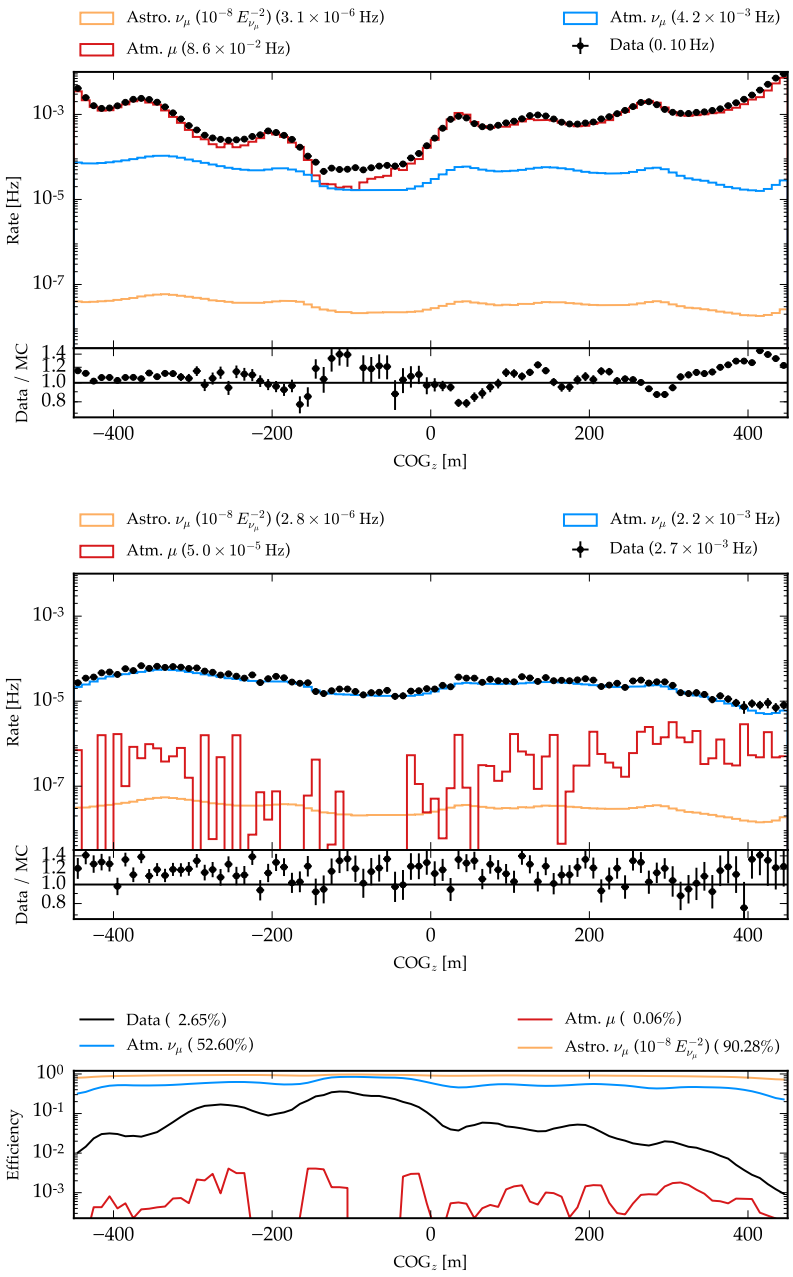

Figure B.17: COG vertical position at BDT score cut in up-going region. Components show are the same as for low-level cut.

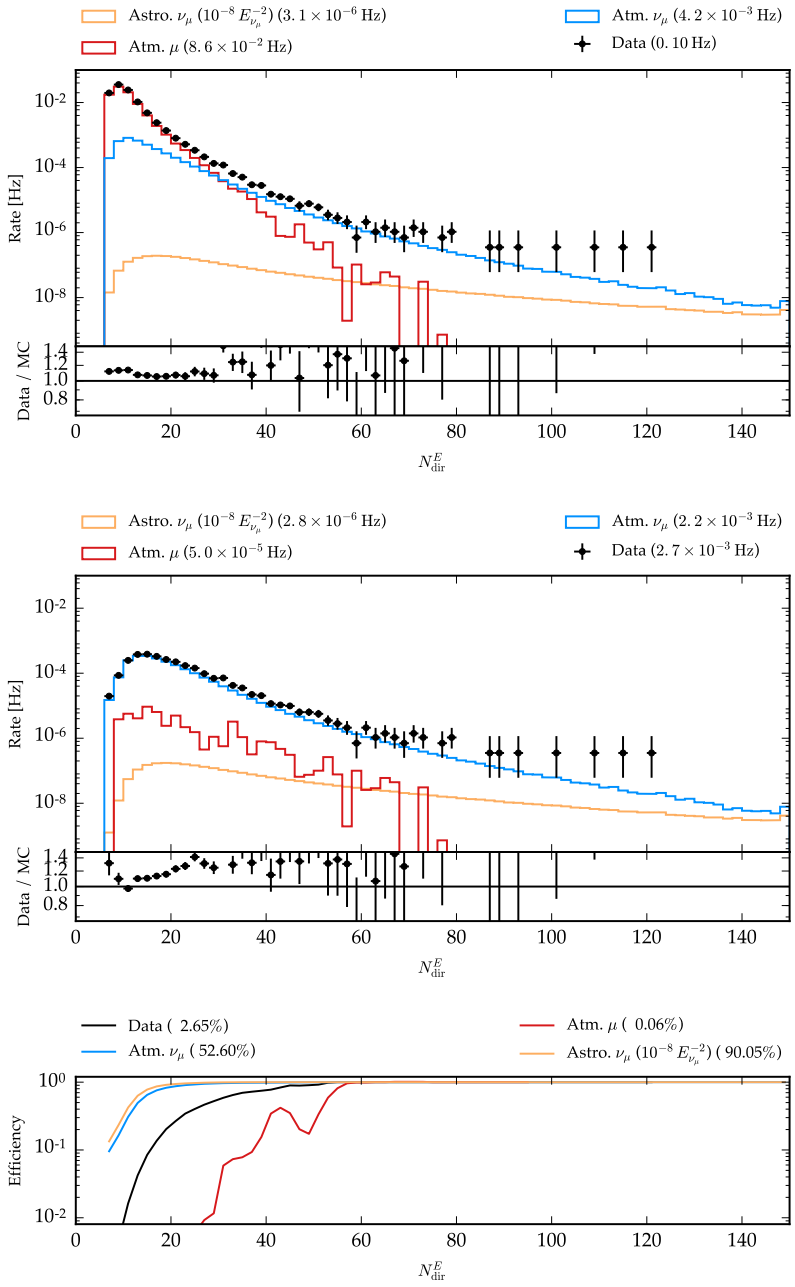

Figure B.18: Number of direct hits (time window E) at BDT score cut in upgoing region. Components show are the same as for low-level cut.

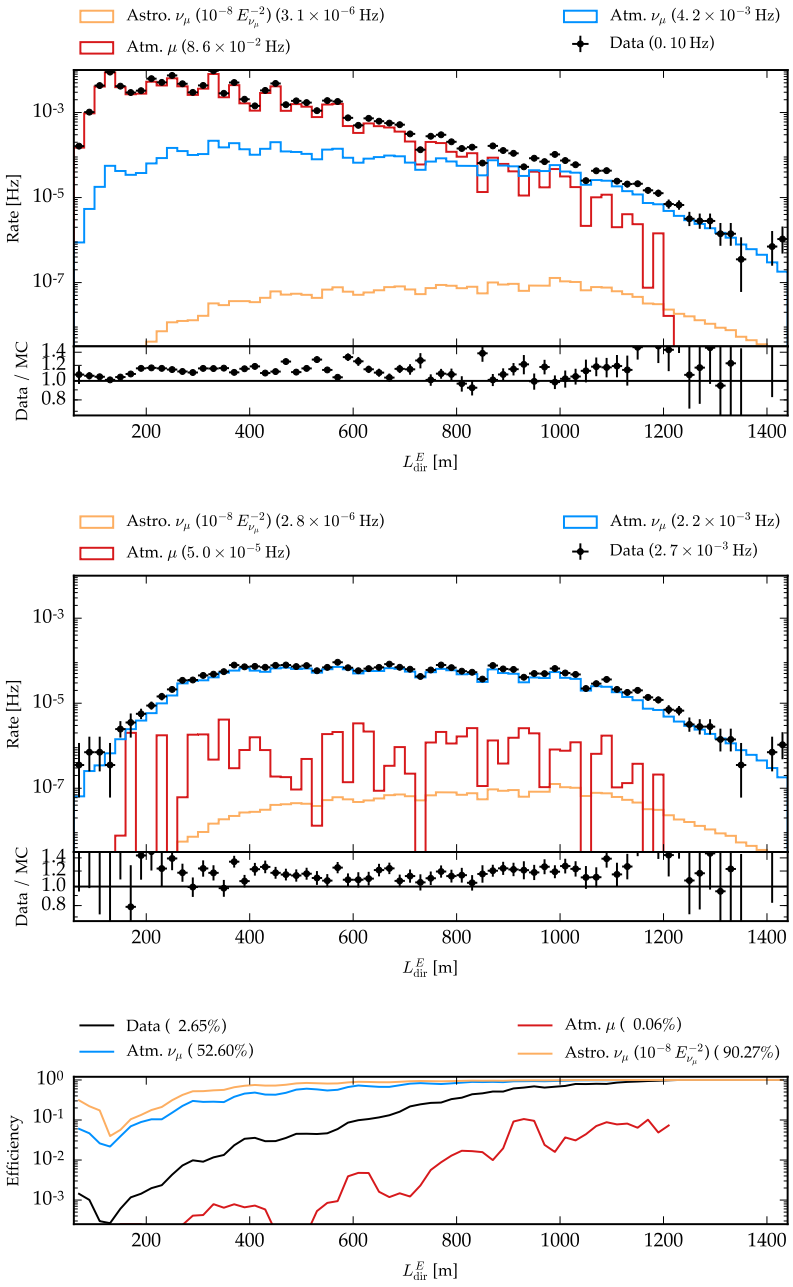

Figure B.19: Direct hit length (time window E) at BDT score cut in up-going region. Components show are the same as for low-level cut.

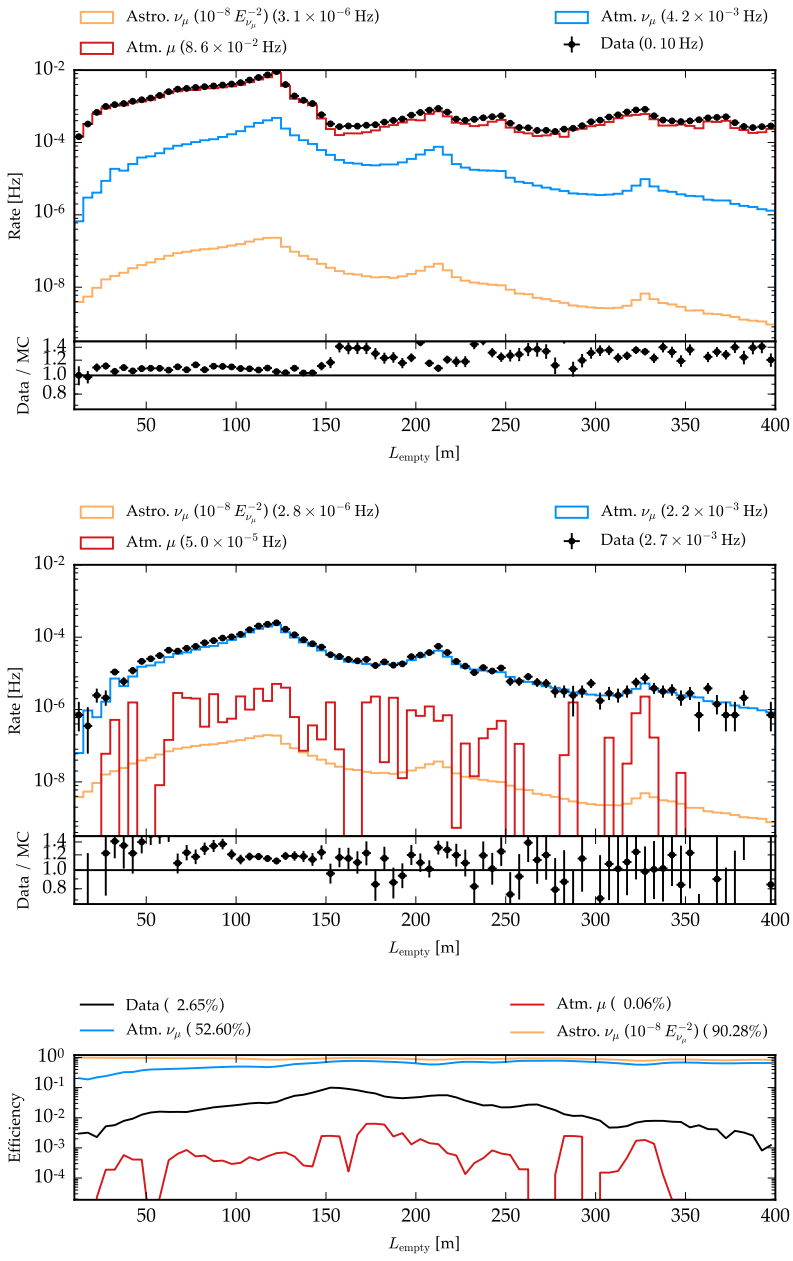

Figure B.20: Empty length between direct hits (time window E) before and after BDT score cut in up-going region. Components show are the same as for low-level cut.

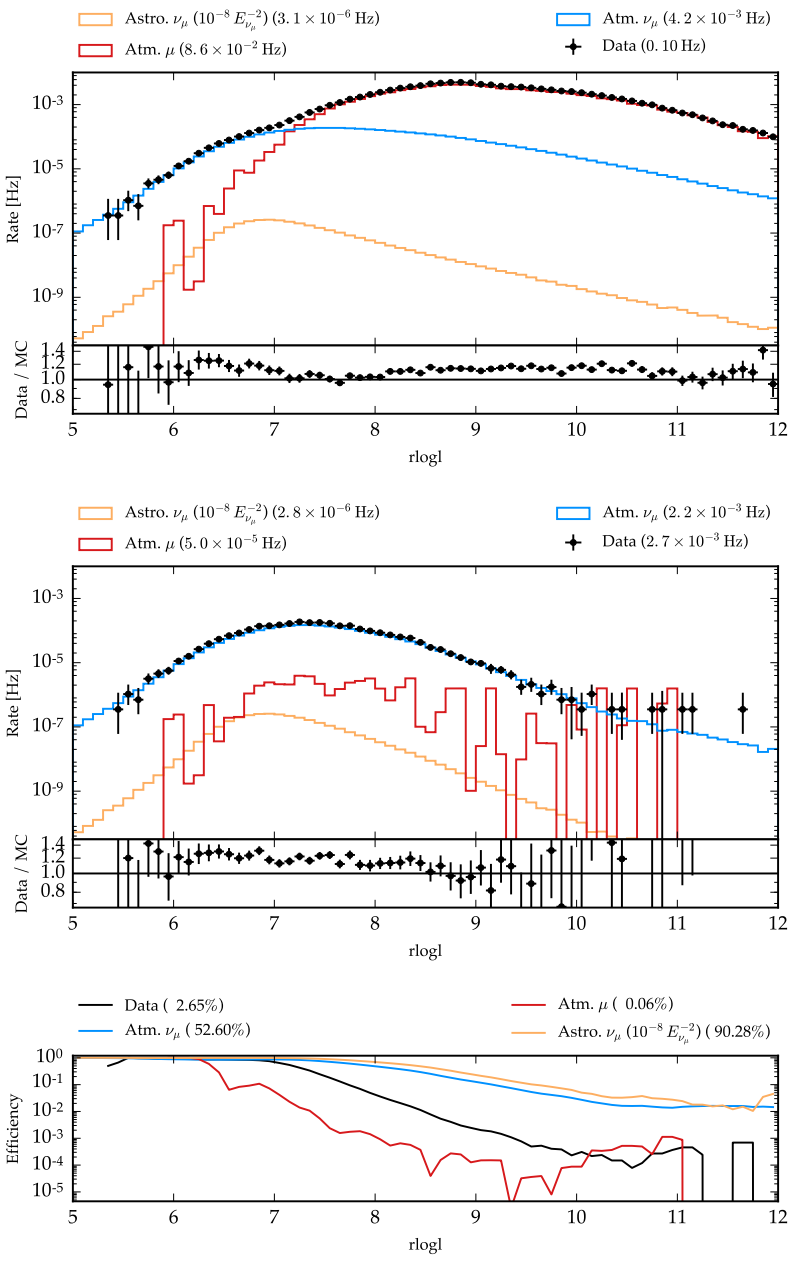

Figure B.21: Reduced likelihood of SplineMPE reconstruction at BDT score cut in up-going region. Components show are the same as for low-level cut.

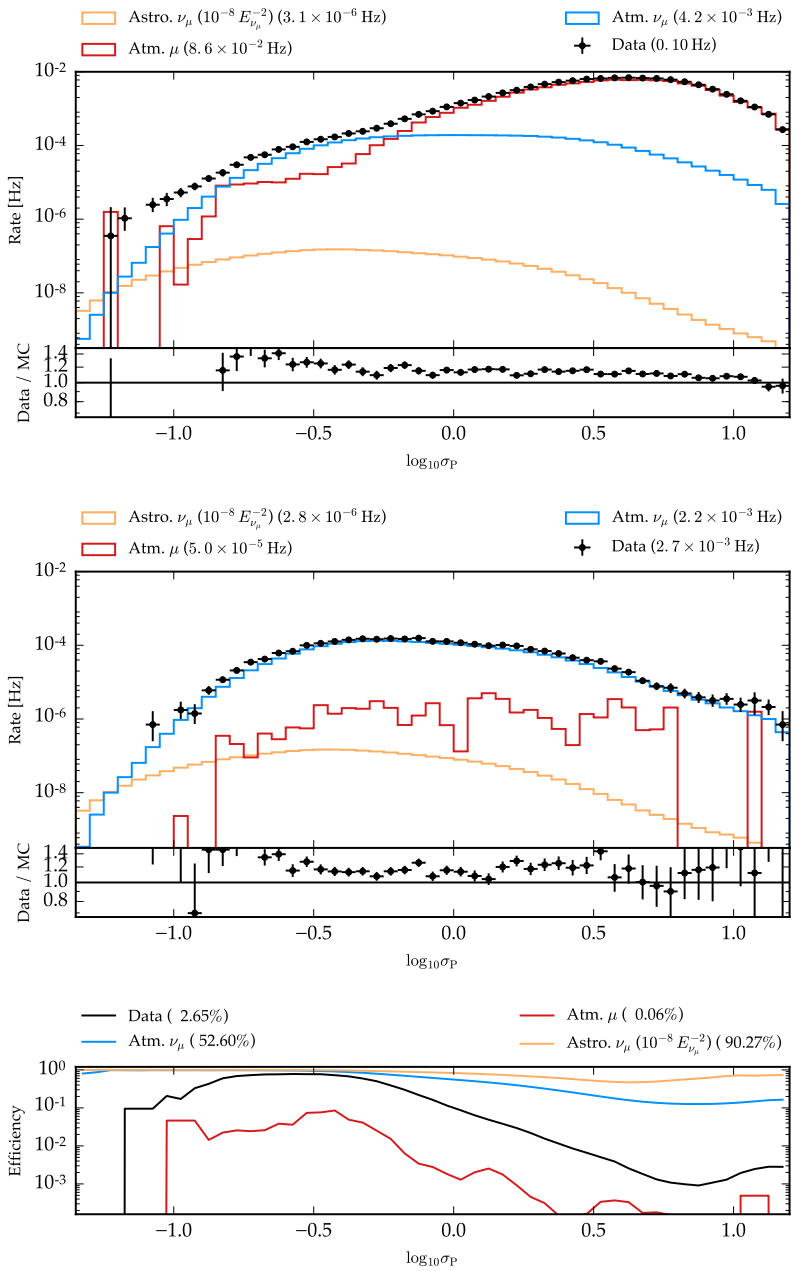

Figure B.22: Logarithm of uncertainty reconstruction at BDT score cut in upgoing region. Components show are the same as for low-level cut.

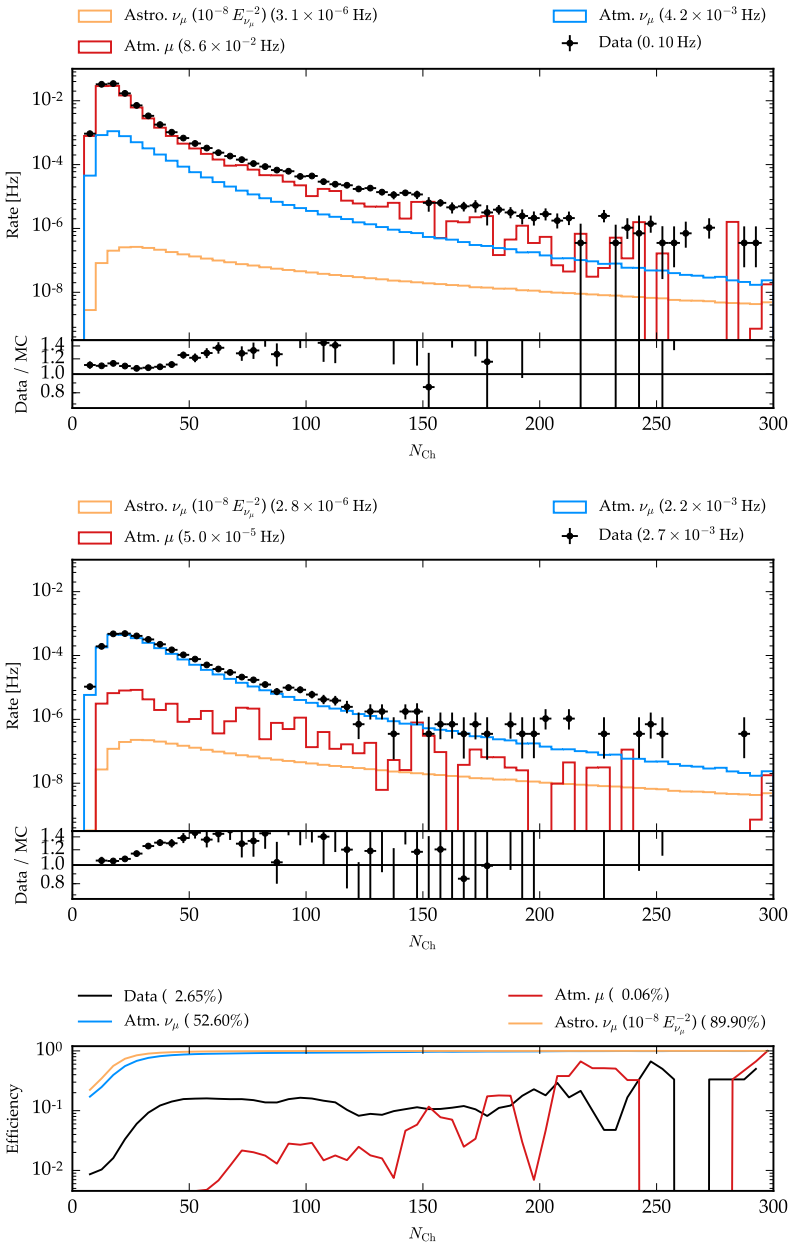

Figure B.23: Number of hit DOMs after cleaning for noise hits at BDT score cut in up-going region. Components show are the same as for low-level cut.

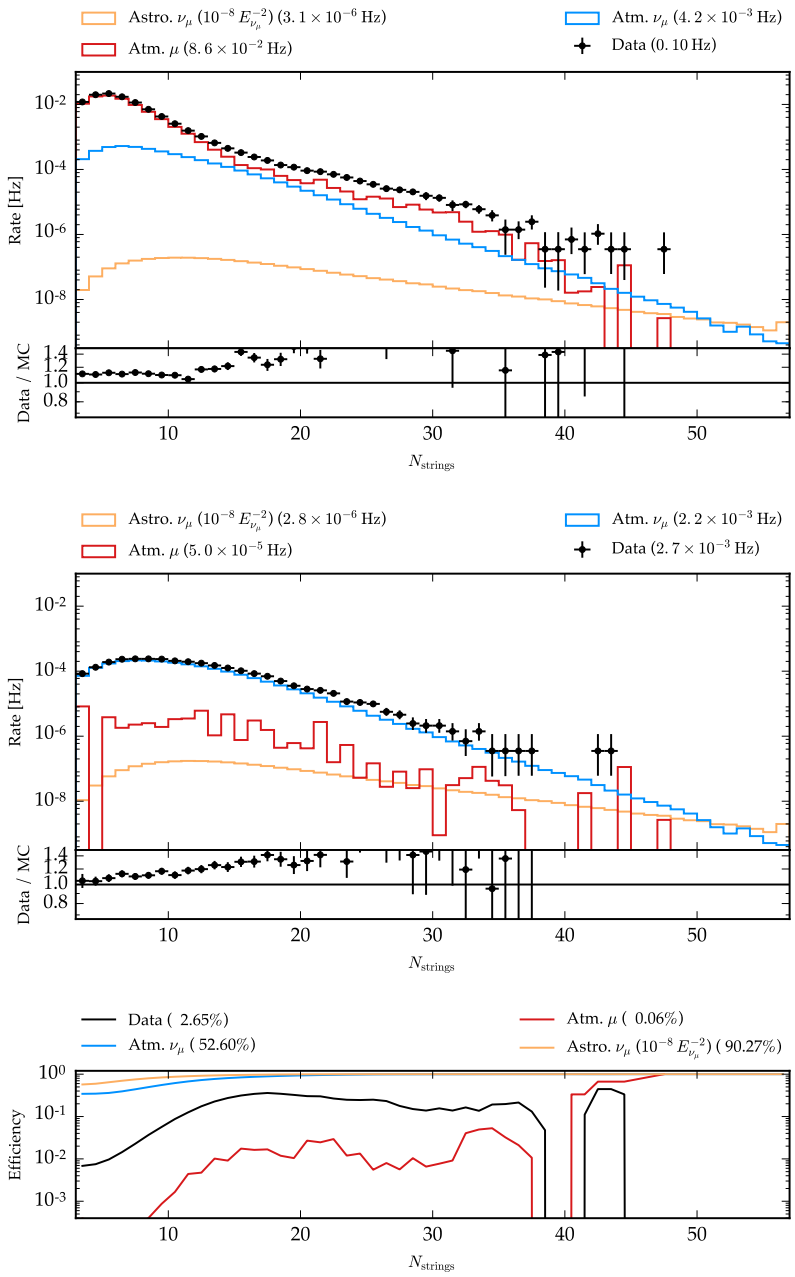

Figure B.24: Number of strings with one or more hits recorded after noise cleaning at BDT score cut in up-going region. Components show are the same as for low-level cut.

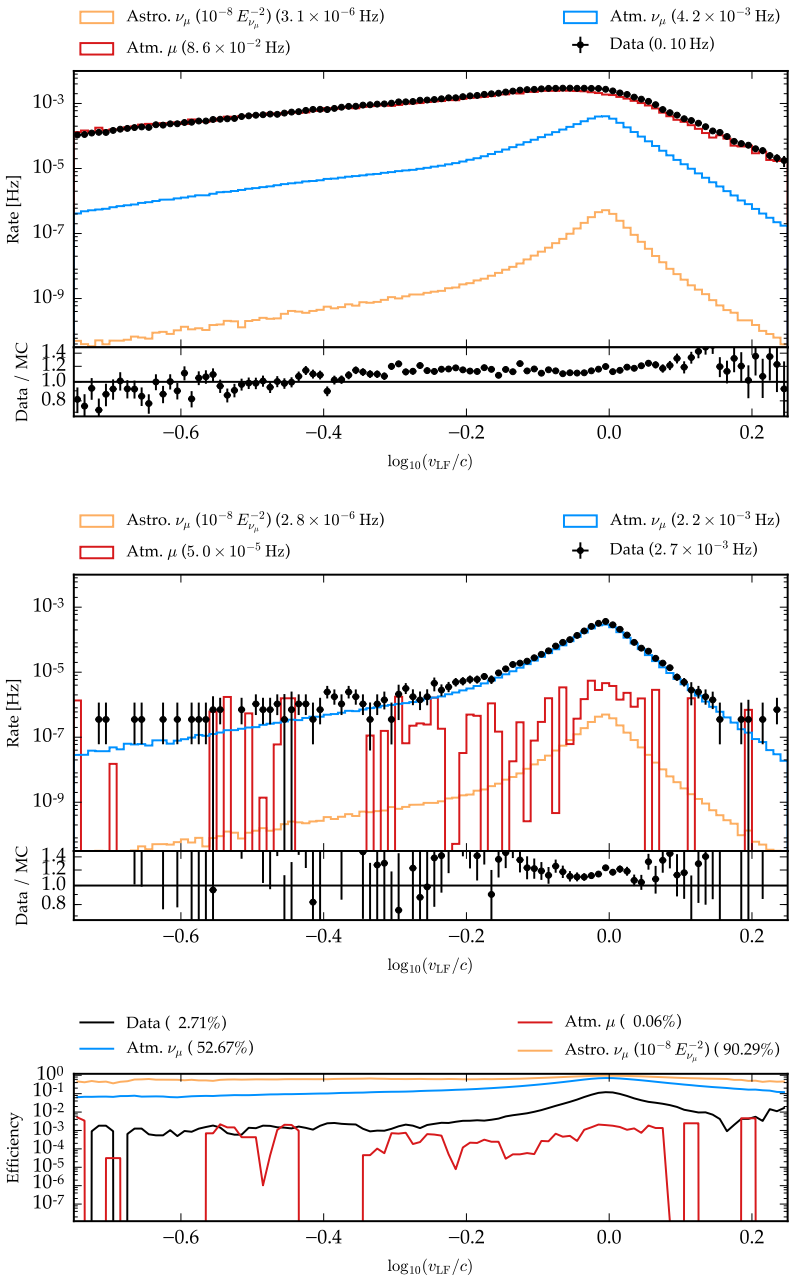

Figure B.25: Linefit reconstructed track velocity at BDT score cut in up-going region. Components show are the same as for low-level cut.

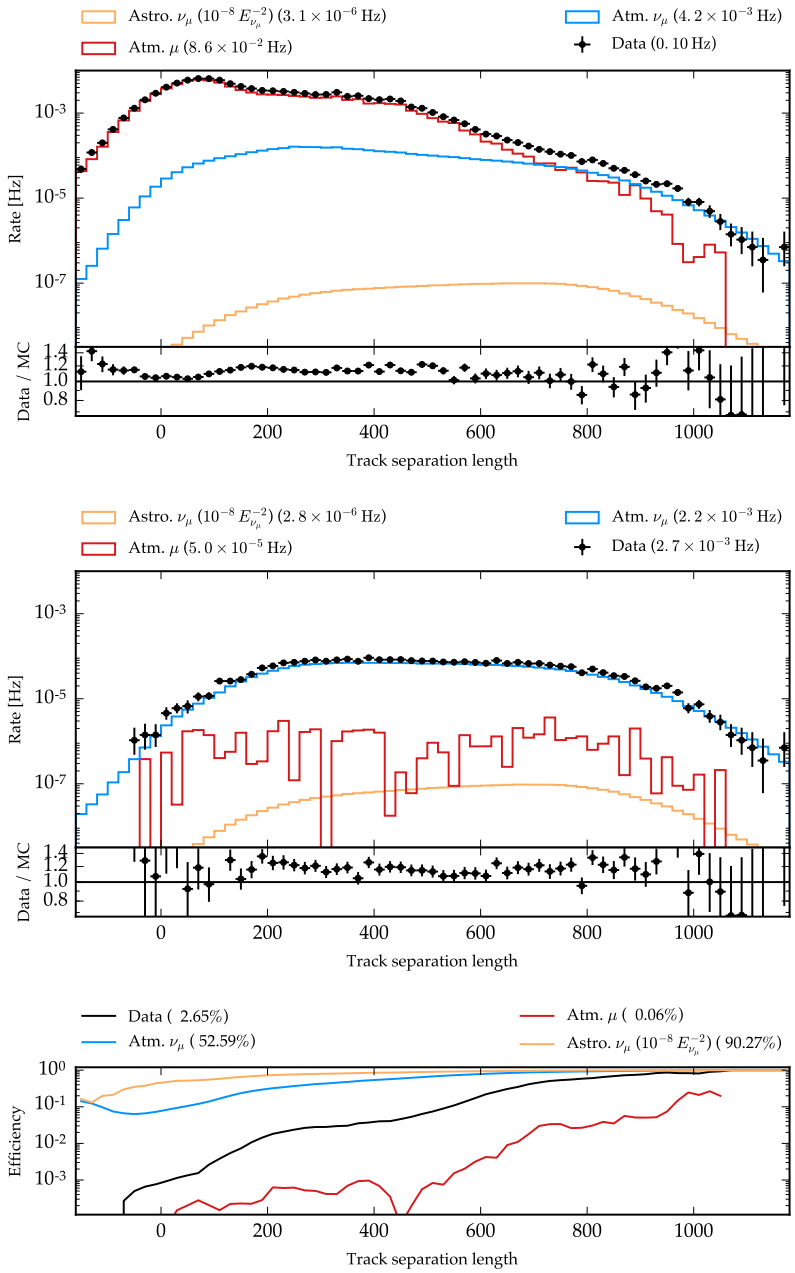

Figure B.26: Track separation length at BDT score cut in up-going region. Components show are the same as for low-level cut.

C IceCube point source searches

C.1 7 year sensitivity to neutrino point source fluxes

In Figure C.1 and Figure C.2, the sensitivity and discovery potential of IceCube is shown for unbroken power-law spectra $\partial\phi/\partial E \propto E^{-\gamma}$ with spectral indices of 1 and 3, respectively. The results are compared to the flux of the previously published analysis of four years exposure.[1]

[1] Aartsen, "Lowering IceCube's Energy Threshold for Point Source Searches in the Southern Sky".

Different characteristic features can be seen because different spectral indices cover different neutrino energy ranges. For very hard spectra of E^{-1}, neutrinos predominantly arrive with very high energies at Earth. Hence, many neutrinos are absorbed when traversing the Earth. As a result, the sensitivity is suppressed in the up-going regime, because only a fraction of the flux is observable. In the down-going regime (southern sky) on the other hand, the performance is highly increased since many high-energy events are observed at the detector and give an excess over the large backgrounds.

This changes for soft spectra (E^{-3}). Due to the high energy threshold, almost no neutrinos are observed in the down-going region except for starting events, reducing the sensitivity strongly. On the other hand, absorption is not a dominant effect anymore, giving a flat sensitivity in the entire southern sky.

Figure C.3 and C.4 show the sensitivity and discovery potential overlaid with the upper limits for the hot spot results and source list searches discussed in Section 7.

C.2 P-value landscape for gamma-ray objects

A zoom into the p-value landscape of all the sources listed in Tables 7.4 to 7.7 is shown from Figures C.5 to C.17. All samples present in the window that is observed are shown with small markers on top of the fit values.

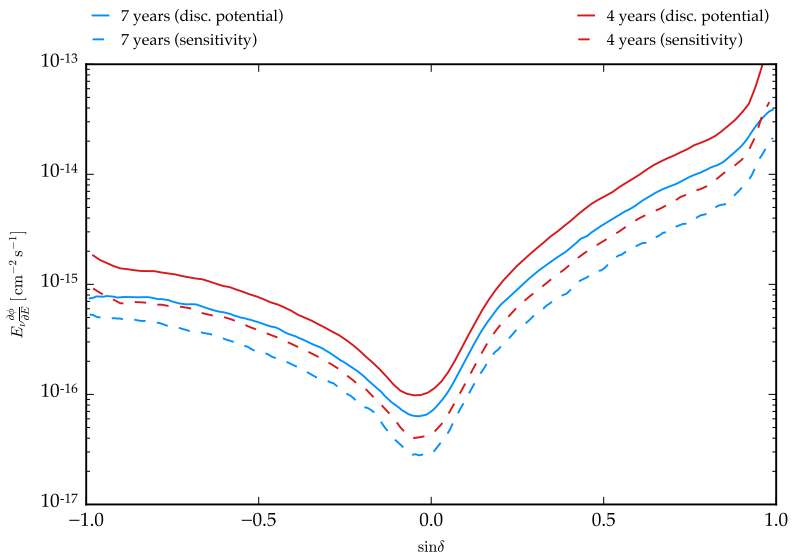

Figure C.1: Sensitivity and discovery potential (5σ) of full seven year sample for different declinations using very hard unbroken neutrino spectra $\partial\phi/\partial E \propto E^{-1}$. The previous results of four years are shown as comparison.

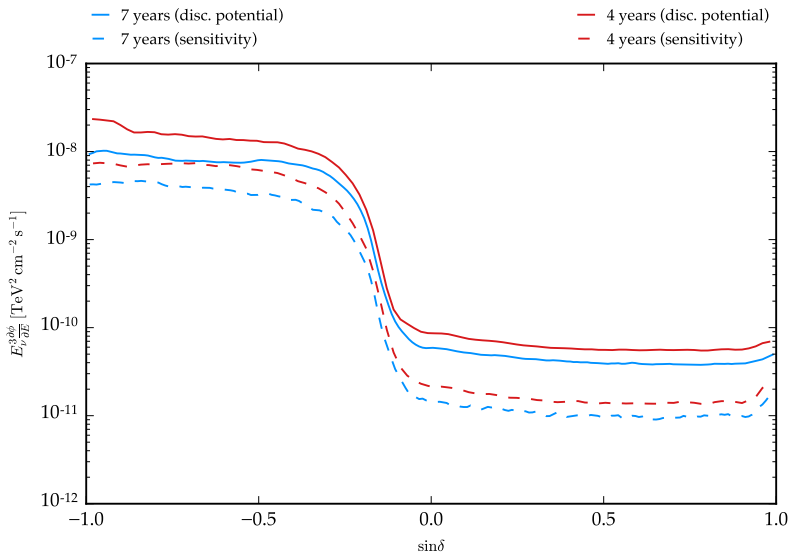

Figure C.2: Sensitivity and discovery potential (5σ) of full seven year sample for different declinations using very soft unbroken neutrino spectra $\partial\phi/\partial E \propto E^{-3}$. The previous results of four years are shown as comparison.

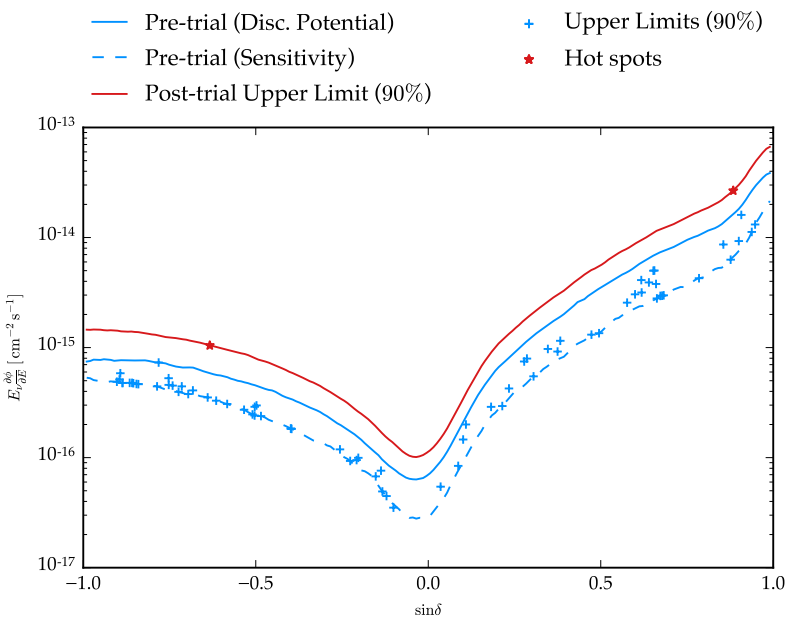

Figure C.3: Upper limits of seven year search versus declination using an unbroken E^{-1} neutrino spectrum (muon neutrinos only). The upper limits of the two source catalogs are compared to the pre-trial sensitivity and discover potential. The upper limit of the full-sky scan with the positions of the two hot spots (stars) is shown as post-trial upper limit.

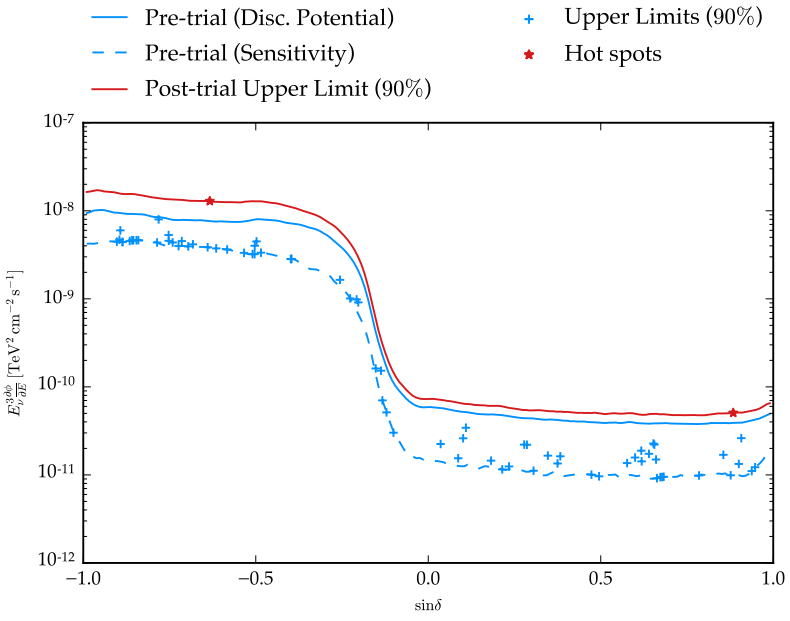

Figure C.4: Same plot as previous figure for unbroken E^{-3} spectrum.

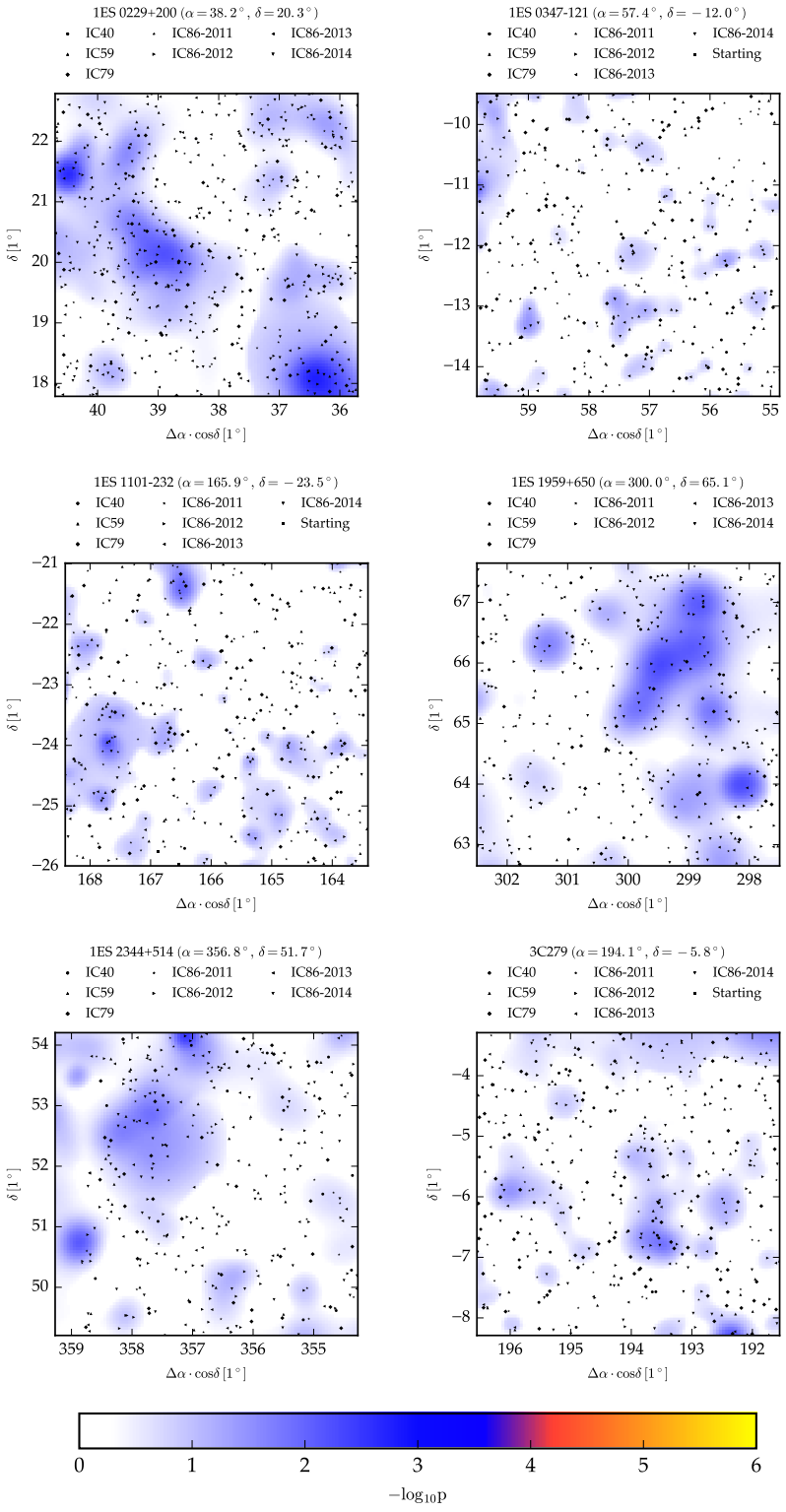

Figure C.5: P-value landscape of six sources tested for steady neutrino emission. Events are shown for all samples present in this declination region.

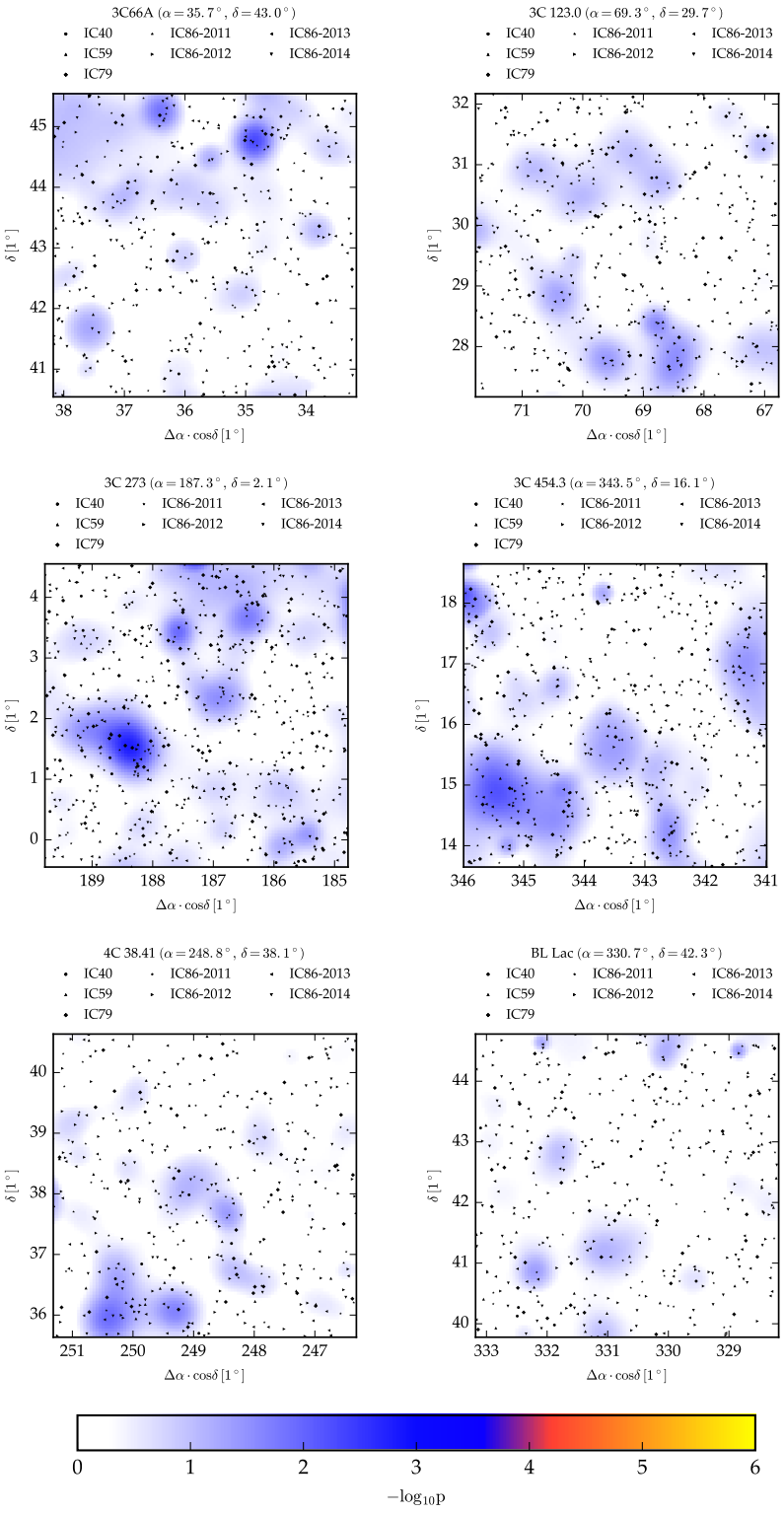

Figure C.6: P-value landscape of six sources

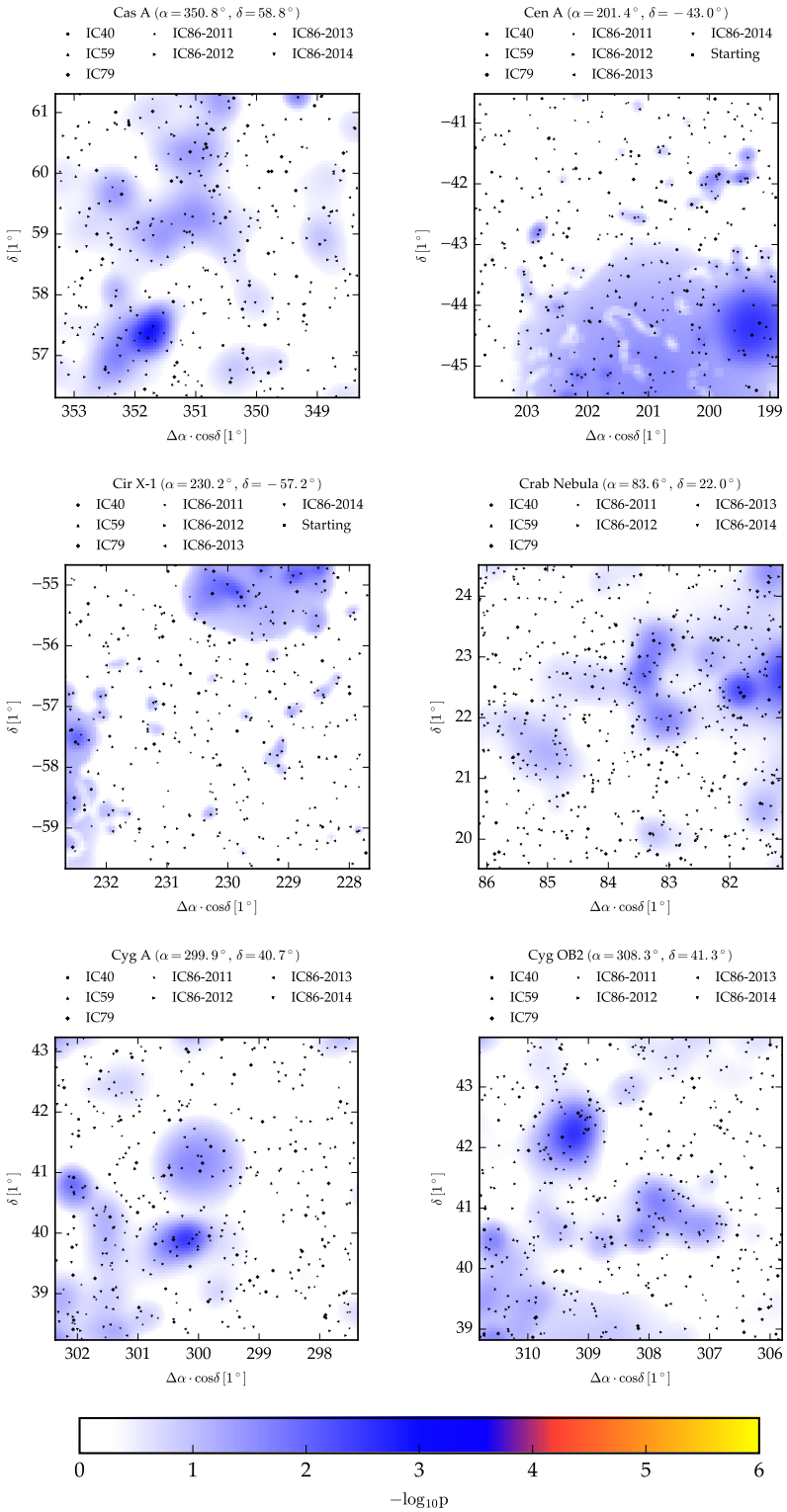

Figure C.7: P-value landscape of six sources

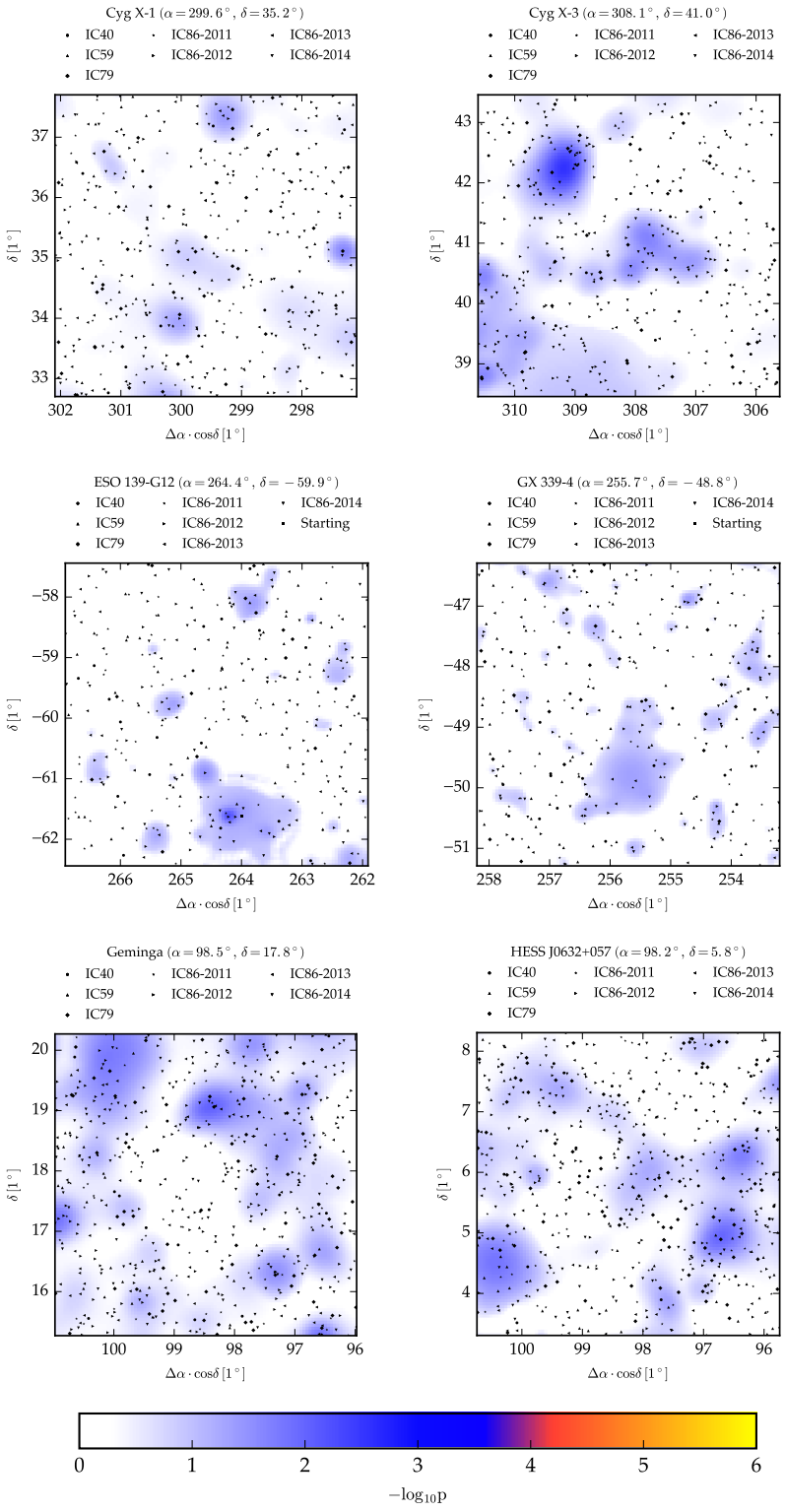

Figure C.8: P-value landscape of six sources

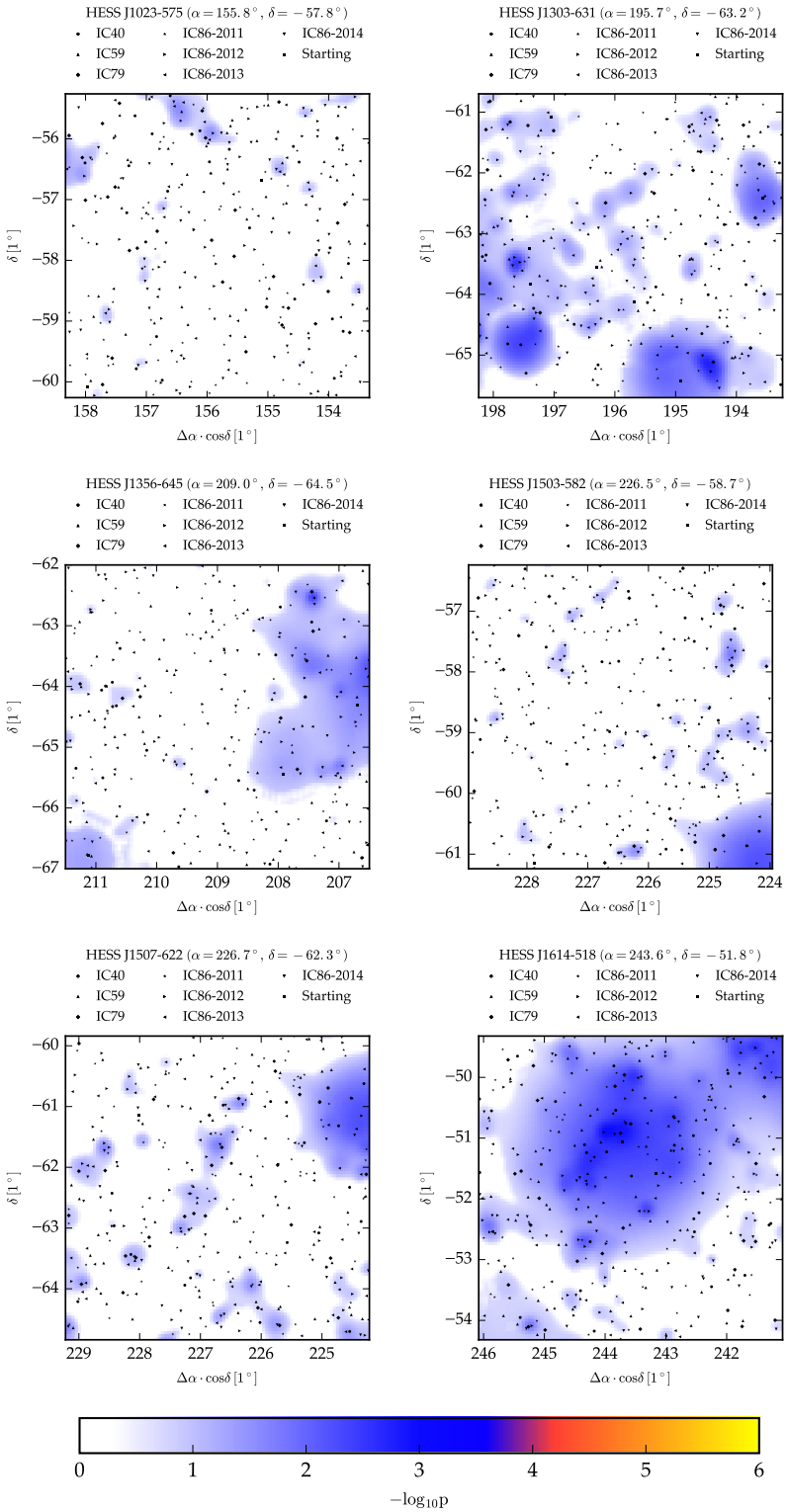

Figure C.9: P-value landscape of six sources

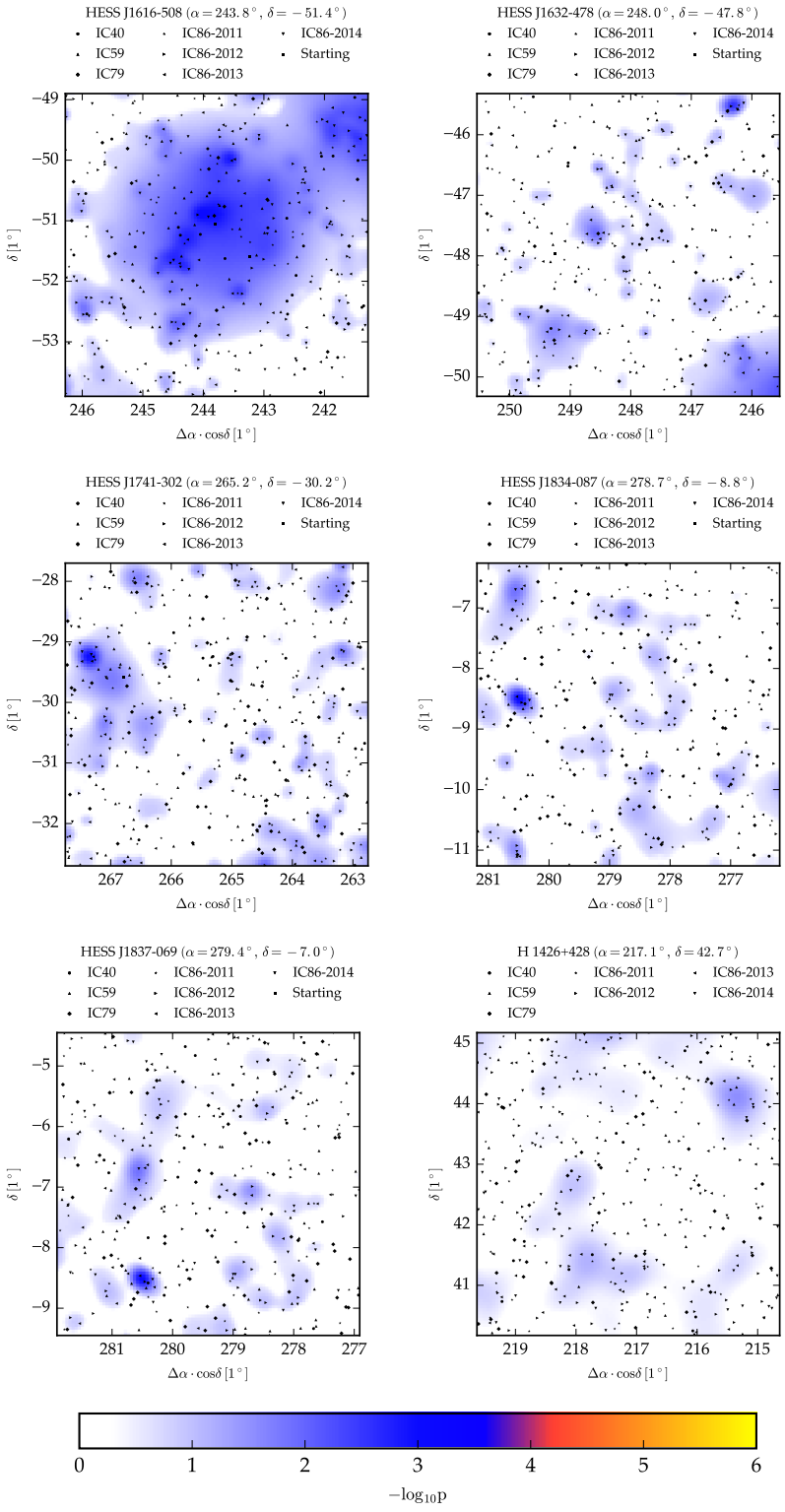

Figure C.10: P-value landscape of six sources

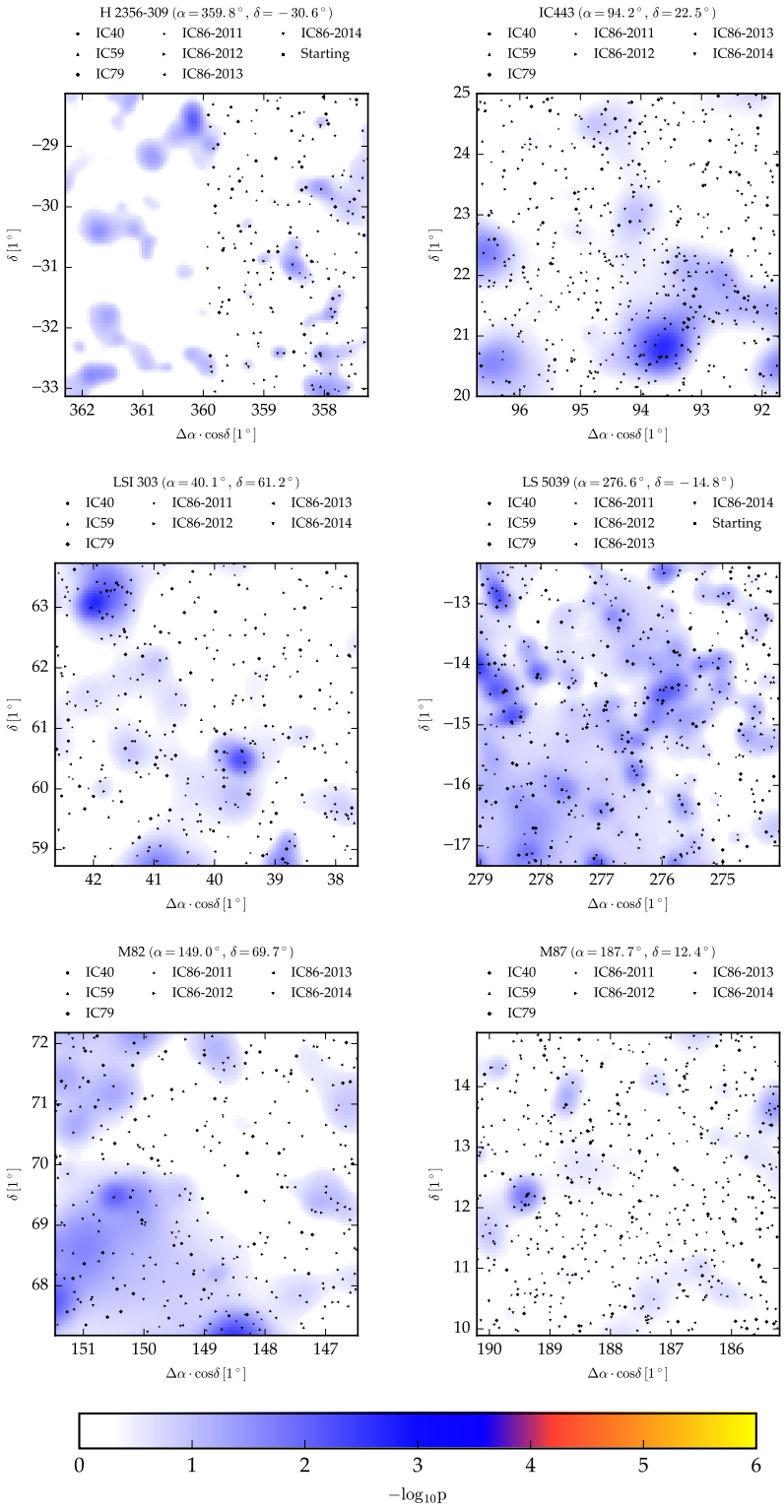

Figure C.11: P-value landscape of six sources

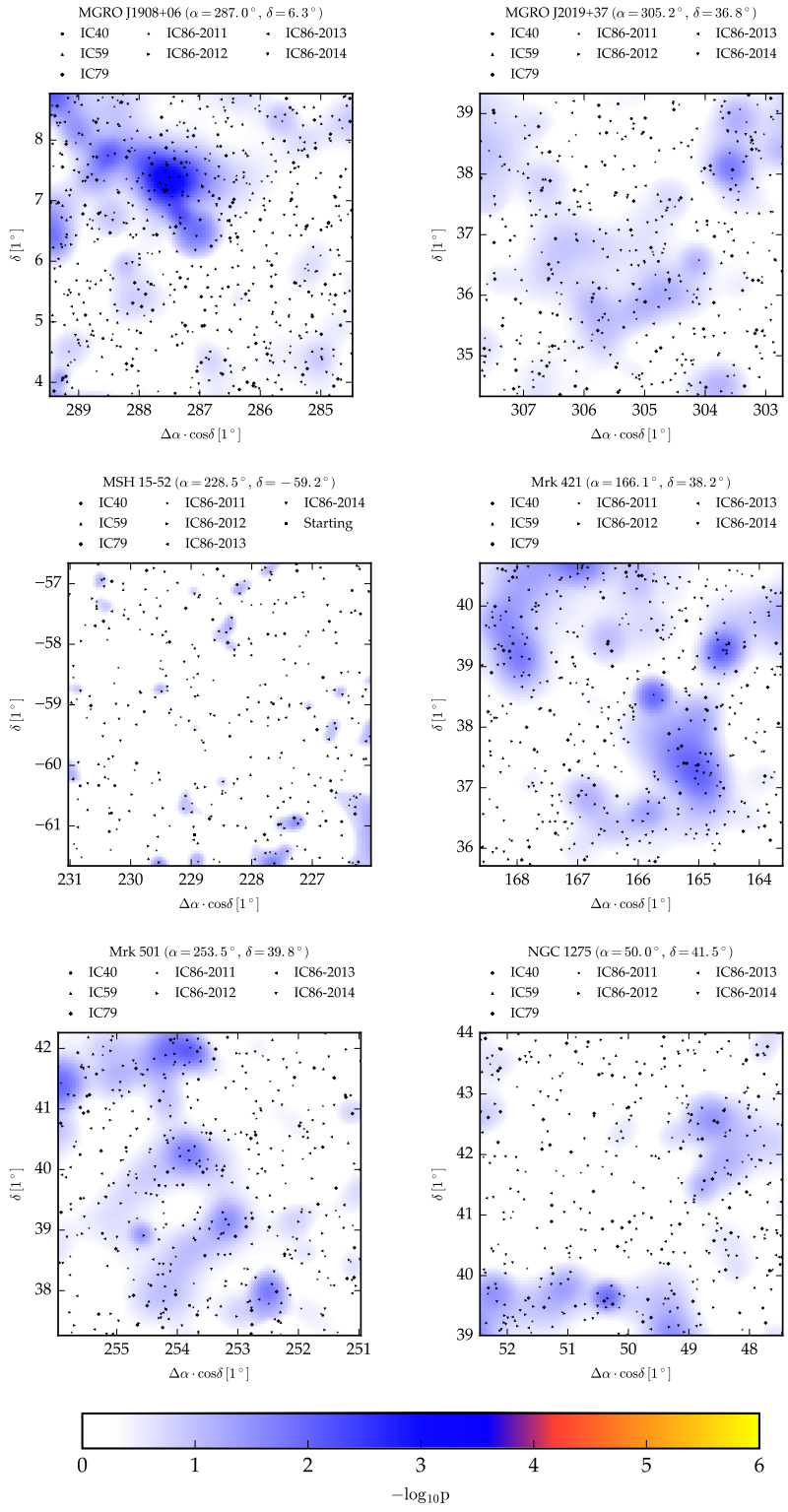

Figure C.12: P-value landscape of six sources

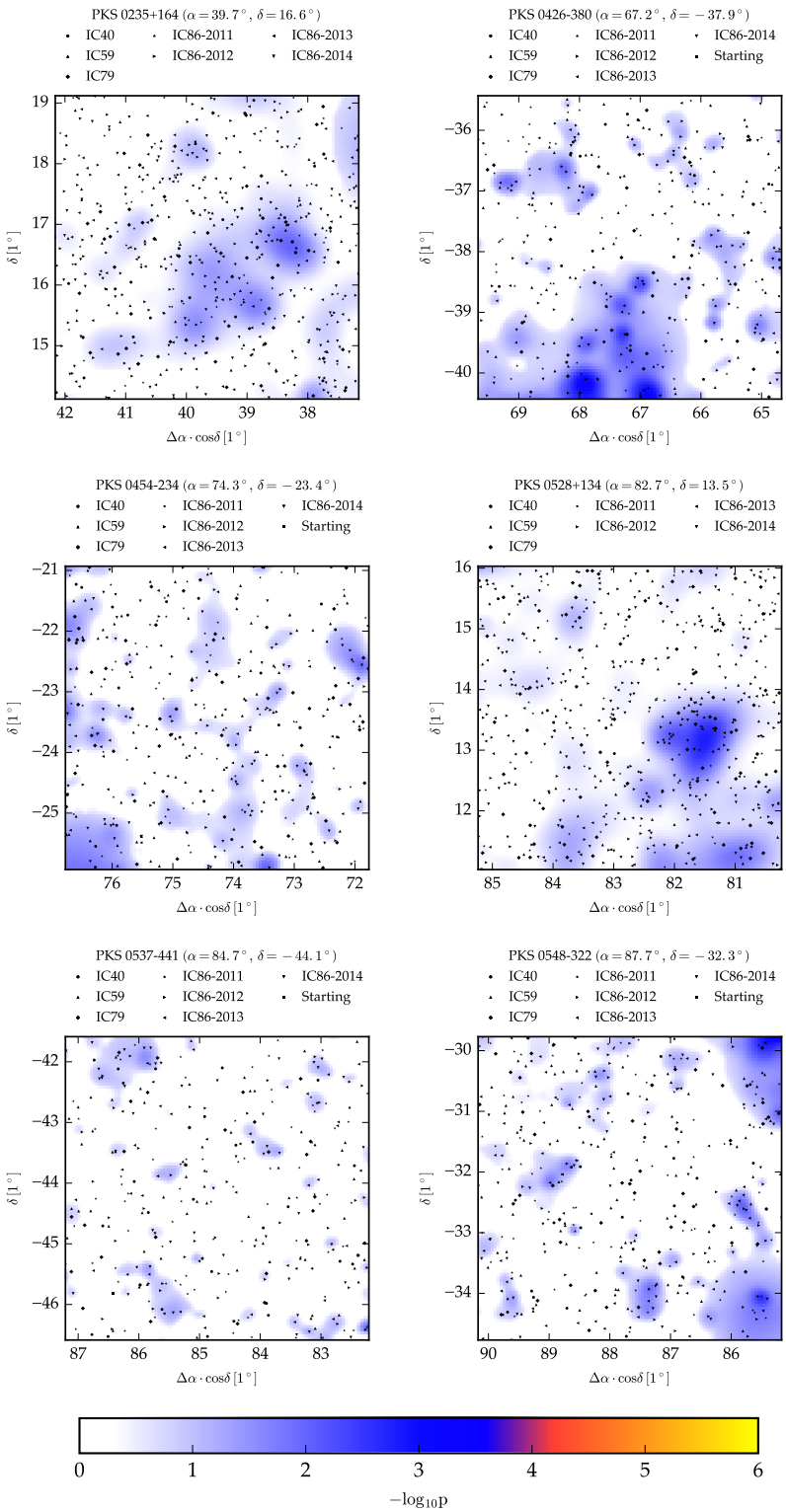

Figure C.13: P-value landscape of six sources

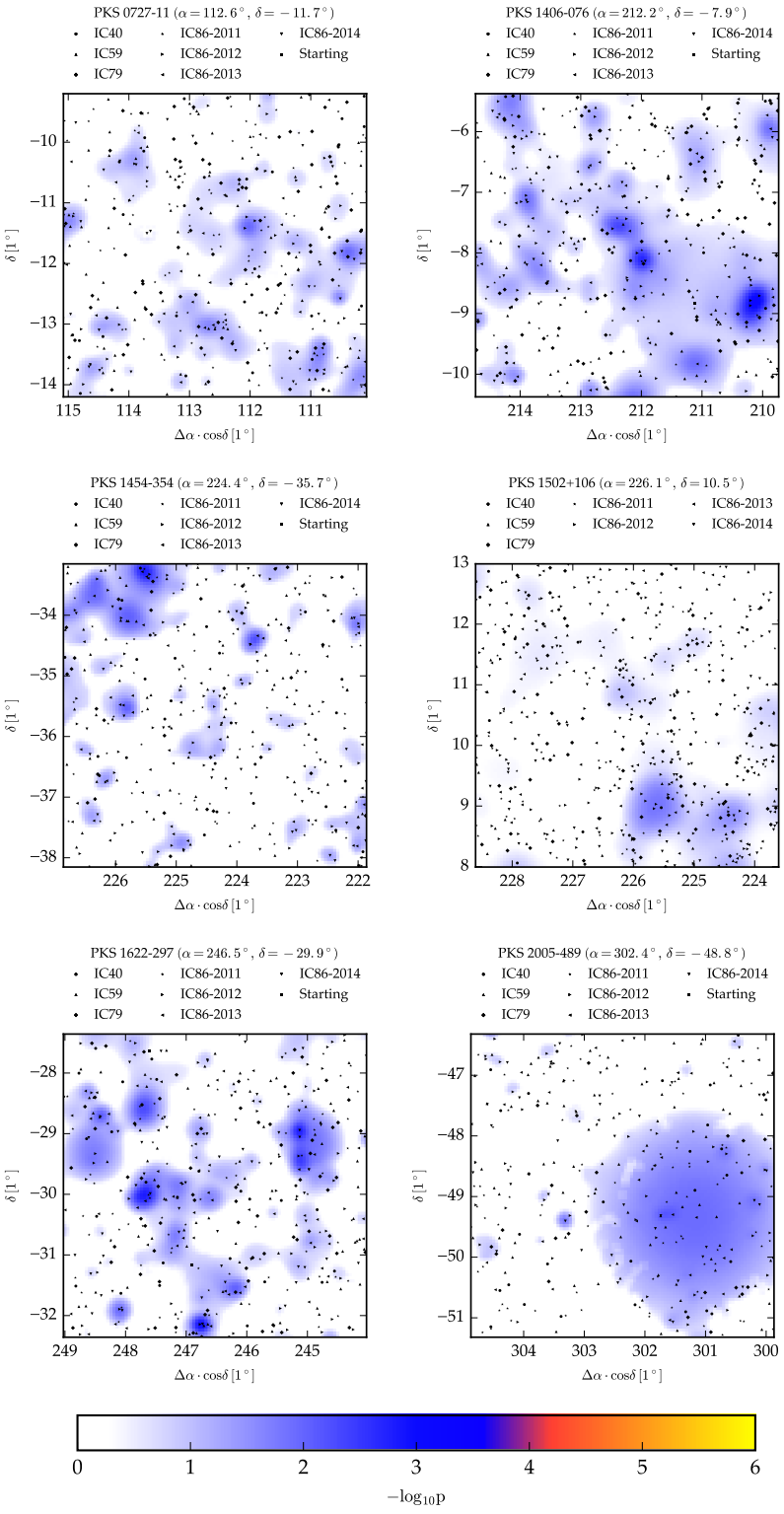

Figure C.14: P-value landscape of six sources

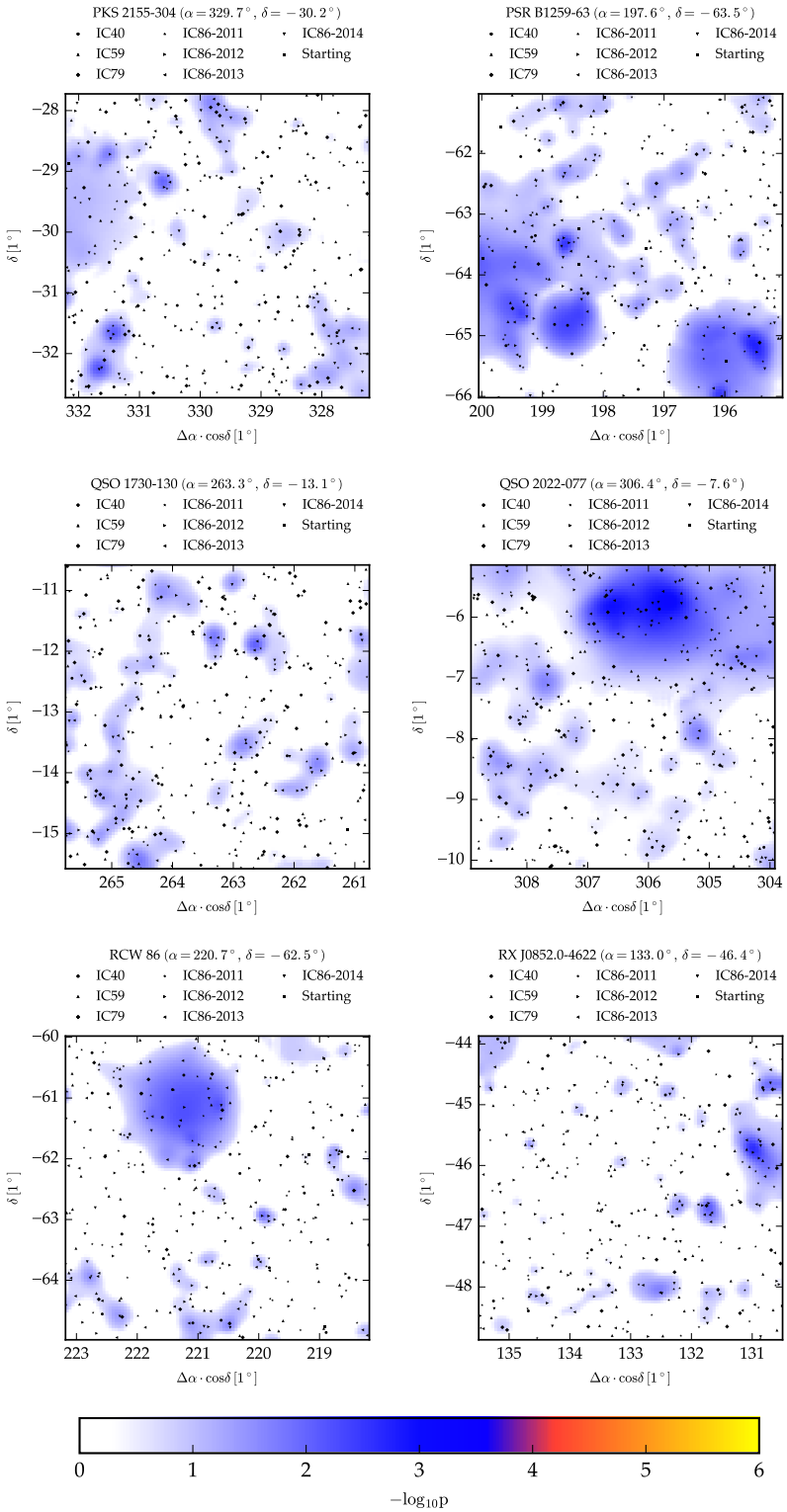

Figure C.15: P-value landscape of six sources

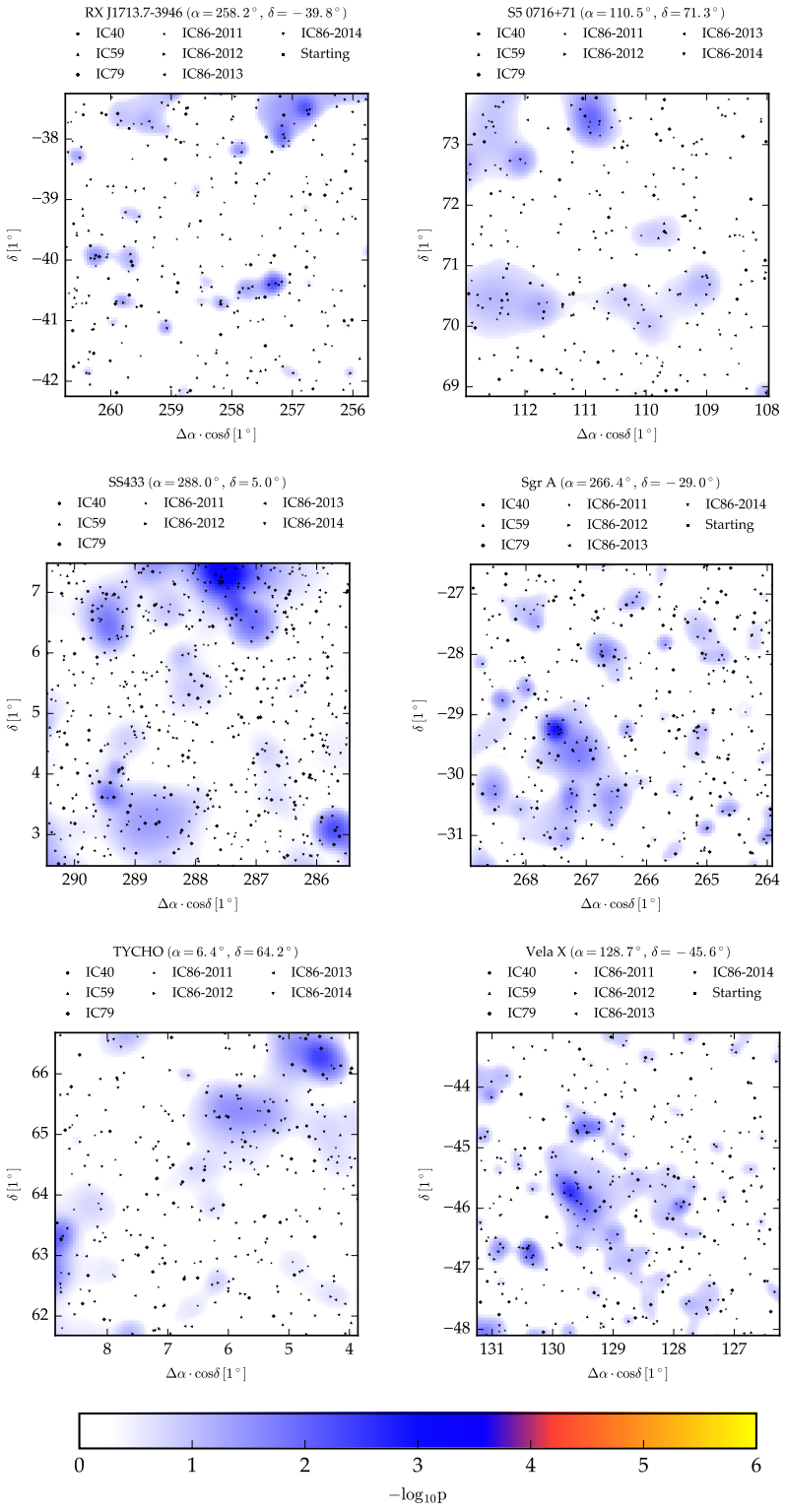

Figure C.16: P-value landscape of six sources

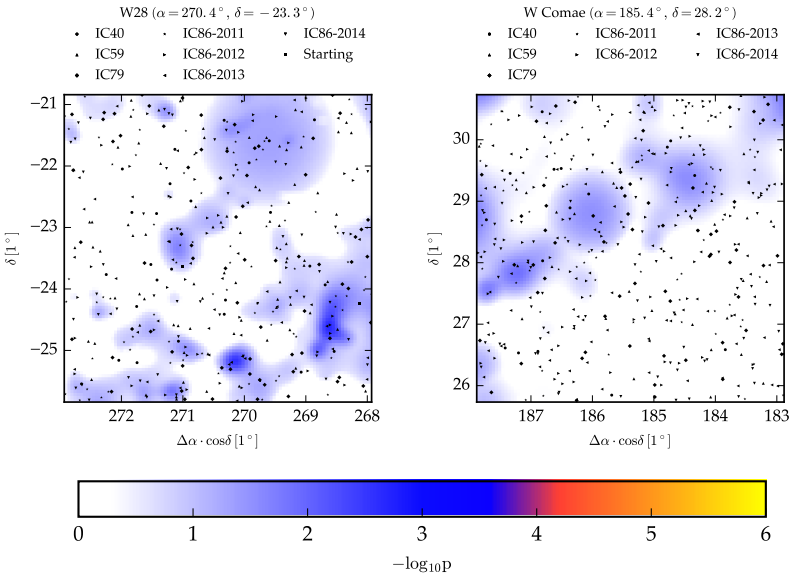

Figure C.17: P-value landscape of two sources

D Multi-messenger correlation test

In the correlation test using multi-messenger approaches in Section 10, three catalogs were used in the test. The strongest result was found for HBL objects of the 2FHL catalog and discussed in most detail. The results of the other catalogs (2WHSP and 3LAC) are listed here in addition to Table **??**.

Figures D.1 to D.3 show the number of counterparts associated in cosmic rays with respect to the expected number of random associations at the flux/FoM and angular separation values where the biggest excess was found. These distributions are used to calculate the local p-value of the excess.

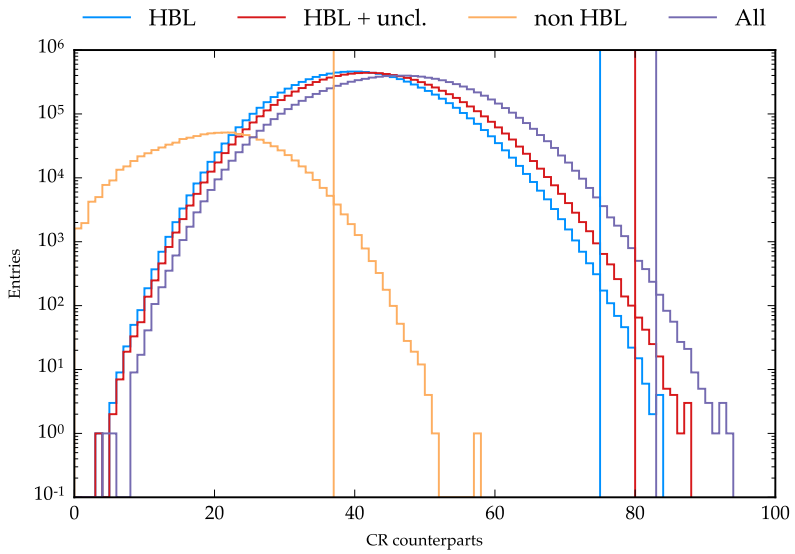

Figure D.1: CR counterparts in 2FHL correlation search. The number of counterparts is shown for different subsets of the 2FHL catalog and compared to the expectation from scrambling.

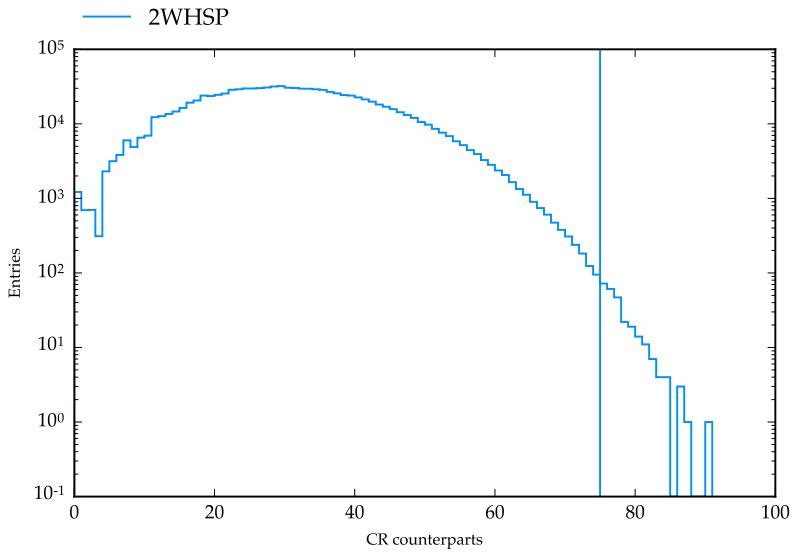

Figure D.2: CR counterparts in the 2WHSP correlation search. Figure equivalent to previous figure.

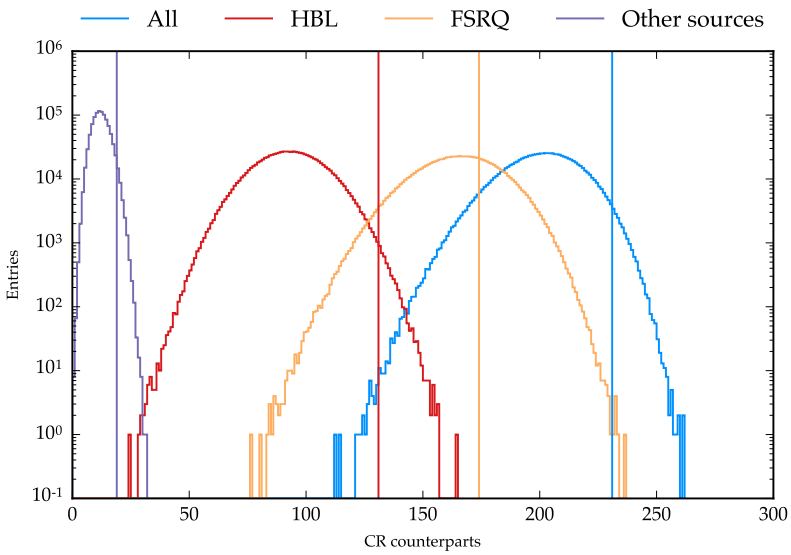

Figure D.3: CR counterparts in the 3LAC correlation search. Figure equivalent to previous figure.

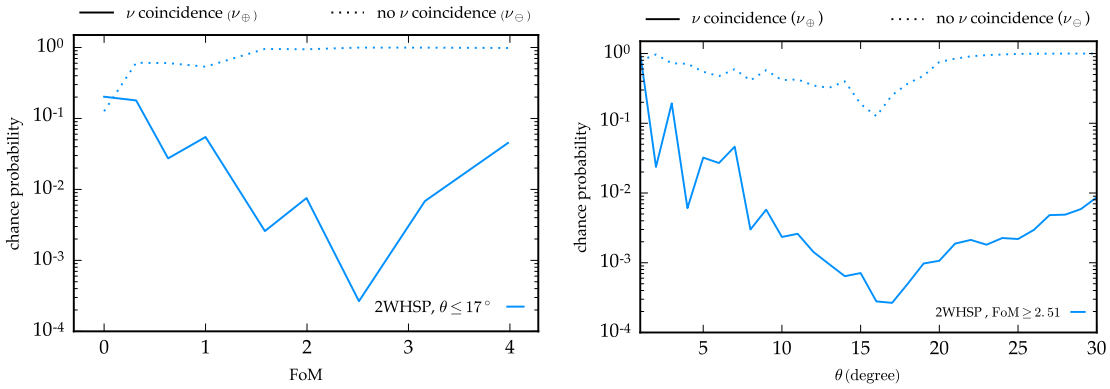

Figure D.4: Scan in figure of merit and angular separation for 2WHSP catalog. Shown is the p-value of background producing at least a result as significant. The left figure shows a scan in flux, the right one in angular separation. The other variable is set to the global minimum (indicated in legend). Dotted lines show the same test for CRs not correlating with neutrinos.

D.1 2WHSP catalog results

Figure D.4 shows the local p-value for scanning the catalog in "figure of merit" and angular separation θ of cosmic rays for the 2WHSP catalog. The catalog consist only of HBL candidates and no partitioning of the catalog is done. The result is significant above 3σ (Figure D.5 and D.6), but slightly less than the 2FHL. In the 2WHSP, no objects close to the Galactic Plane are collected, creating an anisotropy in the object distribution in contrast to the 2FHL.

Figure D.5: Post trial correction of 2WHSP for the correlation test.

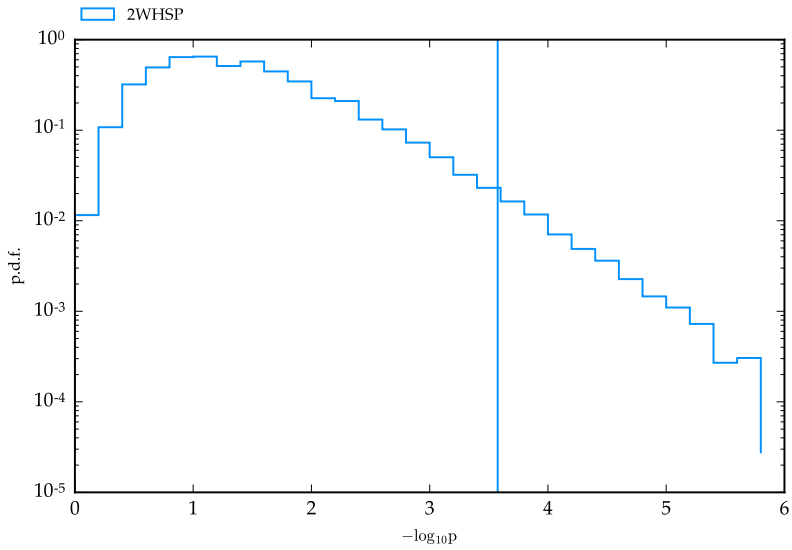

Figure D.6: Outcome of the likelihood ratio test for the 2WHSP catalog. The result for different catalogs is indicated as vertical line and compared to background expectation. Positive values of $\log_{10}\Lambda$ indicate preference of a neutrino connection to cosmic rays and gamma ray objects.

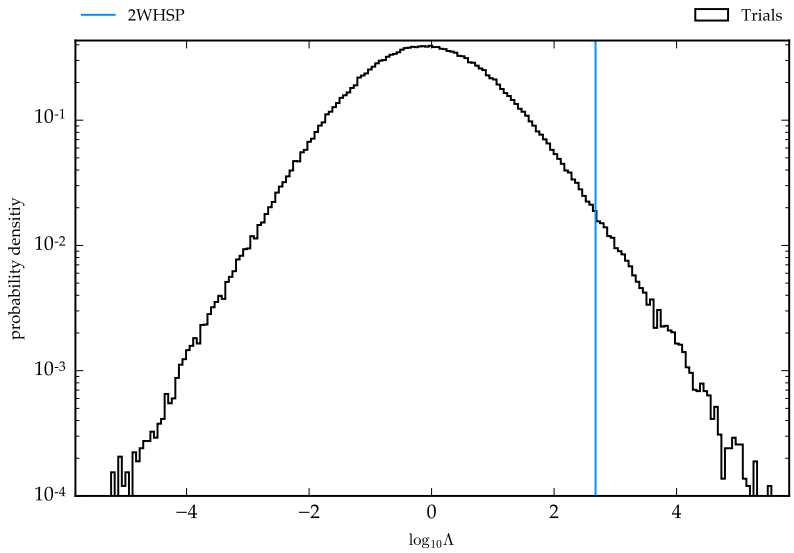

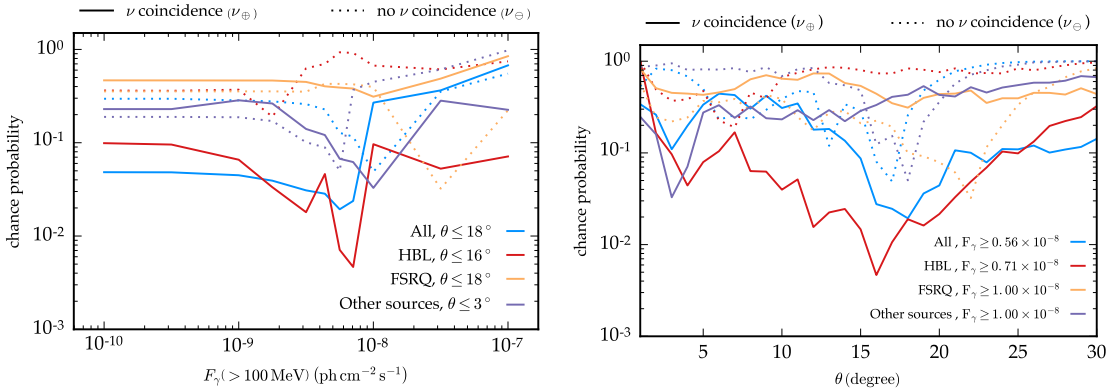

Figure D.7: Scan in flux and angular separation for 3LAC catalog. Shown is the p-value of background producing at least a result as significant. The left figure shows a scan in flux, the right one in angular separation. The other variable is set to the global minimum (indicated in legend). Dotted lines show the same test for CRs not correlating with neutrinos.

D.2 3LAC results

The 3LAC catalog is separated into HBL, FSRQ, and other AGN sources. The scan in flux and CR separation angle is shown in Figure D.7, in addition with the scan using the full catalog. The largest excess is again seen for HBL objects. The post trial significance is lower than for 2FHL and 2WHSP and shown in Figure D.7 and D.8. No hint for correlation is found for FSRQ and other AGN sources.

Figure D.8: Post trial correction of 3LAC for the correlation test.

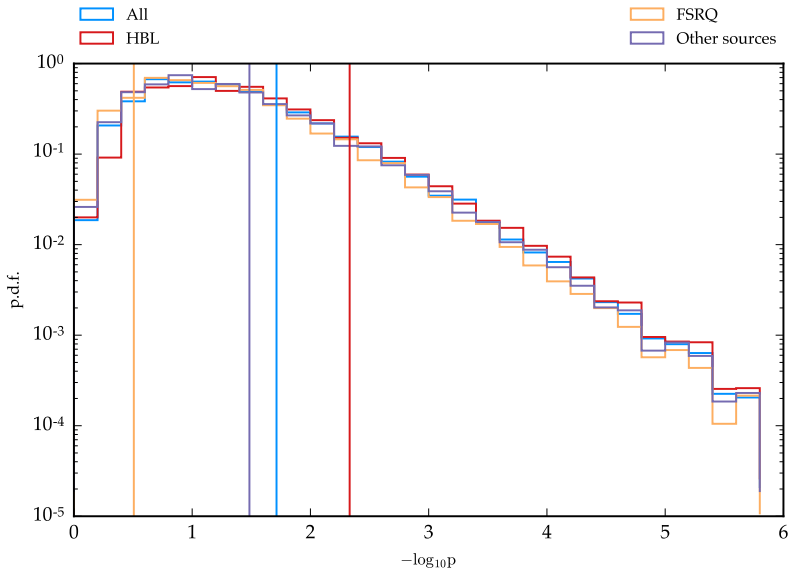

Figure D.9: Outcome of the likelihood ratio test for the 3LAC catalog. The result for different catalogs is indicated as vertical line and compared to background expectation. Positive values of $\log_{10}\Lambda$ indicate preference of a neutrino connection to cosmic rays and gamma ray objects.

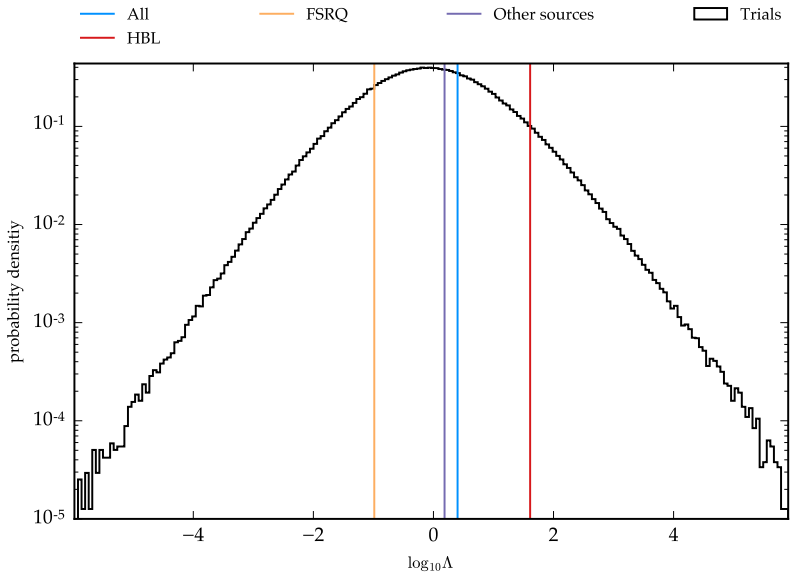

Bibliography

Aab, A. et al. "Searches for Anisotropies in the Arrival Directions of the Highest Energy Cosmic Rays Detected by the Pierre Auger Observatory". *Astrophys. J.* 804.1 (2015) 15. arXiv:1411.6111 [astro-ph.HE] (cit. on pp. 24, 115).

Aartsen, M. G. et al. "A combined maximum-likelihood analysis of the high-energy astrophysical neutrino flux measured with IceCube". *Astrophys. J.* 809.1 (2015) 98. arXiv:1507.03991 [astro-ph.HE] (cit. on pp. 9, 38).

– "All-sky search for time-integrated neutrino emission from astrophysical sources with 7 years of IceCube data" (2016). arXiv:1609.04981 [astro-ph.HE] (cit. on p. 79).

– "An All-Sky Search for Three Flavors of Neutrinos from Gamma-Ray Bursts with the IceCube Neutrino Observatory". *Astrophys. J.* 824.2 (2016) 115. arXiv:1601.06484 [astro-ph.HE] (cit. on pp. 26, 60).

– "Atmospheric and astrophysical neutrinos above 1 TeV interacting in IceCube". *Phys. Rev.* D91.2 (2015) 022001. arXiv:1410.1749 [astro-ph.HE] (cit. on pp. 7–9, 27).

– "Characterization of the Atmospheric Muon Flux in IceCube". *Astropart. Phys.* 78 (2016) 1–27. arXiv:1506.07981 [astro-ph.HE] (cit. on p. 63).

– "Constraints on ultra-high-energy cosmic ray sources from a search for neutrinos above 10 PeV with IceCube" (2016). arXiv:1607.05886 [astro-ph.HE] (cit. on pp. 27, 103).

– "Determining neutrino oscillation parameters from atmospheric muon neutrino disappearance with three years of IceCube DeepCore data". *Phys. Rev.* D91.7 (2015) 072004. arXiv:1410.7227 [hep-ex] (cit. on p. 39).

– "Energy Reconstruction Methods in the IceCube Neutrino Telescope". *JINST* 9 (2014) P03009. arXiv:1311.4767 [physics.ins-det] (cit. on pp. 36, 48).

– "Evidence for Astrophysical Muon Neutrinos from the Northern Sky with IceCube". *Phys. Rev. Lett.* 115.8 (2015) 081102. arXiv:1507.04005 [astro-ph.HE] (cit. on pp. 1, 9, 116, 126).

– "Evidence for High-Energy Extraterrestrial Neutrinos at the IceCube Detector". *Science* 342 (2013) 1242856. arXiv:1311.5238 [astro-ph.HE] (cit. on pp. 1, 5, 7, 36, 75, 127).

– "Flavor Ratio of Astrophysical Neutrinos above 35 TeV in IceCube". *Phys. Rev. Lett.* 114.17 (2015) 171102. arXiv:1502.03376 [astro-ph.HE] (cit. on p. 8).

– "IceCube-Gen2: A Vision for the Future of Neutrino Astronomy in Antarctica" (2014). arXiv:1412.5106 [astro-ph.HE] (cit. on p. 113).

– "Improvement in Fast Particle Track Reconstruction with Robust Statistics". *Nucl. Instrum. Meth.* A736 (2014) 143–149. arXiv:1308.5501 [astro-ph.IM] (cit. on p. 44).

– "Lowering IceCube's Energy Threshold for Point Source Searches in the Southern Sky" (2016). arXiv:1605.00163 [astro-ph.HE] (cit. on pp. 56, 73, 75, 76, 79, 89, C-167).

Aartsen, M. G. et al. “Measurement of South Pole ice transparency with the IceCube LED calibration system”. *Nucl. Instrum. Meth.* A711 (2013) 73–89. arXiv:1301.5361 [astro-ph.IM] (cit. on pp. 36, 40, 85).
– “Observation and Characterization of a Cosmic Muon Neutrino Flux from the Northern Hemisphere using six years of IceCube data” (2016). arXiv:1607.08006 [astro-ph.HE] (cit. on pp. 9, 38, 50, 73, 79, 100, B-141).
– “Observation of the cosmic-ray shadow of the Moon with IceCube”. *Phys. Rev.* D89.10 (2014) 102004. arXiv:1305.6811 [astro-ph.HE] (cit. on pp. 46, 51).
– “Search for Astrophysical Tau Neutrinos in Three Years of IceCube Data”. *Phys. Rev.* D93.2 (2016) 022001. arXiv:1509.06212 [astro-ph.HE] (cit. on pp. 10, 37).
– “Search for correlations between the arrival directions of IceCube neutrino events and ultrahigh-energy cosmic rays detected by the Pierre Auger Observatory and the Telescope Array”. *JCAP* 1601.01 (2016) 037. arXiv:1511.09408 [astro-ph.HE] (cit. on pp. 1, 24, 116, 121).
– “Search for Time-independent Neutrino Emission from Astrophysical Sources with 3 yr of IceCube Data”. *Astrophys. J.* 779 (2013) 132. arXiv:1307.6669 [astro-ph.HE] (cit. on pp. 67, 79, 109).
– “Searches for Extended and Point-like Neutrino Sources with Four Years of IceCube Data”. *Astrophys. J.* 796.2 (2014) 109. arXiv:1406.6757 [astro-ph.HE] (cit. on pp. 1, 51, 56, 75, 79, 109, 134).
– “Searches for small-scale anisotropies from neutrino point sources with three years of IceCube data”. *Astropart. Phys.* 66 (2015) 39–52. arXiv:1408.0634 [astro-ph.HE] (cit. on pp. 79, 134).
– “Searches for Time Dependent Neutrino Sources with IceCube Data from 2008 to 2012”. *Astrophys. J.* 807.1 (2015) 46. arXiv:1503.00598 [astro-ph.HE] (cit. on pp. 60, 79, 134).
– “The IceCube Neutrino Observatory - Contributions to ICRC 2015 Part II: Atmospheric and Astrophysical Diffuse Neutrino Searches of All Flavors”. *Proceedings, 34th International Cosmic Ray Conference (ICRC 2015)*. 2015. arXiv:1510.05223 [astro-ph.HE] (cit. on pp. 8, 100).
– “The IceCube Neutrino Observatory - Contributions to ICRC 2015 Part IV: Searches for Dark Matter and Exotic Particles” (2015). arXiv:1510.05226 [astro-ph.HE] (cit. on p. 39).
Abbasi, R. et al. “IceTop: The surface component of IceCube”. *Nucl. Instrum. Meth.* A700 (2013) 188–220. arXiv:1207.6326 [astro-ph.IM] (cit. on p. 39).
– “Indications of Intermediate-Scale Anisotropy of Cosmic Rays with Energy Greater Than 57 EeV in the Northern Sky Measured with the Surface Detector of the Telescope Array Experiment”. *Astrophys. J.* 790 (2014) L21. arXiv:1404.5890 [astro-ph.HE] (cit. on pp. 24, 115).
– “The Design and Performance of IceCube DeepCore”. *Astropart. Phys.* 35 (2012) 615–624. arXiv:1109.6096 [astro-ph.IM] (cit. on p. 39).
– “The IceCube Data Acquisition System: Signal Capture, Digitization, and Timestamping”. *Nucl. Instrum. Meth.* A601 (2009) 294–316. arXiv:0810.4930 [physics.ins-det] (cit. on pp. 39, 41).
– “Time-Integrated Searches for Point-like Sources of Neutrinos with the 40-String IceCube Detector”. *Astrophys. J.* 732 (2011) 18. arXiv:1012.2137 [astro-ph.HE] (cit. on p. 79).

Abraham, J. et al. "Observation of the suppression of the flux of cosmic rays above 4×10^{19}eV". *Phys. Rev. Lett.* 101 (2008) 061101. arXiv:0806.4302 [astro-ph] (cit. on pp. 18, 26).

– "Properties and performance of the prototype instrument for the Pierre Auger Observatory". *Nucl. Instrum. Meth.* A523 (2004) 50–95 (cit. on p. 115).

Abramowicz, H. et al. "A Parametrization of sigma-T (gamma* p) above the resonance region Q**2 >= 0". *Phys. Lett.* B269 (1991) 465–476 (cit. on p. 85).

Abu-Zayyad, T. et al. "The Cosmic Ray Energy Spectrum Observed with the Surface Detector of the Telescope Array Experiment". *Astrophys. J.* 768 (2013) L1. arXiv:1205.5067 [astro-ph.HE] (cit. on pp. 18, 26).

– "The surface detector array of the Telescope Array experiment". *Nucl. Instrum. Meth.* A689 (2013) 87–97. arXiv:1201.4964 [astro-ph.IM] (cit. on p. 115).

Achterberg, A. et al. "First Year Performance of The IceCube Neutrino Telescope". *Astropart. Phys.* 26 (2006) 155–173. arXiv:astro-ph/0604450 [astro-ph] (cit. on pp. 7, 38).

Ackermann, M. et al. "2FHL: The Second Catalog of Hard Fermi-LAT Sources". *Astrophys. J. Suppl.* 222.1 (2016) 5. arXiv:1508.04449 [astro-ph.HE] (cit. on pp. 100, 118).

– "The Third Catalog of Active Galactic Nuclei Detected by the Fermi Large Area Telescope". *Astrophys. J.* 810.1 (2015) 14. arXiv:1501.06054 [astro-ph.HE] (cit. on p. 119).

Adriani, O. et al. "PAMELA Measurements of Cosmic-ray Proton and Helium Spectra". *Science* 332 (2011) 69–72. arXiv:1103.4055 [astro-ph.HE] (cit. on p. 17).

Adrian-Martinez, S. et al. "First combined search for neutrino point-sources in the Southern Hemisphere with the ANTARES and IceCube neutrino telescopes" (2015). arXiv:1511.02149 [hep-ex] (cit. on pp. 52, 84, 102, 112).

– "Letter of intent for KM3NeT 2.0". *J. Phys.* G43.8 (2016) 084001. arXiv:1601.07459 [astro-ph.IM] (cit. on pp. 33, 112, 133).

– "Searches for Point-like and extended neutrino sources close to the Galactic Centre using the ANTARES neutrino Telescope". *Astrophys. J.* 786 (2014) L5. arXiv:1402.6182 [hep-ex] (cit. on pp. 56, 79, 83).

Ageron, M. et al. "ANTARES: The first undersea neutrino telescope". *Nuclear Instruments and Methods in Physics Research A* 656 (Nov. 2011) 11–38. arXiv:1104.1607 [astro-ph.IM] (cit. on p. 7).

Aguilar, M. et al. "Precision Measurement of the Proton Flux in Primary Cosmic Rays from Rigidity 1 GV to 1.8 TV with the Alpha Magnetic Spectrometer on the International Space Station". *Phys. Rev. Lett.* 114 (2015) 171103 (cit. on p. 17).

Aharonian, F. A. et al. "The Energy spectrum of TeV gamma-rays from the Crab nebula as measured by the HEGRA system of imaging air Cherenkov telescopes". *Astrophys. J.* 539 (2000) 317–324. arXiv:astro-ph/0003182 [astro-ph] (cit. on p. 102).

Ahlers, M. "Multi-messenger aspects of cosmic neutrinos". *EPJ Web Conf.* 116 (2016) 11001 (cit. on p. 6).

Ahlers, M. and Halzen, F. "Pinpointing Extragalactic Neutrino Sources in Light of Recent IceCube Observations". *Phys. Rev.* D90.4 (2014) 043005. arXiv:1406.2160 [astro-ph.HE] (cit. on p. 9).

Ahmad, Q. R. et al. "Measurement of the rate of $\nu_e + d \rightarrow p + p + e^-$ interactions produced by ^8B solar neutrinos at the Sudbury Neutrino Observatory". *Phys. Rev. Lett.* 87 (2001) 071301. arXiv:nucl-ex/0106015 [nucl-ex] (cit. on p. 12).

Ahrens, J. et al. “Muon track reconstruction and data selection techniques in AMANDA”. *Nucl. Instrum. Meth.* A524 (2004) 169–194. arXiv:astro-ph/0407044 [astro-ph] (cit. on pp. 44–47).

Ajello, M. et al. “The Origin of the Extragalactic Gamma-Ray Background and Implications for Dark-Matter Annihilation”. *Astrophys. J.* 800.2 (2015) L27. arXiv:1501.05301 [astro-ph.HE] (cit. on p. 126).

Aleksić, J. et al. “Unprecedented study of the broadband emission of Mrk 421 during flaring activity in March 2010”. *Astron. Astrophys.* 578 (2015) A22. arXiv:1412.3576 [astro-ph.HE] (cit. on pp. 11, 104).

Aloisio, R. et al. “Cosmogenic neutrinos and ultra-high energy cosmic ray models”. *JCAP* 1510.10 (2015) 006. arXiv:1505.04020 [astro-ph.HE] (cit. on pp. 20, 27).

Amato, E., Guetta, D., and Blasi, P. “Signatures of high energy protons in pulsar winds”. *Astron. Astrophys.* 402 (2003) 827–836. arXiv:astro-ph/0302121 [astro-ph] (cit. on p. 102).

Anchordoqui, L. A. et al. “End of the cosmic neutrino energy spectrum”. *Phys. Lett.* B739 (2014) 99–101. arXiv:1404.0622 [hep-ph] (cit. on p. 8).

Anchordoqui, L. A. et al. “Cosmic Neutrino Pevatrons: A Brand New Pathway to Astronomy, Astrophysics, and Particle Physics”. *JHEAp* 1-2 (2014) 1–30. arXiv:1312.6587 [astro-ph.HE] (cit. on pp. 6, 10).

Andres, E. et al. “The AMANDA neutrino telescope: Principle of operation and first results”. *Astropart. Phys.* 13 (2000) 1–20. arXiv:astro-ph/9906203 [astro-ph] (cit. on p. 7).

Argüelles, C. A., Katori, T., and Salvado, J. “New Physics in Astrophysical Neutrino Flavor”. *Phys. Rev. Lett.* 115 (2015) 161303. arXiv:1506.02043 [hep-ph] (cit. on p. 15).

Arsioli, B. et al. “1WHSP: An IR-based sample of $\sim$1000 VHE γ-ray blazar candidates”. *Astron. Astrophys.* 579 (2015) A34. arXiv:1504.02801 [astro-ph.HE] (cit. on p. 118).

Ashie, Y. et al. “Evidence for an oscillatory signature in atmospheric neutrino oscillation”. *Phys. Rev. Lett.* 93 (2004) 101801. arXiv:hep-ex/0404034 [hep-ex] (cit. on p. 12).

Athar, H., Kim, C. S., and Lee, J. “The Intrinsic and oscillated astrophysical neutrino flavor ratios”. *Mod. Phys. Lett.* A21 (2006) 1049–1066. arXiv:hep-ph/0505017 [hep-ph] (cit. on p. 14).

Avrorin, A. D. et al. “Status and perspectives of the BAIKAL-GVD project”. *EPJ Web Conf.* 121 (2016) 05003 (cit. on pp. 33, 112).

Barlow, R. J. “Extended maximum likelihood”. *Nucl. Instrum. Meth.* A297 (1990) 496–506 (cit. on p. 50).

Becker, W. and Aschenbach, B. “Rosat HRI observations of the Crab Pulsar: an improved temperature upper limit for PSR 0531+21” (1995). arXiv:astro-ph/9503012 [astro-ph] (cit. on p. 25).

Belolaptikov, I. A. et al. “The Baikal underwater neutrino telescope: Design, performance and first results”. *Astropart. Phys.* 7 (1997) 263–282 (cit. on p. 7).

Boettcher, M. “Modeling the Emission Processes in Blazars”. *Astrophys. Space Sci.* 309 (2007) 95–104. arXiv:astro-ph/0608713 [astro-ph] (cit. on p. 103).

Bos, F. et al. “Observation of the Cosmic-Ray Shadow of the Moon and Sun with IceCube”. *ASTRA Proceedings* 2 (2015) 5–8 (cit. on p. 46).

Braun, J., Baker, M., et al. "Time-Dependent Point Source Search Methods in High Energy Neutrino Astronomy". *Astropart. Phys.* 33 (2010) 175–181. arXiv:0912.1572 [astro-ph.IM] (cit. on p. 51).

Braun, J., Dumm, J., et al. "Methods for point source analysis in high energy neutrino telescopes". *Astropart. Phys.* 29 (2008) 299–305. arXiv:0801.1604 [astro-ph] (cit. on pp. 49, 51).

Bugaev, E. V. and Shlepin, Yu. V. "Photonuclear interaction of high-energy muons and tau leptons". *Phys. Rev.* D67 (2003) 034027. arXiv:hep-ph/0203096 [hep-ph] (cit. on p. 85).

– "Photonuclear interactions of super-high energy muons and tau-leptons". *Nucl. Phys. Proc. Suppl.* 122 (2003). [,341(2003)] 341–344 (cit. on p. 85).

Bugaev, E. et al. "Propagation of tau neutrinos and tau leptons through the earth and their detection in underwater / ice neutrino telescopes". *Astropart. Phys.* 21 (2004) 491–509. arXiv:hep-ph/0312295 [hep-ph] (cit. on pp. 35, 86).

Bustamante, M., Beacom, J. F., and Winter, W. "Theoretically palatable flavor combinations of astrophysical neutrinos". *Phys. Rev. Lett.* 115.16 (2015) 161302. arXiv:1506.02645 [astro-ph.HE] (cit. on p. 15).

Capozzi, F. et al. "Status of three-neutrino oscillation parameters, circa 2013". *Phys. Rev.* D89 (2014) 093018. arXiv:1312.2878 [hep-ph] (cit. on pp. 13–15).

Chang, Y.-L. et al. "2WHSP: A catalog of HE and VHE gamma-ray blazars and blazar candidates" (2016). arXiv:1609.05808 [astro-ph.HE] (cit. on pp. 118, 119, 123, 124).

Chirkin, D. "Evidence of optical anisotropy of the South Pole ice". *Proceedings, 33rd International Cosmic Ray Conference (ICRC2013): Rio de Janeiro, Brazil* (2013) 0580 (cit. on p. 40).

Coenders, S. *Skylab*. https://github.com/coenders/skylab. 2016 (cit. on pp. 49, 53).

Cowan, C. L. et al. "Detection of the free neutrino: A Confirmation". *Science* 124 (1956) 103–104 (cit. on p. 7).

Davis Jr., R. and Harmer, D. S. "Solar neutrinos" (1964) (cit. on p. 12).

Dev, P. S. B. et al. "Heavy right-handed neutrino dark matter and PeV neutrinos at IceCube". *JCAP* 1608.08 (2016) 034. arXiv:1606.04517 [hep-ph] (cit. on p. 12).

DeYoung, T. "Results from IceCube". *EPJ Web Conf.* 116 (2016) 11004 (cit. on p. 39).

Di Palma, I., Guetta, D., and Amato, E. "Revised predictions of neutrino fluxes from Pulsar Wind Nebulae" (2016). arXiv:1605.01205 [astro-ph.HE] (cit. on p. 102).

Dimitrakoudis, S. et al. "The time-dependent one-zone hadronic model - First principles". *Astron. Astrophys.* 546 (2012) A120. arXiv:1209.0413 [astro-ph.HE] (cit. on p. 11).

Enberg, R., Reno, M. H., and Sarcevic, I. "Prompt neutrino fluxes from atmospheric charm". *Phys. Rev.* D78 (2008) 043005. arXiv:0806.0418 [hep-ph] (cit. on p. 31).

Fang, K. et al. "Is the Ultra-High Energy Cosmic-Ray Excess Observed by the Telescope Array Correlated with IceCube Neutrinos?" *Astrophys. J.* 794.2 (2014) 126. arXiv:1404.6237 [astro-ph.HE] (cit. on p. 126).

Fedynitch, A. et al. "The contribution of charm to high energy atmospheric neutrinos". *Nucl. Part. Phys. Proc.* 265-266 (2015) 271–273 (cit. on p. 31).

Feintzeig, J. "Searches for Point-like Sources of Astrophysical Neutrinos with the IceCube Neutrino Observatory". PhD thesis. University of Wisconsin, Madison, 2014 (cit. on pp. 43, 61, 63, 75–77, 83, 84).

Feldman, G. J. and Cousins, R. D. "A Unified approach to the classical statistical analysis of small signals". *Phys. Rev.* D57 (1998) 3873–3889. arXiv:physics/9711021 [physics.data-an] (cit. on p. 126).

Fermi, E. "On the Origin of the Cosmic Radiation". *Phys. Rev.* 75 (1949) 1169–1174 (cit. on p. 21).

Fesen, R. A., Shull, J. M., and Hurford, A. P. "An Optical Study of the Circumstellar Environment Around the Crab Nebula". *Astronomical Journal* 113 (Jan. 1997) 354–363 (cit. on p. 102).

Formaggio, J. A. and Zeller, G. P. "From eV to EeV: Neutrino Cross Sections Across Energy Scales". *Rev. Mod. Phys.* 84 (2012) 1307. arXiv:1305.7513 [hep-ex] (cit. on pp. 33–35).

Frank, I. M. and Tamm, I. "Coherent visible radiation of fast electrons passing through matter". *C. R. Acad. Sci. URSS* 14 (1937) 109–114 (cit. on p. 33).

Fukuda, Y. et al. "The Super-Kamiokande detector". *Nucl. Instrum. Meth.* A501 (2003) 418–462 (cit. on p. 37).

Gaisser, T. K. "Neutrino astronomy: Physics goals, detector parameters". 1997. arXiv:astro-ph/9707283 [astro-ph] (cit. on p. 38).

Gaisser, T. K. "Spectrum of cosmic-ray nucleons, kaon production, and the atmospheric muon charge ratio". *Astropart. Phys.* 35 (2012) 801–806. arXiv:1111.6675 [astro-ph.HE] (cit. on pp. 8, 19).

Gaisser, T. K., Jero, K., et al. "Generalized self-veto probability for atmospheric neutrinos". *Phys. Rev.* D90.2 (2014) 023009. arXiv:1405.0525 [astro-ph.HE] (cit. on p. 7).

Gaisser, T. K., Stanev, T., and Tilav, S. "Cosmic Ray Energy Spectrum from Measurements of Air Showers". *Front. Phys.(Beijing)* 8 (2013) 748–758. arXiv:1303.3565 [astro-ph.HE] (cit. on p. 19).

Gaisser, T., Engel, R., and Resconi, E. *Cosmic Rays and Particle Physics*. Cambridge University Press, 2016. ISBN: 9781316598436 (cit. on pp. 10, 13, 17–23, 25–30).

Gandhi, R. et al. "Ultrahigh-energy neutrino interactions". *Astropart. Phys.* 5 (1996) 81–110. arXiv:hep-ph/9512364 [hep-ph] (cit. on pp. 34–36).

Gavish, E. and Eichler, D. "On ultra high energy cosmic rays and their resultant gamma rays". *Astrophys. J.* 822.1 (2016) 56. arXiv:1603.04074 [astro-ph.HE] (cit. on p. 126).

Gerz, R. *Crab Nebula*. July 2016. URL: http://www.nasa.gov/sites/default/files/images/148387main_image_feature_567_ys_full.jpg (visited on 07/28/2016) (cit. on p. 25).

Gilmore, R. C. et al. "GeV gamma-ray attenuation and the high-redshift UV background". *Monthly Notices of the Royal Astronomical Society* 399 (Nov. 2009) 1694–1708. arXiv:0905.1144 (cit. on p. 6).

Ginzburg, V. and Syrovatskii, S. *The Origin of Cosmic Rays*. Elsevier Science, 2013. ISBN: 9781483181318 (cit. on p. 21).

Giommi, P. and Padovani, P. "A simplified view of blazars: contribution to the X-ray and γ-ray cosmic backgrounds". *Mon. Not. Roy. Astron. Soc.* 450.3 (2015) 2404–2409. arXiv:1504.01978 [astro-ph.HE] (cit. on p. 126).

Glashow, S. L. "Resonant Scattering of Antineutrinos". *Phys. Rev.* 118 (1960) 316–317 (cit. on pp. 8, 34).

Glüsenkamp, T. "Analysis of the cumulative neutrino flux from Fermi-LAT blazar populations using 3 years of IceCube data". *EPJ Web Conf.* 121 (2016) 05006. arXiv:1502.03104 [astro-ph.HE] (cit. on pp. 1, 79).

– *Muon Filter Proposal IC86-2012*. Tech. rep. http://docushare.icecube.wisc.edu/dsweb/Get/Document-59906/MuonFilter2012_v3_with_addendum.pdf: DESY Zeuthen, 2012 (cit. on p. 43).

– "Search for a cumulative neutrino flux from 2LAC-blazar populations using 3 years of IceCube data". PhD thesis. 2016 (cit. on pp. 60, 101).

Gorski, K. M. et al. "HEALPix - A Framework for high resolution discretization, and fast analysis of data distributed on the sphere". *Astrophys. J.* 622 (2005) 759–771. arXiv:astro-ph/0409513 [astro-ph] (cit. on p. 89).

Górski, K. M. et al. "HEALPix: A Framework for High-Resolution Discretization and Fast Analysis of Data Distributed on the Sphere". *Astrophysical Journal* 622 (Apr. 2005) 759–771. eprint: arXiv:astro-ph/0409513 (cit. on p. 54).

Greisen, K. "Cosmic ray showers". *Ann. Rev. Nucl. Part. Sci.* 10 (1960) 63–108 (cit. on p. 7).

Greisen, K. "End to the cosmic ray spectrum?" *Phys. Rev. Lett.* 16 (1966) 748–750 (cit. on p. 27).

Hallen, P. "On the Measurement of High-Energy Tau Neutrinos with IceCube". Master thesis. RWTH Aachen, 2013 (cit. on p. 48).

Halzen, F. and Kheirandish, A. "High Energy Neutrinos from Recent Blazar Flares" (2016). arXiv:1605.06119 [astro-ph.HE] (cit. on p. 102).

Hanson, K. D. "Construction status and future of the IceCube neutrino observatory". *J. Phys. Conf. Ser.* 60 (2007) 47–51 (cit. on p. 38).

Heck, D. et al. *CORSIKA: a Monte Carlo code to simulate extensive air showers.* Feb. 1998 (cit. on pp. 27, 28).

Hess, V. F. "Über Beobachtungen der durchdringenden Strahlung bei sieben Freiballonfahrten". *Physikalische Zeitschrift* 13 (Nov. 1912) 1084–1091 (cit. on pp. 6, 133).

Hillas, A. M. "Angular and energy distributions of charged particles in electron photon cascades in air". *J. Phys.* G8 (1982) 1461–1473 (cit. on p. 29).

– "The Origin of Ultrahigh-Energy Cosmic Rays". *Ann. Rev. Astron. Astrophys.* 22 (1984) 425–444 (cit. on p. 24).

Hinton, J. A. and Hofmann, W. "Teraelectronvolt astronomy". *Ann. Rev. Astron. Astrophys.* 47 (2009) 523–565. arXiv:1006.5210 [astro-ph.HE] (cit. on p. 6).

Hirata, K. et al. "Observation of a Neutrino Burst from the Supernova SN 1987a". *Phys. Rev. Lett.* 58 (1987). [,727(1987)] 1490–1493 (cit. on p. 37).

Honda, M. et al. "Calculation of atmospheric neutrino flux using the interaction model calibrated with atmospheric muon data". *Phys. Rev.* D75 (2007) 043006. arXiv:astro-ph/0611418 [astro-ph] (cit. on pp. 8, 31, 72, B-141).

Huber, M. "Sensitivity Studies for Blazar Stacking Searches with the IceCube Neutrino Observatory". MA thesis. Technische Universität München, Dec. 2015 (cit. on pp. 60, 77, 133).

IceCube Collaboration. *Digital Optical Module*. Aug. 2016 (cit. on p. 39).

– *IceCube Detector*. Aug. 2016 (cit. on p. 39).

– *Multi messenger astronomy*. May 2016. URL: https://gallery.icecube.wisc.edu/internal/d/318865-1/physicus.pdf (visited on 05/19/2016) (cit. on p. 5).

Johnston, H. *Physics World Breakthrough of the Year*. Dec. 2013 (cit. on p. 1).

Joshi, J. C., Winter, W., and Gupta, N. "How Many of the Observed Neutrino Events Can Be Described by Cosmic Ray Interactions in the Milky Way?" *Mon. Not. Roy. Astron. Soc.* 439.4 (2014). [Erratum: Mon. Not. Roy. Astron. Soc.446,no.1,892(2014)] 3414–3419. arXiv:1310.5123 [astro-ph.HE] (cit. on p. 100).

Kadler, M. et al. "Coincidence of a high-fluence blazar outburst with a PeV-energy neutrino event" (2016). arXiv:1602.02012 [astro-ph.HE] (cit. on p. 102).

Kampert, K.-H. and Unger, M. "Measurements of the Cosmic Ray Composition with Air Shower Experiments". *Astropart. Phys.* 35 (2012) 660–678. arXiv:1201.0018 [astro-ph.HE] (cit. on p. 20).

Kappes, A. et al. "Potential Neutrino Signals from Galactic Gamma-Ray Sources". *Astrophys. J.* 656 (2007). [Erratum: Astrophys. J.661,1348(2007)] 870–896. arXiv:astro-ph/0607286 [astro-ph] (cit. on pp. 11, 101, 102, 112).

Klein, J. R. and Roodman, A. "Blind analysis in nuclear and particle physics". *Ann. Rev. Nucl. Part. Sci.* 55 (2005) 141–163 (cit. on p. 61).

Lattanzi, M. "Planck 2015 constraints on neutrino physics". *J. Phys. Conf. Ser.* 718.3 (2016) 032008 (cit. on p. 13).

Li, T.-P. and Ma, Y.-Q. "Analysis methods for results in gamma-ray astronomy". *Astrophysical Journal* 272 (Sept. 1983) 317–324 (cit. on p. 49).

Majorana, E. "Theory of the Symmetry of Electrons and Positrons". *Nuovo Cim.* 14 (1937) 171–184 (cit. on p. 13).

Maki, Z., Nakagawa, M., and Sakata, S. "Remarks on the unified model of elementary particles". *Prog. Theor. Phys.* 28 (1962) 870–880 (cit. on p. 12).

Mandelartz, M. and Tjus, J. B. "Prediction of the diffuse neutrino flux from cosmic ray interactions near supernova remnants". *Astropart. Phys.* 65 (2015) 80–100. arXiv:1301.2437 [astro-ph.GA] (cit. on pp. 106, 107, 112).

Mao, L. S. "2MASS observation of BL Lac objects II". *New Astronomy* 16 (Dec. 2011) 503–529 (cit. on p. 104).

Murase, K., Ahlers, M., and Lacki, B. C. "Testing the Hadronuclear Origin of PeV Neutrinos Observed with IceCube". *Phys. Rev.* D88.12 (2013) 121301. arXiv:1306.3417 [astro-ph.HE] (cit. on p. 100).

Narsky, I. and Porter, F. *Statistical Analysis Techniques in Particle Physics: Fits, Density Estimation and Supervised Learning*. Wiley, 2013. ISBN: 9783527677290 (cit. on pp. 68, 69).

Neunhöffer, T. "Estimating the angular resolution of tracks in neutrino telescopes based on a likelihood analysis". *Astropart. Phys.* 25 (2006) 220–225. arXiv:astro-ph/0403367 [astro-ph] (cit. on pp. 47, 63, A-139).

Oliphant, T. E. "Python for Scientific Computing". *Computing in Science & Engineering* 9.3 (2007) 10–20 (cit. on p. 53).

Olive, K. A. et al. "Review of Particle Physics". *Chin. Phys.* C38 (2014) 090001 (cit. on pp. 10, 12, 18, 35, 86).

Otten, E. W. and Weinheimer, C. "Neutrino mass limit from tritium beta decay". *Rept. Prog. Phys.* 71 (2008) 086201. arXiv:0909.2104 [hep-ex] (cit. on p. 13).

Padovani, P., Petropoulou, M., et al. "A simplified view of blazars: the neutrino background". *Mon. Not. Roy. Astron. Soc.* 452.2 (2015) 1877–1887. arXiv:1506.09135 [astro-ph.HE] (cit. on pp. 100, 103).

Padovani, P., Resconi, E., et al. "Extreme blazars as counterparts of IceCube astrophysical neutrinos". *Mon. Not. Roy. Astron. Soc.* 457 (2016) 3582. arXiv:1601.06550 [astro-ph.HE] (cit. on pp. 117, 119–121).

Pedregosa, F. et al. "Scikit-learn: Machine Learning in Python". *Journal of Machine Learning Research* 12 (2011) 2825–2830 (cit. on pp. 61, 68).

Peters, B. "Primary cosmic radiation and extensive air showers". *Il Nuovo Cimento (1955-1965)* 22.4 (1961) 800–819. ISSN: 1827-6121 (cit. on pp. 18, 19).

Petropoulou, M., Coenders, S., and Dimitrakoudis, S. "Time-dependent neutrino emission from Mrk 421 during flares and predictions for IceCube". *Astropart. Phys.* 80 (2016) 115–130. arXiv:1603.06954 [astro-ph.HE] (cit. on pp. 11, 104, 106, 118).

Petropoulou, M., Dimitrakoudis, S., et al. "Photohadronic origin of γ-ray BL Lac emission: implications for IceCube neutrinos". *Mon. Not. Roy. Astron. Soc.* 448.3 (2015) 2412–2429. arXiv:1501.07115 [astro-ph.HE] (cit. on pp. 11, 26, 103, 104, 126).

Pierog, T. and Werner, K. "Muon Production in Extended Air Shower Simulations". *Phys. Rev. Lett.* 101 (2008) 171101. arXiv:astro-ph/0611311 [astro-ph] (cit. on p. 20).

Pierre Auger Collaboration. Aug. 2016. URL: https://www.auger.org/images/Cosmic_Rays/Auger_cosmic_ray_shower.jpg (cit. on p. 29).

Pontecorvo, B. "Mesonium and anti-mesonium". *Sov. Phys. JETP* 6 (1957). [Zh. Eksp. Teor. Fiz.33,549(1957)] 429 (cit. on p. 12).

– "Neutrino Experiments and the Problem of Conservation of Leptonic Charge". *Sov. Phys. JETP* 26 (1968). [Zh. Eksp. Teor. Fiz.53,1717(1967)] 984–988 (cit. on p. 12).

Punzi, G. "Comments on likelihood fits with variable resolution". *eConf* C030908 (2003). [,235(2004)] WELT002. arXiv:physics/0401045 [physics.data-an] (cit. on p. 51).

Reimer, A. "Photon-neutrino flux correlations from hadronic models of AGN?" *Proceedings, 34th International Cosmic Ray Conference (ICRC 2015)* (2015) (cit. on pp. 106, 107).

Reines, F. and Cowan, C. L. "The neutrino". *Nature* 178 (1956) 446–449 (cit. on p. 7).

Resconi, E. et al. "Connecting blazars with ultra high energy cosmic rays and astrophysical neutrinos". *Phys. Rev. Lett.* (2016). Submitted (cit. on p. 115).

Rieger, F. M., Ona-Wilhelmi, E. de, and Aharonian, F. A. "TeV Astronomy" (2013). arXiv:1302.5603 [astro-ph.HE] (cit. on p. 25).

Roberts, A. "The Birth of high-energy neutrino astronomy: A Personal history of the DUMAND project". *Rev. Mod. Phys.* 64 (1992) 259–312 (cit. on p. 7).

Rongen, M. "Measuring the optical properties of IceCube drill holes". *EPJ Web Conf.* 116 (2016) 06011 (cit. on p. 40).

Ruffini, R., Vereshchagin, G. V., and Xue, S. S. "Cosmic absorption of ultra high energy particles". *Astrophys. Space Sci.* 361 (2016) 82. arXiv:1503.07749 [astro-ph.HE] (cit. on p. 126).

Schoenen, S. and Rädel, L. "Detection of a multi-PeV neutrino-induced muon event from the Northern sky with IceCube". *The Astronomer's Telegram* 7856 (2015) (cit. on pp. 10, 117).

Schönert, S. et al. "Vetoing atmospheric neutrinos in a high energy neutrino telescope". *Phys. Rev.* D79 (2009) 043009. arXiv:0812.4308 [astro-ph] (cit. on p. 7).

Smith, M. W. E. et al. "The Astrophysical Multimessenger Observatory Network (AMON)". *Astropart. Phys.* 45 (2013) 56–70. arXiv:1211.5602 [astro-ph.HE] (cit. on p. 113).

Stecker, F. W. "Effect of photomeson production by the universal radiation field on high-energy cosmic rays". *Phys. Rev. Lett.* 21 (1968) 1016–1018 (cit. on p. 11).

Taylor, A. M., Ahlers, M., and Hooper, D. "Indications of Negative Evolution for the Sources of the Highest Energy Cosmic Rays". *Phys. Rev.* D92.6 (2015) 063011. arXiv:1505.06090 [astro-ph.HE] (cit. on p. 126).

Tilav, S. et al. "Atmospheric Variations as Observed by IceCube". 2010. arXiv:1001.0776 [astro-ph.HE] (cit. on p. 42).

Urry, C. M. and Padovani, P. "Unified schemes for radio-loud active galactic nuclei". *Publ. Astron. Soc. Pac.* 107 (1995) 803. arXiv:astro-ph/9506063 [astro-ph] (cit. on pp. 25, 26, 102).

van Santen, J. "Neutrino Interactions in IceCube above 1 TeV". PhD thesis. The University of Wisconsin, Madison, 2014 (cit. on pp. 30, 31).

Wallraff, M. and Wiebusch, C. "Calculation of oscillation probabilities of atmospheric neutrinos using nuCraft". *Comput. Phys. Commun.* 197 (2015) 185–189. arXiv:1409.1387 [astro-ph.IM] (cit. on p. 14).

Waxman, E. and Bahcall, J. N. "High-energy neutrinos from astrophysical sources: An Upper bound". *Phys. Rev.* D59 (1999) 023002. arXiv:hep-ph/9807282 [hep-ph] (cit. on p. 38).

Whitehorn, N., Santen, J. van, and Lafebre, S. "Penalized Splines for Smooth Representation of High-dimensional Monte Carlo Datasets". *Comput. Phys. Commun.* 184 (2013) 2214–2220. arXiv:1301.2184 [physics.data-an] (cit. on p. 46).

Yepes-Ramirez, H. "Characterization of optical properties of the site of the ANTARES neutrino telescope". *Nucl. Instrum. Meth.* A725 (2013) 203–206 (cit. on pp. 40, 112).

Zatsepin, G. T. and Kuzmin, V. A. "Upper limit of the spectrum of cosmic rays". *JETP Lett.* 4 (1966). [Pisma Zh. Eksp. Teor. Fiz.4,114(1966)] 78–80 (cit. on p. 27).